CI&CEQ

ISSN 1451 - 9372 (Print)
ISSN 2217 - 7434 (Online)
JULY-SEPTEMBER 2024
Vol.30, Number 3, 179-273

Chemical Industry & Chemical Engineering Quarterly

SERBIA
Belgrade
AChE

The AChE Journal for Chemical Engineering,
Biochemical Engineering, Chemical Technology,
New Materials, Renewable Energy and Chemistry

www.ache.org.rs/ciceq

Journal of the
Association of Chemical Engineers of
Serbia, Belgrade, Serbia

Chemical Industry &
Chemical Engineering
CI&CE Quarterly

EDITOR-In-Chief

Vlada B. Veljković
Faculty of Technology, University of Niš, Leskovac, Serbia
E-mail: veljkovicvb@yahoo.com

ASSOCIATE EDITORS

Srđan Pejanović
Department of Chemical Engineering, Faculty of Technology and Metallurgy, University of Belgrade, Belgrade, Serbia

Dunja Sokolović
Faculty of Technical Sceinces, University of Novi Sad, Serbia

Ivona Radović
Faculty of Technology and Metallurgy, University of Belgrade, Serbia

EDITORIAL BOARD (Serbia)

Đorđe Janaćković, Ivanka Popović, Viktor Nedović, Goran Nikolić, Sanja Podunavac-Kuzmanović, Siniša Dodić, Zoran Todorović, Olivera Stamenković, Marija Tasić, Jelena Avramović, Jasna Canadanovic-Brunet, Ivana Karabegović

ADVISORY BOARD (International)

Dragomir Bukur
Texas A&M University,
College Station, TX,
USA

Milorad Dudukovic
Washington University,
St. Luis, MO, USA

Jiri Hanika
Institute of Chemical Process Fundamentals, Academy of Sciences of the Czech Republic, Prague, Czech Republic

Maria Jose Cocero
University of Valladolid,
Valladolid, Spain

Tajalli Keshavarz
University of Westminster,
London, UK

Zeljko Knez
University of Maribor,
Maribor, Slovenia

Igor Lacik
Polymer Institute of the Slovak Academy of Sciences,
Bratislava, Slovakia

Denis Poncelet
ENITIAA, Nantes, France

Ljubisa Radovic
Pen State University,
PA, USA

Peter Raspor
University of Ljubljana,
Ljubljana, Slovenia

Constantinos Vayenas
University of Patras,
Patras, Greece

Xenophon Verykios
University of Patras,
Patras, Greece

Ronnie Willaert
Vrije Universiteit,
Brussel, Belgium

Gordana Vunjak Novakovic
Columbia University,
New York, USA

Dimitrios P. Tassios
National Technical University of Athens,
Athens, Greece

Hui Liu
China University of Geosciences, Wuhan, China

FORMER EDITOR (2005-2007)

Professor Dejan Skala
University of Belgrade, Faculty of Technology and Metallurgy, Belgrade, Serbia

FORMER ASSOCIATE EDITORS

Milan Jakšić, *ICEHT/FORTH, University of Patras, Patras, Greece*
Jonjaua Ranogajec, *Faculty of Technology, University of Novi Sad, Novi Sad, Serbia*

Journal of the
Association of Chemical Engineers of
Serbia, Belgrade, Serbia

Chemical Industry & Chemical Engineering
CI&CE Quarterly

Vol. 30 Belgrade, July-September 2024 No. 3

Chemical Industry & Chemical Engineering Quarterly (ISSN 1451-9372) is published quarterly by the Association of Chemical Engineers of Serbia, Kneza Miloša 9/I, 11000 Belgrade, Serbia

Editor:
Vlada B. Veljković
veljkovic@yahoo.com

Editorial Office:
Kneza Miloša 9/I, 11000 Belgrade, Serbia
Phone/Fax: +381 (0)11 3240 018
E-mail: shi@ache.org.rs
www.ache.org.rs

For publisher:
Ivana T. Drvenica

Secretary of the Editorial Office:
Slavica Desnica

Marketing and advertising:
AChE Marketing Office
Kneza Miloša 9/I, 11000 Belgrade, Serbia
Phone/Fax: +381 (0)11 3240 018

Publication of this Journal is supported by the Ministry of Education, Science and Technological Development of the Republic of Serbia

Subscription and advertisements make payable to the account of the Association of Chemical Engineers of Serbia, Belgrade, No. 205-2172-71, Komercijalna banka a.d., Beograd

Technical Editor:
Marija B. Tasić

Journal manager:
Aleksandar B. Dekanski

Printed by:
Faculty of Technology and Metallurgy, Research and Development Centre of Printing Technology, Karnegijeva 4, P.O. Box 3503, 11120 Belgrade, Serbia

Abstracting/Indexing:
Articles published in this Journal are indexed in *Thompson Reuters* products: *Science Citation Index - Expanded*™ - access *via Web of Science*®, part of *ISI Web of Knowledge*℠

CONTENTS

The activities of the Association of Chemical Engineers of Serbia are supported by:

**MINISTRY OF SCIENCE,
TECHNOLOGICAL DEVELOPMENT
AND INNOVATION
OF REPUBLIC OF SERBIA**

Faculty of Technology and
Metallurgy, University of Belgrade

Faculty of Science, University of Novi Sad

ITNMS
Institute for Technology of Nuclear
and Other Mineral Raw Materials,
Bekgrade

Faculty of Technology,
University of Novi Sad

Institute of Chemistry, Technology and Metallurgy,
University of Belgrade

Faculty of Technical Sciences
University of Novi Sad

Faculty of Technology,
University of Niš, Leskovac

Faculty of Technical Sciences,
University of Priština, Kosovska Mitrovica

IMS Institute, Belgrade

DCP HEMIGAL
Leskovac

Elixir Prahovo

In memoriam

Professor Milan M. Jakšić
(1932-2022)

Professor Milan M. Jakšić was born in Alaksandrovac (1932), near Kruševac, the last capital of medieval Serbia. He received his high school education in this historic town and graduated with a degree from the Department of Physical Chemistry and Electrochemistry of the Faculty of Technology and Metallurgy at the University of Belgrade in 1958. In 1970, he completed his Ph.D. on the subject 'Advances in modified electrochemical technology for chlorate production' at the University of Belgrade.

His professional journey led him to various roles, including managing the chlorine and chlorate plant at the Factory of Plastics and Chemical Products 'Jugovinil,' in Kaštel Sućurac, near Split, Croatia, from 1958 to 1966. Subsequently, he served as the principal investigator in the Center of Electrochemistry at the Institute of Chemistry, Technology, and Metallurgy of Belgrade, where he founded the Industrial Electrochemistry Division from 1966 to 1978.

Professor Jakšić's extensive academic career included positions such as Professor of Electrochemical Processes at the University of Split in Split, Croatia, from 1963 to 1975. Later, he became a Professor of Physical Chemistry at the Faculty of Agriculture, University of Belgrade, from 1978 to 2000. At the same time, he was a Professor of Physical Chemistry of Surfaces at the Center for Multidisciplinary Studies, University of Belgrade, from 1971 to 2000. Additionally, he did postdoctoral research at the Department of Chemical Engineering of the University of California at Berkeley from 1976 to 1978.

Throughout his career, Professor Jakšić made significant contributions to electrocatalysis. He pioneered and established the fundamental principles underpinning contemporary electrocatalysis, dedicating substantial efforts to advancing synergistically active, reversible electrocatalysts for the hydrogen electrode reaction, a milestone in scientific contributions. In addition, he served as a visiting professor at various institutions, such as the University of Trondheim (NTNU) (1989/90) and the Department of Chemical Engineering at the University of Patras, Greece (1992-1994, and 2000-2001). He worked on the EU project 'Apollon' at the Institute of Chemical Engineering and High Temperature Chemical Processes (later, Institute of Chemical Engineering Sciences)/FORTH, Patras (2001-2006). In 2009, he became an Affiliated Member of the Institute.

His dedication and expertise were acknowledged with awards, including the Belgrade City Prize for Advances in chlorate technology in 1974 and the Annual Award of the Serbian Union of University Professors in 1999. In 2004, he became an honorary citizen of the municipality of Aleksandrovac for his exceptional contribution in securing a donation from the Kingdom of Norway to replace asbestos pipes in the water supply network. In 2006, he received the prestigious IAHE Sir William Grove Award from the International Association of Hydrogen Energy "for Outstanding Contributions to the Theory of Electro-Catalysis in Hydrogen Electrode Reactions." Professor Jakšić's scholarly contributions include 130 papers in international scientific journals, 74 plenary and keynote lectures, more than 400 papers at international scientific meetings, and approximately 70 seminars at various universities worldwide. His research has more than 4000 citations in the Scientific Citation Index (SCI) and has left an indelible mark on the scientific community. He also served on the Editorial Board of the Chemical Industry in Belgrade from 2000 to 2007. He was one of the Yugoslav Association of Hydrogen Energy founders in 2000 and an active member of the Academy of Engineering Sciences of Serbia (former Academy of Engineering Sciences of Yugoslavia) since 2000. Notably, from 2007 to 2022, he was Associate Editor of Belgrade's Chemical Industry and Chemical Engineering Quarterly.

Professor Milan M. Jakšić's impactful career left a lasting imprint in the field of electrochemistry and chemical engineering. His pioneering work on metal surface modification through electrodeposition and aqueous electrolysis is crucial in Green Chemistry and a reference point for current and future researchers. He has been a great teacher, inspiring educator, and role model to many generations of students and researchers, transferring his knowledge and experience with passion and dedication. His colleagues greatly respected him for being a visionary with in-depth knowledge and analytic ability while being modest, warm, and willing to help at any time. He was a true scholar dedicated to science. Everyone who knew him remembers him with love and respect.

На основу чланова 8. и 26. Статута општине Александровац ("Службени лист општине Александровац"
бр. 4/2002) и члана 3. Одлуке о установљењу звања почасни грађанин општине Александровац
("Службени лист општине Александровац" бр. 3/2004) Скупштина општине Александровац
на свечаној седници одржаној 02. јула 2004. године
донела је

ОДЛУКУ О ПРОГЛАШЕЊУ ПОЧАСНОГ ГРАЂАНИНА
ОПШТИНЕ АЛЕКСАНДРОВАЦ

ПРОГЛАШАВА СЕ ЗА:

ПОЧАСНОГ ГРАЂАНИНА
ОПШТИНЕ АЛЕКСАНДРОВАЦ

проф. др **МИЛАН ЈАКШИЋ**
за изузетан допринос у обезбеђењу донације
краљевине Норвешке за замену азбестних цеви
водоводне мреже
Митрово поље – Александровац.

СКУПШТИНА ОПШТИНЕ
АЛЕКСАНДРОВАЦ
БРОЈ: 022-33-1/2004
од 02. јула 2004. године
АЛЕКСАНДРОВАЦ

ПРЕДСЕДНИК
скупштине општине
Александровац
Др Чедомир Петковић

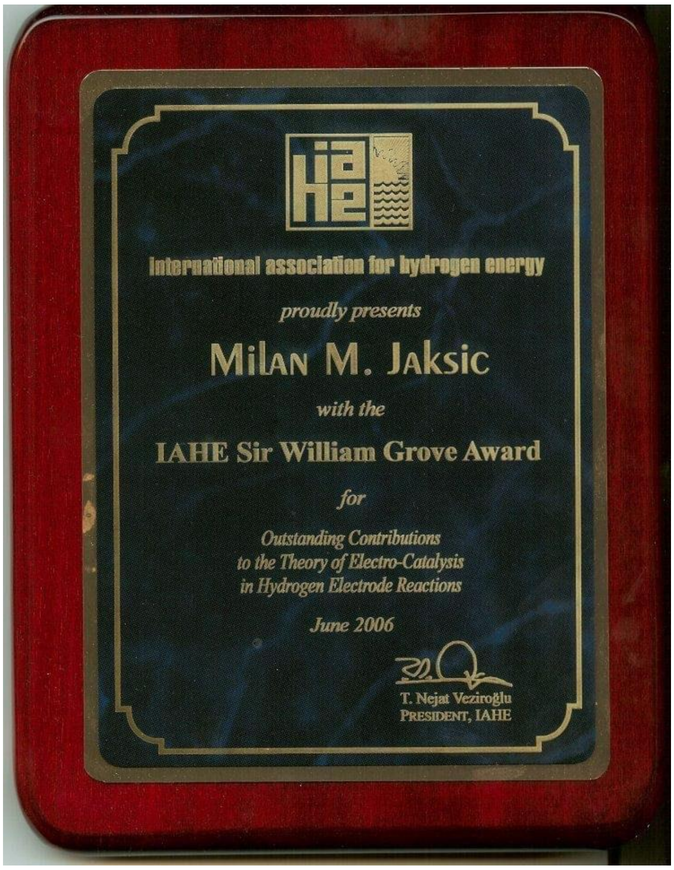

international association for hydrogen energy
proudly presents
MILAN M. JAKSIC
with the
IAHE Sir William Grove Award
for
Outstanding Contributions
to the Theory of Electro-Catalysis
in Hydrogen Electrode Reactions
June 2006

T. Nejat Veziroğlu
PRESIDENT, IAHE

CI&CEQ
Chemical Industry & Chemical Engineering Quarterly

Available online at
Association of the Chemical Engineers of Serbia *AChE*
www.ache.org.rs/CICEQ

Chem. Ind. Chem. Eng. Q. 30 (3) 179–192 (2024) CI&CEQ

ANANTHAKUMAR SUDALAIMANI[1]
BARATHIRAJA RAJENDRAN[2]
THIYAGARAJ JOTHI[3]
ASHOKKUMAR MOHANKUMAR[4]

[1]Department of Mechanical Engineering, Government College of Engineering. Tirunelveli,Tamil Nadu, India

[2]Department of Mechanical Engineering, Einstein College of Engineering, Near MS University, Tirunelveli, Tamil Nadu, India

[3]Department of Mechatronics Engineering, Er. Perumal Manimekalai College of Engineering, Hosur, Tamil Nadu, India

[4]Department of Mechanical Engineering, Government College of Engineering, Bargur, Krishnagiri, Tamil Nadu, India

SCIENTIFIC PAPER

UDC 66:665.3:620

EFFECTS OF EXHAUST GAS RECIRCULATION ON DIESEL ENGINE USING HYBRID BIODIESEL

Article Highlights

- Diesel engines may run on hybrid blends up to 100% without any changes
- EGR rates and appropriate hybrid mixes can solve the smoke/NOx trade-off
- With the addition of WPO to the engine, engine performance is marginally reduced
- Up to a specific load range, CO emissions may be regulated; after that, they start to grow.

Abstract

The primary aim of this study is to alternate between conventional fossil fuels and reduce the emissions of greenhouse gases and sulfur dioxide from diesel engines. In the current study, to mitigate NOx emissions, the exhaust gas recirculation (EGR) technique was implemented utilizing hybrid alternate biodiesel at three varying proportions of 5%, 10%, and 15% at an optimum compression ratio of 20:1. The findings demonstrate that for hybrid alternative biodiesel at a compression ratio of 20:1 and fully loaded, the brake thermal efficiency (BTHE) is 31.8% with 10% EGR. With 15% EGR, the peak pressure for the hybrid biodiesel is lower than it would be without EGR by around 2.28%. When EGR is increased, the ignition delay and NOx emissions are reduced slightly. With only an increase in EGR rates of up to 10%, brake-specific fuel consumption (BSFC) values were reduced efficiently. The hybrid biodiesel with 10% EGR reduces exhaust gas temperature to 341 °C.

Keywords: exhaust gas recirculation, combustion, performance, emission, waste plastic oil; rubber seed oil.

Biofuels encompass various alternative fuels, including biogas, producer gas, natural gas, hydrogen, alcohol, and vegetable oils. However, among these options, biodiesel is a desirable substitute for the automobile industry, particularly in diesel engines. Biodiesel is the most versatile energy source, contributing to approximately 10% of global energy consumption. This renewable fuel has transitioned into a modern, globally traded product, making significant strides in the automotive and electricity sectors. Energy independence and climate change mitigation are the two main drivers of biodiesel development. Biodiesel is the most feasible and sustainable option for replacing gasoline and diesel in isolation or as blends with petroleum-based fuels. Using liquid biodiesel for transportation is a vital strategy to enhance fuel security, foster rural development, and create employ-

---

Correspondence: B. Rajendran, Department of Mechanical Engineering, Einstein College of Engineering, Near MS University, Tirunelveli – 627 012, Tamil Nadu, India.
E-mail: barathiraja.r@einsteincollege.ac.in
Paper received: 3 March, 2023
Paper revised: 3 August, 2023
Paper accepted: 23 August, 2023

https://doi.org/10.2298/CICEQ230303022A

ment opportunities for individuals worldwide.

Biodiesel is made from vegetable oil and usually works in diesel engines run on diesel fuel [20]. Enzymes can be used as catalysts in biodiesel production using sustainable feedstocks. Research on innovative and sustainable biodiesel production technologies to boost output and improve performance might be necessary for competitive biodiesel. Biodiesel is less expensive than fossil fuel, renewable, nontoxic, and doesn't cause global warming. Also, due to the abundance of plastic waste and its potential for use as energy, scholars are very interested in the pyrolysis of plastic waste to reduce pollution and energy crises. Several studies have looked into using plastic oil as an alternative fuel. Waste plastic oil (WPO) may be used for internal combustion engines since it has similar heating values, density, and cetane index to diesel fuel [1]. The literature further suggests that diesel engines may achieve comparable performance, stability, and efficiency by using waste plastic oil [2]. Rafael *et al.* [3] raised the main issues concerning the recent development of plastic-added biodiesel and its blend characteristics, fuel qualities, combustion quality, and environmental impact. Damodharan *et al.* [4] looked into the separation and analysis of WPO from the catalytic pyrolysis process. It helped them determine what the oxygenated *n*-butanol (B) component looks like. The blends D50-WPO30-B20, D50-WPO40-B10, and D50-WCO20-B30 are used as fuels. The B10 blend reduces NOx emissions compared to WPO and diesel. However, compared to WPO, the B30 mix emits more NOx. As the *n*-butanol proportion in the mix rises, brake thermal efficiency (BTE) and fuel usage improve. For compression ignition (CI) engines that work well with WPO, n-butanol could be a feasible additive.

Using WPO mixes in a CI engine, Sachin *et al.* [5] analyzed the performance and emission characteristics. It has been shown that WPO mixes have a lower BTE and a higher brake-specific fuel consumption (BSFC) and exhaust gas temperature. The NOx and CO emissions increase, but the hydrocarbon emissions decrease with an increase in WPO blends. WPO is tested in a CI engine, and its performance parameters were investigated by Mani *et al.* [6]. According to reports, an engine running at 100% WPO emits more NOx, CO, hydrocarbons (HC), and smoke than a diesel engine. Furthermore, the exhaust gas temperature is higher, and the BTE is higher up to 80% of the load.

Recent studies have been performed on the combustion and operative parameters of a CI engine running on hybrid alternative mixtures, such as canola oil and waste palm oil [7], Jatropha and soap nut oils [8], methyl ester of paradise and eucalyptus oil [9], palm and *Calophyllum inophyllum* oil [10], hazelnut soap stock and waste sunflower oil [11], palm and coconut biodiesel blend [12], pal and jatropha biodiesels with additives [13], and sunflower and cottonseed oil methyl esters [14].

Habibullah *et al.* [12] studied the effects of a palm and coconut biodiesel mix (PB20, CB20, PB15CB5, PB10CB10, and PB5CB15) in a CI engine. Higher reductions in BTE, increased BSFC, and NOx emissions are observed for the CB20 blend compared with the PB20 blend. Whereas combined blends reduced NOx emissions and improved BTE and BSFC. The characteristics of blends containing waste sunflower oil and hazelnut soap stock at 5%, 10%, 15%, 17.5%, and 25% were evaluated by Usta *et al.* [11]. The results indicated that a 17.5% blend had the highest BTHE; however, all mixes had greater NOx, CO, and exhaust temperatures than diesel fuel. Performances and emissions of a compression ignition engine operated on a combination of palm and C*alophyllum inophyllum* oil were assessed by Ashrafur *et al.* [10]. Both biodiesel and diesel mixes exhibit higher BSFC and lower EGT than diesel. For higher blends, NO_X emissions increase, whereas CO and HC emissions decrease.

One of the most effective, versatile, and dependable emission reduction solutions for decreasing NOx emissions is exhaust gas recirculation (EGR). The following modifications take place during diesel engine combustion when EGR percentages rise: (i) a higher specific heat capacity, which lowers both the chamber and localized flame temperatures; (ii) a longer flame expansion due to a lower inlet oxygen content, which lowers the local temperature. (iii) When H_2O and CO_2 are cycled, an endothermic disintegration process begins, lowering the flame temperatures [15]. The EGR hydrogen engine was suggested by Ming *et al.* [16] after reviewing the usage of EGR and its effects on diesel engines. Several studies have recently examined the combustion and performance of the CI engine running on biodiesel at various EGR rates, such as soybean biodiesel [17], mahua methyl ester [18], WPO [19], rubber seed oil blends [20], rapeseed methyl ester blends [21], jatropha blends [22], *n*-pentanol blends [23], cotton seed biodiesel blends [24], soybean oil [25], jojoba oil [26], waste apple seeds [27], and chicken wastes [28].

Mani *et al.* [19] inspected the consequences of cooled EGR in a CI engine operated with clean WPO. The results showed that NOx discharges are higher without EGR but up to 20% lower with cooled EGR. Additionally, it has been shown that 20% cooled EGR emits less smoke, CO, and HC. In a CI engine with a cooled EGR, Ramadhas *et al.* [20] inspected the emission and performance parameters of rapeseed oil (RSO) mixes. Due to the reduced temperature in the combustible chamber, the emissions of NOx were also decreased. The BTE of the CI engine increases with EGR. While the emissions of HC and CO rise, the opacity of the smoke remains constant.

Saleh [26] investigated the impact of recirculation of exhaust gases (5–15%) on a CI engine running on biodiesel made from jojoba. The outcomes demonstrated an improved interchange between NOx, HC, and CO releases with an EGR of 5%–15% when NOx emissions were reduced. Rajesh and Saravanan [23] investigated the efficiency and exhaust releases of a CI engine running on several n-pentanol blends of 10, 20, 30, and 45% with varying levels of recirculation of exhaust gas (10%, 20%, and 30%). The findings demonstrated that NOx emissions should be reduced by increasing EGR rates for a 45% blend. However, smoke opacity hardly increased. Further, hydrocarbons and carbon monoxide emissions are observed to be increased for all EGR conditions. Srinivasa [24] experimentally investigated a CI engine running on a mix of biodiesel made from cotton seeds (10%, 20%, and 30%) with various EGRs of 0%, 5%, 10%, 15%, and 20%. The reduction in NO_X emissions is observed for all blends with 15% EGR compared to other EGR rates.

Ibham *et al.* [29] examined the homogeneous charge compression ignition-direct ignition (HCCI-DI) engines using acetone, butanol, and ethanol blends. Acetone, butanol, and ethanol blends minimized NOx emissions while enhancing BTHE and fuel economy. Christopher *et al.* [30] assessed the performance of biodiesel fuels produced from locally sourced canola and sunflower oil feedstocks in South Africa. They claimed that while nitrogen oxide emissions were higher with biodiesel and its diesel blends, smoke emissions were lower.

Based on extensive literature, EGR has emerged as a well-established technique for reducing NOx emissions in compression ignition (CI) engines. This method involves recirculating exhaust gases, effectively diluting the intake air and lowering the combustion temperature, decreasing NOx emissions. However, some research has been examined thus far on applying hybrid alternative biodiesel (specifically, no study has been conducted on a blend of 20% rubber seed oil and 80% waste plastic oil) at an optimized compression ratio of 20:1 in combination with EGR. To address this research gap, a recent experimental investigation employed a novel approach that involved variable EGR rates (0%, 5%, 10%, and 15% based on volume) with the hybrid alternative biodiesel while maintaining a constant compression ratio. The foremost objective was to examine the special effects of EGR on combustion, performance characteristics, and emissions. These findings were then compared with those of standard diesel fuel and plain waste plastic oil to evaluate the potential benefits and drawbacks of the EGR strategy when combined with the hybrid alternative biodiesel.

MATERIALS AND METHODS

Production of rubber seed oil's methyl ester

Jatropha curcas, *Madhuca indica*, *Pongamia pinnata*, Rubber seed oil, etc., are examples of non-edible vegetable oils. Rubber seed is the cheapest and most widely available. India, an agricultural nation, is essential to producing rubber seed. A rubber tree may grow to a height of 25 to 35 meters. In India, 2.5 lakh hectares of rubber plantations generate 35,000 metric tons of seeds and 5,400 metric tons of raw oil annually from those seeds [20].

Figure 1a shows the representation of the rubber seed oil transesterification process. It has two esterification processes: acid esterification and alkaline esterification. This transesterification process can reduce free fatty acids from 22% to 2% while also lowering viscosity. After the transesterification procedure, rubber seed oil's methyl esters were produced.

Production of WPO

Nowadays, plastic materials are widely used, and the disposal of plastic waste is a serious problem. There are different methods of disposing of plastic waste, such as land filling, incineration, pyrolysis, and recycling. The most significant waste plastics are strapping, cable sheathing, plastic film, crates, pipes, and waste plastic from bottles, pots, tubs, and trays.

Waste plastics may be recycled in two different ways. They are recycling processes that use heat and catalysts to break down waste plastic. Thermal degradation is a simple method, whereas catalytic degradation uses the correct proportion of catalyst to plastic waste to yield the maximum amount of liquid hydrocarbon. In the current study, the thermal pyrolysis degradation of solid waste plastics is carried out in the absence of air at temperatures ranging from approximately 500 °C to 800 °C. Pyrolysis yields char and bio-oil. Temperature and heating rate are the key factors affecting how much bio-oil is generated during pyrolysis.

The pyrolysis plant's schematic design is shown in Figure S1 (Supplementary material). The pyrolysis

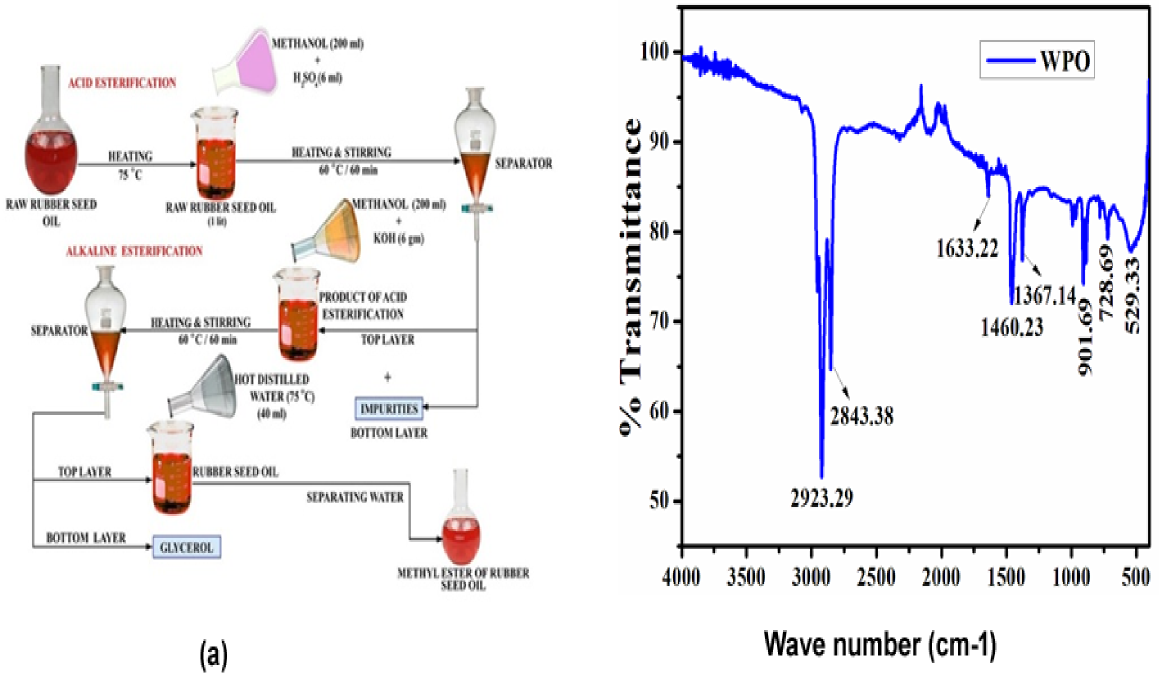

(a)

(b)

Figure 1. Diagram of (a) RSO esterification process (b) FTIR analysis of WPO.

plant consists of a reactor and a condenser unit. A thin sheet encloses the stainless-steel reactor, which has a diameter of 1300 mm. Three 1500-watt electrical heater coils are fixed to the reactor. Glass wool acts as an insulator and is placed between the reactor and the thin sheet. The reactor consists of a mechanical stirrer with motor, safety valve, pressure gauge, feed hopper with control valve, K-type thermocouple, hand hole, and control panel. The purpose of the stirrer is to ensure thorough mixing of the mixture and to uphold a temperature range of 500 °C to 700 °C within the reactor. The excess pressure is released through the safety valve. The reactor's temperature is measured by the thermocouple, displayed in the indicator on the control panel, and controlled by the controller. Following the pyrolysis process, approximately 20 to 25 percent of the waste is removed via a hand hole with a stopcock through the reactor's bottom. The reactor outlet is fixed to the condenser, which consists of a water container and cooling coil through which plastic vapor is condensed. The cooling coil is made up of a stainless-steel tube with a 20 mm diameter and 1800 mm length and is kept inside the water container with a 300 mm diameter and 500 mm height. The container has inlet and outlet valves through which water is circulated.

The condensed liquid is collected in a fuel collection tank made of stainless steel, and the time for delivery of the liquid fuel is around 3.5 hours after the start of the pyrolysis process. The uncondensed gas is passed through an AVL 444 DiGas analyzer, then through a flame arrester containing water to prevent the backfire. Then, washed, uncondensed gas flows through the burner to produce a blue flame that reduces the pollutant in the atmosphere. The condensed liquid from the pyrolysis plant is fractionated using a distillation unit to produce WPO.

Fourier transform infrared spectroscopy (FTIR) analysis of waste plastic oil

The Agilent Cary 630 FTIR spectrometer with an ATR (Attenuated Total Reflectance) detector was used to find all the functional groups in waste plastic oil. The spectral range was from 4000 cm^{-1} to 500 cm^{-1}, with the highest resolution of 2 cm^{-1}. The findings of the WPO's FTIR investigation are shown in Figure 1b. The location of different bond vibrations, such as stretching, distortion, and bending, is described by many distinct peaks.

Table 1 lists the portion of the WPO spectrum that is distinctive. It can be seen from the FTIR spectra that the waste plastic oil has a peak at 2923.29 $cm^{-1,}$ which corresponds to the stretching of hydrogen bonds and the stretching vibration of O-H bonds. Different peaks may be found in the FTIR spectra of WPO, ranging from 1633.22 to 529.33 cm^{-1}. Due to its strong bonding structure with rubber seed oil, the phenolic bond of WPO is the most significant one. There is no phase

Table 1. Characteristic region of WPO spectra.

WPO wave number	Chemical bond	Functional groups	Mode of vibration
529.33	Alkyl halides	C-Br	Stretch
728.69	Alkanes, Aromatics, Alkyl halides	CH_2, C-H, C-Cl	Bend, Bend (mono), Stretch
901.69	Alkenes, and anhydrides	C-H, C-O	Bend (monosubstituted), Stretch
1367.14	Alkanes, alkenes, ethers, ketones, alcohols and phenols	CH_3, C-O-C, C-C, O-H, C-H,	Bend, Bend in plane, Stretch (dialkyl), Stretch
1460.23	Alkanes and aromatics	CH_2, C=C	Bend, Stretch
1633.22	Alkenes, acids, and amides	C=C, C=O	Stretch (isolated & conjugated)
2843.38	Alkanes, aldehydes, and benzoic acid	C-H, O-H	Stretch, Aldehyde stretch
2923.29	Alkanes, benzoic acid, alcohols and phenols	C-H, O-H	Stretch

separation between these two oils when mixing.

Physiochemical properties of diesel, RSO, and WPO

The unique and important properties of biodiesel are cetane number, heating value, viscosity, etc. The viscosity of the biodiesel is a significant property because it influences the vaporization and atomization of the biodiesel. Compared to diesel, it is more lubricating and has higher cetane values. It helps in complete combustion, which increases the engine's energy output. The characteristics of biodiesel also contribute to less fuel system wear and longer fuel injector equipment life. The liquid biodiesel can range in color from golden to dark brown and has a high boiling point but little vapor pressure. Biodiesel has a density of 860 kg/m^3, which is less than water's density, and a flash and fire point that is significantly greater than that of diesel. It has a lower calorific value than diesel and almost no sulfur. Hence, it is used as an additive to diesel. Table 2 summarises the significant physiochemical characteristics of diesel, RSO, and WPO.

Table 2. Diesel, RSO, and WPO's physiological and chemical characteristics.

Properties	Diesel	RSOME	WPO	R-20/P-80
Specific gravity at 15 °C	0.82	0.8102	0.9155	0.893
Net Calorific value, kJ/kg	44800	38650	43340	41362.4
Flash point, °C	50	66	54	56
Fire point, °C	57	68	56	58
Kinematic viscosity at 40 °C, cSt	2	12.75	3.18	3.704
Cetane index	50	56	51	38.4
Water content, wt. %	0.025	0.3	0.01	0.065
Oxygen by difference, %	Nil	22	1.5	5.6

Experimental setup

The EGR system, instrumentation, and experimental setup specifics employed in this study are provided. Figure 2 displays a photographic representation of the experimental setup. An engine with a rated output of 3.7 kW @ 1500 rpm and built on the Kirloskar platform was used in this inquiry. It was vertical, naturally aspirated, and water-cooled. The engine was loaded and unloaded using an eddy current dynamometer coupled to a strain gauge load cell. A Cityzen piezoelectric, air-cooled, durable pressure sensor with a built-in charge amplifier and 360° pulse crank angle encoder was included in this configuration to monitor the combustion pressure and associated crank angle. Data acquisition (DAS) systems were used to gather, store, and analyze data while conducting experiments, and they link pressure sensor inputs to computers.

The cooling water circulation to the engine and calorimeter was measured using rotameters–the computer's "Engine Test Express v14" software package analyzed combustion and engine performance. A burette with top and bottom optical sensors was used to assess fuel usage. The top sensor signals the DAS to begin the counter time as soon as fuel has flowed through it. When fuel reached the bottom sensor, it signaled the DAS to halt the timer and replenish the burette from the fuel tank. This process was repeated three times. It allowed for calculating the engine's mass fuel consumption at varied loads. The air mass consumed was determined using a differential pressure sensor installed in the air surge tank. A K-type thermocouple (AD595) installed in the exhaust manifold measured exhaust gas temperature. A non-contact proximity speed sensor of the PNP (positive negative positive) kind that was mounted close to the flywheel was used to measure the engine speed. Table 3 contains all of the test engine's data.

Exhaust gas recirculation system (EGR)

EGR is one of the best and most often used methods for lowering the output of NOx from internal

Figure 2. Photo view of experimental set-up.

Table 3. Technical details of the experiment's configuration.

Particulars	Specifications
Make and Model	Variable compression ratio multi-fuel, vertical, water-cooled, direct injection, naturally aspirated engine. Legion Brothers, Bangalore, modified the engine to change the compression ratio arrangement. The Kirloskar AV1 engine makes the base crankcase.
Compression ratio range	6:1 to 20:1
Rated brake power	3.7 kW
Rated speed	1500 rpm
No. of cylinders / No. of strokes	01 / 04
Bore x Stroke	80 x 110 mm
Displacement volume	552.64 cc
Nozzle opening pressure	200 bar
Maximum load	10 kg
Speed measurement	PNP-type non-contact proximity speed sensor
Fuel flow measurement	Make - HONEYWELL; Model - LLE102000.
Airflow measurement	Make - Silicon Microstructure Incorporated; Model - SM5812/SM5852
Software	“Engine Test Express v14” Engine performance analysis software

combustion engines. EGR comes in two different varieties: cooled and uncooled. The former is efficient because cooled exhaust gas is mixed with fresh air in the air surge tank, which reduces the temperature and oxygen proportion necessary for combustion.

The EGR maximizes the specific heat of the input charge due to mixing, which results in minimum flame temperatures for a given combustion chamber heat release. This mixture’s entrance into the engine cylinder lowers the maximum temperature in the combustor, which lowers the generation of NOx. The cooled dissipative gas temperature was maintained below the atmospheric temperature by varying the circulation rate of cold water circulated through the EGR unit. The cooled exhaust gas was passed through a fabric filter before entering the surge tank because the surge tank had particulate matter and soot, which affected the burning phenomenon. The exhaust gas was taken through an orifice in the manifold and sent to the gas regulator system to regulate the recirculation quantity. Generally, the range of EGR was about 5% to 20% of exhaust gas.

Utilizing a differential pressure sensor, the flow rate of EGR was calculated by measuring the EGR volume in millimeters of water column. The volume of EGR in the air surge tank divided by the total charge introduced into the cylinder was used to compute the EGR percentage (Sum of engine air intake and EGR volume in millimeters of water column). EGR% equals [volume of EGR/total charge injected into the cylinder] * 100. The benefits of EGR are as follows: EGR can be used in engines without affecting efficiency or fuel economy. It also reduces NOx emissions. The EGR unit is shown in Figure S2.

Experimental errors and uncertainties

The measuring instruments used in the tests were standardized, and the error rates for each were calculated to lower the measurement error rate to the lowest percentage achievable.

Total percent of uncertainty = $\sqrt{}${ uncertainty of $[(TFC)^2 + (load)^2 + (BTHE)^2 + (CO)^2 + (HC)^2 + (NOx)^2 + (SO)^2 + (EGT)^2 + (pressure\ pickup)^2]\} = \sqrt{}\ \{(1)^2 + (0.2)^2 + (1)^2 + (0.2)^2 + (0.2)^2 + (0.2)^2 + (1)^2 + (0.15)^2 + (1)^2\} = \pm$ 2.28 %.

RESULTS AND DISCUSSION

Six experiments were conducted to evaluate performance factors, such as BTHE and BSFC emissions, including NOx, CO, UBHC, smoke, and EGT. These experiments involved varying the fuel and EGR conditions. The initial test exclusively employed diesel fuel, the second utilized WPO exclusively, and the other four employed hybrid biodiesel. The hybrid biodiesel experiments were conducted under different EGR conditions: without EGR, with 5% EGR, 10% EGR, and 15% cooled EGR. All tests were conducted on a compression ignition engine with an optimum compression ratio of 20:1.

Diagram of a pressure-crank angle

Figure 3a illustrates the variations in cylinder pressure patterns under different load conditions for various fuel types and EGR percentages. At full load, diesel exhibits a peak pressure of 62 bar, while hybrid biodiesel without EGR reaches a peak pressure of 70 bar. For hybrid biodiesel with 5%, 10%, and 15% EGR at full load, the peak pressures are 69.1 bar, 68.54 bar, and 68.4 bar, respectively. The maximum pressure for WPO without EGR and at full load is 67 bar.

The decrease in combustion chamber pressure can be observed as the EGR percentage increases. When the EGR circulation rate increases from 0% to 5%, peak pressure readings are lower by 1.28%. Similarly, as the EGR circulation rate rises from 5% to 10%, peak pressure values decrease by around 0.81%. Additionally, as the EGR circulation rate rises from 10% to 15%, peak pressure values decrease by around 0.2%. In the case of hybrid biodiesel with 15% EGR, the peak pressure is approximately 2.28% lower than it would be without EGR. The fundamental cause is that introducing these exhaust gases absorbs the heat energy released during combustion, thereby reducing the cylinder pressure [17].

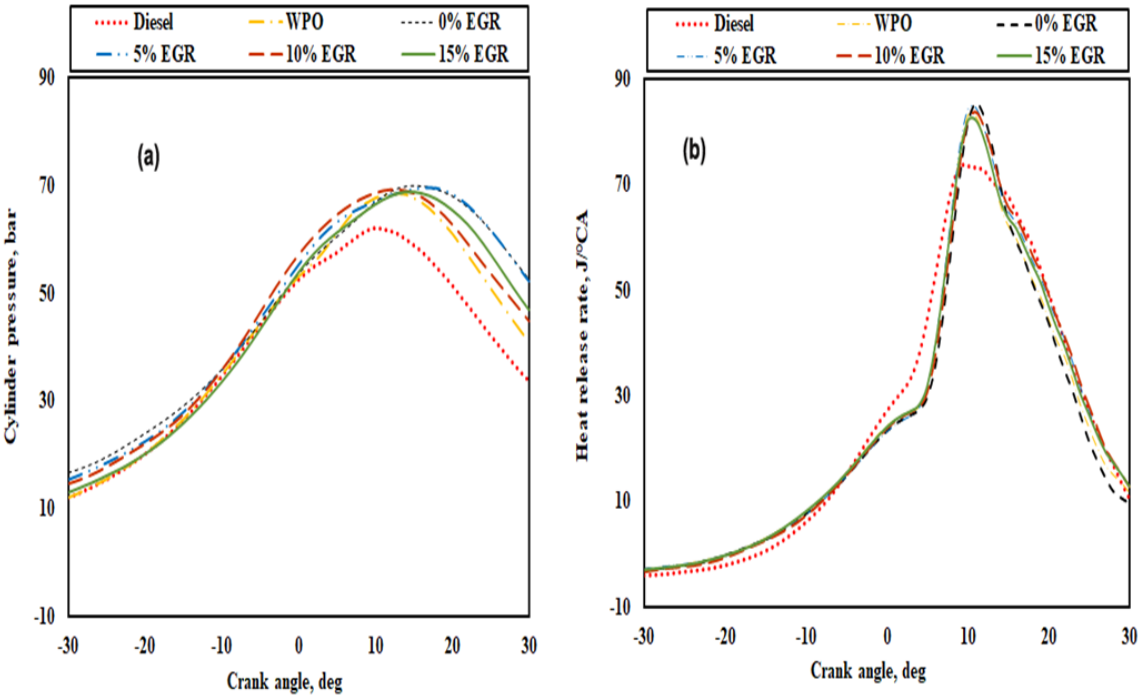

Figure 3. Variation of engine parameters at full load conditions (a) Pressure versus crank angle (b) HRR versus crank angle.

Rate of heat releas

Figure 3b depicts the variation in the heat release rate for the studied fuels at different EGR percentages under typical operating conditions at full load and various crank angles. The heat energy potential in the heat release rate curve is transformed into useful work. In correlation with the increase in EGR levels, Figure 3(b) illustrates a decline in the maximum heat release rate. Under typical operating conditions, diesel and WPO exhibit maximum heat release rates of 73 J/°CA and 83 J/°CA, respectively. However, its value decreases for hybrid fuel at full load from 85.38 J/°CA without EGR to 82.28 J/°CA with 15% EGR. Additionally, it is noteworthy that for hybrid biodiesel at 100% load, the peak rate of heat release values are 84.61 J/°CA and 83.79 J/°CA for 5% and 10% EGR, respectively. As the EGR circulation rate rises from 0% to 15%, the reduction in heat release rate values is around 3.63%. Conversely, as the EGR circulation rate rises from 5% to 10%, the reduction in heat release rate values is around 0.96%. The drop-in heat release rate is attributed to the drop in oxygen concentration, accompanied by a rise in EGR level and a shorter ignition delay. The primary factor contributing to the reduction in NOx emissions is the decrease in heat release rate, which leads to a decrease in peak combustion temperature [19]. The hybrid biodiesel exhibits higher heat emission capacity without EGR operation owing to the availability of excess oxygen for the combustion process.

Ignition delay

The delay period, commonly called ignition delay, denotes the period or crank position stuck between the initiation of injection and the onset of ignition. Ignition delay can be divided into two components: physical and chemical. For fuel to be atomized, mixed, and vaporized, there must be a physical delay. Chemical delay encompasses pre-combustion reactions that impact the thermodynamic efficiency and pre-combustion mixture of air and fuel vapor. Several factors influence the delay period, including injection pressure, nozzle orifice size and design, cylinder air pressure and temperature, fuel viscosity, droplet size distribution, droplet velocities, and fuel volatility. The delay time impacts in-cylinder pressure, NOx emissions, the combustion phase, and the heat release rate. Under normal operating conditions, the ignition delays of hybrid biodiesel are compared across different EGR percentages and load conditions for all investigated oils, as shown in Figure 4a. Without EGR and at full load, the ignition delays for diesel and hybrid biodiesel are 10.8 °CA and 10.5 °CA, respectively. The ignition delays for hybrid biodiesel with 5, 10, and 15% EGR at full load are 10.3 °CA, 10.21 °CA, and 10.11 °CA, respectively. WPO exhibits an ignition delay of 11.8 °CA at full load without EGR.

With the rise in the EGR circulation rate from 0–5%, there is a 1.9% reduction in ignition delay values. Similarly, when the EGR circulation rate rises from 10–15%, the reduction in ignition delay values is around 0.98%. It can be observed that all ignition delays for hybrid biodiesel tend to decrease as the load and EGR increase. It is primarily due to higher internal temperatures at increased loads, which decrease chemical delay and consequently shorten the ignition delay period. Additionally, as the EGR percentage rises, the inlet air temperature increases due to EGR, contributing to a slight decrease in ignition delay [23].

Cylinder peak pressure

Figure 4b shows the results of the study, which looked at how the maximum cylinder pressure changed with load for different fuels with and without EGR. The figure demonstrates that the highest pressure in the cylinder increases with increasing load and decreases with higher EGR flow rates. The amount of fuel delivered, the petroleum fuel volatility, and the ignition delay duration are the key factors determining the maximum cylinder pressure. At full load, the relative peak pressures in the diesel and hybrid biodiesel cylinder are 62 bar, 70 bar, 69.1 bar, 68.54 bar, and 68.4 bar at 0%, 5%, 10%, and 15% EGR, respectively. WPO's maximum cylinder pressure at full load without EGR is 67 bar. When the EGR circulation rate rises from 0% to 5%, the reduction in cylinder peak pressure is around 1.28%. Similarly, when the EGR circulation rate rises from 10% to 15%, the reduction in cylinder peak pressure values is around 0.2%. It is noted that the decrease in maximum cylinder pressure is more significant from 0% to 15% EGR rates due to the reduction in oxygen within the engine cylinder [19].

Brake thermal efficiency (BTHE)

The variation in braking thermal performance for the studied fuels at different EGR rates under varying loads is depicted in Figure 4c. For diesel, WPO, and hybrid biodiesel without EGR operation, the BTHEs are 26.8%, 23.4%, and 30.5%, respectively, at full capacity. When the vehicle is fully loaded, the BTHE is 31% with 5% EGR, 31.8% with 10% EGR, and 31.5% with 15% EGR. When the EGR circulation rate rises from 0–5%, the increase in BTHE is around 1.63%. Similarly, when the EGR circulation rate rises from 5–10%, the increase in BTHE is around 2.58%. The return of exhaust gas to the engine leads to an elevation in the temperature of the intake charge, a faster combustion velocity, and the mixing of dissipated gases with fresh air, resulting in improved fuel combustion.

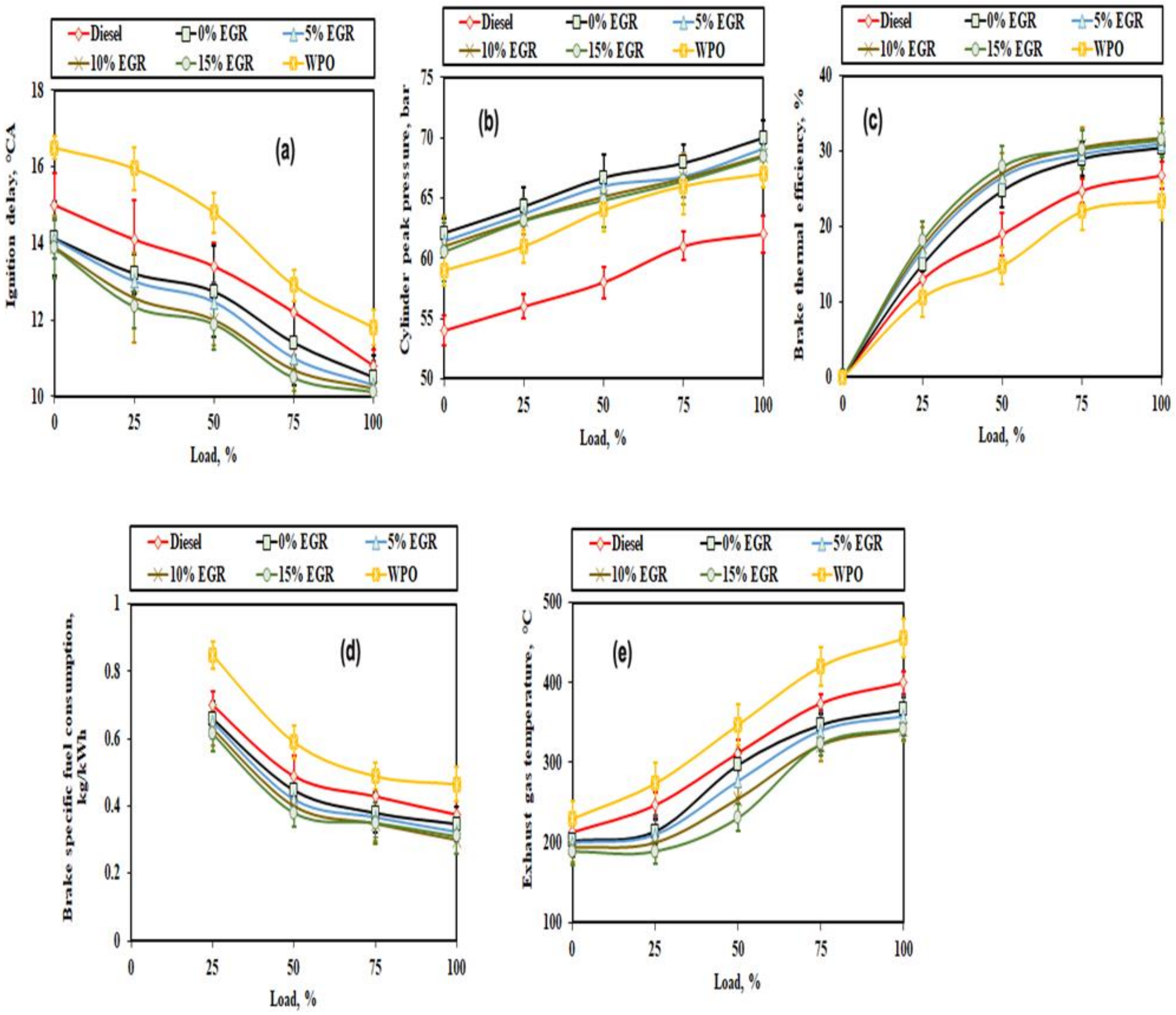

Figure 4. Variation of engine parameters at different load conditions: (a) Ignition delay; (b) Cylinder peak pressure; (c) Brake thermal efficiency (d) Brake specific fuel consumption; (e) Exhaust gas temperature.

Consequently, the thermal efficiency of the engine experiences a marginal increase. A contrasting observation occurs when the EGR circulation rate rises from 10 to 15%. In this scenario, there is a slight decrease of approximately 0.94% in BTHE values. The presence of CO_2 and unburned hydrocarbons in the exhaust gas can potentially reduce oxygen availability in the combustion chamber, causing a decline in BTHE values for the diesel engine [24]. It is important to note that the optimal EGR rate for achieving the highest thermal efficiency may vary depending on specific engine design, fuel type, and operating conditions. Excessive dilution from excessively high EGR rates can negatively impact combustion and overall thermal efficiency.

Brake specific fuel consumption (BSFC)

Figure 4d illustrates the deviation in BSFC for the investigated fuels under varied loads and EGR rates. At 0% EGR and full load, the BSFC values for WPO and diesel are 0.465 and 0.375 kg/kWh, respectively. While the vehicle is fully loaded, the BSFC values for hybrid biodiesel blends are 0.347, 0.324, 0.3, and 0.31 kg/kWh for 0, 5, 10, and 15% EGR, respectively. With a rise in the EGR circulation rate from 0–5%, there is a slight decrease of approximately 6.63% in BSFC values. Similarly, with a rise in the EGR circulation rate from 5 to 10%, there is a 7.4% decrease in BSFC. BSFC decreases up to 10% of the EGR rate. The recirculated exhaust gases contribute energy to the fresh air and fuel mix during burning, reducing the amount of hybrid biodiesel consumed. As a result, fuel consumption related to braking is reduced. However, with an increase in the EGR circulation rate from 10–15%, there is a slight increase of approximately 3.33% in BSFC values. It increases in BSFC at a 15% EGR rate and at 75% and 100% load, which can be attributed to forming a rich mixture and reducing in-cylinder temperatures, leading to incomplete combustion [25].

Exhaust gas temperature

Figure 4e showcases the variations in EGT for the studied fuels under varied loads and EGRs. As can be seen, at full load, the exhaust temperatures for waste plastic oil and diesel are 455 °C and 400 °C, respectively, while the EGT for hybrid biodiesel without EGR is 366 °C. For hybrid biodiesel at full load with 5% EGR, the exhaust gas temperature is 358 °C; with 10% and 15% EGR, it decreases to 341 °C and 342 °C, respectively. When the EGR circulation rate rises from 0–5%, there is a slight decrease of approximately 2.18% in EGT values. Similarly, with a rise in the EGR circulation rate from 5–10%, the reduction in EGT is around 4.74%. The peak combustion temperature decreases as the EGR increases. It indicates a more efficient heat energy utilization with a shorter ignition delay. As a result, the exhaust gas temperature decreases, leading to a reduction in NOx emissions. Increased mixing duration, prolonged burn dilution, a higher heat capacity mixture, and separation from the more complex EGR molecules contribute to the lowered flame temperatures and subsequent decrease in EGT [20].

Oxides of nitrogen emissions

Most NOx emissions consist of nitrogen dioxide and nitric oxide, and their levels are influenced by temperature, oxygen content, and reaction rate. Figure 5a illustrates the significant reduction in NOx emissions achieved by implementing EGR for the studied fuels. Observed NOx emissions for WPO, diesel, and hybrid biodiesel at full load are 1010 ppm, 820 ppm, and 1095 ppm, respectively, without EGR activation. At full load, hybrid biodiesel NOx emission values are 1059 ppm, 900 ppm, and 800 ppm, respectively, for 5%, 10%, and 15% EGR.

With a rise in the EGR circulation rate from 0–5%, there is a 3.28% decrease in NOx emissions. Similarly, as the EGR circulation rate rises from 5% to 10%, the reduction in NOx is around 15%. Additionally, with a rise in the EGR circulation rate from 10% to 15%, there is an 11.11% decrease in NOx emissions. The primary factors contributing to the decrease in NOx emissions with increasing EGR percentages are the increase in total working gas heat capacity and the decrease in combustion temperature. It might be because the exhaust fumes contain inert gases like carbon dioxide and water vapor. When these exhaust gases are recirculated and blended with the intake air, the ancillary gases absorb the heat energy generated during burning, lowering the combustion temperature. Moreover, the EGR substitutes air for O_2 in the combustible chamber, lowering the combustion temperature. At higher EGR rates, NOx emissions can be significantly reduced. On the other hand, higher EGR rates result in higher emissions of HC, CO, and smoke opacity [26].

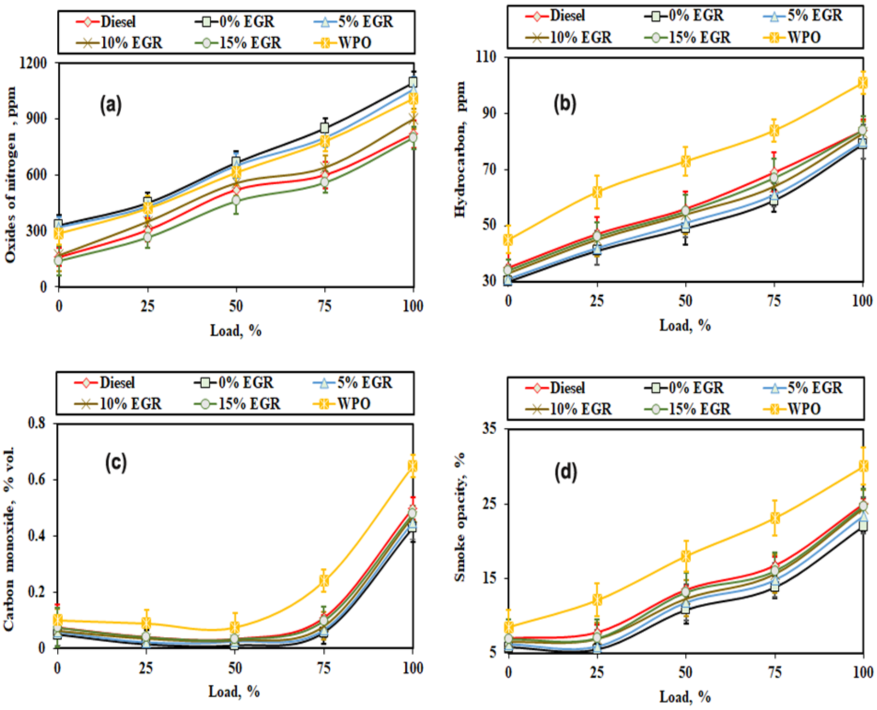

Figure 5. Variation of emissions with different load conditions: (a) Oxides of nitrogen; (b) Hydrocarbon; (c) Carbon monoxide; (d) Smoke opacity.

Hydrocarbon emissions

Figure 5b shows the hydrocarbon (HC) emissions from the variable compression ratio engine for the tested fuels under different loads and EGR rates. Without EGR and at full load, neat WPO exhibits HC emission levels of 101 ppm. Additionally, hybrid biodiesel and diesel display HC emissions of 79 ppm and 84 ppm at full load without EGR, respectively. Under full load, hybrid biodiesel yields HC concentrations of 80 ppm, 83 ppm, and 84 ppm with 5%, 10%, and 15% EGR, respectively. When the EGR circulation rate rises from 0–5%, the increase in HC emissions is around 1.26%. Similarly, with an increase in the EGR circulation rate from 5–10%, there is a slight increase of approximately 3.75% in HC emissions. Furthermore, when the EGR circulation rate rises from 10–15%, the increase in HC emissions is around 1.2%. These increases in HC emissions can be attributed to the higher recirculation of exhaust gases through the engine, which reduces the amount of oxygen available in the combustion chamber. Consequently, more hydrocarbon emissions are produced. Additionally, incomplete combustion occurs due to a lower oxidation rate in the chamber, further contributing to the elevated levels of hydrocarbon emissions in the exhaust gases [26].

Carbon monoxide emissions

During the burning of hydrocarbon fuels, carbon monoxide (CO) is produced as an intermediate by-product, and incomplete combustion leads to CO emissions. Figure 5c illustrates the variations in CO emissions with different loads and EGR rates for the tested fuels. At full load without EGR operation, the CO levels for hybrid biodiesel, diesel, and waste plastic oil (WPO) were found to be 0.43% volume, 0.5% volume, and 0.65% vol., respectively. For 5%, 10%, and 15% EGR operations at full load, the CO emissions are 0.45% volume, 0.47% volume, and 0.48% vol., respectively. With an increase in the EGR circulation rate from 0–5%, there is a slight increase in CO emissions, approximately 4.65%. Similarly, with an increase in the EGR circulation rate from 5 to 10%, the increase in CO emissions is around 4.44%. Furthermore, when the EGR circulation rate rises from 10–15%, the increase in CO emissions is around 2.12%. It is evident that as the EGR level rises, so do the CO emissions. Insufficient oxygen in the intake air leads to incomplete combustion, the primary cause of increased CO emissions. This incomplete combustion is responsible for the higher CO emissions observed at full load. However, lower EGR percentages result in significantly lower CO emissions. With higher EGR percentages, there is a slight rise in CO emissions owing to the insufficient burning of hybrid biodiesel caused by oxygen deficiency. However, the additional oxygen concentration in the biodiesels compensates for the lack of oxygen during EGR operation [26]. As a result, the hybrid biodiesel emits less CO than diesel and WPO at all EGR levels.

Smoke opacity emissions

Figure 5d displays the smoke opacity variations with different loads and EGR rates for hybrid biodiesel, diesel, and WPO. At full load without EGR, the smoke opacity emissions for diesel and WPO are 25% and 30%, respectively, while they are 22% for hybrid biodiesel. Similarly, with 5%, 10%, and 15% EGR at full load, the observed smoke opacity emissions are 23.4%, 24.41%, and 24.7%, respectively. When the EGR circulation rate rises from 0–5%, the increase in smoke opacity is around 6.36%. Likewise, with an increase in the EGR circulation rate from 5 to 10%, there is a slight increase in smoke opacity, approximately 4.31%. Furthermore, when the EGR circulation rate rises from 10–15%, the increase in smoke opacity is around 1.18%. As the EGR percentages rise, the emissions' smoke opacity also rises. The increase in smoke opacity emission is insignificant initially and considerably increases, particularly at higher loads with EGR, because of the partial oxygen replenishment caused by the recirculation of exhaust gases. Also, this demonstrates a decrease in smoke opacity emissions from hybrid biodiesel compared to diesel at all loads [21].

Table 4 compares hybrid biodiesel with different EGRs to diesel at full load, expressed as a percentage increase or decrease.

CONCLUSION

Based on the comprehensive investigation, the following key findings were identified. The utilization of a 10% EGR rate with hybrid biodiesel resulted in improved combustion, performance, and emissions in the VCR engine compared to other test conditions. The utilization of 15% EGR led to a 4% decrease in peak pressure for hybrid biodiesel, highlighting the impact of EGR on combustion dynamics. At fully loaded conditions and with a CR of 20:1, the BTHE for the hybrid biodiesel reached the maximum level of 31.8% when employing 10% EGR. The implementation of hybrid alternative diesel fuel in a compression ignition engine, along with a compression ratio of 20:1 and 10% EGR, resulted in notable outcomes. These include a low exhaust gas temperature of 341°C and minimal fuel consumption, as represented by the BSFC value. Elevated EGR levels slightly increased hydrocarbon, carbon monoxide, and smoke opacity emissions due to

Table 4. A comparison of hybrid biodiesel with different EGR to diesel at full load.

Sl. No.	Parameter	0% EGR	5% EGR	10% EGR	15% EGR
	Combustion Parameters				
1	Ignition delay (°CA)	-2.78	-4.63	-5.46	-6.39
2	Maximum heat release (J/°CA)	+16.96	+15.9	+14.78	+12.71
3	Maximum cylinder pressure (bar)	+12.9	+11.45	+10.55	+10.32
	Performance parameters				
1	Brake thermal efficiency (%)	+13.81	+15.67	+18.66	+17.54
2	Brake-specific fuel consumption (kg/kWh)	-7.47	-13.6	-20	-17.33
3	Exhaust gas temperature (°C)	-8.5	-10.5	-14.75	-14.5
	Emission parameters				
1	Oxides of nitrogen emission (ppm)	+33.54	+29.15	+9.76	-2.43
2	Hydrocarbon emission (ppm)	-5.95	-4.76	-1.19	0
3	Carbon monoxide emission (% volume)	-14	-10	-6	-4
4	Smoke opacity emission (%)	-12	-6.4	-2.36	-1.2

“+” indicates percentage increase; “-” indicates percentage decrease.

reduced fresh air flow into the VCR engine. However, it has reduced ignition delay in the cylinder and lowered NOx emissions in all tests. These findings highlight the potential advantages and applications of hybrid fuel in diverse sectors such as automotive, power generation, maritime applications, etc.

FUTURE SCOPE

For the exploration of the use of mixtures of rubber seed oil and waste plastic oil as fuel in variable compression ratio engines driven by EGR, the following future works are advised. Especially low-speed heavy-duty engines (diesel power generators) and multi-cylinder diesel engines (Heavy vehicles) should be tested for the RSO-WPO mixtures. Diesel engines with minimal heat rejection should be tested for alternative fuel alone (waste plastic oil and rubber seed oil). A numerical study on the effect of EGR on emissions and performance characteristics of a compression ignition engine using hybrid and alternative fuel. To enhance the quality of the WPO and improve its combustion properties, a novel process can be implemented to remove water and oxygen content, thereby reducing the risk of engine component rust and increasing the fuel's calorific value. In future research, parameters like injection diameter, fuel mass, and surface tension will be considered when analyzing EGR's variable compression ratio engine.

NOMENCLATURE

R-20/P-80	20% RSO blended with 80% WPO
A/F	Air fuel ratio
ARAI	Automotive Research Association of India
BSO	Babassu oil
bTDC	Before top dead centre, °CA
BP	Brake power, kW
BSFC	Brake specific fuel consumption, kg/kWh
BTHE	Brake thermal efficiency, %
CO	Carbon monoxide, % volume
cSt	Centi Stoke
DAS	Data acquisition system
EGT	Exhaust gas temperature, °C
HC	Hydrocarbon, ppm
JME	Methyl ester of *Jatropha curcas*
KME	Methyl ester of Karanja oil
MSW	Municipal Solid Waste
NO	Nitric Oxide
NO_2	Nitrogen Dioxide
NOx	Oxides of nitrogen, ppm
KOH	Potassium hydroxide
SFC	Specific fuel consumption, kg/kWh
H_2SO_4	Sulfuric acid
VCR	Variable compression ratio
EGR	Exhaust gas recirculation
WPO	Waste plastic oil

REFERENCES

[1] M.S.N. Awang, N.W. Mohd Zulkifli, M.M. Abbas, S. Amzar Zulkifli, M.A. Kalam, M.H. Ahmad, W.M.A.W. Daud, ACS

Omega 6(33) (2021) 21655–21675. https://doi.org/10.1021/acsomega.1c03073.

[2] C. Kaewbuddee, E. Sukjit, J. Srisertpol, S. Maithomklang, K. Wathakit, N. Klinkaew, W. Arjharn, Energies 13(11) (2020) 2823. https://doi.org/10.3390/en13112823.

[3] R.D. Arjanggi, J. Kansedo, J. Energy Inst. 93(3) (2020) 934–952. https://doi.org/10.1016/j.joei.2019.08.005.

[4] D. Damodharan, B. Rajesh Kumar, K. Gopal, M.V. De Poures, B. Sethuramasamyraja, Rev. Environ. Sci. Bio/Techol. 18(4) (2019) 681–697. https://doi.org/10.1007/s11157-019-09516-x.

[5] S. Kumar, R. Prakash, S. Murugan, R.K. Singh, Energy Convers. Manage. 74 (2013) 323–331. https://doi.org/10.1016/j.enconman.2013.05.028.

[6] M. Mani, G. Nagarajan, S. Sampath, Energy 36 (2011) 212–219. https://doi.org/10.1016/j.energy.2010.10.049.

[7] A.N. Ozsezen, M. Canakci, Ali Turkcan, C. Sayin, Fuel 88 (2009) 629–636. https://doi.org/10.1016/j.fuel.2008.09.023.

[8] Y.H. Chen, T.H. Chiang, J. H. Chen, Fuel 92 (2012) 377–380. https://doi.org/10.1016/j.fuel.2011.08.018.

[9] P.K. Devan, N.V. Mahalakshmi, Appl. Energy 86 (2009) 675–680. https://doi.org/10.1016/j.apenergy.2008.07.008.

[10] S.M. Ashrafur Rahman, H.H. Masjuki, M.A. Kalam, M.J. Abedin, A. Sanjid, H. Sajjad, Energy Convers. Manage. 76 (2013) 362–367. https://doi.org/10.1016/j.enconman.2013.07.061.

[11] N. Usta, E. Ozturk, O. Can, E.S. Conkur, S. Nas, A.H. Con, A.C. Can, M. Topcu, Energy Convers. Manage. 46 (2005) 741–755. https://doi.org/10.1016/j.enconman.2004.05.001.

[12] M. Habibullah, I.M. Rizwanul Fattah, H.H. Masjuki, M.A. Kalam, Am. Chem. Soc. 29(2) (2015) 734-743. https://doi.org/10.1021/ef502495n.

[13] S. Imtenan, H.H. Masjuki, M. Varman, M.A. Kalam, M.I. Arbab, H. Sajjad, S.M. Ashrafur Rahman, Energy Convers. Manage. 83 (2014) 149–158. https://doi.org/10.1016/j.enconman.2014.03.052.

[14] C.D. Rakopoulos, D.C. Rakopoulos, D.T. Hountalas, E.G. Giakoumis, E.C. Andritsakis, Fuel 87 (2008) 147–157. https://doi.org/10.1016/j.fuel.2007.04.011.

[15] H. Venu, L. Subramani, V. D. Raju, Renew. Energy 140 (2019) 245–263. https://doi.org/10.1016/j.renene.2019.03.078.

[16] M. Zheng, G.T. Reader, J.G. Hawley, Energy Convers. Manage. 45(6) (2004) 883–900. https://doi.org/10.1016/S0196-8904(03)00194-8.

[17] O. Can, E. Ozturk, H. Solmaz, F. Aksoy, C. Cinar, H. Serdar Yucesu, Appl. Therm. Eng. 95 (2016) 115–124. https://doi.org/10.1016/j.applthermaleng.2015.11.056.

[18] V.J.J. Prasad, N. Hari Babu, B.V. Appa Rao, J. Renewable Sustainable Energy 1 (2009) 053104. https://doi.org/10.1063/1.3255043.

[19] M. Mani, G. Nagarajan, S. Sampath, Fuel 89 (2010) 1826–1832. https://doi.org/10.1016/j.fuel.2009.11.009.

[20] A.S. Ramadhas, C. Muraleedharan, S. Jayaraj, Clean 36(12) (2008) 978–983. https://doi.org/10.1002/clen.200800108.

[21] A. Tsolakis, A. Megaritis, M.L. Wyszynski, K. Theinnoi, Energy 32 (2007) 2072–2080. https://doi.org/10.1016/j.energy.2007.05.016.

[22] K. Venkateswarlu, B.S.R. Murthy, V.V. Subbarao, K. Vijaya Kumar, Front. Energy 6(3) (2012) 304–310. https://doi.org/10.1007/s11708-012-0195-9.

[23] B. Rajesh kumar, S. Saravanan, Fuel 160 (2015) 217–226. https://doi.org/10.1016/j.fuel.2015.07.089.

[24] K. Srinivasa Rao, Int. J. Mech. Mechatron. Eng. 16(2) (2016) 64–69. https://www.researchgate.net/publication/303573496.

[25] S. Park, H. Kim, B. Choi, J. Mech. Sci. Technol. 23 (2009) 2555–2564. https://doi.org/10.1007/s12206-009-0704-x.

[26] H.E. Saleh, Fuel 88 (2009)1357–1364. https://doi.org/10.1016/j.fuel.2009.01.023.

[27] M.B. Tasić, M.S. Stanković, M.D. Kostić, O.S. Stamenković, V.B. Veljković, Chem. Ind. Chem. Eng. Q. 28 (2022) 237–245. https://doi.org/10.2298/CICEQ210819035T.

[28] N.D.L.D. Silva, F.P.V. Loz, J.I. Soletti, D.D.G. Coelho, Chem. Ind. Chem. Eng. Q. 27 (2021) 155–163. https://doi.org/10.2298/CICEQ191117034S.

[29] I. Veza, A.T. Hoang, A.A. Yusuf, S.G. Herawan, M.E.M. Soudagar, O.D. Samuel, M.F.M. Said, A.S. Silitonga, Fuel 333 (2023) 126377. https://doi.org/10.1016/j.fuel.2022.126377.

[30] C. Enweremadu, O. Samuel, H. Rutto, Environ. Clim. Technol. 26(1) (2022) 630–647. https://doi.org/10.2478/rtuect-2022-0048.

ANANTHAKUMAR SUDALAIMANI[1]
BARATHIRAJA RAJENDRAN[2]
THIYAGARAJ JOTHI[3]
ASHOKKUMAR MOHANKUMAR[4]

[1]Department of Mechanical Engineering, Government College of Engineering. Tirunelveli,Tamil Nadu, India
[2]Department of Mechanical Engineering, Einstein College of Engineering, Near MS University, Tirunelveli, Tamil Nadu, India
[3]Department of Mechatronics Engineering, Er. Perumal Manimekalai College of Engineering, Hosur, Tamil Nadu, India
[4]Department of Mechanical Engineering, Government College of Engineering, Bargur, Krishnagiri, Tamil Nadu, India

NAUČNI RAD

EFEKTI RECIRKULACIJE IZDUVNIH GASOVA NA DIZEL MOTOR PRI KORIŠĆENJU HIBRIDNI BIODIZEL

Primarni cilj ove studije je da se naizmenično koriste konvencionalna fosilna goriva i smanji emisija gasova sa efektom staklene bašte i sumpor-dioksida iz dizel motora. Da bi se smanjila emisija NOx, primenjena je tehnika recirkulacije izduvnih gasova (EGR) korišćenjem hibridnog alternativnog biodizela u tri različite proporcije od 5%, 10% i 15% pri optimalnom odnosu kompresije od 20:1. Rezultati pokazuju da za hibridni alternativni biodizel sa kompresijom od 20:1 i pod punim opterećenjem, toplotna efikasnost kočnice (BTHE) iznosi 31,8% sa 10% EGR. Sa 15% EGR, vršni pritisak za hibridni biodizel je niži nego što bi bio bez EGR-a za oko 2,28%. Kada se EGR poveća, kašnjenje paljenja i emisije NOx se blago smanjuju. Sa povećanjem EGR samo do 10%, vrednosti potrošnje goriva specifične za kočnice (BSFC) se efikasno smanjuju. Hibridni biodizel sa 10% EGR smanjuje temperaturu izduvnih gasova na 341 °C.

Ključne reči: recirkulacija izduvnih gasova, sagorevanje, erformanse, emisija, ulje od otpadne plastike, kaučukuovo ulja.

Chemical Industry & Chemical Engineering Quarterly

Available online at
Association of the Chemical Engineers of Serbia *AChE*
www.ache.org.rs/CICEQ

Chem. Ind. Chem. Eng. Q. 30 (3) 193–206 (2024) CI&CEQ

HEITOR OTACÍLIO NOGUEIRA ALTINO[1]
GIOVANI AUD LOURENÇO[2]
CARLOS HENRIQUE ATAÍDE[1]
CLAUDIO ROBERTO DUARTE[1]

[1]Federal University of Uberlandia, Faculty of Chemical Engineering, Uberlândia, MG, Brazil
[2]Federal Institute of Goiás, Itumbiara, GO, Brazil

SCIENTIFIC PAPER

UDC 621.3.04:621.317:66

THE INFLUENCE OF MOISTURE CONTENT ON DRILLED CUTTINGS' PROPERTIES OF BED PACKING AND FLOWABILITY

Article Highlights

- Extensive analysis of moisture on drilling cuttings' bed packing and flowability
- Four characteristic states are identified according to the moisture level of cuttings
- The interparticle structures become looser and steadier as moisture rises to 15.2%
- Beyond 15.2%, moisture increases provide denser and less stable structures
- Predictive models proposed for moisture's influence on bed packing and flowability

Abstract

To design and operate various equipment of the solids control system in offshore drilling platforms, it is important to establish how the moisture content influences the characteristics of drilled cuttings to form packed beds and flow over solid surfaces. The current study comprehensively analyzes how moisture content, primarily composed of water and representing water-based muds (WBMs), influences the bed packing properties and drilled cuttings' flowability. The particle aggregation/disaggregation dynamics, loose and tapped bulk densities and porosities, compaction dynamics of packed beds, Hausner ratio, and angle of repose of drilled cuttings with ten distinct moisture contents (1.4—44.0 wt%) were analyzed. It was noticed that the increment of moisture content up to 15.2% promoted the formation of looser interparticle structures. However, these structures were steadier, showing greater difficulty flowing and releasing air/liquid. The continuous increment of moisture content beyond 15.2% promoted a complete change in the material behavior. The interparticle structures became denser. The material could flow and release air/liquid more easily. In addition, it was possible to establish a classification of the different behaviors of drilled cuttings according to the moisture content. Predictive models were proposed to describe the influence of the moisture content on the bed packing and flowability properties of drilled cuttings.

Keywords: particle aggregation, particle disaggregation, packed bed, flowability, compaction.

Oil and gas production is an important part of meeting global energy demand, with total production forecast to grow by 17 million barrels of oil equivalent per day by 2025. The expectations are that offshore production will be responsible for approximately 5 million barrels of oil equivalent in 2025, representing 29% of the total oil and gas production [1]. The offshore wells are drilled using a rotating drill bit connected to a drilling platform through a hollow pipe, which is rotated using an electric or hydraulic motor to obtain oil and gas. To maintain the pressure, lubricate, and reduce the temperature of the drill bit, a drilling fluid is injected inside the hollow pipe and returned to the platform through the annulus between the drill string and the wall of the drilled hole. In general, drilling fluids are classified according to their main constituents, such as Water-based muds (WBMs), Oil-based muds (OBMs),

---

Correspondence: C.R. Duarte, Federal University of Uberlandia, Faculty of Chemical Engineering, Av. João Naves de Ávila, 2121, Block 1K, 38408-100 Uberlândia, MG, Brazil.
E-mail: claudioduarte@ufu.br
Paper received: 24 April, 2023
Paper revised: 11 August, 2023
Paper accepted: 28 August, 2023

https://doi.org/10.2298/CICEQ230424023A

and Synthetic-based muds (SBMs). Due to environmental and cost concerns, WBMs have become the preferred choice in this category [2,3]. As the drill bit rotates and grinds the rock formations, small rock particles, known as drilled cuttings, are generated and suspended in the drilling fluid, returning to the platform along with the fluid. The cuttings are separated by a set of unit operations in a solid control system in the platform, and the drilling fluid returns to the drilling process. Depending on the local legislation, the separated cuttings can be disposed of in different ways: re-injection into offshore wells, onshore treatment and disposal, and discharge into marine environments after adequate treatment. To dispose of the drilled cuttings must be conveyed from the drilling platform to the conveying vessels. For this purpose, several methods can be utilized, such as skip-and-ship, conveyor belts, screw conveyors, and pneumatic conveying [4].

One of the main challenges of handling drilled cuttings is that the material is very naturally inconsistent [5]. In particular, drilled cuttings' moisture content (MC) is a critical variable, consisting of a mixture of water and oil. In the case of drilled cuttings containing WBMs, the MC primarily comprises water, as a significant portion of this drilling fluid comprises it [4]. It is possible to observe drilled cuttings in the form of pastes, with more than 60% by weight of MC, and in the form of granular solids, with less than 5%. Such moisture contents depend on several factors, such as drilling rates and conditions, drilling fluids used, solids control equipment efficiency, and from what stage of the solids control system the cuttings originate [4,5]. Nevertheless, this last factor is one of the most important, e.g., some patents describe that the drilled cuttings coming from shale shakers may be free-flowing, non-free-flowing, or pasty, with moistures ranging from 10 to 20% by weight. On the other hand, drilled cuttings from the bottom of Vortex dryers are generally solids with good flowability, with 5% moisture. While drilled cuttings coming from the cuttings processor may be free-flowing or non-free-flowing, depending on how much fluid the equipment removes [6–11].

In the unit operations of the solids control system and the conveying stage to the vessel, the material is stored in silos, tanks, and blow tanks and flows through gutters, discharge valves, and conveying pipes [6–11]. However, due to the significant changes in the moisture content of the material during these processes, the bed packing and flowability properties are completely altered, leading to changes in the bulk behavior of the material. Thus, it is important to know how the MC can affect these properties to design systems to convey, store, and discharge drilled cuttings. Bed packing properties, e.g., are needed to determine the bulk volume of material that can be packed into a blow tank or microwave treatment equipment and the volume changes that can be expected due to systems vibrations [12–15]. The flowability properties describe the relative movement of a bulk of particles among neighboring particles or along solid surfaces, e.g., gutters and pipes [16]. Furthermore, it's important to highlight that during the operation of drilled cuttings handling systems, the lack of knowledge of how *MC* affects these properties can lead to low process efficiencies and clogging problems. In more extreme cases, these clogging problems can stop the entire drilling process once the drilled cuttings cannot be disposed of [4,5,8].

Generally, such properties are governed by complex interactions between internal and external forces. A cohesive behavior is expected if the external forces are lower than the interparticle forces [17]. Friction and cohesion are the major interparticle forces acting on the material. Friction acts at the contact points of the particles, opposing the relative motion between them. In this case, the shape and surface morphology of the particles directly affects the friction forces. Cohesion refers to the forces of attraction between particles, including van der Waals forces, local chemical bonds, electrostatic charges, and liquid bridging forces, originating from net surface tension [17,18]. In the case of sand-like non-porous materials, such as drilled cuttings, moisture is preferentially adhered to the surface of the particles, influencing both frictional and cohesion forces [12,17]. At first, the cohesion forces are the most affected by the increase in moisture due to the strengthening of the liquid bridge bonds between the particles, which reduces the particles' easy movement [17,18]. However, as reported by several authors [18,19], at a certain amount, moisture can also simultaneously act as a lubricant for the particles, reducing frictional forces and increasing the facility for the particles to move.

Several parameters can be used to measure how the properties of bed packing and flowability can be affected by the MC. The loose and tapped bulk densities and porosities indicate how the moisture content can influence the relative rearrangement of particles to form packed beds. The flowability of materials can be indirectly estimated and classified by the Hausner ratio and the angle of repose. In addition, these indicators also provide important information on the inter-particular forces present in the material [16]. It is also highlighted that changes in interparticle forces can induce particles to aggregate into clusters or disaggregate, making it possible to quantify these phenomena by analyzing the particle size distribution of the material [20].

However, studies addressing the influence of *MC* on the packing and flowability characteristics of drilled cuttings are still scarce in the literature. In large part, there is only the description of the material's behavior according to moisture performed by some patents, as previously mentioned [6–11]. Nevertheless, the moisture content ranges at which the material bulk behavior changes and the interparticle forces involved were still not studied. Some authors also report that the flowability of drilled cuttings can be improved by adding the correct amount of dilution fluid, such as water [5]. However, it is not known the saturation point at which it occurs.

Furthermore, even analyzing papers [21,22] that described the effect of moisture content on the bed packing properties of materials similar to drilled cuttings, such as sands, it is possible to observe that low moisture content ranges are generally analyzed, not contemplating the entire range described in patents [6–11].

Among the works consulted, no information was found on the loose and tapped bulk densities and porosities, as well as the Hausner ratio and angle of repose of drilled cuttings with different moisture contents. Thus, a comparative analysis of how the moisture content influences the packing properties and flowability of cuttings and the dynamics of aggregation/disaggregation of the particles is necessary. This analysis may help to elucidate the different effects of moisture on cutting management characteristics reported in the patents [6–11]. Consequently, from a practical point of view, this analysis can improve drilled cuttings management operations.

In this context, this study aimed to analyze how moisture content, primarily consisting of water and representing WBMs, affects the properties of bed packing and flowability of drilled cuttings. For this purpose, the influence of ten distinct moisture contents of drilled cuttings was studied on the particle size distribution, loose and tapped bulk densities and porosities, compaction dynamics of packed beds, Hausner ratio, and angle of repose. The analysis of these parameters allowed the establishment of a classification of the different behaviors of drilled cuttings according to the moisture content, reinforcing this paper's novelty. The main interparticle forces involved and the general handling behavior of the material in each state of the classification were discussed.

Furthermore, predictive models were proposed to describe the influence of the moisture content of drilled cuttings on the studied parameters.

MATERIALS AND METHODS

Drilled cuttings

The drilled cuttings were provided by Petróleo Brasileiro S.A. (Petrobras®). The material was sampled after the processing stage through the shale shakers and originates from the drilling of carbonate rocks in the depth range of 4656 to 4758 meters in Campos Basin, Campos, Rio de Janeiro, Brazil. The drilling process used a polymeric water-based drilling fluid with xanthan gum and modified starch. Table S1 and Figure S1 (Supplementary Material) show details of the characteristics of the dry material.

Oil, water, and solids contents

The contents of oil, water, and solids of the drilled cuttings were determined by the retort test in duplicates, using the gravimetric method, according to API [23], allowing to determine the contents of oil (C_o), water (C_w), and solids (C_s).

Characterization of dry drilled cuttings

The apparent density (ρ_a) was estimated using the technique of liquid pycnometry with pure deionized water at 25.0°C. The actual density (ρ_r) of the drilled cuttings was determined in triplicate utilizing a gas pycnometer (He) (Micromeritics®, Accupyc 1330). The establishment of the apparent and actual densities allows the estimation of the particle porosity (ε_p) by the following equation:

$$\varepsilon_p = 1 - \frac{\rho_a}{\rho_r} \tag{1}$$

The sphericity (φ) of five hundred particles was determined using the image analysis technique. An optical microscope (Nikon®, Eclipse E-200) equipped with a digital camera (Motic®, Moticam 5) was used for capturing the images. The Image-Pro Plus® 6.0 software was used to establish the particles' area (A) and perimeter (P). Sphericity was calculated by the equation:

$$\varphi = \frac{4\pi A}{P^2} \tag{2}$$

The size distribution of the particles was determined in triplicate by the sieving method described by ASTM [24]. To describe the particle size distribution, the Rosin-Rammler-Bennet model (RRB), specified by Eq. (3), was fitted to the experimental data [25].

$$Y(x) = 1 - e^{-\left(\frac{x}{x_0}\right)^n} \tag{3}$$

where $Y(x)$ is the cumulative fraction of material by weight less than size x, x is the particle size, n is the uniformity constant, and x_0 is the characteristic particle size.

The surface morphology and elements of the particles were analyzed by scanning electron microscopy (SEM) and energy dispersive spectroscopy (EDS). Initially, the samples were overlaid with a thin layer of gold (75 nm) using a Leica® EM SCD050 spray device. Then, the characterization was performed using a Zeiss® EVO MA10 microscope and an Oxford® 51-ADD0048 detector. The magnifications of 300x, 1000x, and 5000x were evaluated.

Material humidification procedure

In this paper, the moisture content (MC) is referred to as the sum of the contents of water and oil, as shown by Eq. (4). The saturation level (S) can be defined as the fraction of interparticle volume of a packed bed that is filled with a liquid and was calculated by Eq. (5).

$$MC(\%g.g^{-1}) = \frac{m_w + m_o}{m_w + m_o + m_s}100 \tag{4}$$

$$S(\%mL.mL^{-1}) = \frac{V_{liq}}{V_t - V_s}100 \tag{5}$$

where m_w is the mass of water, m_o is the mass of oil, m_s is the mass of solid, V_{liq} is the total volume of liquid (water + small amounts of oil in the solid particles) in the bed, V_t is the total volume of the dry bed, and V_s is the volume occupied by the solid (based on actual density). The residual oil in the solid particles was identified by gas chromatography coupled to mass spectrometry (Shimadzu®, GCMS-QP2010) as 1- pentadecene ($C_{15}H_{30}$). The oil density of 0.781 ± 0.001 g/mL was obtained by liquid pycnometry at 20°C. The oil viscosity of 2.4×10^{-3} Pa.s was determined in a rheometer (Brookfield®, R/S plus) at 20°C.

It's important to highlight that, in general, WBMs are mainly composed of water (≈76%) [4]. Therefore, pure water was employed to humidify the cuttings, aiming to simulate the impact of WBMs content on particle aggregation/disaggregation, bed packing, and flowability dynamics. It is also important to highlight that although the dry drilled cuttings had a residual amount of oil (1-pentadecene), the quantity of it was very small (1%<) and reduced even more (0.5%<) when the material was humidified for higher MCs, due to the solid concentration reduction. Therefore, the material was not submitted by any cleaning process of the oil before the humidification process. Thus, the primary effect of moisture on the drilled cuttings properties analyzed was considered to be due to the action of the water.

The material was humidified to reach ten different MCs: 1.3%, 5.4%, 7.7%, 10.0%, 12.5%, 15.2%, 21.0%, 27.6%, 35.2% and 44.0%, as seen in Figure 1. The compositions of oil, water, and solids for each MC analyzed can be observed in Table S2. These moisture contents correspond to the saturation levels of 5.4%, 18.9%, 25.7%, 32.5%, 39.2%, 46.0%, 59.5%, 73.0%, 86.5% and 100.0%, which covers the three characteristic wet powder states, described here only as a reference: pendular (0% to 25%), funicular (25% to 80-90%), and capillary (80-90% to 100%) [18,19]. The humidification procedure included adding the necessary material to a zip-lock bag. Then, the deionized water needed to reach the desired MC was added. The bag was sealed, and the mixture was manually mixed for over 10 min. The bag remained closed for at least 1 h to complete the homogenization of the mixture. This specific duration was established as the minimum required time to ensure uniform moisture distribution across the entire zip lock bag. After this time, the desired characteristics of the material were analyzed (aggregation/disaggregation dynamic, bed packing, and flowability). It's important to highlight that the humidified material was not reused from one analysis to the other. In each analysis, a new humidification process was performed. The material was submitted to a retort test to check if the desired moisture content was obtained.

Optical microscopy

Optical microscopy was used to observe the effect of the MC on the visual aspect of drilled cuttings and to quantify the particle agglomeration/aggregation. An optical microscope (Nikon®, Eclipse E-200) equipped with a digital camera (Motic®, Moticam 5) was used for capturing the images. The mean diameter of more than one hundred particles and particles' clusters was obtained using the Image-Pro Plus® 6.0 software for each MC studied. It is important to highlight that the particle diameter alteration analyzed can also be due to water absorption by the drilling cuttings. Nevertheless, due to the low particle porosity of the material (0.0355), this can be considered a minor effect.

Determination of bed packing properties

The loose (ρ_0) and tapped (ρ_t) bulk densities of drilled cuttings were determined in triplicate according to the main norms for bulk density establishment [26,27]. The automated system for bulk density data acquisition of granular materials described by Altino *et al.* [28] was used for this purpose. The number, frequency, and amplitude of the taps were 3000, 250 taps/min, and 16.0 mm. These conditions were observed by Altino *et al.* [28] to promote the optimal packing of sand "S50". Thus, due to the similarity between drilled cuttings and sands and the strong interparticle cohesion forces induced by moisture, these conditions were chosen to be utilized in this paper. A plastic tube (internal diameter of 21.20 mm, external diameter of 25.00 mm, and height of 275 mm) was concentrically placed on the graduated cylinder to pack the material in the graduated cylinder. The material was introduced into the plastic tube by pouring constant amounts of material from the same height with a funnel. After filling the tube with the material, the tube was removed at a constant speed of 12.2 ± 1.5 mm/s. The powder gradually flowed off the tube and packed into the graduated cylinder. For each *MC* analyzed, the mass of the material was selected to promote the initial packing volume of 100 mL. This packing method ensured precise initial volumes of packed material with low variability.

The loose porosity (ε_0), tapped bulk porosity (ε_t), and effective porosity (ε_{eff}) of the material were respectively determined by Eqs. (6–8) [28,29]. The calculations involving ε_0, ε_t, and ε_{eff} were performed by discounting the mass of liquid (water + small amounts of oil (1-pentadecene) in the solid particles) from the total mass of the packed bed. As porosity describes the bed structure, there is no point in considering the liquid's mass [22].

$$\varepsilon_0 = \frac{V_{intra} + V_t}{V_{bulk}} + \frac{V_{add}}{V_{bulk}} \tag{6}$$

$$\varepsilon_t = \frac{V_{intra} + V_{opt}}{V_{bulk}} \tag{7}$$

$$\varepsilon_{eff} = \frac{V_{intra} + V_t + V_{add} - V_{liq}}{V_{bulk}} \tag{8}$$

where V_{bulk} is the bulk volume, V_{intra} is the intra-particular volume, V_t is the sum of the inter-particular voids when the granular system is in an optimal packaging state, V_{add} is the additional volume trapped in the packaged material, and V_{liq} is the volume of liquid occupying the interparticle voids spaces.

The ability of the material to release trapped air/liquid was evaluated by the additional porosity (ε_{add}), calculated by Eq. (9). While the air/liquid release kinetic due to the compaction of the pecked bed was measured by the granular relaxation index ($\tau_{½}$), according to Eq. (10). This parameter represents the ratio between the packing fraction variation and the number of taps needed to reach the middle of the compaction process ($N_{½}$) [29].

$$\varepsilon_{add} = \frac{\varepsilon_0 - \varepsilon_t}{\varepsilon_0} \tag{9}$$

$$\tau_{1/2} = \left(D_t - D_0\right) N_{1/2} \tag{10}$$

where D_t is the packing fraction of the compacted material, and D_0 is the packing fraction of the loose material.

The experiments were performed at room temperature (25.2 ± 0.5°C) with relative air moisture of 55.4 ± 2.7%, sufficient to eliminate the static charges visually.

Determination of flowability indicators

The flowability of the drilling cuttings was analyzed by two indicators: static angle of repose (*AoR*) and the Hausner ratio (*HR*) in triplicates. The first one was determined based on the funnel method described by ASTM [30]. Further details of the experimental system can be found in Altino *et al.* [28]. It is important to highlight that for the material with moisture contents higher than 15.2%, it was impossible to determine the angle of repose due to the slurry behavior of the mixture. The second indicator (*HR*) was calculated by the ratio between the tapped bulk density and the loose bulk density, based on the method described by the WHO [31].

RESULTS AND DISCUSSION

Characterization of dry drilled cuttings

Table S1 shows that the base material had low water and oil contents, being suitable to be humidified. Nevertheless, to understand how moisture can affect the behavior of the drilled cuttings, It is important to classify it as a porous or non-porous material. In general, for porous materials, moisture fills the particle porous and adds weight to the bed, increasing the density of the material. On the other hand, for non-porous materials, surface moisture contributes to liquid bridge forces, altering the interparticle forces (cohesion forces) [22]. According to Ishizaki *et al.* [32], porous materials have particle porosities (ε_p) that range between 0.2 and 0.95. Thus, according to particle porosity obtained by Eq. (1) for the drilled cuttings studied, it can be classified as a non-porous material.

The sphericity (φ) of the drilled cuttings was according to the value reported by Hyun *et al.* [33] (0.80). The apparent (ρ_a) and real (ρ_r) densities of the material also were according to the real density reported by Petri *et al.* [34] (2.6830 g.cm^{-3}). The Sauter mean diameter (D_{Sauter}), on the other hand, was lower than the value reported by Petri *et al.* [34] (238 µm). Based on the values of real density and Sauter mean diameter of Table S1, the drilled cuttings can be classified as Geldart B-type [35].

The SEM micrographs in Figure S1 show particles without defined pores with various sizes and shapes, rough surfaces, and asperities. The presence of particle agglomerates can also be observed, highlighting the material's cohesiveness. The EDS results (Figure S1d) evidenced the existence of several elements in drilled cuttings particles. Carbon and gold appear in large quantities. However, it's important to highlight that the particles were coated with gold and attached to a conductive carbon adhesive tape (Nisshin®, Nem Tape) to carry out the analyses. It is also possible to observe significant amounts of calcium, oxygen, and magnesium. The drilled cuttings analyzed were sourced from carbonate rocks. According to Reeder [36], those rocks are mainly formed by calcite ($CaCO_3$), dolomite ($CaMg(CO_3)_2$), and aragonite ($CaCO_3$), which may be the source of the observed elements.

Effect of moisture content on drilled cuttings properties

Particle aggregation and disaggregation

The effect of the *MC* on the visual aspect of the drilled cuttings is shown in the micrographs in Figure 1. The small variations between the scales of the figures allowed for performing a comparative analysis of MC's influence on the cuttings' visual aspect. The increase of *MC* up to 15.2% (Figure 1f) promoted a reduction in the number of fine particles and small particles' clusters, while the size of the larger particles' clusters increased. For higher *MC*s, the material started to change to a pasty state, increasing the number of fine particles and small particle clusters and reducing the size of the larger clusters. The increase of particles' clusters and reduction of fines and small particles' clusters with increased *MC* can be either agglomeration or aggregation [37,38]. Nevertheless, as the clustering of the particles showed to be reversible by the increase of *MC*, the phenomena can be classified as aggregation [38].

To quantify the alterations of the particle sizes in the function of the *MC*, the mean particle diameter and the number of fines lower than 75 μm were determined [37]. The results are presented in Figure 2. It is crucial to emphasize that the particle sizes quantification was performed centered around the mean Sauter diameter (161.73 μm, Table S1) once the optical microscopy does not allow the analysis of the whole particle size range of the drilled cuttings (20–3350 μm). However, these results offer valuable insights into how the moisture content affects the aggregation and disaggregation dynamics of the particles with sizes similar to the mean particle size of the material. A scheme, shown in Figure 3, was created to elucidate the phenomena better. The *MC*s' limits, states, and substates illustrated in Figure 3 were established in this paper based on the similar behaviors of the particles considering aggregation, bed packing, and flowability characteristics. These limits are also marked in Figure 2.

In the dry state (1) (Figure 3), the saturation level range is of the pendular state. The particles were dispersed, and the mean particle diameter remained almost constant with the increment of *MC*. It is expected, considering the weak liquid bridge forces generally observed in the pendular state [18]. Proceeding to the aggregated substate (2a) (Figure 3),

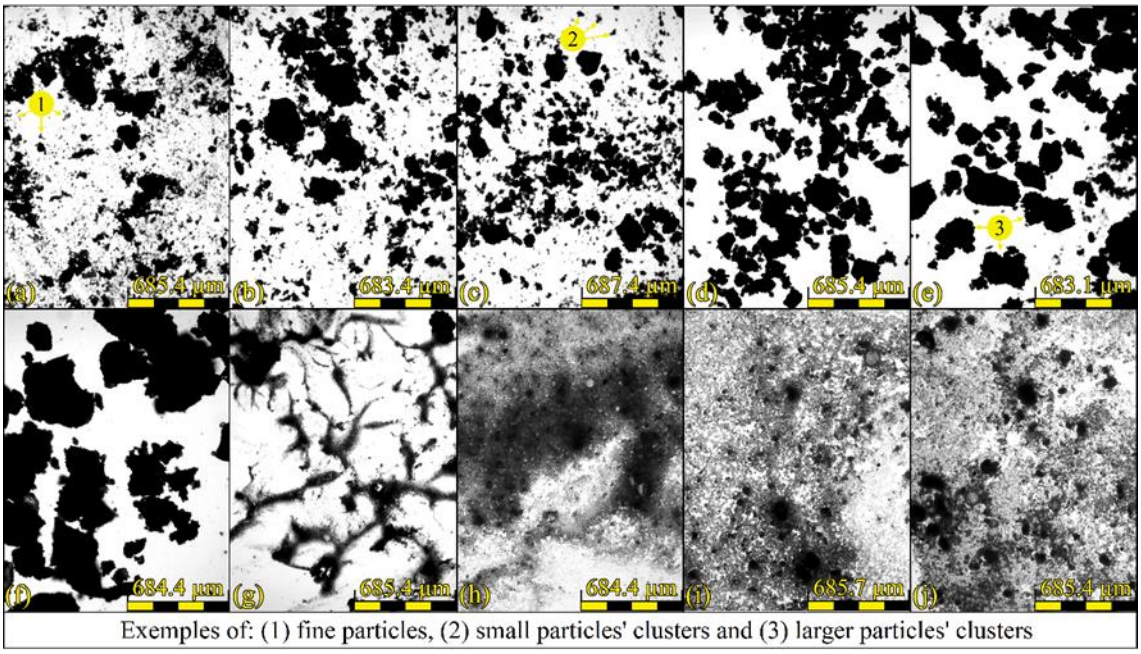

Figure 1. Micrographs of drilled cuttings with different moisture contents: (a) 1.3%; (b) 5.4%; (c) 7.7%; (d) 10.0%; (e) 12.5%; (f) 15.2%; (g) 21.0%; (h) 27.6%; (i) 35.2% and (j) 44.0.

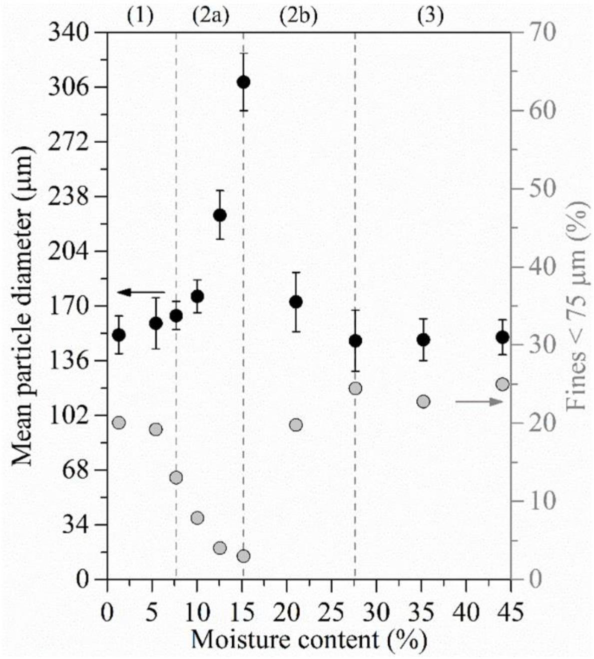

Figure 2. Effect of the moisture content on the mean particle diameter and content of fines of drilled cuttings, assessed using optical microscopy.

as the *MC* increases, the mean diameter increases increases, and the content of fines reduces up to the *MC* of 15.2% (2a). The saturation level range is of the funicular state. Thus, increasing *MC* may induce liquid bridges to form, increasing the interparticle forces and promoting the aggregation of fines and small particles into clusters of larger diameters. After this, on disaggregated substate (2b) (Figure 3), the amount of liquid seems to be just enough to start a gradual dispersion of the aggregates into clusters of smaller diameter and fines. The MC of 15.2% is believed to be sufficient to start the saturation of some interparticle spaces, spacing out particles and reducing the cohesion forces. At the same time, when enough moisture is present on the surface of the particles, it creates a layer of liquid that can act as a lubricating film between the particles, reducing the resistance to particle motion by minimizing the frictional forces at the contact points [17]. Thus, it is hypothesized that the reduction of the cohesion forces on substate (2b) and the lubricating action of the particle's surfaces allowed the dispersion of the aggregates.

Finally, at 27.6%, a saturation point is achieved, initiating the slurry state (3) (Figure 3), where the saturation level is of a capillary state. It's possible to observe that the aggregates were dispersed so that the mean particle diameter and fine amount were similar to those of the dry state (1). It is important to highlight that the aggregation and desegregation of particles are very complex phenomena, and several factors may also contribute to the observed results. For example, the drilled cuttings studied were sourced from carbonate rocks, which are well-known for their very low solubility in water [39]. This characteristic can impact the dynamics of particle aggregation/desegregation and particle sizes. Furthermore, the initial sample may contain clusters that tend to disaggregate under high moisture content. This observation is supported by the slightly higher amount of fines observed in the slurry state (3) (≈ 24%) compared to the dry state (1) (≈20%).

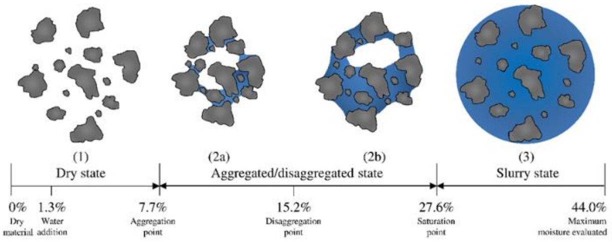

Figure 3. Schematic of the behavior of the particles with increasing moisture content.

Bed packing properties

The compaction curves of drilled cuttings with different *MC*s are shown in Figure S2. To check if the tapping number was enough to achieve the stationary state, the values of ρ_t were compared with values of asymptotic bulk density (ρ_∞). This last parameter was acquired by the fit of the KWW model [40] to the experimental data. The results presented in Table S3 show good adjustments of the model to the data, as demonstrated by high values of coefficients of determination (R^2). A Student's t-test, performed between ρ_t and ρ_∞, showed, with 95% reliability, that there is no statistically significant difference between the data, as evidenced by the *p-values* in this table. Thus, the number of taps provided for obtaining the tapped bulk density was sufficient to reach the stationary state predicted by the model for each *MC* analyzed.

The influence of *MC* on the loose (ρ_0) and tapped (ρ_t) *bulk* densities of drilled cuttings is displayed in Figure S3. The effect of *MC* on the packed bed characteristics can be better interpreted by analyzing the loose (ε_0) and tapped (ε_t) bulk porosities, displayed in Figure 4. The states' limits of Figure 3 were marked for better data analysis. The loose and tapped *bulk* porosities represent the fraction of void volume regarding the total volume of the bed, no matter whether these voids are filled with liquid or air. In states (1) and (2a), it is possible to observe that the loose and tapped bulk porosities increase with the increment of moisture up to 15.2% for ε_0 and 12.5% for ε_t. This behavior can be attributed to increased cohesion forces through strengthening liquid bridges between particles, as illustrated in Figure 3 (2a) [22,41]. Consequently, the particles have more difficulty rearranging their relative positions to form denser pecked beds (lower porosity), resulting in looser-packed beds [22]. It may be expected that ε_t would also show a turning point at *MC* of 15.2%, as was observed for ε_0. Nevertheless, in the compaction process, energy is applied to the packed bed to cause the rearrangement of the relative positions of the particles. Thus, as the compaction process proceeds, the void spaces are reduced, and the saturation level gradually increases [16]. The saturation level is estimated to increase due to compaction from 46.0% to 53.3% at an *MC* of 15.2%. In this higher saturation level, the cohesion and friction forces are reduced, allowing the particles to rearrange into a denser bed configuration.

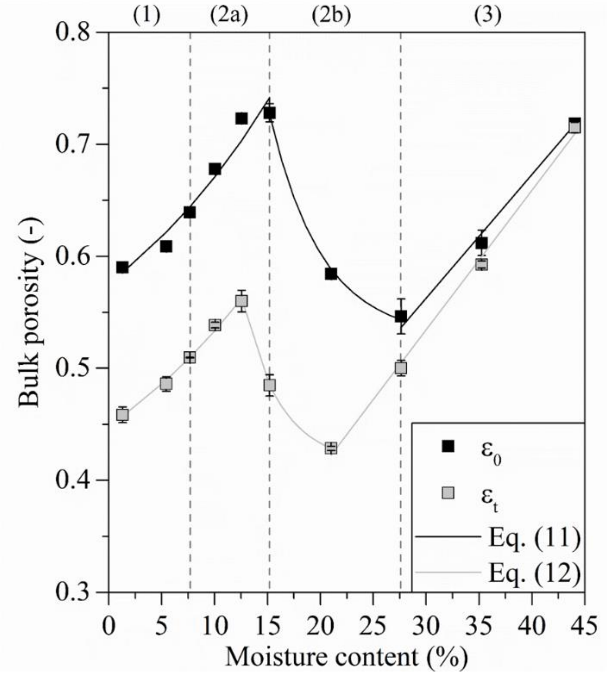

Figure 4. Effect of moisture content on loose (ε_0) and tapped (ε_t) bulk porosities of drilled cuttings.

After this point, on the substate (2b) of Figure 4, the increase of *MC* resulted in a decrease of ε_0 and ε_t, probably due to the reduced cohesion forces previously mentioned [22,41]. This reduction goes up at 27.6% for ε_0 and 21.0% for ε_t. It is interesting to highlight that, at these points, the porosities observed were similar to those of the dry material (1.3%). Once again, it may be expected that ε_t would present a turning point at 27.6%, as perceived for ε_0. However, as cited before, the compaction process increases the saturation level. In this case, the saturation level is calculated to increase by compaction from 73.0% to 100.0%, passing from a funicular state to a capillary state. On the state (3), the increment of *MC* induces the increase of ε_0 and ε_t. The material is saturated in this state. Thus, the larger amount of liquid with the increase of *MC* may have caused a dilution effect on the mixture, reducing its density and increasing the porosity. The bulk porosity is inversely related to bulk density. Therefore, as expected, the effects observed for loose and tapped bulk porosities were respectively inverse observed for loose and tapped bulk densities (Figure S3). The ε_0 and ε_t showed an exponential correlation with *MC* on states (1) and (2) and a linear correlation on the state (3). Thus, Eqs. (11) (R^2 = 0.981) and (12) (R^2 = 0.997) were proposed to describe ε_0 and ε_t in the function of *MC*.

$$\varepsilon_0 = \begin{cases} 0.15e^{0.05MC} + 0.42 & \mathit{for} \quad MC < 15.2\% \\ 4.44e^{-0.20MC} + 0.53 & \mathit{for} \quad 15.2\% \le MC < 27.6\% \\ 0.01MC + 0.23 & \mathit{for} \quad MC \ge 27.6\% \end{cases} \tag{11}$$

$$\varepsilon_t = \begin{cases} 0.14e^{0.05MC} + 0.31 & \mathit{for} \quad MC < 12.5\% \\ 4.44e^{-0.27MC} + 0.41 & \mathit{for} \quad 12.5\% \le MC < 21.0\% \\ 0.01MC + 0.16 & \mathit{for} \quad MC \ge 21.0\% \end{cases} \tag{12}$$

The influence of *MC* on the effective bulk porosity (ε_{eff}) is shown in Figure 5. This parameter represents the air-filled void volume fraction compared to the bed's total volume. As *MC* increases, the ε_{eff} increases by little at state (1), which can be expected due to the low interparticle forces previously mentioned for this state. This result also suggests that the increase of ε_0 (Figure 4) in this state is probably due to the increment of liquid-filled void volumes. Moving to substate (2a), the *MC* seems enough to increase the cohesion forces and promote the formation of air-looser beds. On the substate (2b), the increase in *MC* promoted a reduction of ε_{eff}, which can be credited to reducing those forces, allowing the particles to reorient in denser interparticle configurations. The ε_{eff} continued reducing with the increase in moisture in the state (3) up to near-zero values, in contrast to the increment of ε_0 observed for this state in Figure 4. This result suggests that liquid-filled void volumes gradually increase in detriment to reducing the air-filled ones as the material gets saturated. This parameter showed an exponential correlation with the *MC*, having two different behaviors, before and after the *MC* of 15.2%; thus, Eq. (13) (R^2 = 0.994) seems appropriate to represent this correlation.

$$\varepsilon_{eff} = \begin{cases} 3.2x10^{-4}e^{0.38MC} + 0.56 & \mathit{for} \quad MC < 15.2\% \\ 4.7x10^{0}e^{-0.13MC} & \mathit{for} \quad MC \ge 15.2\% \end{cases} \tag{13}$$

The influence of *MC* on the additional bulk porosity (ε_{add}) of drilled cuttings is shown in Figure S4. This parameter reflects the ability of the powder to release the additional amount of air trapped in the packed bed [29]. The increment of *MC* resulted in the increase of ε_{add} up to the end of the substate (2a). As previously discussed, in this substate, the increment of *MC* may induce the formation of looser uncompacted packed bed structures. Thus, more air is trapped in the packing process, which is further released in the compaction process, increasing ε_{add}. On the substate

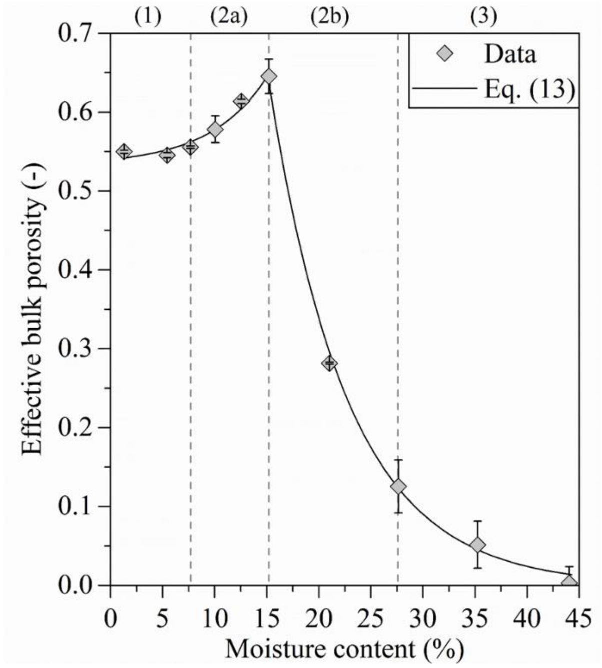

Figure 5. Effect of moisture content on the effective bulk porosity (ε_{eff}) of drilled cuttings.

(2b), the particles are believed to move more easily and form denser uncompacted bed structures, similar to the compacted ones, reducing ε_{add}. Finally, in the state (3), the voids are completely saturated, creating a liquid-solid mixture so that low amounts of air are trapped on the structure, probably in the form of bubbles, reducing the additional bulk porosity to near-zero values. As observed for ε_{eff}, ε_{add} showed an exponential correlation with the *MC*, having two different behaviors. Thus, Eq. (14) (R^2 = 0.994), similar to Eq. (13), was used to represent the relationship between ε_{add} and *MC*.

$$\varepsilon_{eff} = \begin{cases} 3.2x10^{-4}e^{0.38MC} + 0.56 & for \quad MC < 15.2\% \\ 4.7x10^{0}e^{-0.13MC} & for \quad MC \geq 15.2\% \end{cases} \tag{14}$$

To analyze the effect of moisture on the relative facility of the particles to rearrange their positions, the granular relaxation index ($\tau_{½}$) was estimated and is shown in Figure 6. This parameter was estimated based on the compaction curves in Figure S2. On state (1), the increase in *MC* resulted in almost no change in this parameter, as expected. Nevertheless, on substate (2a), the $\tau_{½}$ increased exponentially to 15.2%. The increase of the interparticle forces with the *MC* in this state promoted the formation of steadier structures with higher bulk porosity (Figure 4, (2a)). In other words, the particles had more difficulty moving their relative positions, requiring more taps to compact the more porous packed structure. The increase of *MC* resulted in an exponential decrease of $\tau_{½}$ on the substate (2b), which indicates that the mobility of the particles was increased, probably due to the reduction of the aftermentioned interparticle forces and lubricant action of the liquid. In state (3), the voids were saturated with liquid; thus, the first taps quickly released the low amount of air trapped. Eq. (15) (R^2 = 0.978) represented the correlation between *MC* and $\tau_{½}$.

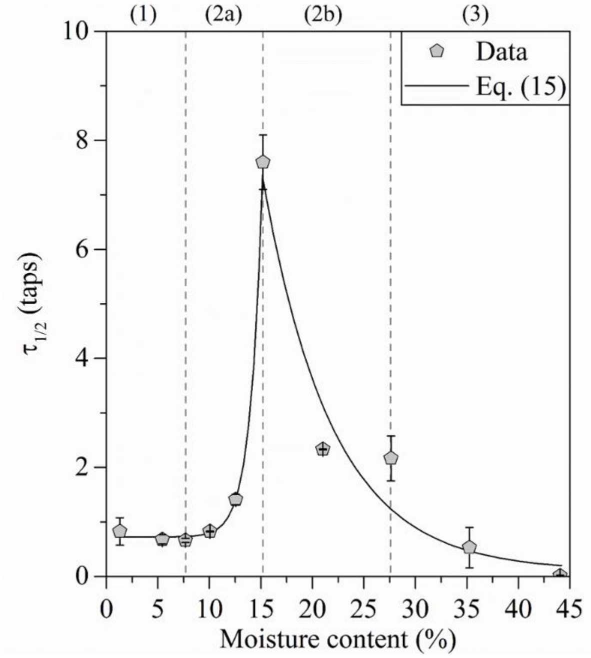

Figure 6. Effect of moisture content on the granular relaxation index ($\tau_{½}$) of drilled cuttings.

$$\tau_{1/2} = \begin{cases} 1.4x10^{-5}e^{0.86MC} + 0.72 & for \quad MC < 15.2\% \\ 6.8x10^{1}e^{-0.15MC} + 0.10 & for \quad MC \geq 15.2\% \end{cases} \tag{15}$$

Flowability indicators

The correlation between the Hausner ratio and the angle of repose for all moisture contents analyzed is shown in Figure S5, along with the classifications of flowability [42]. A weak logarithmic tendency was perceived. Thus, Eq. (16) was fitted to the data with an R^2 of 0.996, which indicates a good adjustment to the model. It is observed that the flowability determined from *HR* corresponded to that determined using *AoR*, which highlights the coherence between the data.

$$AoR(°) = 47.377 ln(HR) + 25.910 \tag{16}$$

Figure 7 shows the Hausner ratio from drilled cuttings with different *MC*s and the flowability classifications and state limits of Figure 3. The same tendencies were also observed for *AoR*. The increment of moisture from the dry state (1) up to the end of the aggregated substate (2a) resulted in a reduction in the material's flowability from "fair" to "very poor." This phenomenon was also similarly observed by distinct authors [17,41,43] analyzing different materials and is usually attributed to increased cohesion forces. The increment of those forces may reduce the mobility between particle-particle and particle-wall surfaces, resulting in lower flowabilities [16]. On the disaggregated (2b) and slurry (4) states, the flowability is gradually increased from “very poor” to “excellent” with the increment of moisture. This phenomenon is hypothesized to be due to the intensification of the particle surfaces' lubrication and reduction of the relative effect of cohesion forces, increasing the flowability. The Eq. (17) (R^2 = 0.999) was used to represent the correlation between MC and HR.

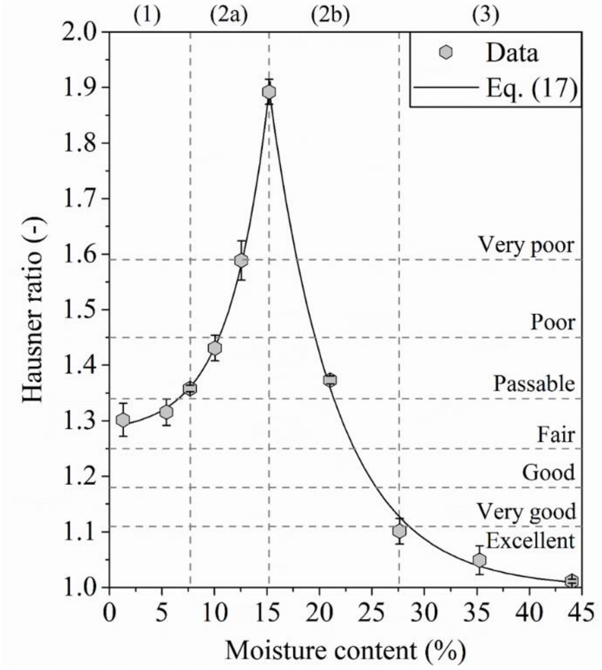

Figure 7. Effect of moisture content on Hausner ratio (HR) of drilled cuttings.

$$HR = \begin{cases} 6.8x10^{-3}e^{0.29MC} + 1.30 & for \quad MC < 15.2\% \\ 7.2x10^{0}e^{-0.13MC} + 0.95 & for \quad MC \geq 15.2\% \end{cases} \tag{17}$$

General drilled cuttings handling behavior

Figure 8 summarizes the general effect of *MC* on the main powder handling properties studied: loose porosity (ε_0), tapped bulk porosity (ε_t) and effective porosity (ε_{eff}), additional porosity (ε_{add}), Hausner ratio (*HR*), and granular relaxation index ($\tau_{½}$). For better comparison, the data were normalized to a common scale ranging from zero to one using the following equation:

$$z_i = \frac{x_i - x_{\min}}{x_{\max} - x_{\min}} \tag{18}$$

where z_i is the normalized value, x_i is the non-normalized value, x_{max} is the maximum non-normalized value, and x_{min} is the minimum non-normalized value.

It is possible to notice that the increment of *MC* up to 15.2% promoted the formation of looser interparticle structures. However, these structures were steadier, showing greater difficulty flowing and releasing air/liquid. These phenomena were attributed to the increase of cohesion forces with *MC*. The continuous increment of *MC* beyond 15.2% promoted a complete change in the material behavior. The interparticle structures became denser. The material could flow and release air/liquid more easily. These phenomena were hypothesized to be due to the reduction of cohesion and friction forces (lubrication action).

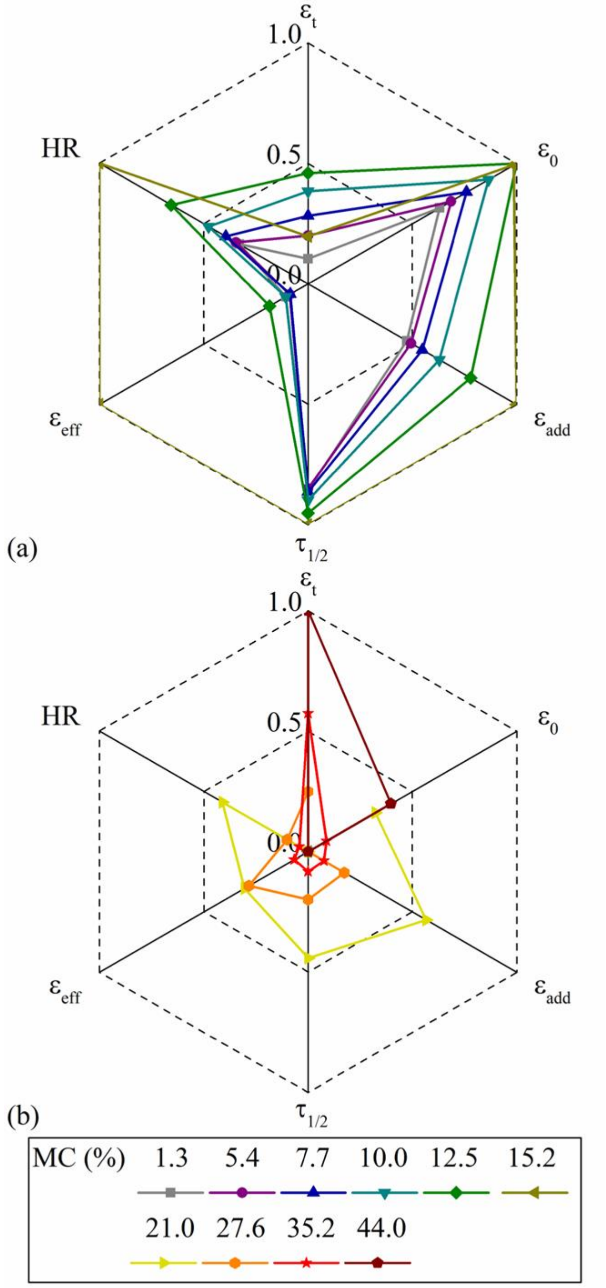

Figure 8. Summary of moisture content effects on drilled cuttings' powder handling parameters.

Generally, the drilled cuttings in the aggregated/disaggregated state (Figure 8 (10.0–21.0%)) showed the worst properties once the material showed cohesive behavior with low flowability.

Even though the addition of high *MC* in the slurry state (Figure 8 (21.0–44.0%)) promoted an apparent improvement of some properties, handling such saturated bulk material in real applications might cause unexpected problems. The material initially seems to be well flowing, but soon after a small quantity of liquid is drained off, a state is attained (state (2)) where flowability gets poor again [16]. Thus, cuttings in the dry state (Figure 8 (1.3–10.0)) seem to be the best to handle since they present more stable properties and relatively good flowability.

Bed packing and flowability properties correlations

As observed by many authors, the Hausner ratio (*HR*), Angle of repose (*AoR*), loose bulk density (ρ_0), and porosity (ε_0) can be described as functions of the mean diameter of particles (D) and Archimedes number (Ar) for several granular materials [22,43–47]. To check if there is a correlation between these parameters for drilling cuttings with different *MC*s, a multiple regression analysis was carried out by fitting Eq. (19) to the data. The analysis was also extended to the additional (ε_{add}) and effective bulk porosities (ε_{eff}) parameters.

$$y_i = ae^{bx_i} + c \qquad (19)$$

where y_i is the predicted variable (*HR*, *AoR*, ρ_0, ε_0, ε_{add}, and ε_{eff}), x_i is the estimating variable (*D* or *Ar*), and *a, b,* and *c* are correlation parameters. The mean diameters of the particles/aggregates, obtained by the optical microscopy analysis (Figure 2), were used to represent D. The Ar, described by Eq. (20), is a significant parameter characterizing the interplay between the floating force and the viscous force. Specifically, it quantifies the gravitational force acting on the particles, promoting their movement and filling empty voids. Nevertheless, the same number also embodies the opposing forces, such as buoyancy and viscosity, which counteract the particles' ability to occupy these voids [22].

$$Ar = \frac{\rho_f(\rho_p - \rho_f)gD^3}{\mu^2} \qquad (20)$$

where ρ_f is the fluid density, ρ_p is the particle density, *g* is the gravity acceleration, *D* is the particle mean diameter, and μ is the fluid dynamic viscosity. Some hypotheses were assumed to make this analysis possible. For MCs ≤ 21.0% (states (1) and (2)), the system was considered to be composed of particles and aggregates containing water on their surface and inner structure immersed in the air as a fluid. Therefore, ρ_p was calculated by considering the influence of the added water, and *D* was considered as the mean diameter of the particles/aggregates (Figure 2) obtained by the optical microscopy analysis for each *MC*. For MCs ≥ 21.0% (state (3)), the system was considered to be composed of particles and aggregates immersed in water as a fluid once the saturation level was at the capillary state. Thus, ρ_p was considered the actual density (ρ_r), and D was still taken as the mean diameter of the particles/aggregates.

The analysis showed that significant correlations were only obtained for ρ_0, ε_{add}, ε_{eff}, and *HR* as a function of *D* and *Ar*, as seen in Figure S6. A good correlation between *AoR* in the function of *D* and *Ar* was also observed; nevertheless, the correlations for this parameter were not shown due to the limited amount of AoR data. The results of Figures S6a and S6b showed that Eqs. (21) and (22) accurately describe (±10%) most of the values of ρ_0 in the function of *D* and *Ar*, respectively.

$$\rho_0 = 360.170e^{-4.2x10^{-2}D} + 0.777, \text{ for } 1.3\% \le MC < 21.0\% \cup 21.0\% < MC \le 44.0\% \qquad (21)$$

$$\rho_0 = 1.137e^{-7.6x10^{-11}Ar} + 0.663, \text{ for } 1.3\% \le MC < 21.0\% \cup 21.0\% < MC \le 44.0\% \qquad (22)$$

The ρ_0 decreases with the increase of *D* and *Ar* (Figures S6a and S6b), which was contrary to observations made by many authors [22,43–47]. However, a fundamental difference exists between the analyses conducted by these authors and the analyses presented in this paper. In those previous works, the effect of dry particles' diameters on ρ_0 is observed, resulting in a decrease in bulk density for finer particles due to van der Waals forces [45]. On the other hand, in the analyses performed in this paper, the increase in particle size is related to particle aggregation, possibly due to the increase of liquid bridge forces as the MC increases up to 15.2%. Consequently, it is expected that ρ_0 decreases with the increase of *D* as stronger liquid bridge forces form, preventing particles from rearranging into a denser configuration. For *MC* values higher than 15.2%, the values of *D* for the slurry state (3) become similar to those of the dry state (1), owing to the desegregation of the particles' clusters (Figure 2). Nevertheless, significantly higher values of ρ_0 are observed for the slurry state (3), probably because the void spaces were filled with water, increasing the bed weight. The primary influence on *Ar* is the particle size, as the *D* term is raised to the power of three in the definition of *Ar* [47]. Therefore, a similar effect of *Ar* on ρ_0 is observed. These results indicate that several complex phenomena are involved in the relationship between ρ_0, *D*, and *Ar* when the MC varies over a large range. As a result, although Eq. (21) and (22) can represent most of the data, they cannot predict, for instance, the point of MC of 21.0%.

Figures S6c–S6f displayed that Eqs. (23–26) accurately describe (±5% or ±10%) most of the values of ε_{add} and ε_{eff} in the function of *D* and *Ar*. It is observed that ε_{add} and ε_{eff} decrease as *D* and *Ar* increase. Once again, several complex phenomena are involved, but as observed similarly for ρ_0, the results indicate that the bed becomes looser with the increase of *D* and *Ar*. It is worth noting that the use of *Ar* is preferable to *D* since the data on the slurry state can be predicted more accurately, probably because *Ar* considers the effect of the fluid properties.

$$\varepsilon_{add} = -1.051e^{-7.1x10^{-3}D} + 0.588, \text{ for } 1.3\% \le MC < 21.0\% \quad (23)$$

$$\varepsilon_{add} = -3.672e^{-5.6x10^{-12}Ar} + 3.655, \text{ for } 1.3\% \le MC < 44\% \quad (24)$$

$$\varepsilon_{eff} = -1.348e^{-1.6x10^{-2}D} + 0.617, \text{ for } 1.3\% \le MC < 15.2\% \quad (25)$$

$$\varepsilon_{eff} = -0.953e^{-1.4x10^{-10}Ar} + 0.681, \text{ for } 1.3\% \le MC < 21.0\% \cup 21.0\% < MC \le 44.0\% \quad (26)$$

Finally, Figures S6g and S6h exhibited that Eqs. (27) and (28) accurately describe (±5%) most of the values of *HR* in the function of *D* and *Ar*. However, once again, the values of *HR* in the slurry state could only be predicted in the function of *Ar*. It is also observed that *HR* increases with *D* and *Ar*, which is consistent with the hypothesis that the increase in the aggregated sizes is related to the strengthening of liquid bridge forces up to 15.2%, well-known to reduce the particle's mobility [17]. The material becomes saturated for higher MCs, leading to the disaggregation of the particle clusters and an increase in flowability.

$$HR = -3.211e^{-1.7x10^{-3}D} + 3.767, \text{ for } 1.3\% \le MC < 21.0\% \quad (27)$$

$$HR = 0.256e^{-6.0x10^{-11}Ar} + 0.745, \text{ for } 1.3\% \le MC < 44.0\% \quad (28)$$

CONCLUSION

An extensive analysis was conducted to assess the impact of moisture content on drilled cuttings, examining particle aggregation/disaggregation dynamics, packed bed properties, and flow behavior. Four characteristic states were identified according to the results: dry (1.3–7.7%), aggregated (7.7–15.2%), disaggregated (15.2–27.6%), and slurry (27.6–44.0%). The increment of moisture promoted the gradual aggregation of the particles into clusters of larger diameters in dry and aggregated states, which were disaggregated in higher moistures in the disaggregated and slurry states. Higher moisture in the dry state resulted in the creation of looser interparticle structures. Subsequent increments in moisture within the aggregated substate facilitated the emergence of air-filled void spaces, leading to even more loosely arranged structures. In the disaggregated substate, the air-filled void spaces were reduced, to the detriment of liquid-filled void spaces increase, densifying the structures. In the slurry state, the liquid-filled spaces were large enough to produce looser structures again. The flowability of the cuttings was reduced with the moisture increase from "fair" at the dry state to "very poor" at the end of the aggregated substate. By continuously increasing moisture, flowability was gradually improved on the disaggregated and slurry states up to "excellent."

ACKNOWLEDGMENTS

The authors are grateful for financial and technical support from the Coordination for the Improvement of Higher Education Personnel (CAPES), the National Council for Scientific and Technological Development (CNPq), and Petróleo Brasileiro S.A (Petrobras®).

REFERENCES

[1] EnscoRowan, Offshore Market Recovery, EnscoRowan, Houston (2019), p. 28. https://www.valaris.com/home/default.aspx.

[2] C. Apostolidou, E. Sarris, A. Georgakopoulos, J. Pet. Sci. Eng. 208 (2022) 109758. https://doi.org/10.1016/j.petrol.2021.109758.

[3] A.K. Alkalbani, G.T. Chala, A.M. Alkalbani, Ain Shams Eng. J. 14 (2023) 102147. https://doi.org/10.1016/j.asej.2023.102147.

[4] IOGP, Drilling waste management technology review, The International Association of Oil & Gas Producer, London (2016), p. 102. https://www.iogp.org/bookstore/product/drilling-waste-management-technology-review/.

[5] S. Seaton, R.G. Morris, SPE/EPA/DOE Exploration and Production Environmental Conference, in Proceeding of SPE/EPA/DOE Exploration and Production Environmental Conference, Galveston, USA (2005) p. 157–164. https://doi.org/10.2118/94194-MS.

[6] G.A. Burnett, C. Crabb, D. Wood, K.W. Seyfert, J.M. McIntosh, US 2006/0102390A1 (2006).

[7] G.A. Burnett, C. Crabb, D. Wood, K. Seyffert, J. McIntosh, US 20070215386A1 (2007).

[8] G.A. Burnett, D. Wood, K.W. Seyffert, W.C. Herben, J.M. Mcintosh, C. Crabb, US 7195084B2 (2007).

[9] G.A. Burnett, D. Wood, K.W. Seyffert, W.C. Herben, J.M. Mcintosh, C. Crabb, EP 1766181B1 (2011).

[10] G.A. Burnett, D. Wood, K.W. Seyffert, W.C. Herben, J.M.

Mcintosh, C. Crabb, WO 2005/124096AI (2004).

[11] G.A. Burnett, C. Crabb, D. Wood, K.W. Seyffert, J. Mcintosh, EP 2165951A1 (2011).

[12] D. Mills, Pneumatic Conveying Design Guide, Elsevier, Oxford (2004) p. 650.

[13] G.E. Klinzing, F. Rizk, R. Marcus, L.S. Leung, Pneumatic Conveying of Solids: A Theoretical and Practical Approach, Springer, New York (2010) p. 600. https://doi.org/10.1080/07373939308916871.

[14] J.P. Robinson, S.W. Kingman, C.E. Snape, S.M. Bradshaw, M.S.A. Bradley, H. Shang, R. Barranco, Chem. Eng. Res. Des. 88 (2010) 146–154. https://doi.org/10.1016/j.cherd.2009.07.011.

[15] R. Pesic, T. Kaludjerovic-Radoicic, N. Boskovic-Vragolovic, Z. Arsenijevic, Z. Grbavcic, Chem. Ind. Chem. Eng. Q. 21 (2015) 419–427. https://doi.org/10.2298/CICEQ140618044P.

[16] D. Schulze, Powders and Bulk Solids, Springer, New York (2008) p. 516. 978-3-540-73768-1.

[17] A. Crouter, L. Briens, AAPS PharmSciTech 15 (2014) 65–74. https://doi.org/10.1208/s12249-013-0036-0.

[18] T.O. Althaus, E.J. Windhab, Powder Technol. 215-216 (2012) 59–65. https://doi.org/10.1016/j.powtec.2011.09.007.

[19] P. Pierrat, H.S. Caram, Powder Technol. 91 (1997) 83–93. https://doi.org/10.1016/S0032-5910(96)03179-8.

[20] H.G. Kristensen, Adv. Pharm. Sci. 7 (1995) 221–272. https://doi.org/10.1016/S0065-3136(06)80006-3.

[21] K.P. Panayiotopoulos, C.E. Mullins, J. Soil Sci. 36 (1985) 129–139. https://doi.org/10.1111/j.1365-2389.1985.tb00318.x.

[22] H. Kalman, D. Portnikov, Powder Technol. 381 (2021) 285–297. https://doi.org/10.1016/j.powtec.2020.12.019.

[23] API, Recommended Practice for Field Testing Oil-Based Drilling Fluids: API Recommended Practice 13B-2, Washington (2012), p. 67.

[24] ASTM, Standard Test Method for Sieve Analysis of Fine and Coarse Aggregates (C136-06), ASTM International, West Conshohocken (2015), p. 5. https://doi.org/10.1520/C0136_C0136M-14.

[25] P.A. Vesilind, Resour. Recover. Conserv. 5 (1980) 275–277. https://doi.org/10.1016/0304-3967(80)90007-4.

[26] ASTM, Standard test methods for determining loose and tapped bulk densities of powders using a graduated cylinder (D7481-18), American Society for Testing and Materials, (2018), p. 4. https://doi.org/10.1520/D7481-18.

[27] USP, The United States Pharmacopeia: the National Formulary, United States Pharmacopeia Convenction, Rockville (2018), p. 1136.

[28] H.O.N. Altino, G.A. Lourenço, C.H. Ataíde, Powder Technol. 391 (2021) 184–197. https://doi.org/10.1016/j.powtec.2021.06.013.

[29] K. Traina, R. Cloots, S. Bontempi, G. Lumay, N. Vandewalle, F. Boschini, Powder Technol. 235 (2013) 842–852. https://doi.org/10.1016/j.powtec.2012.11.039.

[30] ASTM, Standard Test Method for Measuring the Angle of Repose of Free-Flowing Mold Powders (C1444-00), American Society for Testing and Materials, (2000). p. 4. https://doi.org/10.1520/C1444-00.

[31] WHO. Bulk density and tapped density of powders (WHOdocument QAS/11.450), WorldHealth Organization, Dept. of Essential Medicines and Pharmaceutical Policies, (2012).

[32] K. Ishizaki, S. Komarneni, M. Nanko, Porous Materials, Springer, Boston (1998), p. 249. https://doi.org/10.1007/978-1-4615-5811-8.

[33] C. Hyun, S. Shah, S. Osisanya, SPE Annual Technical Conference and Exhibition, in Proceeding of the SPE Annual Technical Conference and Exhibition, Dallas, USA (2000), p. 905–918. https://doi.org/10.2523/63269-MS.

[34] I. Petri, M.S. Pereira, J.M. dos Santos, C.R. Duarte, C.H. Ataíde, C.M. d. Á. Panisset, J. Pet. Sci. Eng. 134 (2015) 23–29. https://doi.org/10.1016/j.petrol.2015.07.022.

[35] D. Geldart, Powder Technol. 7 (1973) 285–292. https://doi.org/10.1016/0032-5910(73)80037-3.

[36] R.J. Reeder, Carbonates: Mineralogy and Chemistry, Stony Book, New York (1983), p. 394. https://doi.org/10.1515/9781501508134.

[37] H.G. Kristensen, T. Schaefer, Drug Dev. Ind. Pharm. 13 (1987) 803–872. https://doi.org/10.3109/03639048709105217.

[38] A. Singer, Z. Barakat, S. Mohapatra, S.S. Mohapatra, Nanocarriers Drug Deliv. (2019) 395–419. https://doi.org/10.1016/b978-0-12-814033-8.00013-8.

[39] S. Golubić, J. Schneider, in Biogeochemical Cycling of Mineral-Forming, P.A. Trudinger and D.J. Swaine, Elsevier, (1979) Amsterdam, p. 122. https://doi.org/10.1016/S0166-1116(08)71056-2.

[40] P. Philippe, D. Bideau, Europhys. Lett. 60 (2002) 677–683. https://doi.org/10.1209/epl/i2002-00362-7.

[41] H. Lu, X. Guo, Y. Jin, X. Gong, Chem. Eng. Res. Des. 133 (2018) 326–334. https://doi.org/10.1016/j.cherd.2018.03.023.

[42] S. Gaisford, M. Saunders, Essentials of Pharmaceutical Preformulation, John Wiley & Sons, Chichester (2012), p. 252. https://doi.org/10.1002/9781118423226.

[43] H. Kalman, Powder Technol. 393 (2021) 582–596. https://doi.org/10.1016/j.powtec.2021.08.010.

[44] D. Geldart, E.C. Abdullah, A. Hassanpour, L.C. Nwoke, I. Wouters, Chin. Particuol. 4 (2006) 104–107. https://doi.org/10.1016/s1672-2515(07)60247-4.

[45] H. Kalman, D. Portnikov, Powder Technol. 381 (2021) 477–487. https://doi.org/10.1016/j.powtec.2020.12.014.

[46] I.M.F. Wouters, D. Geldart, Part. Part. Syst. Charact. 13 (1996) 254–259. https://doi.org/10.1002/ppsc.19960130408.

[47] H. Kalman, Powder Technol. 382 (2021) 573–593. https://doi.org/10.1016/j.powtec.2021.01.012.

HEITOR OTACÍLIO NOGUEIRA ALTINO[1]
GIOVANI AUD LOURENÇO[2]
CARLOS HENRIQUE ATAÍDE[1]
CLAUDIO ROBERTO DUARTE[1]

[1]Federal University of Uberlandia, Faculty of Chemical Engineering, Uberlândia, MG, Brazil

[2]Federal Institute of Goiás, Itumbiara, GO, Brazil

NAUČNI RAD

UTICAJ SADRŽAJA VLAGE NA SVOJSTVA I PROTOČNOST PAKOVANOG SLOJA OD OTPADAKA BUŠENJA

Za projektovanje i upravljanje različitom opremom sistema za kontrolu čvrstih materija u platformama za bušenje na moru, važno je utvrditi kako sadržaj vlage utiče na karakteristike otpadaka od bušenja koja utiču na formiranje pakovanih slojeva i strujanje preko čvrstih površina. Ovaj rad pruža sveobuhvatnu analizu o tome kako sadržaj vlage, prvenstveno sastavljen od vode i koji predstavlja mulj na bazi vode (VBM), utiče na svojstva i protočnost pakovaog sloja otpadaka. Analizirana je dinamika agregacije/deagregacije čestica, nasipne mase i poroznosti rastresitog i zbijenog sloja, dinamika zbijanja pakovanih slojeva, Hausnerov koeficijent i ugao nagiba otpadaka sa deset različitih sadržaja vlage (1,4–44,0 tež%). Uočeno je da povećanje sadržaja vlage do 15,2% podstiče formiranje labavije interčestične strukture. Međutim, ove strukture su bile stabilnije, pokazujući veće teškoće pri proticanju i oslobađanju vazduha/tečnosti. Kontinualno povećanje sadržaja vlage preko 15,2% je doprinelo potpunoj promeni ponašanja materijala. Međučestične strukture postale su gušće. Materijal je mogao lakše da teče i oslobađa vazduh/tečnost. Pored toga, bilo je moguće uspostaviti klasifikaciju različitog ponašanja otpadaka prema sadržaju vlage. Predloženi su prediktivni modeli za opisivanje uticaja sadržaja vlage na svojstva i protočnost pakovanog sloja od otpadaka bušenja..

Ključne reči: agregacija čestica, dezagregacija čestica, pakovani sloj, protočnost, zbijanje.

Chemical Industry & Chemical Engineering Quarterly

Available online at
Association of the Chemical Engineers of Serbia *AChE*
www.ache.org.rs/CICEQ

Chem. Ind. Chem. Eng. Q. 30 (3) 207–221 (2024) CI&CEQ

ANANTHAKUMAR SUDALAIMANI[1]
BARATHIRAJA RAJENDRAN[2]
THIYAGARAJ JOTHI[3]
MATHANBABU MARIAPPAN[4]

[1]Department of Mechanical Engineering, Government College of Engineering. Tirunelveli, Tamil Nadu, India

[2]Department of Mechanical Engineering, Einstein College of Engineering, Near MS University, Tirunelveli, Tamil Nadu, India

[3]Department of Mechatronics Engineering, Er. Perumal Manimekalai College of Engineering, Hosur, Tamil Nadu, India

[4]Department of Mechanical Engineering, Government College of Engineering, Bargur, Krishnagiri, Tamil Nadu, India

SCIENTIFIC PAPER

UDC 621.436-222:662.61:665.3

COMBUSTION, EMISSION, AND PERFORMANCE CHARACTERISTICS OF HYBRID BIOFUEL AT DIFFERENT COMPRESSION RATIOS

Article Highlights

- Future automobile energy utilities
- Hybrid biofuel was prepared by transesterification and pyrolysis methods
- Brake thermal efficiencies of hybrid biofuel fuels were higher than those of conventional fuel

Abstract

The primary aim of this study is to alternate between conventional fossil fuels and reduce the emissions of greenhouse gases and smoke from diesel engines. The current study aimed to improve the performance and emission characteristics of a variable compression ratio (VCR) diesel engine operated with hybrid biodiesel. Experiments were done with the best hybrid biodiesel, which was made by mixing 20% rubber seed oil (RSO) with 80% waste plastic oil (WPO). The tests were done at four compression ratios (CRs): 16:1, 17:1, 18:1, and 20:1. Under a CR of 20:1 and at full load, the engine's brake thermal efficiency went up by 30.5%, its brake-specific fuel consumption went down by 0.347 kg/kWh, and notably diminished emissions of carbon monoxide (0.43% volume), hydrocarbons (79 ppm), and smoke (22%). However, with increasing CRs, NOx emissions rose unfavourably (1092 ppm) compared to diesel (820 ppm). Also, diesel and clean (WPO) were compared to see how the CR values affected combustion, performance, and emissions. Compared to diesel, under maximum load and the CR of 20:1, hybrid biodiesel demonstrated approximately 3.7% higher brake thermal efficiency. The findings suggest potential applications for this hybrid biodiesel in the automobile sector, the power generation industry, and marine applications.

Keywords: rubber seed oil, waste plastic oil, performance, emission, variable compression ratio.

The emissions from the CI engine create major air pollution, which can affect human health. Therefore, many researchers explored different alternate fuels that minimized air pollution. They combined two biofuels that can be utilised in CI engines as an alternative fuel. Liu *et al.* [1] produced rubber seed oil (RSO) using an ultra-stable Y (USY) zeolite catalyst. This catalyst is suitable for producing liquid fuels from RSO. Wuttichai *et al.* [2] studied the composition and properties of the extracted RSO and high-free fatty acid oil after transesterification using different catalysts like CaO, sodium metasilicate-based egg shells, and CaO with waste coral fragments. Christine *et al.* [3] studied the synthesis of WPO by catalytic pyrolysis using

---

Correspondence: B. Rajendran, Department of Mechanical Engineering, Einstein College of Engineering, Near MS University, Tirunelveli - 627 012, Tamil Nadu, India.
E-mail: barathiraja1980@gmail.com
Paper received: 3 February, 2023
Paper revised: 28 August, 2023
Paper accepted: 7 September, 2023

https://doi.org/10.2298/CICEQ230203024A

nitrogen as a carrier gas. The WPO is extracted from polythene bags. The catalysts used are silica, alumina, barium carbonate, Y zeolite, and zeolite.

Recent studies have been performed by many researchers on the combustion and performance parameters of a CI engine operated with alternate fuels such as waste palm oil [4], apple seed oil [5], biodiesel derived from chicken waste [6], rice bran oil [7], tamanu oil [8], and marula seed oil [9]. A variable compression ratio (VCR) engine's combustion efficacy and exhalation smoke properties were studied by Nagaraja *et al.* [4]. Their CR values varied from 16:1 to 20:1 with 90 °C pre-heated palm oil, and their blends ranged from 5% to 20%. The outcome shows that the output smoke temperature is diminished for all experiments and that CO and HC emissions drop as blend percentages and CR values increase.

Using Eagle Marmelo oil, Krishnamoorthi and Malayalamurthi [10] investigated the effect of varying CR and nozzle holes. The findings show that a higher CR value improves combustion characteristics. Elevation in the CR is also associated with decreased BSFC, HC, CO, and smoke emissions and improved thermal efficiency. Singh and Shukla [11] investigated the combustion characteristics of the VCR engine by varying CR from 15:1 to 18:1 using castor biodiesel blends varying from B00 to B50. The results indicated that cylinder pressure reached its maximum at the CR of 18:1 and B50 blend, and the net heat release rate decreased for B00 at CR 15:1.

Mohit *et al.* [7] conducted tests on a VCR diesel engine using rice bran oil blends ranging from 10% to 40% at CR values ranging from 15:1 to 18:1. The study focused on analysing the performance and exhaust emission parameters of these tested blends. Mohammed *et al.* [12] explored the impact of different waste cooking oil blends ranging from 10% to 50% at CR values of 14:1, 16:1, and 18:1 on a CI engine. The study delved into assessing performance, emission, and combustion parameters in this context. The findings suggest that brake-specific fuel consumption decreases as the compression ratio (CR) increases for all blends.

Tamanu oil blends were experimentally examined on VCR engines (16:1, 18:1, 20:1, and 22:1) by Antony and Bose [8]. In contemplation of an increase in performance and lower emissions, the test findings showed that this alternative fuel could be mixed with diesel up to 40% at an ideal CR value of 20:1. Moreover, according to researcher suggestions, as the CR values rise, the BTHE values rise as well. By employing esterified tamanu oil, Raj and Kandasamy [13] experimented to ascertain the operating conditions of the VCR engine. The outcome demonstrates that emissions are decreased, and engine performance is increased. Gandure and Ketlogetswe [9] compared the performance of marula seed oil and diesel on a VCR engine. According to the findings, the engine performance with marula oil is very close to that with diesel at CR 16:1. The operation behaviour of the engine, exhalation smoke properties, and flame efficiency of a VCR engine employed on waste cooking and sunflower oil methyl esters and their mixes of 20%, 40%, 60%, and 80% were studied by Muralidharan and Vasudevan [14].

The findings show that increased CR values are associated with a greater ignition interval and a slower heat dissipation rate. Amarnath *et al.* [15] assess the engine operation behaviour and exhalation qualities of smoke in a VCR engine using the methyl esters of Karanja and Jatropha. According to the findings, both biodiesels function better at superior CR values. In comparison to diesel pollutants, biodiesel produces fewer emissions. Ashok Kumar *et al.* [16] researched a VCR engine fuelled with Pinnai oil blends at CR ranging from 15:1 to 18:1 and investigated the performance parameters. They also examined the engine's operations, combustion efficiency, and emission behaviour. The findings showed that the mixes' BSFC values were extremely close to those of diesel.

The CI engine operations, flame efficiency of the engine, combustion efficiency, and exhalation qualities of smoke were examined by Ravi *et al.* [17]. As the CR rises, the engine’s performance improves. They provided a detailed analysis of NOx reduction methods like EGR. Rinaldini *et al.* [18] assessed the performance of a CI engine running on WPO and the behaviour of its emissions. The findings indicated that WPO causes an increase in NOx emissions. According to Mani *et al.* [19], the WPO was used as fuel in a CI engine, and though CO and HC exhalations were relatively excessive, the BTHE of the WPO was equal to that of diesel. Devaraj *et al.* [20] investigated WPPO blended with 5% and 10% diethyl ether in a CI engine and looked at the engine parameters, emission characteristics, and combustion efficiency. The findings showed that although smoke pollution has decreased, BTE with WPPO has improved. In their study, Ibrahim *et al.* [21] examined a compression-ignition engine's emissions and combustion efficacy utilizing a 50:50 volume percentage blend of crude RSO and palm oil. According to reports, higher blend ratios result in higher NOx emissions and exit smoke temperatures while decreasing CO emissions.

Coir-pith gas and RSO blends are analysed in a diesel engine by Ramadhas *et al.* [22]. Higher specific energy consumption and increased exhaust emissions are obtained with blends at all load conditions. Senthilkumar and Sankaranarayanan [23] investigated the diesel engine characteristics at WPO. The findings demonstrate that WPO increases carbon monoxide, NOx, and HC pollution more rapidly than diesel. In their research, Kasiraman *et al.* [24] investigated the operational parameters of a compression-ignition (CI) engine using neat cashew nut shell oil (CSNO) and camphor oil (CMPRO) as fuel. It is reported that the CMPRO 30 blend showed good performance compared with diesel in terms of BTE and heat energy dissipation at full load. Hifjur *et al.* [25] evaluated the diesel engine using Mahua and Simarouba oil blends B10 and B20 in 50:50 volumes. It is reported that the B10 blend can be used for long-term use based on assessing fewer soot deposits after 100 hours of engine operation than diesel.

HCCI-DI engines powered by acetone-butanol-ethanol were studied by Ibham *et al.* [27]. As a result of the addition of acetone, butanol, and ethanol, NOx emissions were successfully reduced, and brake thermal efficiency and fuel consumption were also improved. Christopher *et al.* [28] evaluated the performance parameters of biodiesel produced from local South African canola and sunflower oil feedstocks. According to their report, the smoke emissions from biodiesel and its diesel blends were lesser than those from pure diesel, but there was an increase in nitrogen oxide emissions. Garavand *et al.* [29] utilized a combination of diesel, waste fish oil biodiesel, and 2%, 4%, 6%, and 8% ethanol to fuel diesel engines while incorporating graphene quantum dots to enhance their properties. Their findings revealed that the mixture containing 45 ppm GQD, 6% ethanol, 10% biodiesel, and 90% diesel exhibited the highest braking force and engine torque and lower unburnt hydrocarbon and NOx emissions.

Samuel *et al.* [30] researched a hydrodynamic cavitation reactor for producing biodiesel from low-free-fat acid RSO. They studied the impacts of transesterification variables, including 3%–5% wt. KOH, 30–50 minutes of reaction time, and a 3.5/7.0 ethanol/RSO molar ratio. The study found that at a 6/1 ethanol/oil molar ratio, a 4.5 wt. % KOH concentration, and a 40-minute reaction period, RSO production reached 92.5% of the maximum. Singh *et al.* [31] focused on utilising microalga Spirulina blends with diesel in a VCR engine with various loads, CRs, and blend concentrations. At a 16:1 CR and 20% blend concentration, the engine had a 31.357% BTE and a 0.274 kg/kWh BSFC. It also had lower nitrogen oxide levels of 1804.9 ppm, CO_2 levels of 869.075 g/kWh, and PM levels of 0.2807 g/kWh. Hananto *et al.* [32] examined how the emissions from the CI engine create major air pollution, which can affect human health. Their findings indicated that the introduction of butanol into diesel engines led to lower exhaust gas temperatures and CO emissions while simultaneously increasing HC emissions and smoke opacity. Therefore, many researchers, including Samuel *et al.* [33], explored alternate fuels that minimise air pollution.

The literature review highlights that the VCR engine exhibits optimal performance, achieving maximum power output while maintaining low emissions when fuelled with unmixed pure biodiesel and hybrid alternative fuels. However, no prior research has been conducted on the utilization of a specific hybrid alternative biodiesel comprising a blend of 20% RSO and 80% waste plastic oil (WPO), particularly at varying CR values ranging from 16:1 to 20:1. The primary objective of this research is to analyse and compare the effects of different CR values on several performance and combustion characteristics, including BTHE, BSFC, cylinder peak pressure, ignition delay, and HRR. Additionally, the study aims to evaluate emissions, such as EGT, NOx, HC, CO, and smoke opacity, when using the aforementioned hybrid alternative biodiesel. Comparisons will be made with the performance and emissions characteristics of conventional diesel and neat WPO. This analysis is valuable for engine manufacturers who produce high CR engines in large volumes, as it assists in selecting an optimum CR. Allowing these manufacturers to enhance engine performance and emissions control will also lead to the development of more environmentally friendly and efficient engines.

MATERIALS AND METHODS

Production of RSO methyl esters

RSO is a non-edible oil made from rubber seeds. It is usable as biodiesel. Biodiesel is created when RSO is transformed into methyl, ethyl, or butyl esters. Due to its low volatile property and excessive viscous behaviour compared to diesel, biodiesel in IC engines causes issues such as pumping, atomization, injector choking, piston wear, etc. The raw RSO contains saturated and unsaturated fatty acid compositions. The unrefined RSO contains 22% free fatty acids (FFA). Methanol is a reactant in the biodiesel synthesis process because it is more reactive and readily available on the market. The RSO consists of three esters and around 20% glycerine. The glycerine can be replaced with alcohol to make a less viscous biodiesel by transesterification.

Non-edible RSO has been considered a potential feedstock in India. Therefore, it has been selected as fuel in the present investigation. Eq. (1) describes the chemical process that transforms unprocessed RSO into a methyl ester of RSO. R1, R2, and R3 represent long hydrocarbon or fatty acid chains. The transesterification process requires two stages because the RSO contains 22% free fatty acids. The first stage is acid esterification, in which the reactant methanol and sulfuric acid catalyst react with the FFA present in raw RSO to produce methyl ester and water. It is given by Eq. (2). This process reduces the free fatty acid level.

After that, using potassium hydroxide as an additive, the low FFA prior-processed oil can undergo second-stage alkaline esterification processing to transform the triglycerides into methyl esters and the fatty acids into soap and water. It is given in Eq. (3):

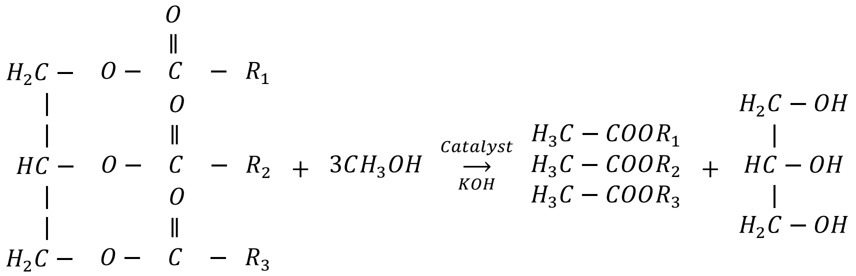

$$\begin{array}{l} H_2C-\ O-\ \overset{\overset{O}{\|}}{C}\ -\ R_1 \\ \ | \\ HC-\ O-\ \overset{\overset{O}{\|}}{C}\ -\ R_2 \\ \ | \\ H_2C-\ O-\ \overset{\overset{O}{\|}}{C}\ -\ R_3 \end{array} + 3CH_3OH \xrightarrow[KOH]{Catalyst} \begin{array}{l} H_3C-COOR_1 \\ H_3C-COOR_2 \\ H_3C-COOR_3 \end{array} + \begin{array}{c} H_2C-OH \\ | \\ HC-OH \\ | \\ H_2C-OH \end{array} \qquad (1)$$

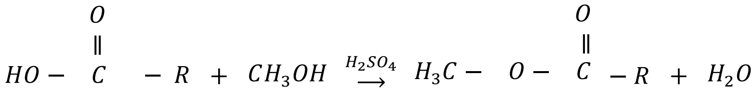

$$HO-\ \overset{\overset{O}{\|}}{C}\ -R + CH_3OH \xrightarrow{H_2SO_4} H_3C-\ O-\ \overset{\overset{O}{\|}}{C}\ -R + H_2O \qquad (2)$$

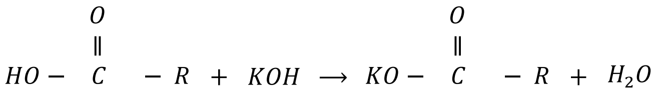

$$HO-\ \overset{\overset{O}{\|}}{C}\ -R + KOH \longrightarrow KO-\ \overset{\overset{O}{\|}}{C}\ -R + H_2O \qquad (3)$$

Using methanol as the reactant and sulfuric acid as the catalyst, 22% of the FFA is reduced to less than 2% within the initial stage of acid esterification. The second phase of transesterification is finished when potassium hydroxide, a catalyst, is applied to the previously processed oil for alkaline esterification to produce the methyl ester of RSO. The transesterification conditions leading to the production of RSO methyl ester encompassed a 4/10 methanol/RSO molar ratio, 6 ml of H_2SO_4 acid catalyst, 6 g of KOH alkaline catalyst, a reaction time of 60 minutes, a magnetic stirrer speed set at 1000 rpm, and a reaction temperature of 60 °C. These conditions resulted in a yield of 76% relative to the maximum possible output.

Production of the WPO

The thermochemical pyrolysis process breaks waste plastics down into valuable yields at elevated temperatures, also without oxygen. Pyrolysis produces volatile fractions and impurities such as carbonised char or solid residues. Saturated and fragrant hydrocarbons and non-condensable gas with a significant calorific value comprise the volatile fractions. The distillation process converts volatile fractions into WPO [19].

Figure 1a depicts the distillation plant's conceptual layout. A thin cylindrical vessel encloses the stainless steel reactor. The silicone oil fills the gap between the reactor and the cylindrical vessel, and an electrical heating coil is submerged in the oil. A metallic sheet surrounds and insulates the outer layer with glass wool. The distillation plant consists of a pressure gauge, a pressure relief valve, a feed hopper with a control valve, a thermocouple sensor, an oil level indicator, a control panel, and a slag drain.

The slag drain removes the residual oil after distillation. The outlet of the plant is connected to the water-cooled condenser. The condensed liquid from the pyrolysis plant is poured into the distillation plant through a feed hopper with a control valve. The valve is fully closed after pouring the oil. The heat is transferred from the coil to the silicone oil and then to the plastic oil. The reactor temperature increases from 200 °C to 350 °C, evaporating the plastic vapours. The plastic vapour from the plant is passed through the condenser. The condensate liquids are gathered at the fractioned oil collector, creating WPO.

The pyrolysis conditions in this study involved (i) maintaining the pyrolysis plant reactor temperature between 500 °C and 700 °C and (ii) maintaining the inside temperature of the distillation plant reactor between 200 °C and 350 °C, based on equivalent petro-diesel fractional properties. The optimum yield of WPO was calculated as follows: Initially, 10 kg of waste plastic was used. After degradation, WPO yielded 75% to 80%, leaving 20% to 25% of waste. The fractionated plastic oil obtained after distillation accounted for 60 to 65% of the conversion. The liquid fuel was delivered approximately 3.5 hours after the initiation of the pyrolysis process.

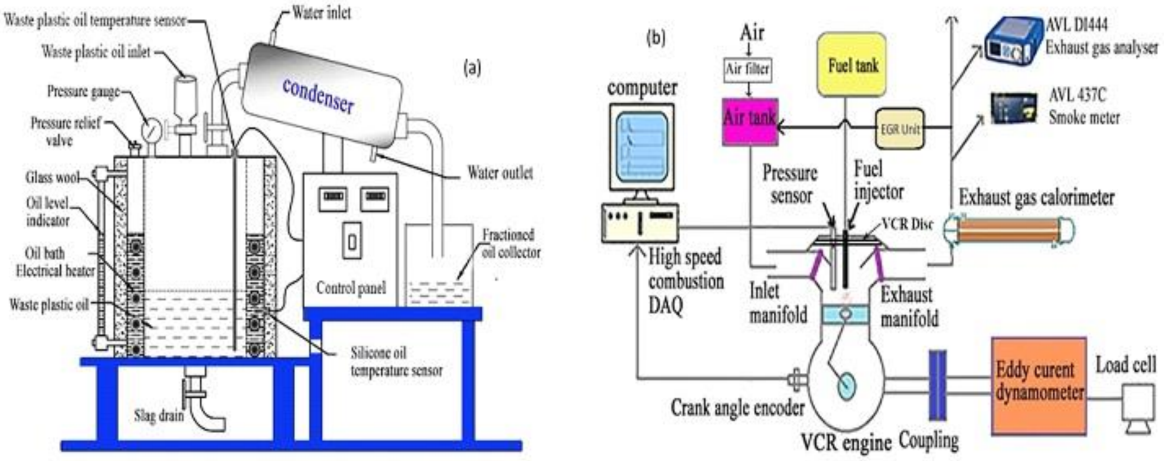

Figure 1. Schematic diagram of (a) Distillation plant (b) Experimental setup.

Gas chromatography and mass spectrometry (GC-MS) analysis of WPO

The main feature of GC-MS is that it combines the features of gas-liquid chromatography and mass spectrometry. The WPO is characterised using a GC instrument. The working principle of a mass spectrometer is followed by the separation of gas-phase ions according to mass/charge ratio and their sequential detection. The mass spectrometry (MS) instrument is operated at a temperature of 220 °C, with the ion source temperature set at 200 °C, covering mass-to-charge numbers from 20 to 1200 m/z. Figure 2a illustrates the schematic diagram of the GC-MS instrument. The GC-MS chromatogram of WPO is depicted in Figure 2b.

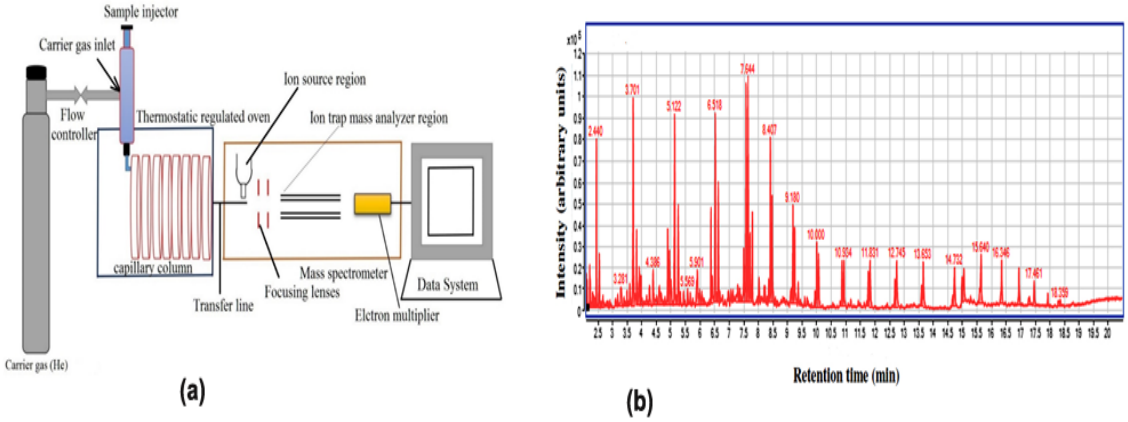

Figure 2. Diagram of (a) GC-MS instrument (b) GC-MS chromatogram of WPO.

The foremost constituents of WPO obtained from GC-MS analysis are given in Table 1. It can be seen that the WPO consists of 20 compounds. From Table 1, the compounds are in the range from C_7 to C_{22} approximately. It shows that WPO has similarities to diesel. In addition, the oil properties of $C_{12}H_{25}$ are closest to diesel. From the area percentage, the average chemical formula of the WPO is calculated as $C_{11.55}H_{21.8}$, but the average chemical formula of common diesel is $C_{12}H_{24}$.

Physio-chemical properties of RSO, WPO and diesel

Table 2 summarises the essential physical and chemical characteristics of RSO, WPO, and diesel in accordance with ASTM standards.

Experimental setup

Figure 1b illustrates the experimental arrangement. The engine used for this research is the Kirloskar (AV1) engine, a vertical, direct-injection, water-cooled, naturally aspirated engine with a rated

Table 1. Main components of WPO obtained from GC-MS analysis.

Peak	Reaction Time (min)	Area %	Chemical formula	Chemical compounds
1	2.440	60.54	$C_9H_{16}O$	Cyclopentanone, 2-(1-methylpropyl)-
2	3.281	16.71	$C_{10}H_8N_2O_2S_2$	N-(4-Oxo-2-thioxo-thiazolidin-3-yl)-benzamide
3	3.701	100	$C_7H_{14}O_2S$	trans-2, 4-Dimethylthiane, S, S-dioxide
4	4.386	18.59	C_9H_8	Benzene, 1-ethynyl-4-methyl-
5	5.122	93.42	$C_{11}H_{24}O$	1-Undecanol
6	5.901	33.63	$C_{12}H_{22}O_3$	1, 3-Dioxan-4-one, 2-heptyl-6-methyl
7	6.518	80.52	$C_7H_{14}O_2S$	trans-2, 4-Dimethylthiane, S, S-dioxide
8	7.644	89.56	$C_{12}H_{25}F$	Dodecane, 1-fluoro-
9	8.407	62.9	$C_{18}H_{36}$	5-Octadecene, (E)-
10	9.18	43.05	$C_7H_{14}O_2S$	trans-2,4-Dimethylthiane, S, S-dioxide
11	10.000	32.67	$C_7H_{14}O_2S$	trans-2, 4-Dimethylthiane, S, S-dioxide
12	10.934	26.48	$C_{12}H_{25}F$	Dodecane, 1-fluoro-
13	11.831	27.87	$C_{12}H_{25}F$	Dodecane, 1-fluoro-
14	12.745	32.86	$C_{12}H_{25}F$	Dodecane, 1-fluoro-
15	13.653	33.85	$C_{14}H_{30}O$	Heptane, 1, 1'-oxybis-
16	14.732	32.79	$C_{14}H_{30}O$	Heptane, 1, 1'-oxybis-
17	15.64	39.08	$C_{12}H_{25}F$	Dodecane, 1-fluoro-
18	16.346	31.8	$C_{12}H_{25}F$	Dodecane, 1-fluoro-
19	17.461	16.77	$C_{22}H_{46}$	2, 2-Dimethyleicosane
20	18.359	4.77	$C_{12}H_{10}O_4S$	2-Hydroxy-3-(thiophen-2-yl)methyl-5-methoxy-1, 4-benzoquinone

Table 2. Physio-chemical properties of diesel, RSO and WPO.

Properties	ASTM Method	Biofuel ASTM D6751 limits	Diesel	RSOME	WPO	R 20 P 80
Specific gravity at 15 °C	D 4052	0.87 to 0.89	0.82	0.8102	0.9155	0.893
Net calorific value, kJ/kg	D 4809	-	44800	38650	43340	41362.4
Flashpoint, °C	D 93	Min. 130	50	66	54	56
Fire point, °C	D 93	-	57	68	56	58
Kinematic viscosity at 40 °C, cSt	D 445	1.9 to 6.0	2	12.75	3.18	3.704
Cetane index	D 613	48 to 70	50	56	51	38.4
Water content, wt. %	D 2709	Max. 0.050	0.025	0.3	0.01	0.065
Oxygen by difference, %	E 385	-	Nil	22	1.5	5.6

power of 3.7 kW at 1500 rpm. The CR of the engine is modified from 16:1 to 20:1. Legion Brothers of Bangalore is responsible for the modification work. Table 3 contains all of the test engine's specifications.

VCR arrangement

A manual change of CR is possible by using a specially designed CR graduation disc attached to the cylinder head. The graduation disc will not affect the combustion chamber geometry. In the current study, the cylinder head disc plate is rotated and moved up and down to alter the clearance volume of the cylinder, which in turn alters the CR.

Figure 3 depicts a photograph of a CR graduation disc and tightening lever. The calculation for the CR values is found in Eq. (4):

$$\textit{Compression ratio} = \frac{\textit{Total cylinder volume}\,(V_s + V_c)}{\textit{Clearence volume}\,(V_c)} \qquad (4)$$

where $V_s = \pi d^2 l/4$ is the swept volume of the cylinder (m^3), V_c is the clearance volume of the cylinder (m^3), d is the bore diameter (80 mm), and l is the stroke length (110 mm).

Combustion parameters measurement

Combustion pressure sensor with charge amplifier

It is necessary to obtain the values of cylinder gas pressure and crank angle to acquire essential combustion characteristics like peak pressure, peak pressure occurrence, maximum rate of pressure rise, HRR, combustion duration, ignition delay, mass percentage burned, etc. The in-cylinder gas pressure was measured using a piezoelectric pressure transducer manufactured by Cityzen (model CY-CP-

Table 3. Technical specifications of the experimental setup.

Particulars	Specifications
Make and Model	VCR multi-fuel, vertical, water-cooled, direct injection, naturally aspirated engine. Legion Brothers, Bangalore, modified the engine to change the compression ratio arrangement. The Kirloskar AV1 engine makes the base crankcase.
Compression ratio range	6:1 to 20:1
Rated brake power	3.7 kW
Rated speed	1500 rpm
No. of cylinders / No. of strokes	01 / 04
Bore x Stroke	80 x 110 mm
Displacement volume	552.64 cc
Nozzle opening pressure	200 bar
Maximum load	10 kg
Software	“Engine Test Express v14” Engine performance analysis software

200B), integrated with a Cityzen charge amplifier. Through the action of a diaphragm on the quartz components, the cylinder gas pressure detected by the sensor becomes an electrostatic charge. The experiment involves measuring the crank angle and in-cylinder gas pressure for 50 consecutive cycles. A data acquisition system (DAS) with a resolution of 0.5 °CA is employed to eliminate the impact of cycle-to-cycle changes. The DAS uses a high-impedance connection to capture the charge amplifier's output and save it in an Excel file on the PC. The low-level charge is converted into a proportional voltage by the amplifier.

Figure 3. Photographic image of CR graduation disc and pointer.

Experimental errors and uncertainties

The tests utilized standardized measuring instruments, and the error rates for each instrument were computed to minimize the measurement error rate to the lowest possible percentage. The first reading of the independent variables like load, speed, and others were computed using the percentage uncertainty of the corresponding instruments provided in Appendix 1. The total percentage of uncertainty was ± 2.28 %.

RESULTS AND DISCUSSION

In this segment, we examine the effects of the CR values on CI engine operations, combustion, and emission parameters for the VCR engine when it is run on hybrid alternative fuel (R-20/P-80 blend) at various CR values of 16:1, 17:1, 18, and 20:1. Furthermore, diesel and neat WPO are also compared.

Pressure-crank angle graph

In terms of crank angle, the pressure computation is a crucial instrument. It also provides enough data to perform a combustion analysis and calculate the heat release rate from the fuel. An engine's maximum pressure rises as more fuel is consumed during the pre-mixed combustion stages. Figure 4a represents the fluctuation in engine pressure at maximum load conditions for hybrid alternative fuel (R-20/P-80 blend), neat WPO, and diesel. Typically, raising the CR values enhances engine pressure and engine operations. According to Figure 4a, diesel has a peak pressure of 62 bar, and hybrid alternative fuel has a peak pressure of 66 bar at a 16:1 CR. The hybrid alternative fuel with a 17:1 CR has a peak pressure of 66.5 bar. When fully loaded, the peak pressures at the 18:1 and 20:1 CRs are 68.5 bar and 70 bar, respectively. WPO maximum pressure was also attained at 67 bar at a 16:1 CR. The elevated pressure at 20:1 CR is higher for hybrid alternative fuel than the peak pressure at 16:1 CR. As a result of the higher viscous property, lower volatile behaviour, and higher oxygen content of biofuels, this increase in cylinder pressure is made possible by enhancing the CR, which is more advantageous for biofuels than diesel. Higher CRs seem to improve the performance of biodiesel [5–8].

Heat Release Rate (HRR)

In C.I. engines, the HRR value is measured as the sum of the work done and the change in internal or chemical energy of the fuel released during the combustion process. Figure 4b compares the heat release rates of WPO and diesel at full load with different CRs for hybrid alternative fuel. The HRR values of hybrid alternative fuel (R-20/P-80 blend) are 80, 82.5, 83.8, and 85.38 J/°CA, with CR values of 16:1, 17:1, 18:1, and 20:1. At a 16:1 CR, the diesel and WPO have maximum heat release rates of 73.8 and 83 J/°CA, respectively. The HRR value increased with an enhancement of the CR value because of the excellent spray developed in the combustion chamber, the enrichment air entrainment phenomenon, enhanced biofuel volatility properties, faster prior mixing of blends, and greater diffusive combustion stages [5–8].

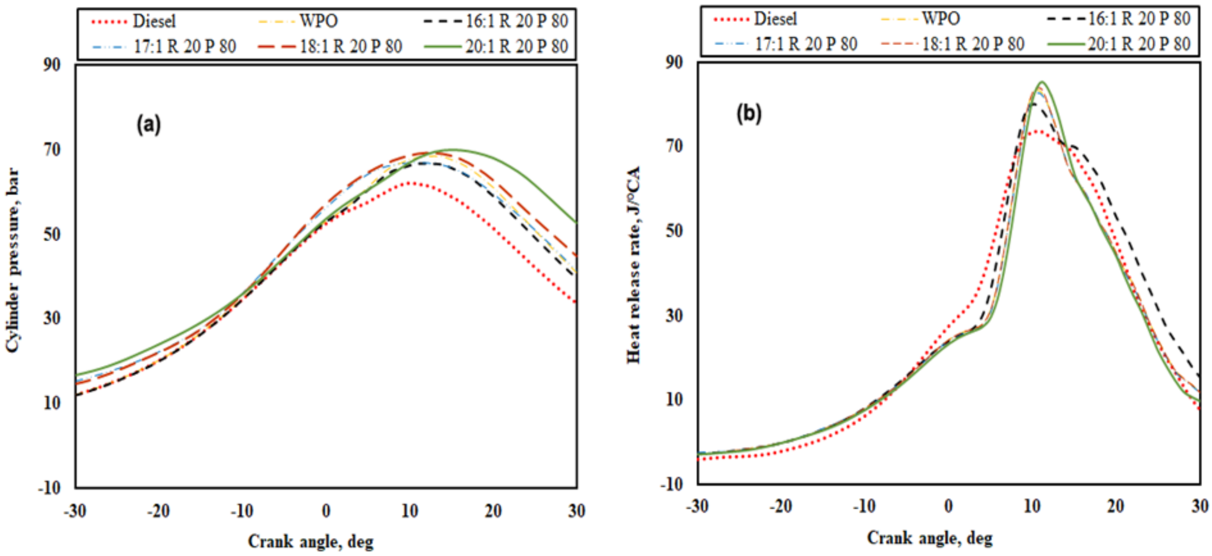

Figure 4. Variation of Engine parameters at full load conditions: (a) Pressure versus crank angle; (b) HRR versus crank angle.

Ignition delay

Figure 5 (a) illustrates the relationship between the load and the ignition delay for the tested fuels at varying CRs. The hybrid alternative fuel has ignition delays at full load of 11.6 °CA, 11.5 °CA, 10.6 °CA, and 10.5 °CA, respectively, with CR values of 16:1, 17:1, 18:1, and 20:1. Similarly, the diesel and WPO ignition delays were observed at 10.8 °CA and 11.8 °CA, respectively, at a CR value of 16:1 with maximum load settings.

In this study, the fuel-air mixture's pre-ignition creates a rise in cylinder heat, which causes the ignition delays to reduce with increasing loads at different CRs. Moreover, the ignition delay gets shorter as CRs rise. The air and gas temperature inside the cylinder rises due to higher CR values, aiding in the charge's early burning. Thus, the ignition delay is decreased. Compared to 17:1, 18:1, and 20:1 CRs, the 16:1 CR results in a longer ignition delay for hybrid alternative fuel because there are more premixed combustion phases and less diffusion combustion, respectively [6–9].

Cylinder peak pressure/ Engine maximum pressure

The degree of engine maximum pressure mainly depends on the volume of diesel or alternative fuel evaporated during the ignition gap interval. However, the evaporation of liquid fuel is significantly influenced by viscosity. The change in engine maximum pressure with full load for the tested fuels at various CRs is shown in Figure 5b. The maximum engine pressure for hybrid alternative fuel is 58, 59, 61, and 62.1 bar, respectively, at the no-load state for CRs of 16:1, 17:1,

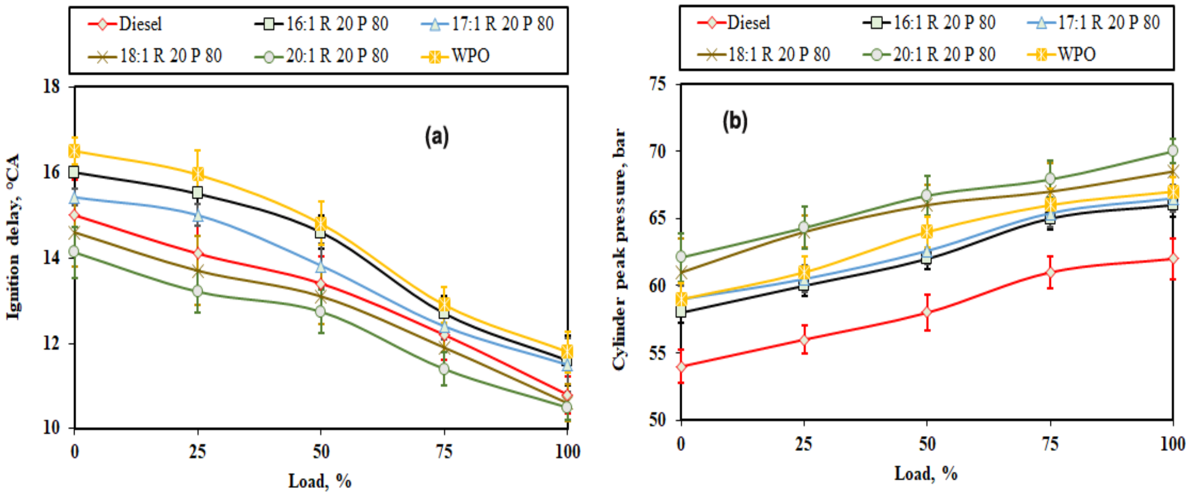

Figure 5. Variation of engine parameters at different load conditions: (a) Ignition delay versus load; (b) Cylinder peak pressure versus load.

18, and 20:1. The engine maximum pressure of hybrid alternative fuel at CRs of 16:1, 17:1, 18:1, and 20:1 is 66, 66.5, 68.5, and 70 bar, respectively, at maximum loaded condition. The engine maximum pressure of diesel and alternative biofuel WPO at a CR of 16:1 is 62 bar and 67 bar, respectively. Because of a greater combustion temperature in the quicker prior mixing of air-fuel combustion stages and a decrease in CV values, which raises the density of the blends in the course of combustion [7–11]. In addition, the cylinder peak pressure of hybrid alternative fuel (R-20/P-80 blend) is higher at a higher CR of 20:1.

Brake thermal efficiency (BTHE)

Figure 6a depicts the impact of the CR values on the BTHE of the tested fuels. According to the experimental results, the BTHE values increased with increasing load under all test conditions. At maximum load conditions, the BTHE for diesel, WPO, and hybrid alternative fuel at a 16:1 CR are 26.8%, 23.4%, and 25.8%, respectively. The BTHE of an R-20/P-80 blend at CRs of 16:1, 17:1, 18, and 20:1 is 12%, 12.8%, 14.2%, and 15%, respectively, at 25% load. At full load, the BTHE for hybrid alternative fuel at CRs of 17:1, 18:1, and 20:1 is 26.8%, 28.74%, and 30.5%, respectively. The BTHE values of hybrid alternative fuels are higher than diesel and WPO. At full load, the CR of 17:1 offers almost similar efficiency, but the BTHE values increased when the CRs of 18:1 and 20:1 for the R-20 / P-80 blends were increased because the fuels burn more efficiently at higher temperatures and pressures and have reduced volatility at higher CRs, which are supported by the intake air's higher temperature and pressure [8–14]. According to the results of the experimental research, the threshold CR for hybrid alternative fuel is 17.1, and higher brake thermal efficiency is attained when the pressure is maintained above the threshold limit. Additionally, when the CR is lowered to 16:1 or 17:1, it is discovered that the BTHE values of the hybrid alternative fuel are worse than diesel. The hybrid alternative fuel's extended ignition delay at low CRs (16:1 or 17:1) is responsible for the inadequate combustion characteristics.

Brake specific fuel consumption (BSFC)

Figure 6b depicts the change in BSFC for the different blends under varied loads and CR values. Figure 6b clearly shows that the BSFC falls as the CR rises, and the BSFC of the WPO and its RSO blends also reflects a similar trend compared to diesel. The BSFC values of WPO and diesel at a 16:1 CR are 0.465 kg/kWh and 0.375 kg/kWh, respectively, at maximum load. For CRs of 16:1, 17:1, 18, and 20:1, the BSFC values for the hybrid alternative fuel under 25% load circumstances are 0.75, 0.721, 0.68, and 0.66 kg/kWh, respectively. The BSFC values for the hybrid alternative fuel at maximum load conditions are 0.41, 0.39, 0.362, and 0.347 kg/kWh for CRs of 16:1, 17:1, 18, and 20:1. By comparing the BSFC values of diesel and WPO at CRs of 18:1 and 20:1. It is found that the hybrid alternative fuel has lower BSFC values due to a lower clearance volume, better combustion, and lower heat losses. The above factors produce more heat energy to obtain the desired brake thermal efficiency. Higher CRs also result in higher maximum engine pressure, significantly boosting engine power production while lowering fuel consumption per unit of output [10–15]. Additionally, the more considerable clearance volume, the least amount of heat generated, and the lower cylinder gas temperature are the causes of the rise in the BSFC values of the hybrid alternative

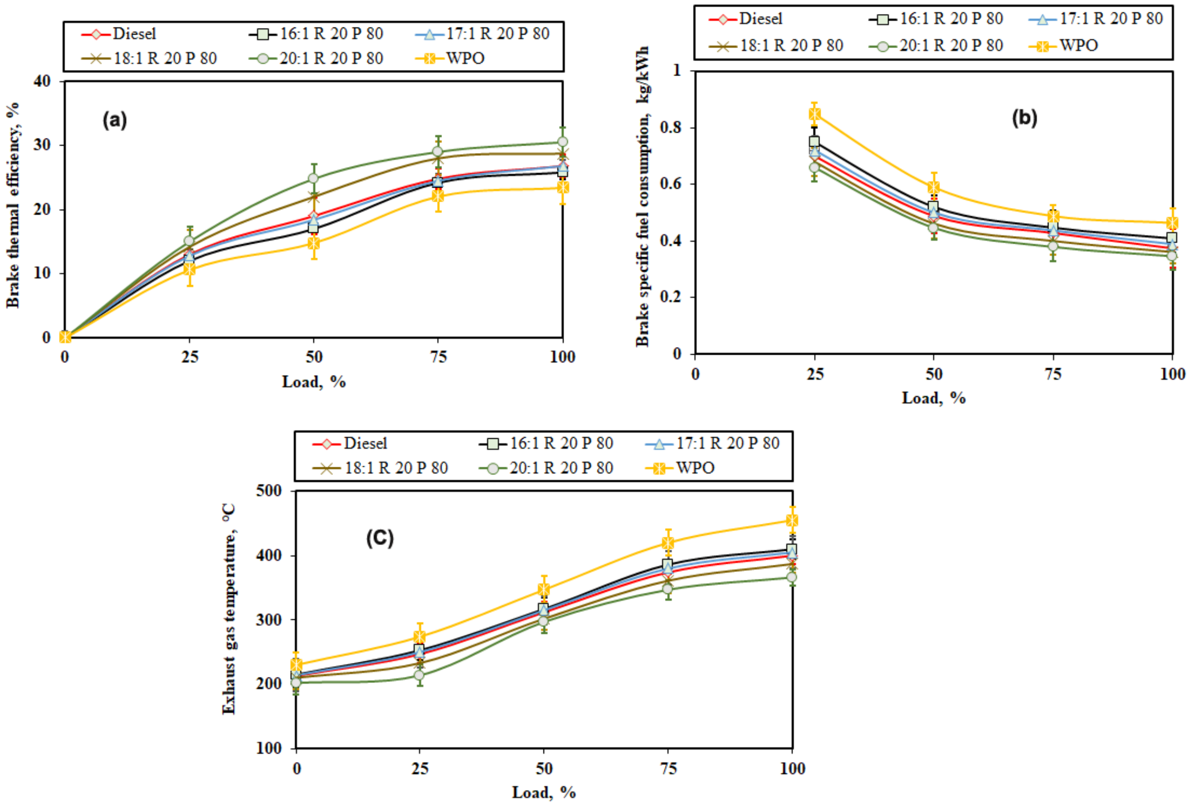

Figure 6. Variation of engine parameters at different load conditions: (a) Brake thermal efficiency; (b) Brake specific fuel consumption; (c) Exhaust gas temperature.

fuel at CRs of 16:1 and 17:1. The combustion chamber must consume more blends to accomplish it.

Exhaust gas temperature (EGT)

Figure 6c depicts the temperature fluctuations of the exhaust gases for the operated fuels as a function of different load and CR conditions. According to experimental findings, the EGT values of hybrid alternative fuel rise with increasing load and fall with increasing CRs, as shown in Figure 6c. Furthermore, the minimum EGT contributes to the maximum BTHE. Due to its higher viscosity and density than diesel, the EGT values of the hybrid alternative fuel at 16:1 and 17:1 CRs are higher than diesel during the operational period.

EGT values for the hybrid alternative fuel for CRs of 16:1, 17:1, 18:1, and 20:1 are 215 °C, 214 °C, 210 °C, and 202 °C, respectively, with no load. The EGT values of the exhaust gas temperature of the hybrid alternative fuel at CRs of 16:1, 17:1, 18:1, and 20:1, are 410 °C, 405 °C, 387 °C and 366 °C respectively, at maximum load. Similarly, the EGT values of the WPO and diesel for the 16:1 CR are 455 °C and 400 °C, respectively, at maximum load conditions. The increase in blend temperature inside the cylinder, which reduces the ignition period and results in more efficient and thorough fuel burning, is one of the potential causes of the decrease in EGT at higher CRs of 18:1 and 20:1 [14–19]. This fuel blend burns more efficiently than diesel and converts more energy per unit of fuel.

Oxides of nitrogen emissions

Nitric oxide (NO) and nitrogen dioxide (NO_2) are often referred to as "oxides of nitrogen emission"–the interaction of oxygen and nitrogen gases during burning fresh air and fuel results in NOx emissions. The crucial factors for generating NOx pollution are the extreme burnt gas temperature, the degree of oxygen content, and the residence time for the reactions. A tiny quantity of N_2 in gasoline derived from vegetable oils helps create NOx emissions in addition. Figure 7a illustrates the variance in nitrogen oxide emanations from diesel, WPO, and hybrid alternative fuel exhaust at various CR values and loads. For CRs of 16:1, 17:1, 18:1, and 20:1, the hybrid alternative fuel emits 205 ppm, 250 ppm, 300 ppm, and 330 ppm of NOx, respectively. When the engine is operating at maximum load, and a standard CR value of 16:1, diesel and the hybrid alternative fuel emit 820 ppm and 920 ppm of NOx, respectively; meanwhile, the NOx emission values for CRs of 17:1, 18:1, and 20:1 are 960 ppm, 1050 ppm, and 1095 ppm, respectively. Similar to this, WPO emits 1010 ppm of NOx at full load and a standard CR value of 16:1. According to experimental results, the maximum cylinder temperature causes the NOx emission for the hybrid alternative fuel to rise at the higher CRs of 18:1 and 20:1, in comparison to diesel and WPO. As a result, as the CR values rise, the fuel-burning temperature rises, releasing more NOx into the atmosphere [15–21].

Low NOx emissions are caused by insufficient oxygen supply at lower CRs of 16:1 and 17:1, which causes incomplete fuel combustion and lower in-cylinder temperatures. However, higher CRs produce more NOx pollution because more oxygen is available, resulting in complete combustion and proper breakdown of the fuel particles when the fuel is injected. When the cetane number is reduced, it prolongs the ignition delay period, increasing fuel accumulation and leading to higher NOx emissions.

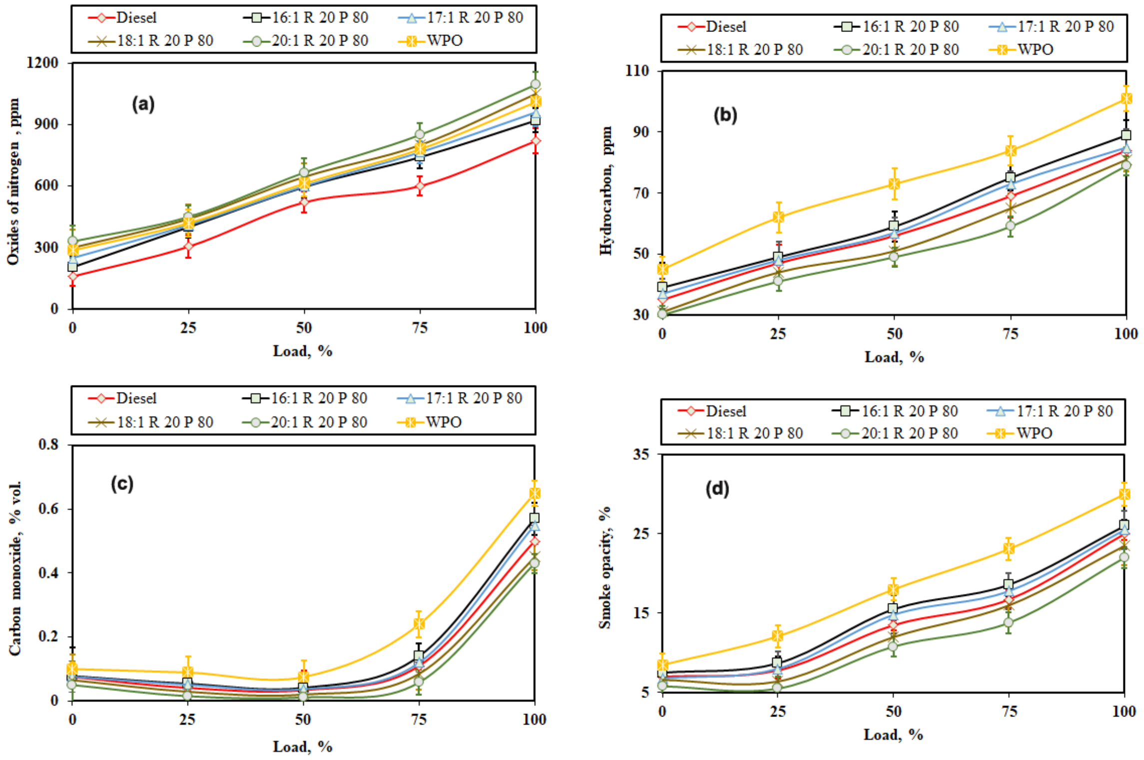

Figure 7. Variation of emissions with different load conditions: (a) Oxides of nitrogen; (b) Hydro carbon; (c) Carbon monoxide; (d) Smoke opacity.

Hydrocarbon (HC) emissions

The amount of HC released by engines in their exhaust smoke is a sign of inefficient fuel burned while the engine is running and an indicator of combustion efficiency. The fuel characteristics and engine operating circumstances majorly impact the HC emissions into the atmosphere, which are made up of partially burned fuel. The change in HC emission levels for the samples with various CR values and loads is shown in Figure 7b. At CRs of 16:1, 17:1, 18, and 20:1, the HC emission from hybrid alternative fuel is 39 ppm, 37 ppm, 31 ppm, and 30 ppm, respectively, with no load. For a full load, the HC emission from hybrid alternative fuel is 89 ppm, 85 ppm, 81 ppm, and 79 ppm, respectively, at CRs of 16:1, 17:1, 18, and 20:1. While the HC emissions from diesel and WPO are delivered at 84 ppm and 101 ppm at conditions of maximum load and 16:1 CR, respectively.

Increased CR reduces the ignition period, effectively reducing the over-mixing of the A/F values and emitting a low quantity of HC particles into the atmosphere. Because of the increased temperature and pressure during combustion in the engine cylinder and the oxidation of unburned hydrocarbons, HC emissions are decreased at greater CRs [18–22]. The increased combustion temperature might negatively impact NOx emissions. More gasoline is gathered in the delay period for CRs of 16:1 and 17:1. Additionally, there will be insufficient compression heat and ignition delays. Due to this, HC emissions are higher than those of diesel.

Carbon monoxide (CO) emissions

In many nations, CO pollution is the most prevalent harmful air and a toxic gas. Additionally, it has no flavour, colour, or odour. The A/F relation to the stoichiometric proportions significantly impacts CO emissions caused by inadequate blend combustion. Figure 7c depicts the variation of carbon monoxide emissions for tested fuels with loads and CRs. The CO emissions for diesel and R 20 P 80 blend at a standard CR of 16:1 are found to be 0.5% volume and 0.57% volume, respectively, at full load.

At no load, hybrid alternative fuel emits 0.078% volume, 0.076% volume, 0.065% volume, and 0.05% volume of CO pollution at CRs of 16:1, 17:1, 18, and 20:1. The CO pollution emitted by hybrid alternative fuel at full load for CRs of 17:1, 18:1, and 20:1 is 0.55% volume, 0.45% volume, and 0.43% volume, respectively. Similarly, the CO pollution emitted by WPO at full load for CRs of 16:1 is 0.65% volume. The factors influencing the CO emissions for hybrid alternative fuel are lower CRs of 16:1 and 17:1, higher spray coverage, bigger fuel droplets, improper swirling, and a lower cylinder temperature. The improved air-fuel mixing, greater air temperature within the combustion chamber, and shorter ignition lag may contribute to lower CO emissions at higher CRs [20–24]. The fuel burns quicker and more thoroughly as a result.

Smoke opacity emissions

The most noticeable byproduct of a diesel engine is the emitted gas flow, which contains trapped solid soot molecules and is known as smoke opacity emission. The formation of smoke opacity emissions occurs due to the extreme air deficiency in the CI engine, and the smoke opacity output rises as the A/F values fall. Figure 7d presents the fluctuations of smoke opacity emission with various CR values and loads for tested fuels. At full load conditions, the smoke opacity emissions for diesel, WPO, and hybrid alternative fuel at a 16:1 CR are 25%, 30%, and 26%, respectively. At no load, the hybrid alternative fuel's smoke opacity emission at CRs of 16:1, 17:1, 18, and 20:1 is 7.5%, 6.8%, 6.6%, and 5.8%, respectively. At maximum load, the smoke opacity emission for hybrid alternative fuel at CRs of 17:1, 18:1, and 20:1 is 25.5%, 23.5%, and 22%, respectively.

According to experimental results, the smoke opacity emission rises when the engine load levels are increased, while the emission declines with an increase in CRs from 16:1 to 20:1. When a blend's CR is increased, it improves fuel combustion and raises combustion temperature, both of which reduce smoke opacity. Higher CR values result in greater brake thermal efficiency, which claims to support the preceding fact, whereas at a lower CR of 16:1 and 17:1, incomplete combustion of fuel takes place. Hence, more smoke opacity emission is produced [22–26]. Table 4 gives the percentage increase or decrease of combustion, performance, and emission parameters at different CRs for hybrid alternative fuel at full load.

Table 4. A comparison of hybrid biodiesel with different compression ratios to diesel at full load.

Sl. No.	Parameter	16:1 CR	17:1 CR	18:1 CR	20:1 CR
	Combustion Parameters				
1	Ignition delay (°CA)	+7.41	+6.48	-1.85	-2.78
2	Maximum heat release (J/°CA)	+9.59	+13.01	+14.79	+16.96
3	Maximum cylinder pressure (bar)	+6.45	+7.26	+10.48	+12.9
	Performance parameters				
1	Brake thermal efficiency (%)	-3.73	0	+7.24	+13.81
2	Brake-specific fuel consumption (kg/kWh)	+9.33	+4	-3.47	-7.47
3	Exhaust gas temperature (°C)	+2.5	+1.25	-3.25	-8.5
	Emission parameters				
1	Oxides of nitrogen emission (ppm)	+12.19	+17.07	+28.05	+33.54
2	Hydrocarbon emission (ppm)	+5.95	+1.19	-3.57	-5.95
3	Carbon monoxide emission (% volume)	+14	+10	-10	-14
4	Smoke opacity emission (%)	+4	+2	-6	-12

"+" indicates percentage increase; "-" indicates percentage decrease.

CONCLUSION

An experiment was carried out using RSO blended with WPO (R-20/P-80) on a single-cylinder, water-cooled VCR engine. The combustion, performance, and emission properties of the hybrid alternative biofuels were compared to diesel and neat WPO. To achieve a robust study soon, (i) conducting extended durability tests to assess the engine's long-term performance and reliability when running on hybrid biodiesel at different CRs, (ii) developing computational models to simulate and analyse the combustion process in the engine when using hybrid biodiesel, aiding in design improvements, (iii) evaluating the engine's performance during cold starts and warm-up phases when operating on hybrid biodiesel at different CRs, (iv) assessing the compatibility of the engine's fuel system components with the hybrid biodiesel to ensure reliable and consistent fuel delivery, (v) examining the engine's components and systems for any potential wear and tear caused by the use of hybrid biodiesel at varying CRs and (vi) conducting on-road or real-world testing of the engine with hybrid biodiesel to evaluate its performance, fuel economy, and emissions in real-world driving conditions can be additional examined. The results of this investigation lead to the following deductions:

At 20:1 CR, the cylinder peak pressure of the hybrid biofuels (70 bar) is higher due to the higher combustion temperature, and the ignition lag is less than that of diesel (62 bar). As the CR values increase, the rate at which heat is released increases due to proper fuel spraying and optimal coverage of the blends in the cylinder. Compared to diesel, at maximum load and a 20:1 CR value condition, the BTHE value of the hybrid biofuel is around 3.7% higher, and the BSFC value is 7.45% lower. In addition, the EGT at full load and a CR of 20:1 are 8.5% lower than diesel. The hydrocarbon and carbon monoxide emissions for the hybrid alternative biofuel at full load and 20:1 CR are 5.9% and 14% less than diesel, respectively. When compared to diesel, NOx emissions are significantly greater for all CRs. The smoke opacity emission of the hybrid alternative biofuel at full load and 20:1 CR is 12% less than that of diesel.

The findings mentioned above underscore the diverse potential advantages and applications of hybrid fuel across various sectors, including automotive, power generation, and maritime applications.

LIST OF SYMBOLS AND ABBREVIATIONS

A/F	-	Air fuel ratio
ARAI	-	Automotive Research Association of India
BP	-	Brake power, kW
BSFC	-	Brake-specific fuel consumption, kg/kWh
BSO	-	Babassu oil
BTDC	-	Before the top dead centre, °CA
BTHE	-	Brake thermal efficiency, %
CO	-	Carbon monoxide, % volume
cSt	-	Centi Stoke
CR	-	Compression ratio
CV	-	Clearance volume, m^3
DAS	-	Data acquisition system
EGT	-	Exhaust gas temperature, °C
H_2SO_4	-	Sulphuric acid
HC	-	Hydrocarbon, ppm
HRR	-	Heat release rate, J/^{0}CA
JME	-	Methyl ester of *Jatropha curcas*
KME	-	Methyl ester of karanja oil
KOH	-	Potassium hydroxide
MSW	-	Municipal solid waste
NO	-	Nitric oxide
NO_2	-	Nitrogen dioxide
NOx	-	Oxides of nitrogen, ppm
R-20/P- 80	-	20% RSO blended with 80% WPO
SFC	-	Specific fuel consumption, kg/kWh
VCR	-	Variable compression ratio
WPO	-	Waste plastic oil
WPPO	-	Waste plastic pyrolysis oil
wt.	-	Weight, kg

REFERENCES

[1] L. Li, K. Quan, J. Xu, F. Liu, S. Liu, S. Yu, X. Ge, Fuel 123 (2014) 189–193. https://doi.org/10.1016/j.fuel.2014.01.049.

[2] W. Roschat, T. Siritanon, B. Yoosuk, T. Sudyoadsuk, V. Promarak, Renewable Energy 101 (2017) 937–944. https://doi.org/10.1016/j.renene.2016.09.057.

[3] C. Cleetus, S. Thomas, S. Varghese, J. Energy 2013- ID 608797 (2013). https://doi.org/10.1155/2013/608797.

[4] S. Nagaraja, K. Sooryaprakash, R. Sudhakaran, Procedia Earth Planet. Sci. 11 (2015) 393–401. https://doi.org/10.1016/j.proeps.2015.06.038.

[5] M.B. Tasić, M.S. Stanković, M.D. Kostić, O.S. Stamenković, V.B. Veljković, Chem. Ind. Chem. Eng. Q. 28 (2022) 237–245. https://doi.org/10.2298/CICEQ210819035T.

[6] N.D.L.D. Silva, F.P.V. Loz, J.I. Soletti, D.D.G. Coelho, Chem. Ind. Chem. Eng. Q. 27 (2021) 155–163. https://doi.org/10.2298/CICEQ191117034S.

[7] M. Vasudeva, S. Sharma, S.K. Mohapatra, K. Kundu, Springer Plus 5 293 (2016) 1–13. https://doi.org/10.1186/s40064-016-1945-7.

[8] G.A. Miraculas, N. Bose, Adv. Mat. Res. 984 (2014) 850–854. https://doi.org/10.4028/www.scientific.net/AMR.984-985.850.

[9] J. Gandure, C. Ketlogetswe, IEEE (2011) 1–4. https://doi.org/10.1109/AFRCON.2011.6071993.

[10] M. Krishnamoorthi, R. Malayalamurthi, Energy 128 (2017) 312–328. https://doi.org/10.1016/j.energy.2017.04.038.

[11] B. Singh, S.K. Shukla, Biofuels 7 (2016) 471–477. https://doi.org/10.1080/17597269.2016.1163210.

[12] M. El_Kassaby, M.A Nemit_Allah, Alex. Eng. J. 52 (2013) 1–11. https://doi.org/10.1016/j.aej.2012.11.007.

[13] M.T. Raj, M.K.K. Kandasamy, Int. J. Energy Environ. Eng. 3 (2012) 1–8. https://doi.org/10.1186/2251-6832-3-18.

[14] K. Muralidharan, D. Vasudevan, Appl. Energy 88 (2011) 3959–3968. https://doi.org/10.1016/j.apenergy.2011.04.014.

[15] H.K Amarnath, P. Prabhakaran, S.A Bhat, R. Paati, Int. J. Green Energy 11 (2014) 675–694. https://doi.org/10.1080/15435075.2013.777905.

[16] T.A. Kumar, R. Chandramouli, T. Mohanraj, Ecotoxicol. Environ. Saf. 121 (2015) 51–56. https://doi.org/10.1016/j.ecoenv.2015.06.008.

[17] N.R. Kumar, C. Sekhar, S. Adinarayana, Int. J. Appl. Sci. Eng. 11 (2013) 41–49. https://gigvvy.com/journals/ijase/articles/ijase-201303-11-1-041.pdf.

[18] C.A. Rinaldini, E. Mattarelli, T. Savioli, G. Cantore, M. Garbero, A. Bologna, Fuel 183 (2016) 292–303.

https://doi.org/10.1016/j.fuel.2016.06.015

[19] M. Mani, C. Subash, G. Nagarajan, Appl. Therm. Eng. 29 (2009) 2738–2744. https://doi.org/10.1016/j.applthermaleng.2009.01.007.

[20] J. Devaraj, Y. Robinson, P. Ganapathi, Energy 85 (2015) 304–309. https://doi.org/10.1016/j.energy.2015.03.075.

[21] I. Khalil, A.R.A. Aziz, S. Yusuf, Appl. Mech. Mater. 695 (2015) 323–327. https://doi.org/10.4028/www.scientific.net/AMM.695.323.

[22] A.S. Ramadhas, S. Jayaraj, C. Muraleedharan, Renewable Energy 33 (2008) 2077–2083. https://doi.org/10.1016/j.renene.2007.11.013.

[23] P. Senthilkumar, G. Sankaranarayanan, J. Energy Inst. 89 (2016) 504–512. https://doi.org/10.1016/j.joei.2015.07.006.

[24] G. Kasiraman, B. Nagalingam, M. Balakrishnan, Energy 47 (2012) 116–124. https://doi.org/10.1016/j.energy.2012.09.022.

[25] H. Raheman, P.C. Jena, S.S Jadav, Int. J. Energy Environ. Eng. 4 (2013) 1–9. https://doi.org/10.1186/2251-6832-4-6.

[26] R. Barathiraja, P. Thirumal, G. Saraswathy, I. Rahamathullah, Chem. Ind. Chem. Eng. Q. 28 (2022) 169–178. https://doi.org/10.2298/CICEQ201120028B.

[27] I. Veza, A.T. Hoang, A.A. Yusuf, S.G. Herawan, M.E.M. Soudagar, O.D. Samuel, M.F.M. Said, A.S. Silitonga, Fuel 333 (2023) 126377. https://doi.org/10.1016/j.fuel.2022.126377.

[28] C. Enweremadu, O. Samuel, H. Rutto, Environ. Clim. Technol. 26(1) (2022) 630–647. https://doi.org/10.2478/rtuect-2022-0048.

[29] A.T. Garavand, A.H. Maleni, T.M. Gundoshmian, O.D. Samuel, Energy Convers.Manag.: X 16 (2022) 100304. https://doi.org/10.1016/j.ecmx.2022.100304.

[30] O.D. Samuel, M.O. Okwu, S.T. Amosun, T.N. Verma, S.A. Afolalu, Ind. Crops Prod. 141 (2019) 111658. https://doi.org/10.1016/j.indcrop.2019.111658.

[31] T.S. Singh, U. Rajak, O.D. Samuel, P.K. Chaurasiya, K. Natarajan, T.N. Verma, P. Nashine, Fuel 285 (2021) 119103. https://doi.org/10.1016/j.fuel.2020.119103.

[32] A.L. Hananto, A. Fauzi, A. Suhara, I. Davison, M. Spraggon, S.G. Herawan, O.D. Samuel, A.A. Yusuf, M. Idris, I. Veza, Results Eng. 19 (2023) 101334. https://doi.org/10.1016/j.rineng.2023.101334.

[33] O.D. Samuel, B.U. Oreko, J.O. Oyejide, S. Idi, O.S. Fayomi, J. Phys. Conf. Ser. 1378 (2019) 042024. https://doi.org/10.1088/1742-6596/1378/4/042024.

ANANTHAKUMAR SUDALAIMANI[1]
BARATHIRAJA RAJENDRAN[2]
THIYAGARAJ JOTHI[3]
MATHANBABU MARIAPPAN[4]

[1]Department of Mechanical Engineering, Government College of Engineering. Tirunelveli, Tamil Nadu, India

[2]Department of Mechanical Engineering, Einstein College of Engineering, Near MS University, Tirunelveli, Tamil Nadu, India

[3]Department of Mechatronics Engineering, Er. Perumal Manimekalai College of Engineering, Hosur, Tamil Nadu, India

[4]Department of Mechanical Engineering, Government College of Engineering, Bargur, Krishnagiri, Tamil Nadu, India

NAUČNI RAD

KARAKTERISTIKE SAGOREVANJA, EMISIJE I PERFORMANSI HIBRIDNOG BIOGORIVA PRI RAZLIČITIM ODNOSIMA KOMPRESIJE

Primarni ciljevi ove studije su naizmenično korišćenje konvencionalnih fosilnih goriva, smanjenje emisija gasova sa efektom staklene bašte i dima iz dizel motora, kao i poboljšanje karakteristika performansi i emisija štetnih gasova dizel motora sa promenljivim kompresijom koji radi sa hibridnim biodizelom. Eksperimenti su rađeni sa najboljim hibridnim biodizelom, koji je napravljen namešavanjem 20% kaučukovog ulja sa 80% ulja od otpadne plastike . Ispitivanja su obavljena pri četiri stepena kompresije: 16:1, 17:1, 18:1 i 20:1. Pri stepenu kompresije od 20:1 i pri punom opterećenju, termička efikasnost motora porasla je za 30,5%, specifična potrošnju goriva pala je za 0,347 kg/kWh, a značajno je smanjena emisija ugljen-monoksida (0,43% v/v), ugljovodonike (79 ppm) i dima (22%). Međutim, sa povećanjem stepena kompresije, emisije azotovih oksida su porasle nepovoljno (1092 ppm) u poređenju sa dizelom (820 ppm). Takođe, upoređeni su dizel i čist biodizel of ulja otpadne plastije da bi se videlo kako vrednosti stepena kompresije utiču na sagorevanje, performanse i emisije. U poređenju sa dizelom, pod maksimalnim opterećenjem i stepenom kompresije od 20:1, hibridni biodizel je pokazao približno motora. Nalazi ukazuju na potencijalnu primenu ovog hibridnog biodizela u automobilskom sektoru, industriji proizvodnje energije i pomorskim aplikacijama.

Ključne reči: kaučukovo ulje, ulje otpadne plastike, performance, emisije, promenljivi stepen kompresije.

Chemical Industry & Chemical Engineering Quarterly

Available online at
Association of the Chemical Engineers of Serbia *AChE*
www.ache.org.rs/CICEQ

Chem. Ind. Chem. Eng. Q. 30 (3) 223–230 (2024) CI&CEQ

RENGASAMY RAJARAMAN[1]
RAJAMANICKAM MUTHUCUMARASWAMY[2]

[1]Department of Mathematics, R.M.K. Engineering College, Kavaraipettai, India

[2]Department of Mathematics, Sri Venkateswara College of Engineering, Sriperumbudur, India

SCIENTIFIC PAPER

UDC 621.3:54:532.5

IMPACT OF CHEMICAL REACTION, VISCOUS DISSIPATION, AND THERMAL RADIATION ON MHD FLOW PAST AN OSCILLATING PLATE

Article Highlights

- Velocity rises at the time of generative reaction and drops during destructive reaction
- The crank-Nicolson method was used to solve the dimensionless governing equations
- The flow pattern is affected significantly due to plate oscillation and radiation parameters
- The time it takes to reach a steady state relies heavily on the radiation parameter and phase angle

Abstract

This study analyzes the consequences of first-order chemical reactions, radiation, and viscous dissipation on the unsteady magnetohydrodynamic natural convective flow of a viscous incompressible fluid over a vertically positioned semi-boundless oscillating plate with uniform mass diffusion and temperature. An implicit finite-difference technique is employed to solve a set of dimensionless, coupled, nonlinear partial differential equations. The numerical results for fluid velocity, concentration, and temperature at the plate under different dimensionless parameters are graphically displayed. Due to first-order homogeneous chemical reactions, it has been discovered that the velocity rises at the time of a generative reaction and drops during a destructive reaction. A decline in velocity is observed with an increase in the phase angle, radiation parameter, and chemical reaction parameter. Further, it has been revealed that plate oscillation, radiation, chemical reactions, and the magnetic field significantly influence the flow behavior.

Keywords: MHD; oscillating; finite-difference; viscous dissipation; chemical reaction.

Heat and mass transfer through MHD flow are essential in many industrial applications, including nuclear reactor cooling, power generation systems, and aerodynamics. MHD finds applications in chemical synthesis, plasma jets, crystal growth, and electromagnetic pumps. The magnetic field impacts of ionized gases, electrolytes, and liquid metals must be analyzed to understand natural convection flow. The development of fins, gas turbines, nuclear power plants, and various propulsion systems for spacecraft, satellites, missiles, and aircraft all depend massively on understanding radiative heat and mass transfer. Several studies have been conducted on how magnetic fields affect heat and mass transfer in different scenarios. Sparrow and Cess [1] looked at how a magnetic field affects the movement of heat through free convection. Chamkha [2] develops a numerical solution that considers a magnetic field, absorption, and mass suction or blowing by investigating an unstable flow with heat and mass transfer on a vertical permeable plate in a fluid-saturated porous medium. Raptis [3] examined the effect of radiation on mass transfer and natural convective oscillatory flow in an optically thin viscous fluid. Hussanan *et al.* [4] analyzed the unstable natural convective flow over an oscillating

---

Correspondence: R. Rajaraman, Department of Mathematics, R.M.K. Engineering College, Kavaraipettai-601206, India.
E-mail: rajamaths80@gmail.com
Paper received: 26 May, 2023
Paper revised: 6 August, 2023
Paper accepted: 2 October, 2023

https://doi.org/10.2298/CICEQ230526025R

plate subjected to Newtonian heating. Chemical reactions can be categorized as homogeneous or heterogeneous depending on the catalyst used. Homogeneous reactions involve two gases or two liquids, while heterogeneous reactions involve a liquid and a gas. A chemical reaction with a reaction rate proportional to the concentration of a single reactant is called a first-order reaction. Additionally, chemical reactions can significantly impact mass diffusion rates. Numerous research studies have investigated how chemical reactions affect fluid flow in diverse environments. Soundalgekar *et al.* [5] investigated the influence of a chemical reaction on the impetuous motion of an unending vertical plate on species concentrations. Muthucumaraswamy and Kulaivel [6] developed an analytical solution for fluid flow across a semi-endless vertical plate that starts suddenly, accounting for first-order homogeneous chemical reactions, mass diffusion, and heat flux.

Muthucumaraswamy [7] studied the effects of chemical reactions on fluid flow over a vertical plate oscillating with uniform mass diffusion at varying temperatures. On the other hand, Vijayalakshmi and Selvajayanthi [8] employed numerical methods to analyze the transient flow of fluid over a vertical plate that oscillates continuously. Ibrahim *et al.* [9] conducted a study to investigate the heat and mass transfer characteristics in a laminar flow of an electrically conducting, heat-generating/absorbing Newtonian fluid. This study also considered the impacts of radiation, mass flux, and a first-order homogeneous chemical reaction. The study conducted by Manivannan *et al.* [10] investigated the effects of radiation and first-order homogeneous chemical reactions on the unsteady flow of a viscous incompressible fluid through an isothermal vertical oscillating plate. Ahmed *et al.* [11] investigated the influence of magnetohydrodynamics, radiation, and first-order chemical reactions on the heat and mass transfer flow through an impulsively generated semi-endless vertical plate. Santhana Lakshmi and Muthucumaraswamy [12] examined the effects of chemical reactions on the unsteady flow of an isothermal vertical plate that accelerates exponentially, with variations in mass diffusion also considered. Hari Krishna *et al.* [13] studied the MHD fluid flow over an oscillating inclined porous plate, exploring the effects of radiation and chemical reactions and variations in temperature and mass diffusion. Srihari Babu and Jaya Rami Reddy [14] studied the unsteady magnetohydrodynamics of a fluid flowing past a porous plate subjected to radiation and chemical reactions. The plate accelerates vertically under the influence of a transverse magnetic field, while the temperature and mass diffusion vary due to the existence of a heat source or sink. Sweta Matta *et al.* [15] investigated how radiation and chemical reactions affected unsteady MHD natural convective fluid flow through a porous plate with mass transfer. Ibrahim Danjuma Yale *et al.* [16] investigated the effects of chemical reactions and thermal radiation on the unsteady MHD flow across a vertically accelerating plate.

The term' dissipation' refers to energy loss in fluid dynamics. In viscous fluid flows, the fluid's velocity extracts energy from its motion (kinetic energy) and converts it to its internal energy. It necessitates heating the fluid. It is known as ‘viscous dissipation,’ an irreversible process. Viscous dissipation in buoyancy-induced flows was explored by Mahajan and Gebhart [17]. Kishan and Amrutha [18] analyzed the nonlinear MHD steady flow of a viscous, incompressible, electrically conducting Boussinesq fluid across a vertically stretching surface subjected to viscous dissipation, chemical reactions with mass transfer, a uniform magnetic field, and thermal stratification. Rao and Shivaiah [19] investigated the effects of a chemical reaction and viscous dissipation on the unsteady magnetohydrodynamic flow over a semi-infinite, vertical porous plate. Rajakumar *et al.* [20] investigated the combined effects of radiation absorption, chemical reactions, and viscous dissipation on the unsteady MHD natural convective flow across a vertically moving semi-boundless porous plate. Satyabrat Kar *et al.* [21] explored the impact of viscous dissipation and chemical reactions on the magnetohydrodynamic flow of an incompressible, viscous fluid across a semi-infinite, vertically oriented porous plate that is submerged in a porous medium. They used the perturbation technique to determine the velocity, temperature, and concentration solutions. Reddy *et al.* [22] examined the effects of chemical reactions on the magnetohydrodynamic natural convective flow in a porous medium over an exponentially stretched surface subjected to a heat source and viscous dissipation. Kishore *et al.* [23] investigated the effect of hydromagnetic flow over an oscillating vertical plate contained in a porous medium while considering thermal radiation, surface conditions, viscous dissipation, and chemical reactions. The authors analyzed how these factors affected the flow and found that they significantly shaped the system's overall behavior.

Balla and Naikoti [24] investigated the unsteady MHD natural convective flow of an electrically conducting viscous, incompressible Newtonian fluid. Zigta [25] investigated a magnetohydrodynamic flow between limitless vertical Couette channel walls, considering the factors of thermal radiation, chemical reactions, and viscous dissipation. Prabhakar

Reddy [26] examined the impact of chemical reactions, viscous dissipation, and radiation on the unsteady MHD natural convective flow through a vertical porous plate with a parabolic starting motion. The Ritz finite element method was used to solve the governing equations numerically. Prasad *et al.* [27] studied the impact of various factors on fluid flow through a semi-boundless inclined permeable plate. Specifically, they looked at how chemical reactions and viscous dissipation impact the flow and the role of MHD, free convection, radiation, absorption, and heat generation.

However, so far, no specialists have proposed a quantitative investigation of the influence of chemical reactions on an unsteady MHD-free convective flow over a semi-limitless swaying upward plate with heat radiation and viscous dissipation. Therefore, the current study seeks to assess the effects of first-order chemical reactions on the unsteady MHD flow over an oscillating semi-infinite vertical plate while also considering thermal radiation and viscous dissipation. The finite difference method will be employed for the analysis.

MATHEMATICAL FORMULATION

Consider the unsteady magnetohydrodynamic natural convective flow of an electrically conducting, optically thin, radiating, heat-absorbing, viscous, incompressible fluid along a semi-boundless vertical plate oscillating at a uniform ambient temperature T'_∞ and concentration C'_∞. The vertical plate is taken as the $x-axis$, and the $y-axis$ is perpendicular to it, as shown in Figure 1. When the plate begins oscillating in its plane with the velocity $u_0 \cos\omega' t'$ at the time $t'>0$, its temperature and concentration level are elevated to T'_w and C'_w respectively.

The following assumptions are made for deriving the governing flow equations:

The flow is unsteady, laminar, and two-dimensional. Rosseland approximation is commonly applied to approximate the radiant heat flux in the energy equation. Fluid is viscous, incompressible, and electrically conducting. Viscous dissipation is taken into account in the energy equation. The fluid has constant properties except the density in the body force. The Boussinesq approximation is commonly applied to handle the effects of density variations in the body force term while assuming an incompressible fluid. A uniform magnetic field of strength *B₀* is applied normally to the plate, and the magnetic Reynolds number of the flow is assumed to be small; the induced magnetic field can be neglected compared to the applied magnetic field. There is a first-order chemical reaction between the diffusing species and the fluid.

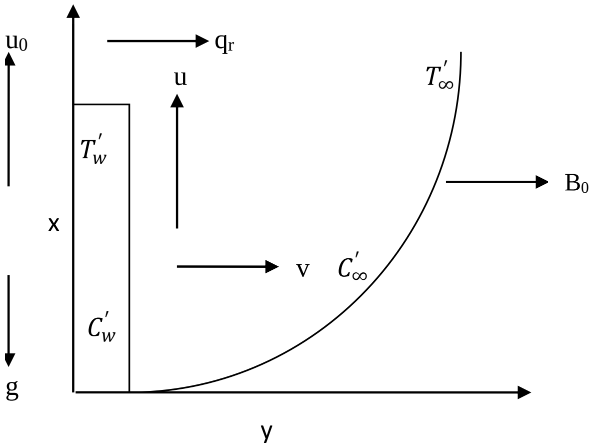

Figure 1. Physical model of the problem.

Equation of continuity:

$$u_x + u_y = 0 \tag{1}$$

Equation of momentum:

$$u_{t'} + uu_x + vu_y = g\beta\left(T' - T'_\infty\right) + g\beta^*\left(C' - C'_\infty\right) + \upsilon u_{yy} - \frac{\sigma B_0^2 u}{\rho} \tag{2}$$

Energy equation:

$$T'_{t'} + uT'_x + vT'_y = \frac{k}{\rho C_p} T'_{yy} - \frac{1}{\rho C_p}\left(q_r\right)_y + \frac{\upsilon}{\rho C_p}\left(u_y\right)^2 \tag{3}$$

Mass diffusion equation:

$$C'_{t'} + uC'_x + vC'_y = DC'_{yy} - K_1\left(C' - C'_\infty\right) \tag{4}$$

subject to

$$\left.\begin{array}{l} I.C: t' \le 0: u = 0, v = 0, T' = T'_\infty, C' = C'_\infty \\ B.C: t' > 0: u = u_0 \cos\omega' t', v = 0, T' = T'_w, C' = C'_w \ \ at\ y = 0 \\ \qquad\qquad u = 0, T' = T'_\infty, C' = C'_\infty \quad at\ x = 0 \\ \qquad\qquad u \to 0, T' \to T'_\infty, C' \to C'_\infty \ \ as\ y \to \infty \end{array}\right\} \tag{5}$$

where $u\ and\ v$ are velocity factors of a fluid in $x\ and\ y$ direction respectively, t'-time, g-acceleration due to gravity, β^*-coefficient of volumetric concentration, β-volumetric coefficient of thermal expansion, B_0-magnetic field, k-thermal conductivity, K_1-chemical reaction parameter, υ-kinematic viscosity, ρ- density of the fluid, μ - viscosity coefficient, $\mathcal{C}_p$ -specific heat at constant pressure, $\mathcal{C}'$ - species concentration in the fluid, $\mathcal{T}'$ - temperature of the fluid near the plate, $\mathcal{C}'_\infty$ - concentration at the free stream, $\mathcal{T}'_\infty$ - temperature of the fluid at free stream, u_0 - velocity of the plate, $\omega' t'$ - phase angle, $\mathcal{C}'_w$ -plate concentration and $\mathcal{T}'_w$ - plate temperature.

The local radiant for a gray gas that is optically thin is expressed by

$$(q_r)_y = -4a^*\sigma\left(\mathcal{T}'^4_\infty - \mathcal{T}'^4\right) \tag{6}$$

where q_r - radiative heat flux, a^* - absorption constant, and σ - electrical conductivity.

Assuming no significant variations in temperature across the flow, Eq. (6) can be linearized by extending $\mathcal{T}'^4$ in a Taylor series about $\mathcal{T}'_\infty$ and discarding the higher-order terms, resulting in

$$\mathcal{T}'^4 \cong 4\mathcal{T}'^3_\infty \mathcal{T}' - 3\mathcal{T}'^4_\infty \tag{7}$$

Because of Eqs. (6) and (7), Eq. (3) modifies to

$$\begin{gathered}\mathcal{T}'_{t'} + u\mathcal{T}'_x + v\mathcal{T}'_y = \frac{k}{\rho C_p}\left(\mathcal{T}'_{yy}\right) + \\ \frac{16a^*\sigma\mathcal{T}'^3_\infty\left(\mathcal{T}'_\infty - \mathcal{T}'\right)}{\rho C_p} + \frac{\upsilon}{\rho C_p}\left(u_y\right)^2\end{gathered} \tag{8}$$

Consider the following dimensionless quantities:

$$\left.\begin{gathered}X = \frac{xu_0}{\upsilon}, Y = \frac{yu_0}{\upsilon}, U = \frac{u}{u_0}, V = \frac{v}{u_0}, t = \frac{t'u_0^2}{\upsilon}, \omega = \frac{\omega'\upsilon}{u_0^2}, K = \frac{\upsilon K_1}{u_0^2}, \\ \mathcal{T} = \frac{\mathcal{T}' - \mathcal{T}'_\infty}{\mathcal{T}'_w - \mathcal{T}'_\infty}, \mathcal{C} = \frac{\mathcal{C}' - \mathcal{C}'_\infty}{\mathcal{C}'_w - \mathcal{C}'_\infty}, Gr = \frac{\upsilon g\beta\left(\mathcal{T}'_w - \mathcal{T}'_\infty\right)}{u_0^3}, Gc = \frac{\upsilon g\beta^*\left(\mathcal{C}'_w - \mathcal{C}'_\infty\right)}{u_0^3}, \\ \Pr = \frac{\upsilon}{\alpha}, Sc = \frac{\upsilon}{D}, Ec = \frac{u_0^2}{C_p\left(\mathcal{T}'_w - \mathcal{T}'_\infty\right)}, R = \frac{16a^*\upsilon^2\sigma\mathcal{T}'^3_\infty}{ku_0^2}, M = \frac{\sigma B_0^2\upsilon}{\rho u_0^2}\end{gathered}\right\} \tag{9}$$

where X is the dimensionless coordinate along the plate, Y is the dimensionless coordinate normal to the plate, U and V are dimensionless velocity components in the X and Y directions respectively, $\mathcal{T}$ is the dimensionless temperature, C is the dimensionless concentration, Gr and Gc are the respective thermal Grashof and mass Grashof numbers, Pr is the Prandtl number, Sc is the Schmidt number, Ec is the Eckert number, R is the radiation parameter, M is the magnetic parameter, α is the thermal diffusivity, t is the dimensionless time, ω is the frequency of oscillation, K is the dimensionless chemical reaction parameter, and D is the mass diffusion coefficient.

Given Eq. (9), the dimensionless form of Eqs. (1–4) are:

$$U_X + V_Y = 0 \tag{10}$$

$$U_t + UU_X + VU_Y = Gr\mathcal{T} + Gc\mathcal{C} + U_{YY} - MU \tag{11}$$

$$\mathcal{T}_t + U\mathcal{T}_X + V\mathcal{T}_Y = \frac{1}{\Pr}\left(\mathcal{T}_{YY}\right) - \frac{R\mathcal{T}}{\Pr} + Ec\left(U_Y\right)^2 \tag{12}$$

$$\mathcal{C}_t + U\mathcal{C}_X + V\mathcal{C}_Y = \frac{1}{Sc}\mathcal{C}_{YY} - K\mathcal{C} \tag{13}$$

subject to

$$\left.\begin{gathered}t \le 0: U = 0, V = 0, \mathcal{T} = 0, \mathcal{C} = 0 \\ t > 0: U = \cos\omega t, V = 0, \mathcal{T} = 1, \mathcal{C} = 1 \; at \; Y = 0 \\ U = 0, \mathcal{T} = 0, \mathcal{C} = 0 \quad at \; X = 0 \\ U \to 0, \mathcal{T} \to 0, \mathcal{C} \to 0, \; as \; Y \to \infty\end{gathered}\right\} \tag{14}$$

METHOD OF SOLUTION

The Crank-Nicolson methodology, an unequivocally stable implicit finite-difference strategy, solves the dimensionless governing Eqs. (10–13), subject to the dimensionless boundary condition Eq. (14) of the problem, and the corresponding finite-difference equations are:

$$\begin{gathered}\frac{\left[U^{n+1}_{i,j} - U^{n+1}_{i-1,j} + U^n_{i,j} - U^n_{i-1,j} + U^{n+1}_{i,j-1} - U^{n+1}_{i-1,j-1} + U^n_{i,j-1} - U^n_{i-1,j-1}\right]}{4\Delta X} \\ + \frac{\left[V^{n+1}_{i,j} - V^{n+1}_{i,j-1} + V^n_{i,j} - V^n_{i,j-1}\right]}{2\Delta Y} = 0\end{gathered} \tag{15}$$

$$\begin{gathered}\frac{\left[U^{n+1}_{i,j} - U^n_{i,j}\right]}{\Delta t} + U^n_{i,j}\frac{\left[U^{n+1}_{i,j} - U^{n+1}_{i-1,j} + U^n_{i,j} - U^n_{i-1,j}\right]}{2\Delta X} \\ + V^n_{i,j}\frac{\left[U^{n+1}_{i,j+1} - U^{n+1}_{i,j-1} + U^n_{i,j+1} - U^n_{i,j-1}\right]}{4\Delta Y} \\ = \frac{Gr}{2}\left[\mathcal{T}^{n+1}_{i,j} + \mathcal{T}^n_{i,j}\right] + \frac{Gc}{2}\left[\mathcal{C}^{n+1}_{i,j} + \mathcal{C}^n_{i,j}\right] - \\ \frac{M}{2}\left[U^{n+1}_{i,j} + U^n_{i,j}\right] + \\ \frac{\left[U^{n+1}_{i,j-1} - 2U^{n+1}_{i,j} + U^{n+1}_{i,j+1} + U^n_{i,j-1} - 2U^n_{i,j} + U^n_{i,j+1}\right]}{2(\Delta Y)^2}\end{gathered} \tag{16}$$

$$\begin{gathered}\frac{\left[\mathcal{T}^{n+1}_{i,j} - \mathcal{T}^n_{i,j}\right]}{\Delta t} + U^n_{i,j}\frac{\left[\mathcal{T}^{n+1}_{i,j} - \mathcal{T}^{n+1}_{i-1,j} + \mathcal{T}^n_{i,j} - \mathcal{T}^n_{i-1,j}\right]}{2\Delta X} + \\ V^n_{i,j}\frac{\left[\mathcal{T}^{n+1}_{i,j+1} - \mathcal{T}^{n+1}_{i,j-1} + \mathcal{T}^n_{i,j+1} - \mathcal{T}^n_{i,j-1}\right]}{4\Delta Y} \\ = \frac{1}{\Pr}\frac{\left[\mathcal{T}^{n+1}_{i,j-1} - 2\mathcal{T}^{n+1}_{i,j} + \mathcal{T}^{n+1}_{i,j+1} + \mathcal{T}^n_{i,j-1} - 2\mathcal{T}^n_{i,j} + \mathcal{T}^n_{i,j+1}\right]}{2(\Delta Y)^2} - \\ \frac{R}{2\Pr}\left[\mathcal{T}^{n+1}_{i,j} + \mathcal{T}^n_{i,j}\right] + Ec\left[\frac{U^n_{i,j+1} - U^n_{i,j}}{\Delta Y}\right]^2\end{gathered} \tag{17}$$

$$\frac{\left[C^{n+1}_{i,j}-C^{n}_{i,j}\right]}{\Delta t}+U^{n}_{i,j}\frac{\left[C^{n+1}_{i,j}-C^{n+1}_{i-1,j}+C^{n}_{i,j}-C^{n}_{i-1,j}\right]}{2\Delta X}+V^{n}_{i,j}\frac{\left[C^{n+1}_{i,j+1}-C^{n+1}_{i,j-1}+C^{n}_{i,j+1}-C^{n}_{i,j-1}\right]}{4\Delta Y}=\frac{1}{Sc}\frac{\left[C^{n+1}_{i,j-1}-2C^{n+1}_{i,j}+C^{n+1}_{i,j+1}+C^{n}_{i,j-1}-2C^{n}_{i,j}+C^{n}_{i,j+1}\right]}{2\left(\Delta Y\right)^{2}}-\frac{K}{2}\left[C^{n+1}_{i,j}+C^{n}_{i,j}\right] \tag{18}$$

Here, i and j denotes the x and y coordinates of the grid point and n is the time variable. A rectangular mesh with sides $X_{\max}=1$ *and* $Y_{\max}=10$ is assumed. The mesh sizes are fixed as $\Delta X=0.05$, $\Delta Y=0.125$, and $\Delta t=0.01$ as time step.

RESULTS AND DISCUSSION

The graphical representation of the impact of velocity, concentration, temperature, skin friction, Nusselt number, and Sherwood number on various physical parameters is illustrated in this section through numerical results. The default physical parameters used in this analysis are phase angle *ωt=π/6*, thermal Grashof number *Gr=5*, mass Grashof number *Gc=5*, radiation parameter *R=2* (strong thermal radiation), magnetic parameter *M=2*, Eckert number *Ec=0.5*, chemical reaction parameter *Ec=0.2*, Prandtl number *Pr=0.71* (air), and Schmidt number *Sc=0.6* (water vapor).

Figure 2 depicts the velocity patterns obtained for various phase angle values. From the graph, it is evident that as the phase angle rises, the velocity drops. This observation illustrates that increased oscillation levels lead to reduced velocity.

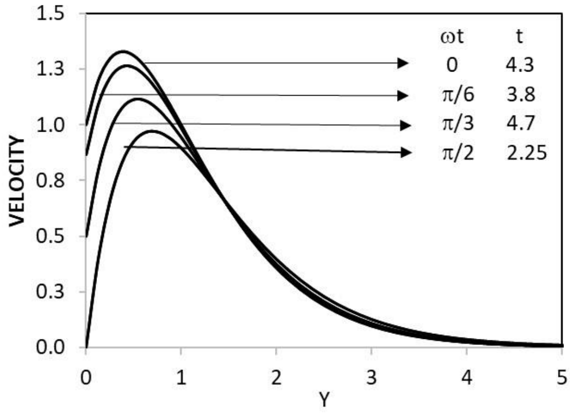

Figure 2. Velocity profiles for different values of ωt.

The impact of the radiation parameter *R* on velocity is represented in Figure 3. The research findings indicate that the flow velocity tends to decrease with an increase in the radiation parameter. It suggests that a higher presence of heat radiation leads to a reduction in velocity.

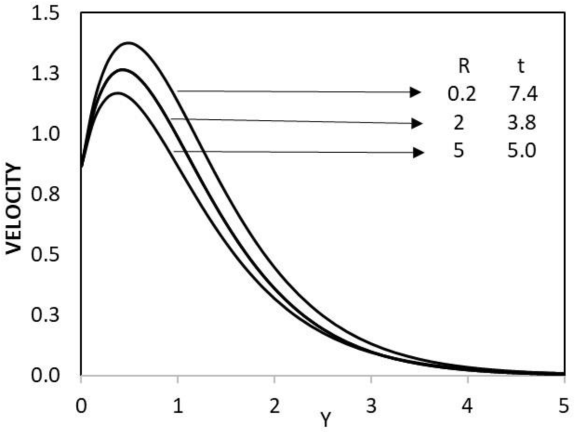

Figure 3. Velocity profiles for different values of R.

The graphical representation in Figure 4 displays the correlation between the chemical reaction parameter *K* and the velocity field. The investigations have revealed that an increase in the chemical reaction parameter results in a decrease in velocity. This observation highlights that velocity rises during generative reactions while falling during destructive reactions.

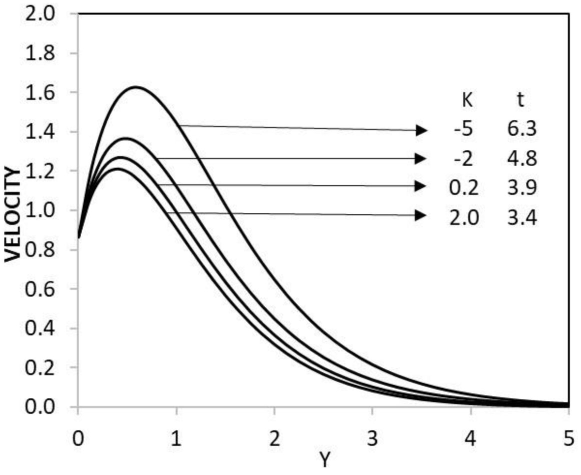

Figure 4. Velocity profiles for different values of K.

Figure 5 illustrates how various chemical reaction parameter *K* values influence the dimensionless concentration profile. The research findings indicate that an increase in the chemical reaction parameter results in a reduction in concentration. Specifically, the wall concentration rises during generative reactions and falls during destructive reactions.

The concentration profile for various values of the Schmidt number *Sc* is shown in Figure 6. The graph clearly illustrates that when the Schmidt number increases, the plate concentration decreases significantly. This observation holds in the physical context, as a higher value of *Sc* greatly hampers molecular diffusivity.

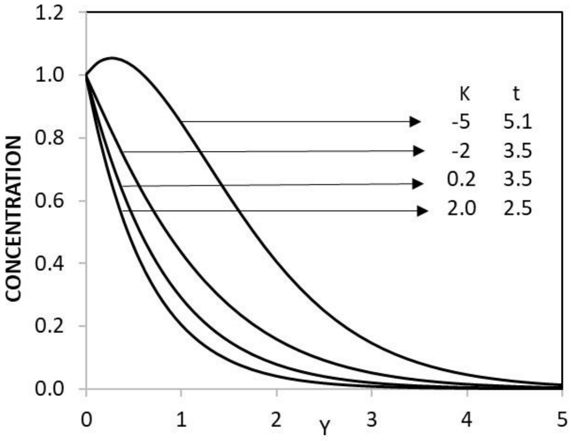

Figure 5. Concentration profiles for different values of K.

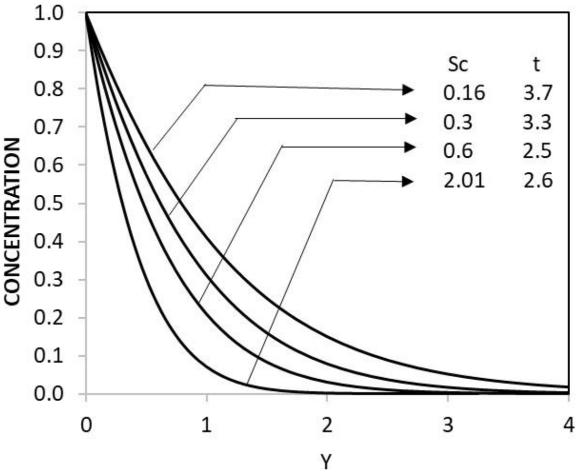

Figure 6. Concentration profiles for different values of Sc.

The influence of the thermal radiation parameter *R* on the dimensionless fluid temperature is illustrated in Figure 7. The results demonstrate that as the radiation parameter increases, the velocity and temperature of the boundary layer decrease.

Figure 8 depicts the effect of the Eckert number Ec on dimensionless fluid temperature. The research has revealed that increasing the dissipation parameter leads to an elevation in temperature. Viscous dissipation affects flow fields by raising energy levels, resulting in higher fluid temperatures and increased buoyancy forces.

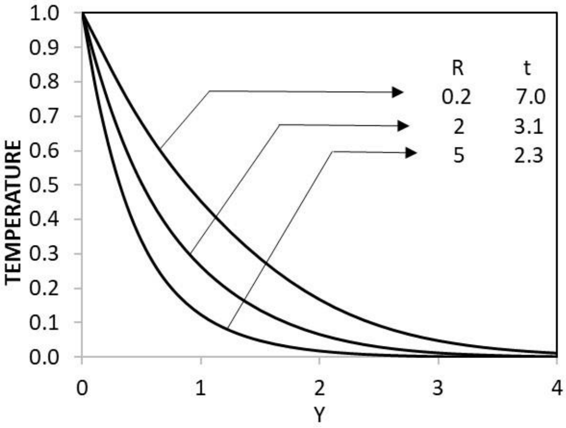

Figure 7. Temperature profiles for different values of R.

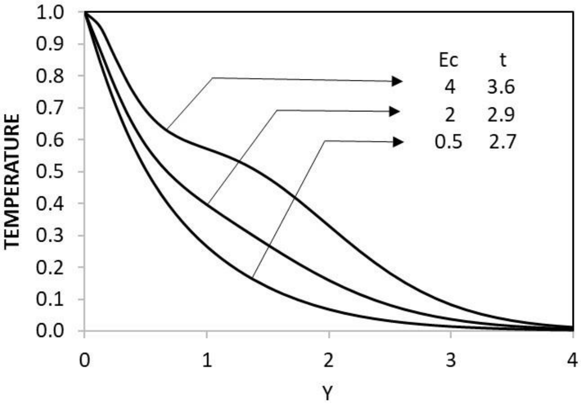

Figure 8. Temperature profiles for different values of Ec.

CONCLUSION

A numerical study explored the impact of chemical reactions, thermal radiation, and viscous dissipation on an unsteady MHD flow over an oscillating semi-boundless vertical plate with constant surface temperature and mass diffusion. An implicit finite-difference method was utilized to solve the governing flow equations. The impact of various parameters on the fluid velocity, concentration, and temperature are demonstrated graphically. The current investigation reveals the following major findings:

Velocity drops when the phase angle, radiation, and chemical parameters increase. When the Eckert number rises, the velocity and temperature profiles also rise. The temperature drops as the radiation parameter rises. A drop in concentration was seen with an increase in the chemical reaction parameter and the Schmidt number.

REFERENCES

[1] E.M. Sparrow, R.D. Cess, Int. J. Heat Mass Transfer 3 (1961) 267–274. https://doi.org/10.1016/0017-9310(61)90042-4.

[2] A.J. Chamkha, Int. J Eng. Sci. 42 (2004) 217–230. https://doi.org/10.1016/S0020-7225(03)00285-4.

[3] A. Raptis, Therm. Sci. 15 (2011) 849–857.

https://doi.org/10.2298/TSCI101208032R.

[4] A. Hussanan, M.I. Anwar, F. Ali, I. Khan, S. Shafie, Heat Transf. Res. 45 (2014) 119–135. http://doi.org/10.1615/HeatTransRes.2013006385.

[5] U.N. Das, R. Deka, V.M. Soundalgekar, Forsch. Ingenieurwes. 60 (1994) 284–287. https://doi.org/10.1007/bf02601318.

[6] R. Muthucumaraswamy, T. Kulaivel, Forsch. Ingenieurwes. 68 (2003) 101–104. https://doi.org/10.1007/s10010-003-0112-9.

[7] R. Muthucumaraswamy, Chem. Ind. Chem. Eng. Q. 16 (2010) 167–173. https://doi.org/10.2298/CICEQ091231024M.

[8] A.R. Vijayalakshmi, M. Selvajayanthi, Int. J. Appl. Mech. Eng. 19 (2014) 181–193. https://doi.org/10.2478/ijame-2014-0013.

[9] F.S. Ibrahim, A.M. Elaiw, A.A. Bakr. Commun. Nonlinear Sci. Numer. Simul. 13 (2008) 1056–1066. https://doi.org/10.1016/j.cnsns.2006.09.007.

[10] K. Manivannan, R. Muthucumaraswamy, V. Thangaraj. Therm. Sci. 13 (2009) 155–162. https://doi.org/10.2298/TSCI0902155M.

[11] S. Ahmed, J. Zueco, L.M. Lopez-Ochoa. Chem. Eng. Commun. 20 (2013) 419–436. https://doi.org/10.1080/00986445.2013.775645.

[12] C. Santhana Lakshmi, R. Muthucumaraswamy. J. Chem. Pharm. Sci. 8 (2015) 700–705. http://www.jchps.com/issues/Volume%208_Issue%204/jchps%208(4)%2019%20C.%20Santhana%20Lakshmi.pdf.

[13] Y. Hari Krishna, M.V. Ramana Murthy, N.L. Bhikshu, G. Venkata Ramana. Int. J. Chem. Sci. 15 (2017) 1–12. https://www.tsijournals.com/abstract/effects-of-radiation-and-chemical-reaction-on-mhd-flow-past-an-oscillating-inclined-porous-plate-with-variable-temperatu-13297.html.

[14] V. Srihari Babu, K. Jaya Rami Reddy, Global J. Pure Appl. Math. 13 (2017) 5341–5358. https://www.ripublication.com/gjpam17/gjpamv13n9_74.pdf.

[15] S. Matta, B.S. Malga, L. Appidi, P. Kumar, Indian J. Sci. Technol. 14 (2021) 707–717. https://doi.org/10.17485/IJST/v14i8.20.

[16] A. Shehu, I.D. Yale, A.M.T. Uchiri, World J. Adv. Eng. Technol. Sci. 6 (2022) 81–87. https://doi.org/10.30574/wjaets.2022.6.2.0084.

[17] R.L. Mahajan, B. Gebhart, Int. J. Heat Mass Transfer 32 (1989) 1380–1382. https://doi.org/10.1016/0017-9310(89)90038-0.

[18] N. Kishan, P. Amrutha, J. Nav. Archit. Mar. Eng. 7 (2010) 11–18. https://doi.org/10.3329/jname.v7i1.3254.

[19] J.A. Rao, S. Shivaiah, Appl. Math. Mech. (Engl. Transl.) 32 (2011) 1065–1078. https://doi.org/10.1007/s10483-011-1481-6.

[20] K.V.B. Rajakumar, K.S. Balamurugan, Ch.V. Ramana Murthy, M. Umasenkara Reddy, Global J. Pure Appl. Math. 13 (2017) 8297–8322. https://www.ripublication.com/gjpam17/gjpamv13n12_11.pdf.

[21] S. Kar, N. Senapati, B.K. Swain, Int. J. Adv. Appl. Sci. 8 (2019) 83–94. https://doi.org/10.11591/ijaas.v8.i1.pp83-94.

[22] N.N. Reddy, V. Srinivasa Rao, B. Ravindra Reddy, Case Stud. Therm. Eng. 25 (2021) 100879. https://doi.org/10.1016/j.csite.2021.100879.

[23] P.M. Kishore, N.V.R.V. Prasada Rao, S. Vijaya Kumar Verma, S. Venkata Ramana, Int. J. Math. Arch. 4 (2013) 74–86. http://www.ijma.info/index.php/ijma/article/view/1854.

[24] C.S. Balla, K. Naikoti, Alexandria Eng. J. 54 (2015) 661–671. https://doi.org/10.1016/j.aej.2015.04.013.

[25] B. Zigta, Int. J. Appl. Mech. Eng. 23 (2018) 787–801. https://doi.org/10.2478/ijame-2018-0043.

[26] B. Prabhakar Reddy, Int. J. Appl. Mech. Eng. 24 (2019) 343–358. https://doi.org/10.2478/ijame-2019-0022.

[27] T.R.K.D. Vara Prasad, T. Linga Raju, K.V.B. Rajakumar, Heat Transfer 52 (2022) 1254–1274. https://doi.org/10.1002/htj.22739.

RENGASAMY RAJARAMAN[1]
RAJAMANICKAM MUTHUCUMARASWAMY[2]

[1]Department of Mathematics, R.M.K. Engineering College, Kavaraipettai, India

[2]Department of Mathematics, Sri Venkateswara College of Engineering, Sriperumbudur, India

NAUČNI RAD

UTICAJ HEMIJSKE REAKCIJE, VISKOZNE DISIPACIJE I TOPLOTNOG ZRAČENJA NA MAGNETOHIDRODINAMIČKI PROTOK PREKO OSCILIRAJUĆE PLOČE

Ova studija analizira posledice hemijskih reakcija prvog reda, zračenja i viskozne disipacije na nestacionarni magnetohidrodinamički prirodni konvektivni tok viskoznog nestišljivog fluida preko vertikalne polubeskonačne oscilirajuće ploče sa ujednačenom masenom difuzijom i temperaturom. Implicitna tehnika konačnih razlika se koristi za rešavanje skupa bezdimenzionalnih, spregnutih, nelinearnih parcijalnih diferencijalnih jednačina. Numerički rezultati za brzinu tečnosti, koncentraciju i temperaturu na ploči pod različitim bezdimenzionalnim parametrima su grafički prikazani. Zbog homogenih hemijskih reakcija prvog reda, otkriveno je da brzina raste u vreme generativne reakcije, a pada tokom destruktivne reakcije. Pad brzine se primećuje sa povećanjem faznog ugla, parametra zračenja i parametra hemijske reakcije. Dalje, otkriveno je da oscilacije ploče, zračenje, hemijske reakcije i magnetno polje značajno utiču na ponašanje protoka.

Ključne reči: MHD; oscilirajuća ploča; konačna razlika; viskozna disipacija; hemijska reakcija.

CI&CEQ
Chemical Industry & Chemical Engineering Quarterly

Available online at
Association of the Chemical Engineers of Serbia *AChE*
www.ache.org.rs/CICEQ

Chem. Ind. Chem. Eng. Q. 30 (3) 231–241 (2024) CI&CEQ

THITIPORN SUTTIKUL[1,2]
SIRIMAS MANTHUNG[1]
SASIKARN NUCHDANG[3]
DUSSADEE RATTANAPHRA[3]
THONGCHAI PHOTSATHIAN[4]

[1]Division of Chemical Process Engineering Technology, Faculty of Engineering and Technology, King Mongkut's University of Technology North Bangkok, Rayong, Thailand

[2]The Plasma and Automatic Electric Technology Research Group, King Mongkut's University of Technology North Bangkok, Rayong, Thailand

[3]Research and Development Division, Thailand Institute of Nuclear Technology, Pathum Thani, Thailand

[4]Division of Instrumentation and Automation Engineering Technology, Faculty of Engineering and Technology, King Mongkut's University of Technology North Bangkok, Rayong, Thailand

SCIENTIFIC PAPER

UDC 66.094.3:54:533.9

ONE–STEP CONVERSION OF ETHANE TO ETHYLENE OXIDE IN AC PARALLEL PLATE DIELECTRIC BARRIER DISCHARGE

Article Highlights

- For the first time, DBD was used to perform a one-step direct conversion of C_2H_6 to EO
- The effects of the applied voltage, input frequency, and O_2/C_2H_6 feed molar ratio were examined
- Higher voltage and lower frequency generated more electrons, resulting in higher current
- The higher activity resulted from more electrons interacting with reactant gas molecules

Abstract

This work studied the one-step conversion of ethane (C_2H_6) to ethylene oxide (EO) in an AC parallel plate dielectric barrier discharge (DBD) system with two frosted glass plates under ambient temperature and atmospheric pressure. EO is directly produced from C_2H_6 in a single step without the requirement to separate and recycle ethylene. The effects of the applied voltage, input frequency, and O_2/C_2H_6 feed molar ratio on the EO synthesis performance were examined. The results showed that a higher applied voltage and lower input frequency generated more highly energetic electrons, resulting in a higher current. More electrons collided with reactant gas molecules to initiate plasma reactions, increasing C_2H_6 and O_2 conversions. The increased O_2/C_2H_6 feed molar ratio enhanced C_2H_6 and O_2 conversions. The optimum conditions were found to be an applied voltage of 7 kV, input frequency of 550 Hz, and O_2/C_2H_6 feed molar ratio of 1:1, which demonstrated the highest EO selectivity (42.6%), EO yield (19.4%), and lowest power consumption per EO molecule produced (6.7×10^{-18} Ws/molecule).

Keywords: dielectric barrier discharge, epoxidation, ethane oxidative dehydrogenation, ethylene oxide, one-step reaction.

The manufacture of ethylene oxide (EO) is a rapidly expanding industry in which silver is used as a catalyst. The market for ethylene oxide is expected to increase at a compound annual growth rate (CAGR) of 4.56% over the forecast period, from US$48.240 billion in 2019 to US$65.912 billion in 2026 [1]. Ethylene oxide (C_2H_4O, EO) is a versatile chemical that is utilized as a starting material for the production of a variety of beneficial goods. For instance, ethylene glycol, a primary product of EO, is used as a feedstock to synthesize antifreeze and plastics, such as polyethylene terephthalate [2-5]. Surfactant, ethanolamine solvent, and glycol ether solvent were produced by EO alkoxylation processes [5]. In addition, EO is generally used as a sterilizer for medical

---

Correspondence: T. Suttikul, Division of Chemical Process Engineering Technology, Faculty of Engineering and Technology, King Mongkut's University of Technology North Bangkok, Rayong Campus, Rayong 21120, Thailand.
E-mail: thitiporn.s@eat.kmutnb.ac.th
Paper received: 28 February, 2023
Paper revised: 17 July, 2023
Paper accepted: 3 October, 2023

https://doi.org/10.2298/CICEQ230228026S

equipment and supplies such as needles, surgical cords, and surgical supplies [6].

Partial oxidation of ethylene (C_2H_4), the so-called ethylene epoxidation, commercially produces EO using Ag-based catalysts with promoters (Re, Cs, Mo, Cl, etc.) and provides a considerably high EO selectivity of 80-90% [7–9]. C_2H_4 used as a reactant in forming EO, is typically obtained via oxidative dehydrogenation of ethane (ODHE). The exothermic ODHE reaction takes place at temperatures between 673 and 873 K [10], while C_2H_4 epoxidation utilizing Ag/(LSA) α-Al_2O_3 only requires a reaction temperature below 573 K [11]. There have been several attempts to develop a bifunctional catalyst that would enable the direct synthesis of EO from ethane (C_2H_6) in a single step without the requirement to separate and recycle C_2H_4. A NiAgO catalyst directly produced EO from C_2H_6 [12]. After that, a Y_2O_3 promoter was used to improve the properties of the catalyst, particularly its electrophilic nature [13]. For the direct conversion of C_2H_6 to EO, the NiAgYO catalyst demonstrated higher EO selectivity and yield than NiAgO. The interaction between Y and Ag, which caused the absorbed oxygen species to possess proper electrophilic character, led to the enhanced performance of the NiAgYO catalyst. However, the NiAgYO catalyst exhibited low EO selectivity and yield of 19.8% and 7.6%, respectively, at 563 K. Therefore, it is highly desirable to continue the development of an active catalyst and to identify potential innovative, low-temperature operating techniques that can improve reaction performance.

Nonthermal plasma (NTP) is an ionized gas typically produced by an electric discharge [14]. Various reactive species, including vibrationally or electrically activated molecules, radicals, atoms, and ions, are produced when free electrons in the plasma impact gas particles. The major property of NTP is that the temperature of the electrons can be in the range of 10^4–10^5 K, while the bulk gas temperature is close to ambient (300–1000 K). Dielectric barrier discharge (DBD) is a type of nonthermal plasma (NTP) that can operate at ambient temperature (nearly 298 K) and atmospheric pressure, resulting in relatively low energy consumption. DBD has received the most attention for plasma-enhanced catalysis, such as the conversion of CO_2 and CH_4 into synthesis gas and value-added liquid chemical [15–17], volatile organic compound decomposition [18–20], remediation of contaminated soil [21-23], and C_2H_4 epoxidation [24–28], which our research team studied. A separate feed of C_2H_4 from O_2 with a suitable C_2H_4 feed position was demonstrated to decrease undesired reactions such as cracking, partial oxidation, and hydrogenation in investigations of DBD, corona discharge, and dielectric barrier discharge jet (DBDJ) systems [27], as compared to a mixed feed [24]. The DBDJ achieved the highest energy efficiency of 703.65 mmol/kJ (Table 1). However, packing a catalyst in the plasma zone of a DBDJ reactor is cumbersome, and the discharge becomes unstable. In comparison to DBD with an Ag catalyst loaded on a single smooth glass plate [26], it was discovered that the DBD-alone system using two frosted glass plates improved the C_2H_4 epoxidation performance by achieving a reasonably high EO selectivity and yield of 68.2% and 10.9%, respectively [28]. The results are attributable to the fact that frosted glass plates offered more sharp points than smooth glass plates, generating more uniform plasma with a better distribution of energy densities. Pulse corona discharge, a kind of NTP, was used to study the ODHE with carbon dioxide at room temperature and atmospheric pressure over several catalysts [29]. The corona discharge using a Pd/γ-Al_2O_3 catalyst had a 46.7% C_2H_4 selectivity and 30.0% C_2H_6 conversion. Non-oxidative ethane dehydrogenation (EDH) was investigated in a packed-bed DBD reactor [30]. As a result, C_2H_4 is the primary byproduct, followed by acetylene (C_2H_2), methane (CH4), and C_3/C_4 hydrocarbons. A SiO_2-supported Pd catalyst can change the product selectivity and distort the electric field. From the literature mentioned above, we hypothesize that DBD can be used for the ODHE reaction to form C_2H_4 and then further convert to EO.

In this study, the one-step conversion of C_2H_6 and O_2 to EO was investigated for the first time in an AC parallel-plate DBD with two frosted glass plates. The effects of various operating parameters, including the applied voltage, input frequency, and O_2/C_2H_6 feed molar ratio, on the EO synthesis performance were experimentally studied to determine the optimum conditions.

MATERIALS AND METHODS

Gases for the reaction experiment

In this work, C_2H_6 with a purity of 99.5%, oxygen with a purity of 99.5%, and helium with a purity of 99.995% (high purity grade) were blended to produce a feed gas. C_2H_6 was supplied by Linde (Thailand) Public Co., Ltd., whereas Thai Industrial Gas Co., Ltd. supplied oxygen and helium.

Setup and reaction testing experiments

The one-step conversion of C_2H_6 to EO was investigated in a parallel-plate DBD reactor at atmospheric pressure and ambient temperature (approximately 298 K). A schematic diagram of the experimental setup is illustrated in Fig. 1, and an

Table 1. Comparison of the catalyst-alone and DBD-alone systems on the EO synthesis performance.

System (conditions)	Conversion (%)			Selectivity (%)		Yield (%)		Power consumption			Energy efficiency (mmol/kJ)
	C_2H_6	C_2H_4	O_2	EO	C_2H_4	EO	C_2H_4	C_2H_6 converted	C_2H_4 converted	EO produced	
Parallel DBD using a clear glass plate [24] (Mixed feed, O_2/C_2H_6 molar ratio of 1/1, applied voltage of 19 kV, an input frequency of 500 Hz, and a total feed flow rate of 50 cm^3/min)	-	91.0	93.7	6.2	-	5.6	-	-	4.0 x 10^{-17}	$^{\#}$6.1 x 10^{-16} *102.0	N/A
Corona discharge [25] (Separate feed [C_2H_4 feed position of 0.2 cm], O_2/C_2H_4 molar ratio of 0.5/1, applied voltage of 18 kV, input frequency of 500 Hz, and total feed flow rate of 100 cm^3/min)	-	2.3	44.3	78.1	-	1.8	-	-	4.7 x 10^{-18}	$^{\#}$6.1 x 10^{-16} *1.0	0.02
DBDJ [27] (Separate feed [C_2H_4 feed position of 0.3 cm], O_2/C_2H_4 molar ratio of 0.25/1, applied voltage of 9 kV, input frequency of 500 Hz, and total feed flow rate of 1,625 cm^3/min)	-	50.0	91.2	55.2	-	27.6	-	-	3.3 x 10^{-21}	$^{\#}$ 6.0 x 10^{-21} *1.0 x 10^{-3}	703.65
Parallel DBD using two frosted glass plates [28] (Separate feed [C_2H_4 feed position of 0.5], O_2/C_2H_4 molar ratio of 0.2/1, applied voltage of 23 kV, input frequency of 500 Hz, and total feed flow rate of 50 cm^3/min)	-	19.8	99.5	68.1	-	10.9	-	-	1.9 x 10^{-16}	$^{\#}$2.8 x 10^{-16} *46.8	0.03
Catalytic process using Cs-Re15% Ag/α-Al_2O_3 [40] (Reaction temperature of 499K, O_2/C_2H_4 molar ratio of 0.25/1, space velocity of 5,000 h^{-1})	-	10.0	N/A	83.5%	-	N/A	-	-	N/A	N/A	N/A
Catalytic process using 0.32% Sn-1.39% Cu-17.16% Ag/$SrTiO_3$ [41] (Reaction temperature of 548K, O_2/C_2H_4 molar ratio of 1/1, space velocity of 6,000 h^{-1})	-	5.4	N/A	99.2	-	5.4	-	-	N/A	N/A	N/A
Parallel DBD using two frosted glass plates (This work) (Mixed feed, O_2/C_2H_6 molar ratio of 1/1, applied voltage of 7 kV, an input frequency of 550 Hz, and a total feed flow rate of 50 cm^3/min)	45.3	-	99.2	42.6	-	19.4	-	2.9 x 10^{-18}	-	$^{\#}$6.7 x 10^{-18} *1.1	0.73
Cylindrical DBD using unloaded SiO_2 catalyst [30] (Mixed feed, 5% C_2H_6 in helium, applied voltage of 10 kV, and a total feed flow rate of 60 cm^3/min)	~20	-	-	-	~26	-	~3.8	N/A	-	-	0.13
Catalytic process using 5% Ni-Ag-O [12] (Reaction temperature of 583K, O_2/C_2H_6 molar ratio of 1/1, gaseous hourly space velocity of 24,000 $mLh^{-1}g^{-1}$)	9.3	-	N/A	12.8	-	1.2	-	N/A	-	N/A	N/A
Catalytic process using 5% NiAgYO [13] (Reaction temperature of 563K, O_2/C_2H_6 molar ratio of 1/1, gaseous hourly space velocity of 12,000 $mLh^{-1}g^{-1}$)	38.4	-	N/A	19.8	-	7.6	-	N/A	-	N/A	N/A

Unit of power consumption; peak marked with *hash* corresponds to Ws/EO molecule produced, with an *asterisk* to kWh per mol of EO.

explanation of the DBD reactor can be found in our previous work [28]. The 2 mm frosted glass plate was washed with distilled water and then cleaned with acetone before use as a dielectric material in the DBD reactor. A microdischarge was produced at a distance of 3 mm between the two parallel frosted glass plates by a specially designed AC power supply. The domestic AC electricity (220 V and 50 Hz) was transformed using three steps to a high-voltage AC (applied voltage of 1–25 kV), according to our prior study [31]. A digital power analyzer (True RMS Single Phase Power Analyzer, 380801, Extech Instruments Corporation) was used to monitor input current and power. The power analyzer digitalized the incoming voltage and current waveforms, which then used the voltage and current product over time to calculate the plasma power. A function generator drove the power supply to obtain desired frequency and voltage ranges of 300–800 Hz and 5–11 kV. The temperature was measured using a type K thermocouple with an Agilent U1273A digital multimeter. The temperature of the outside surface of the DBD reactor was kept at 298 ± 1 K by air cooling. The exit gas temperature was 298 ± 0.5 K for all experiments.

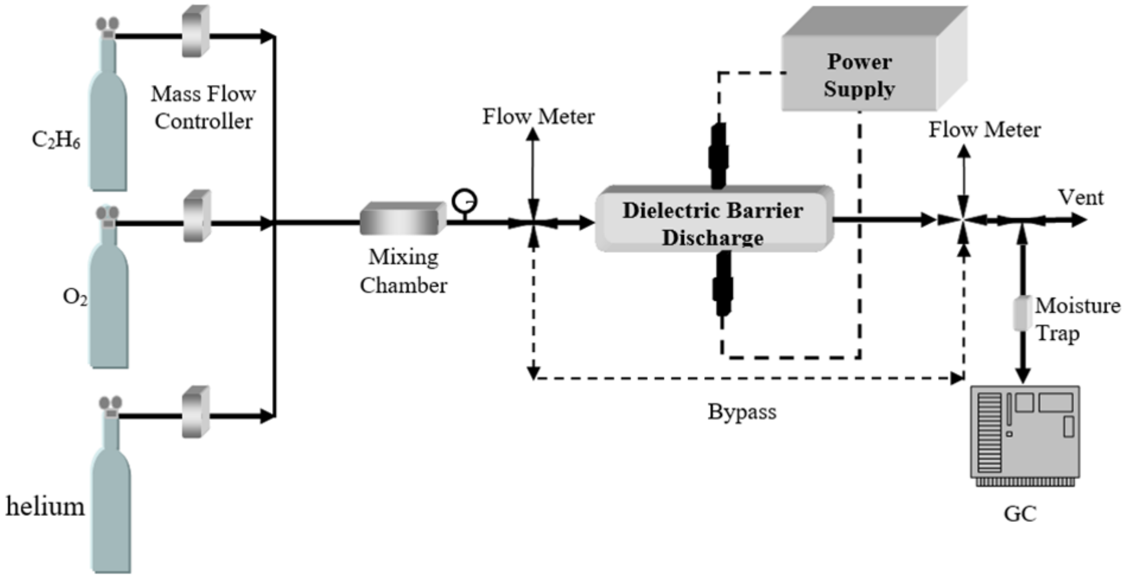

Figure 1. Schematic diagram of the experimental setup of the DBD system for EO production.

For plasma reaction testing, the reactant gases (C_2H_6 and O_2) were mixed with helium as a balancing gas to obtain a total flow rate of 50 cm^3/min and an O_2/C_2H_6 molar ratio of 0.5:1. All gases were fed into the DBD reactor using electronic mass flow controllers (AALBORG Instruments & Controls, USA). After the AC power supply was turned on to initiate the plasma reactions, the composition of the effluent gas was analyzed by online gas chromatography (GC, PerkinElmer Clarus 590, USA) with a flame ionization detector (FID) and thermal conductivity detector (TCD) every 20 minutes and at least three times for each reaction. The composition of the hydrocarbon (HC) molecules, such as CH_4, C_2H_2, C_2H_4, C_2H_6, propene (C_3H_6), propane (C_3H_8), butane (C_4H_{10}), and EO, was determined using an FID detector outfitted with a PoraPLOT U column. The composition of the nonhydrocarbon molecules, including hydrogen (H_2), O_2, carbon monoxide (CO), and carbon dioxide (CO_2), was evaluated using a TCD detector fitted with a Shin Carbon ST column.

Each reaction was carried out three times. The average data with less than 5% variation were used to compute the C_2H_6 and O_2 conversions, the selectivity towards EO, H_2, CO, CH_4, C_2H_2, C_2H_4, C_3H_8, and C_4H_{10}, the EO yield, and the amount of coke formation using the following equations:

$$\text{Reactant conversion}(\%) = \frac{(M_{in} - M_{out})}{M_{in}} \cdot 100\% \tag{1}$$

$$\text{Product selectivity}(\%) = \frac{C_P P}{\sum(C_R R)} \cdot 100\% \tag{2}$$

$$H_2 \text{ selectivity}(\%) = \frac{H_p P}{H_R R} \cdot 100\% \tag{3}$$

$$\text{EO yield}(\%) = \frac{C_2H_6 \ conversion(\%) \cdot EO \ selectivity(\%)}{100} \tag{4}$$

$$\text{Coke}(\%) = \frac{\sum(C_R R)_{input} - \sum(C_R R + C_P P)_{output}}{\sum(C_R R)_{input}} \cdot 100\% \tag{5}$$

where M_{in} is the moles of reactant in the input, M_{out} is the moles of reactant in the output, C_R is the number of carbon atoms in the reactant, R is the moles of reactant converted, C_P is the number of carbon atoms in the product, P is the moles of product produced, H_R is the number of hydrogen atoms in the reactant (C_2H_6), and H_P is the number of hydrogen atoms in the product (H_2).

Eqs. (6) and (7) were used to calculate power consumption in a unit of Ws per C_2H_6 molecule converted or per EO molecule produced and energy efficiency in a unit of mmol/kJ used, respectively.

$$\text{Power consumption} = \frac{Power(W)\cdot 60}{A\cdot M} \tag{6}$$

$$\text{Energy efficiency}\left(\frac{mmol}{kJ}\right) = \frac{\text{Rate of reactant converted}\left(\frac{mol}{\text{min}}\right)\cdot 10^{6}}{Power(W)\cdot 60} \tag{7}$$

where A is Avogadro's number (6.022 x 10^{23} molecules/mol), and M is the rate of C_2H_6 molecules converted in feed or the rate of EO molecules produced (mol/min).

RESULTS AND DISCUSSION

Possible chemical reactions

The following equations represent possible chemical pathways in the DBD reactor used in this study. First, high-energy electrons cracked O_2 into active oxygen species (Eq. 8). The active oxygen species then reacted with C_2H_6 to form C_2H_4 and water, a process known as oxidative dehydrogenation of C_2H_6 Eq. (9). As expected, C_2H_4 epoxidation produced the desired EO (Eq. 10).

O_2 dissociation [32]:

$$O_2 + e \rightarrow 2O + e \tag{8}$$

Oxidative dehydrogenation of C_2H_6 [33]:

$$C_2H_6 + O \rightarrow C_2H_4 + H_2O \tag{9}$$

C_2H_4 epoxidation [28]:

$$C_2H_4 + O \rightarrow C_2H_4O \tag{10}$$

In addition to EO and C_2H_4, CH_4, CO, C_3H_8, and H_2 were also produced from plasma reactions. The partial and complete oxidation reactions created CO, CO_2, H_2, and H_2O molecules (Eqs. 11–14). The GC analysis revealed no CO_2 peak (low amount until it could not be detected), which could be because high energy electrons cracked CO_2 into CO and oxygen species (Eq. 15). The CH_4 and C_3H_8 molecules could be formed by cracking reactions, as shown in Eqs. (16–19), followed by hydrocarbon free radical coupling reactions (Eqs. 20–23).

Partial and complete oxidation [34]:

$$C_2H_6 + 2O \rightarrow 2CO + 3H_2 \tag{11}$$

$$C_2H_6 + 5O \rightarrow 2CO + 3H_2O \tag{12}$$

$$C_2H_6 + 4O \rightarrow 2CO_2 + 3H_2 \tag{13}$$

$$C_2H_6 + 7O \rightarrow 2CO_2 + 3H_2O \tag{14}$$

Cracking [28, 32, 35, 36]:

$$CO_2 + e \rightarrow CO + O + e \tag{15}$$

$$C_2H_6 + e \rightarrow 2CH_3 + e \tag{16}$$

$$C_2H_6 + e \rightarrow C_2H_5 + H + e \tag{17}$$

$$C_2H_4 + e \rightarrow 2CH_2 + e \tag{18}$$

$$H_2 + 2e \rightarrow 2H + 2e \tag{19}$$

Coupling [35–37]:

$$CH_3 + H \rightarrow CH_4 \tag{20}$$

$$CH_2 + 2H \rightarrow CH_4 \tag{21}$$

$$C_2H_5 + CH_3 \rightarrow C_3H_8 \tag{22}$$

$$2CH_2 \rightarrow C_2H_4 \tag{23}$$

Effect of applied voltage

The direct conversion of C_2H_6 to EO was investigated in the DBD reactor using two frosted glass plates under atmospheric pressure and ambient temperature (~ 298 K) without the requirement of other external heat sources. Figure 2 shows the influence of the applied voltage on the reaction performance regarding the C_2H_6 and O_2 conversions, current, EO selectivity and yield, other product selectivities, and power consumption. The applied voltage was investigated in the 5–11 kV range, while an input frequency of 500 Hz, flow rate of 50 cm^3/min, and O_2/C_2H_6 feed molar ratio of 0.5:1 were fixed. As shown in Fig. 2a, the C_2H_6 conversion significantly increases from 23.3 to 39.7% with increasing applied voltage from 5 to 11 kV. When the applied voltage was increased from 5 to 7 kV, the O_2 conversion considerably increased from 58.4 to 96.9%. Then, O_2 conversion gradually increased to 98.4% as the applied voltage increased to 11 kV. The generated discharge became unstable at applied voltages greater than 11 kV, so the DBD reactor voltages increased to 11 kV. Plasma could not be generated when the applied voltage was less than 5 kV. The C_2H_6 conversion was significantly lower than the O_2 conversion since the DBD system was operated under oxygen-lean conditions with a feed molar ratio of O_2/C_2H_6 of 0.5:1. For complete oxidation, the theoretical molar ratio of O_2/C_2H_6 is 3.5:1. A higher current resulted from a greater number of excited electrons being produced by the higher applied voltage

(Fig. 2a). As a result, increases in the C_2H_6 and O_2 conversions were observed.

As shown in Fig. 2b, the EO selectivity and yield increase, reach the highest values at 7 kV, and decrease with increasing applied voltage over 7 kV. It is interesting to note that one of the primary products of the plasma reactions was CH_4. Product selectivities were arranged as follows: CH_4 > EO > C_2H_4 > CO >> C_3H_8 > H_2 (Fig. 2c). The results indicated that the cracking reactions (Eqs. 16–18), followed by the hydrogenation reactions (Eqs. 20–21), into CH_4, were certainly promoted in the studied DBD system. The selectivities towards CH_4 and H_2 are drastically enhanced over the entire applied voltage range of 5–11 kV, as illustrated in Fig. 2c. A higher applied voltage resulted in a greater number of excited electrons, which increased C_2H_6 and O_2 conversions, and the selectivities towards EO, CH_4, and H_2 (Fig. 2a and 2b). When the applied voltage exceeded 7 kV, excess excited electrons could crack more C_2H_6 and C_2H_4 molecules, forming lower molecules such as CH_4 and H_2 instead of the desired EO. As a result, the EO selectivity above 7 kV decreased, but the selectivities towards CH_4 and H_2 increased continuously. The C_2H_4 selectivity, on the other hand, tended to considerably decrease as the applied voltage was increased from 5 to 11 kV. At an applied voltage of 7 kV, the C_3H_8 selectivity increased to its maximum level, mirroring the EO selectivity. The CO selectivity increased with increasing applied voltage, except for the greatest voltage of 11 kV. It could be because the highest applied voltage of 11 kV generated highly energetic electrons that possibly decomposed hydrocarbons into coke and hydrogen and additionally cracked the produced CO into coke and oxygen species in the studied DBD, as follows [38,39]:

$$C_xH_y \rightarrow xC + 1/2yH_2 \qquad (24)$$

$$CO + e \rightarrow C + O + e \qquad (25)$$

Figure 2d illustrates the power consumption used to convert C_2H_6 and to yield EO as a function of applied voltage. A higher applied voltage consumed more power (data not represented here) and produced more highly energetic electrons, which led to a higher current (Fig. 2a). As a result, more electrons collided with reactant gas molecules to initiate plasma reactions, giving rise to more C_2H_6 molecules being converted and EO molecules being produced. As shown in Fig. 2d, the power consumption per C_2H_6 molecule converted increased slightly with increasing applied voltage, while the applied voltage of 7 kV exhibited the highest energy efficiency in terms of the minimum power consumption per EO molecule produced. The results showed that the applied voltage of 7 kV was optimum for the maximum EO production in the studied DBD system because of the highest EO selectivity and EO yield and lowest power consumption per EO molecule produced.

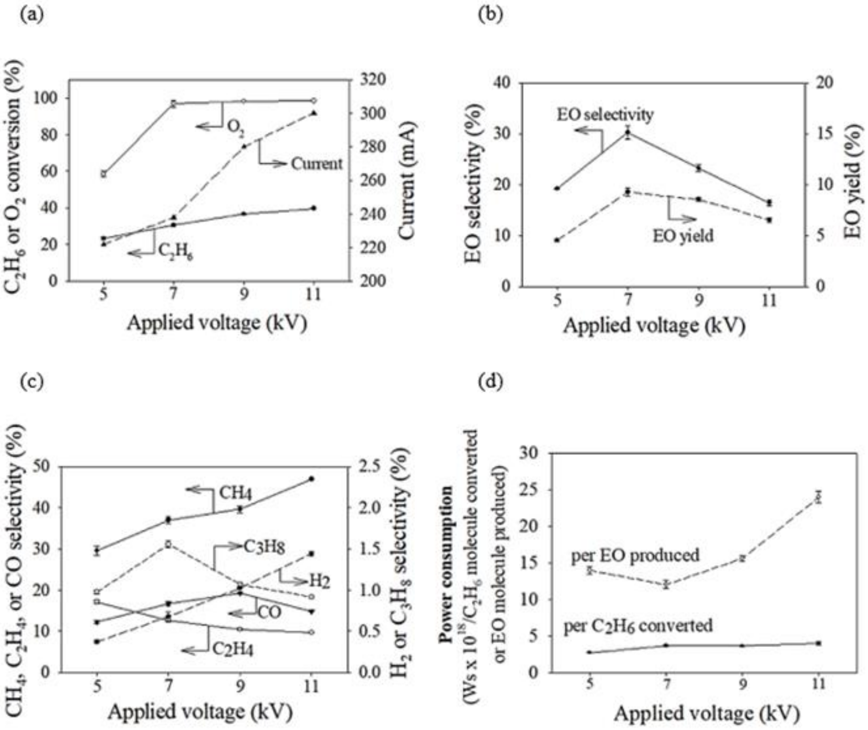

Figure 2. Effect of the applied voltage on (a) C_2H_6 and O_2 conversions and current, (b) EO selectivity and yield, (c) other product selectivities, and (d) power consumption. (Input frequency of 500 Hz, flow rate of 50 cm^3/min, and O_2/C_2H_6 feed molar ratio of 0.5:1).

Effect of the input frequency

The effect of input frequency on the plasma reaction performance was examined by changing the input frequency from 450 to 600 Hz, while the applied voltage, O_2/C_2H_6 feed molar ratio, and total feed flow rate were maintained at 7 kV, 0.5:1, and 50 cm^3/min, respectively. At input frequencies below 450 Hz, the studied plasma processes produced unreasonably low EO selectivity (less than 5%, data not shown), whereas those over 600 Hz produced unstable plasma. As shown in Fig. 3a, an increased applied voltage from 450 to 550 Hz enhanced the C_2H_6 and O_2 conversions from 13.0% and 61.1% to 32.4% and 98.2%, respectively. Afterward, they rapidly decreased with further increasing applied voltage over 550 Hz.

Both EO selectivity and yield increased with increasing input frequency and reached maximum levels at the same input frequency of 550 Hz, mirroring both C_2H_6 and O_2 conversions (Fig. 3b). As the input frequency increased from 450 to 500 Hz, the selectivities towards CH_4, C_2H_4, C_3H_8, and H_2 increased; however, as the input frequency ascended above 500 Hz, the selectivities towards these products declined (Fig. 3c). Interestingly, only the CO selectivity had a similar tendency as the current in that it decreased noticeably with increasing input frequency. The results can be attributed to an increase in current with a reduction in input frequency (Fig. 3a), which produced more excited electrons and promoted all plasma processes. The selectivities towards EO, CH_4, C_2H_4, C_3H_8, H_2, and CO dramatically increased with a decrease in input frequency from 600 Hz to 550 Hz (for EO) or 500 Hz (for the others). When the input frequency was lower than 550 Hz, more excited electrons collided with O_2 molecules, resulting in more active oxygen species and further oxidation of EO to CO (Eq. 26). At the lowest input frequency of 450 Hz, excited electrons could collide with C_2H_6 molecules to form hydrocarbons (C_2H_5, CH_3, and CH_2) and hydrogen free radicals by cracking reactions (Eqs. 16–19). Instead of producing CH_4 and C_3H_8 molecules (Eqs. (20–22), C_2H_5 free radicals could recombine to produce C_2H_6 molecules (Eq. 27), resulting in lower C_2H_6 conversions. Additionally, the CH_3 and CH_2 free radicals could combine to form C_2H_4 molecules (Eq. 28), which were then further oxidized to produce CO and H_2O (Eq. 29).

$$C_2H_4O + 3O \rightarrow 2CO + 2H_2O \qquad (26)$$

$$C_2H_5 + H \rightarrow C_2H_6 \qquad (27)$$

$$CH_3 + CH_2 \rightarrow C_2H_4 + H \qquad (28)$$

$$C_2H_4 + 4O \rightarrow 2CO + 2H_2O \qquad (29)$$

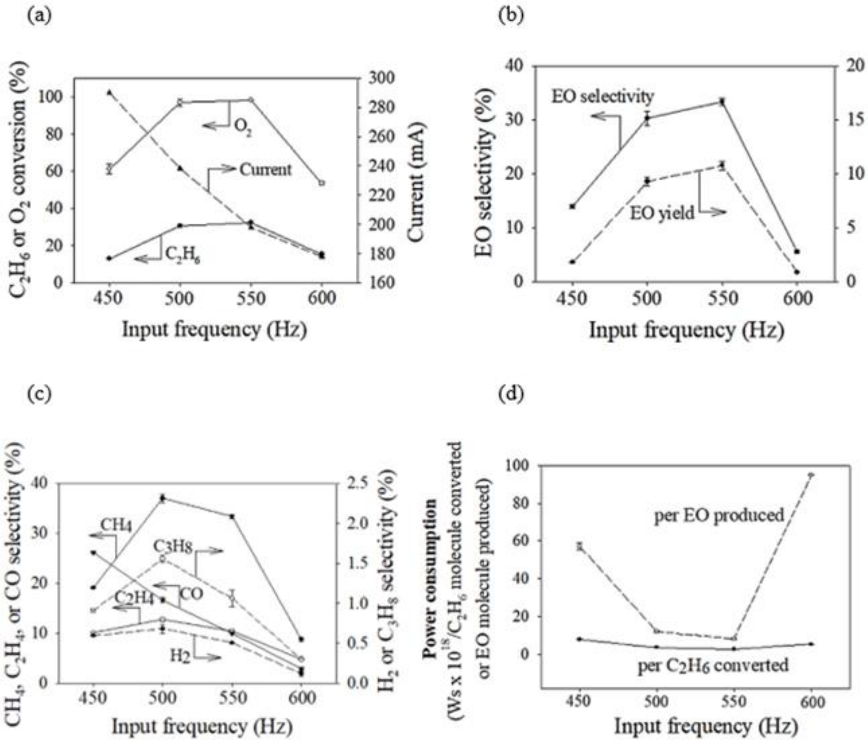

Figure 3. Effect of the input frequency on (a) C_2H_6 and O_2 conversions and current, (b) EO selectivity and yield, (c) other product selectivities, and (d) power consumption. (Applied voltage of 7 kV, flow rate of 50 cm^3/min, and O_2/C_2H_6 feed molar ratio of 0.5:1).

As shown in Fig. 3d, both the power consumption per C_2H_6 molecule converted and per EO molecule produced tend to decrease with increasing input frequency to 550 Hz, which gives the highest C_2H_6 conversion and EO selectivity. The optimal input frequency of 550 Hz was chosen for a subsequent experiment because it provided the greatest C_2H_6 and O_2 conversions, EO selectivity and yield, and lowest power consumption.

Effect of the O_2/C_2H_6 feed molar ratio

The O_2/C_2H_6 feed molar ratio has a significant influence on the process performance of the investigated DBD, as shown in Fig. 4. The O_2/C_2H_6 feed molar ratio was studied in the range of 0.5:1 to 1.25:1 under constant operating conditions, including an applied voltage of 7 kV, input frequency of 500 Hz, and flow rate of 50 cm^3/min. The C_2H_6 conversion increased significantly from 32.4 to 48.2%. The O_2 conversion increased slightly from 98.2 to 99.2% when the O_2/C_2H_6 feed molar ratio increased from 0.5:1 to 1.25:1 (Fig. 4a). The DBD system was operated in oxygen lean conditions, which resulted in low C_2H_4 conversion (32.4–48.2%) and high O_2 conversion (> 98%).

The EO selectivity and yield increased with increasing O_2/C_2H_6 feed molar ratio from 0.5:1 and reached maximum values at an O_2/C_2H_6 feed molar ratio of 1:1 (Fig. 4b). However, they adversely diminished with further increases in the O_2/C_2H_6 feed molar ratio beyond 1:1. As shown in Fig. 4c, the CH_4 selectivity increases with an increase in the O_2/C_2H_6 feed molar ratio from 0.5:1 to 1.25:1, but the C_3H_8 and CO selectivities decline. The H_2 selectivity was slightly changed in the range of 0.5–1.9%, whereas the C_2H_4 selectivity tended to decrease when the O_2/C_2H_6 feed molar ratio was 1:1. At O_2/C_2H_6 feed molar ratios beyond 1:1, the C_2H_4 selectivity was gradually enhanced. Interestingly, the C_2H_4 selectivity trended opposite to the EO selectivity. It could result from the formation of EO from C_2H_4, an intermediate in the oxidative dehydrogenation of ethane. The higher the O_2/C_2H_6 feed molar ratio is, the more oxygen species are available to initiate C_2H_6 oxidative dehydrogenation (Eq. 9) and C_2H_4 epoxidation (Eq. 10), increasing EO selectivity and yield. However, the partial and total oxidation reactions (Eqs. 11–14) were minimized as a consequence of this study's investigation of oxygen-lean settings. The coke formation, as determined by a carbon balance, tended to increase from 3.9 to 5.5% (data not shown) when the O_2/C_2H_6 feed molar ratio was enhanced from 0.5:1 to 1.25:1. The results indicated that the higher oxygen content resulted in the possibility for further EO oxidation to CO (Eq. 26), and the formed CO might break into coke and oxygen species (Eq. 25) at an O_2/C_2H_6 feed molar ratio over 1:1.

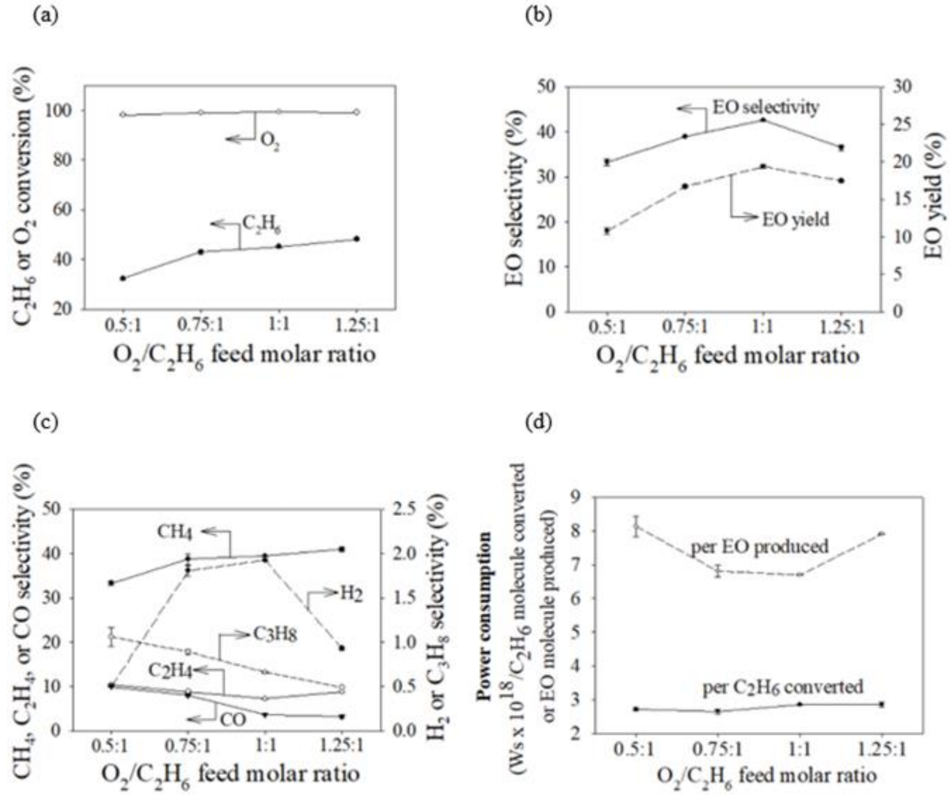

Figure 4. Effect of the O_2/C_2H_6 feed molar ratio on (a) C_2H_6 and O_2 conversions and current, (b) EO selectivity and yield, (c) other product selectivities, and (d) power consumption. *(Applied voltage of 7 kV, input frequency of 550 Hz, and flow rate of 50 cm^3/min).*

Figure 4d illustrates the power consumption required to convert C_2H_6 and to produce EO as a function of the O_2/C_2H_6 feed molar ratio. The power consumption per C_2H_6 molecule converted tended to gradually increase as the O_2/C_2H_6 feed molar ratio increased to 1.25:1. On the other hand, the power consumption per EO molecule produced decreased considerably and reached a minimum level at an O_2/C_2H_6 feed molar ratio of 1:1. From all the results, the optimum O_2/C_2H_6 feed molar ratio was 1:1 for maximizing EO production in the DBD system, which exhibited the highest EO selectivity (42.6%) and EO yield (19.4%) and lowest power consumption per EO molecule produced (6.7×10^{-18} Ws/molecule).

Comparisons of the catalyst-alone and different DBD-alone systems on the EO production performance

Ag-based catalysts loaded on various supports, such as Al_2O_3 and $SrTiO_3$, have long been known for their unique ability to selectively oxidize C_2H_4 to EO in an oxygen atmosphere. Table 1 compares three catalyst-alone and two DBD-alone systems under their optimum conditions. The Cs-Re15% Ag/α-Al_2O_3 catalyst was used in a catalyst-alone system to provide an outstanding C_2H_4 epoxidation performance regarding the EO selectivity of 83.5% [40]. Additionally, the catalyst-alone system with the following composition: 0.32% Sn, 1.39% Cu, and 17.16% Ag/$SrTiO_3$ exhibited an extremely high EO selectivity of 99.2% [41]. On the other hand, both studies reported low C_2H_4 conversions of 10.0% (for Cs-Re15% Ag) and 5.4% (for 0.32% Sn, 1.39% Cu, 17.16% Ag/$SrTiO_3$). In comparison to catalyst-alone systems, the DBD-alone system with two frosted glass plates considerably improves the C_2H_4 conversion (19.8%) and EO yield (10.9%) while maintaining a reasonably high EO selectivity (68.1%) [28]. According to the findings of this study, the DBD-alone system using a C_2H_6 reactant resulted in the highest EO yield of 19.4% and a moderately high EO selectivity of 42.6%. Interestingly, the EO selectivity, EO yield, and C_2H_6 conversion of the DBD-alone system were obviously higher than those of the catalyst-alone system using 5% Ni-Ag-O (EO selectivity of 12.8%, EO yield of 1.2%, and C_2H_6 conversion of 9.3%) [12] and NiAgYO (EO selectivity of 19.8%, EO yield of 7.6%, and C_2H_6 conversion of 38.4%) [13]. As previously indicated, when compared to the 5% Ni-Ag-O system, the DBD-alone system's ability to function at room temperature (303 K) without the use of an external heat source allowed it to reduce further oxidation to CO_x, increasing EO selectivity and yield. The lower the applied voltage in the studied DBD system, the lower the consumed power. On the other hand, the higher the input frequency is, the lower the consumed power. As a result, the DBD used in this work required less power consumption per EO produced (6.7×10^{-18} Ws/EO molecule produced, equivalent to 1.1 kWh/mole of EO) than the DBD used in the prior work (2.8×10^{-16} Ws/EO molecule produced, equivalent to 46.8 kWh/mole of EO) [28]. The EDH carried out in the cylindrical DBD using an unloaded SiO_2 catalyst [30] and the C_2H_4 epoxidation accomplished in the parallel DBD using two frosted glass plates [28] are examples of the two-step pathway. Table 1 demonstrates that the one-step approach had a higher energy efficiency (0.73 mmol/kJ) than the two-step pathway (0.13 mmol/kJ for the EDH and 0.03 for the C_2H_4 epoxidation). Interestingly, the power consumption of the one-step approach (1.1 kWh/ mole of EO) was extremely lower than that of the two-step pathway (48.0 kWh/ mole of EO). It demonstrated the benefits of the one-step technique, including its lower cost of materials (C_2H_6 vs. C_2H_4), improved energy efficiency, and lower power consumption requirements. Although the present study's results indicate reasonably high EO production performance and low power consumption, it is still necessary to increase EO selectivity. It will be done in a further study by combining a DBD system with efficient catalysts, such as Ni to enhance the possibility of C_2H_6 oxidative dehydrogenation to C_2H_4, Ag to improve the likelihood of C_2H_4 epoxidation, or Cu to decrease coke formation.

CONCLUSION

The direct conversion of C_2H_6 and O_2 to produce EO in one step at ambient temperature and atmospheric pressure was studied for the first time in a DBD reactor using two parallel frosted glass plates. The effects of different operating parameters, such as applied voltage, input frequency, and O_2/C_2H_6 feed molar ratio, on the EO synthesis performance were also investigated to attain the optimum conditions. The highest EO selectivity of 42.6%, EO yield of 19.4%, and lowest power consumption per EO molecule produced of 6.7×10^{-18} Ws/molecule were achieved at the optimum applied voltage of 7 kV, input frequency of 550 Hz, and O_2/C_2H_6 feed molar ratio of 1:1. Compared to the catalyst-alone system using an Ag catalyst, the studied DBD system was demonstrated to be a potential alternative for the direct conversion of C_2H_6 to EO, resulting in obviously higher C_2H_6 conversion, EO selectivity and yield. A DBD system in cooperation with effective catalysts should be investigated further to improve EO selectivity.

ACKNOWLEDGMENT

This research was funded by King Mongkut's University of Technology, North Bangkok (Contact no. KMUTNB-64-KNOW-24), and the Office of the Permanent Secretary, Ministry of Higher Education, Science, Research, and Innovation (Grant No. RGNS 63-087), and supported in part by the Thailand Institute of Nuclear Technology (Public Organization) to the University Program. A special thank you to Material and Process Engineering Technology (MPet), Faculty of Engineering and Technology, KMUTNB, for providing the catalyst preparation equipment.

REFERENCES

[1] H. Alzahrani, J. Bravo-Suárez, J. Catal. 418 (2023) 225–236. https://doi.org/10.1016/j.jcat.2023.01.016.

[2] G. Boskovic, D. Wolf, A. Brückner, M. Baerns, J. Catal. 224 (2004) 187–196. https://doi.org/10.1016/j.jcat.2004.02.030.

[3] A. Talati, M. Haghighi, F. Rahmani, Adv. Powder Technol. 27 (2016) 1195–1206. https://doi.org/10.1016/j.apt.2016.04.003.

[4] J.M. Hollis, F.J. Lovas, P.R. Jewell, L.H. Coudert, Astrophys. J. 571 (2002) L59. https://iopscience.iop.org/article/10.1086/341148.

[5] T. Salmi, M. Roche, J. Hernández Carucci, K. Eränen, D. Murzin, Curr. Opin. Chem. Eng. 1 (2012) 321–327. https://doi.org/10.1016/j.coche.2012.06.002.

[6] S. Dolmaseven, N. Yuksel, M.F. Fellah, Sens. Actuators, A 350 (2023) 114109. https://doi.org/10.1016/j.sna.2022.114109.

[7] T. Pu, H. Tian, M.E. Ford, S. Rangarajan, I.E. Wachs, ACS Catal. 9 (2019) 10727–10750. https://doi.org/10.1021/acscatal.9b03443.

[8] W. Diao, C.D. DiGiulio, M.T. Schaal, S. Ma, J.R. Monnier, J. Catal. 322 (2015) 14–23. http://dx.doi.org/10.1016/j.jcat.2014.11.007.

[9] C.-J. Chen, J.W. Harris, A. Bhan, Chem. Eur. J. 24 (2018) 12405–12415. https://doi.org/10.1002/chem.201801356.

[10] A. Alamdari, R. Karimzadeh, S. Abbasizadeh, Rev. Chem. Eng. 37 (2021) 481–532. https://doi.org/10.1515/revce-2017-0109.

[11] P.H. Keijzer, J.E. van den Reijen, C.J. Keijzer, K.P. de Jong, P.E. de Jongh, J. Catal. 405 (2022) 534–544. https://doi.org/10.1016/j.jcat.2021.11.016.

[12] Y. Wu, A. Yan, Y. He, B. Wu, T. Wu, Catal. Today 158 (2010) 258–262. https://doi.org/10.1016/j.cattod.2010.03.041.

[13] J. Gao, D. Zhou, Y. Wu, T. Wu, Catal. Commun. 30 (2013) 51–55. http://dx.doi.org/10.1016/j.catcom.2012.10.023.

[14] A. Fridman, A. Gutsol, Y.I. Cho, Adv. Heat Transfer 40 (2007) 1–142. https://doi.org/10.1016/S0065-2717(07)40001-6.

[15] D. Li, V. Rohani, F. Fabry, A. Parakkulam Ramaswamy, M. Sennour, L. Fulcheri, Appl. Catal., B 261 (2020) 118228. https://doi.org/10.1016/j.apcatb.2019.118228.

[16] Y.P. Zhang, Y. Li, Y. Wang, C.J. Liu, B. Eliasson, Fuel Process. Technol. 83 (2003) 101–109. http://dx.doi.org/10.1016/S0378-3820(03)00061-4.

[17] Y. Li, C.J. Liu, B. Eliasson, Y. Wang, Energy Fuels 16 (2002) 864–870. https://doi.org/10.1021/ef0102770.

[18] B. Lee, E.S. Jo, I. Heo, T.-H. Kim, D.-W. Park, Chem. Eng. Process.179 (2022) 109070. https://doi.org/10.1016/j.cep.2022.109070.

[19] U.H. Dahiru, F. Saleem, F.T. Al-sudani, K. Zhang, A.P. Harvey, Chem. Eng. Process.178 (2022) 109035. https://doi.org/10.1016/j.cep.2022.109035.

[20] S. Li, Y. Li, X. Yu, X. Dang, X. Liu, L. Cao, J. Clean. Prod. 368 (2022) 133073. https://doi.org/10.1016/j.jclepro.2022.133073.

[21] Y. Zhang, H. Zhang, A. Zhang, P. Héroux, Z. Sun, Y. Liu, Chem. Eng. J. 458 (2023) 141406. https://doi.org/10.1016/j.cej.2023.141406.

[22] C.A. Aggelopoulos, D. Tataraki, G. Rassias, Chem. Eng. J. 347 (2018) 682–694. https://doi.org/10.1016/j.cej.2018.04.111.

[23] J. Sima, J. Wang, J. Song, X. Du, F. Lou, Y. Pan, Q. Huang, C. Lin, Q. Wang, G. Zhao, Chemosphere 317 (2023) 137815. https://doi.org/10.1016/j.chemosphere.2023.137815. http://www.ijma.info/index.php/ijma/article/view/1854.

[24] T. Sreethawong, T. Suwannabart, S. Chavadej, Plasma Chem. Plasma Process. 28 (2008) 629–642. https://doi.org/10.1007/s11090-008-9149-8.

[25] T. Suttikul, S. Yaowapong-aree, H. Sekiguchi, S. Chavadej, J. Chavadej, Chem. Eng. Process. 70 (2013) 222–232. https://doi.org/10.1016/j.cep.2013.03.018.

[26] T. Suttikul, B. Paosombat, M. Santikunaporn, M. Leethochawalit, S. Chavadej, Ind. Eng. Chem. 53 (2014) 3778–3786. https://doi.org/10.1021/ie402659c.

[27] T. Suttikul, S. Kodama, H. Sekiguchi, S. Chavadej, Plasma Chem. Plasma Process. 34 (2014) 187–205. https://doi.org/10.1007/s11090-013-9492-2.

[28] S. Chavadej, W. Dulyalaksananon, T. Suttikul, Chem. Eng. Process.107 (2016) 127–137. http://dx.doi.org/10.1016/j.cep.2016.05.010.

[29] X. Zhang, A. Zhu, X. Li, W. Gong, Catal. Today 89 (2004) 97–102. https://doi.org/10.1016/j.cattod.2003.11.015.

[30] F. Cameli, P. Dimitrakellis, G.D. Stefanidis, D.G. Vlachos, Plasma Chem. Plasma Process. (2023). https://doi.org/10.1007/s11090-023-10343-w.

[31] T. Suttikul, C. Tongurai, H. Sekiguchi, S. Chavadej, Plasma Chem. Plasma Process. 32 (2012) 1169–1188. https://doi.org/10.1007/s11090-012-9398-4.

[32] C. Liu, A. Marafee, B. Hill, G. Xu, R. Mallinson, L. Lobban, Ind. Eng. Chem. 35 (1996) 3295–3301. https://doi.org/10.1021/ie960138j.

[33] B.L. Farrell, V.O. Igenegbai, S. Linic, ACS Catal. 6 (2016) 4340–4346. https://doi.org/10.1021/acscatal.6b01087.

[34] A.V. da Rosa, J.C. Ordóñez, Fundamentals of Renewable Energy Processes, Academic Press, Oxford (2022), pp. 425. https://doi.org/10.1016/B978-0-12-816036-7.00021-X.

[35] J.J. Zou, C.J. Liu, Carbon Dioxide as Chemical Feedstock, M. A. Editor Ed., Wiley-VCH, Weinheim (2010), pp. 274–279. https://doi.org/10.1002/9783527629916.ch10.

[36] R. Sanchez-Gonzalez, Y. Kim, L.A. Rosocha, S. Abbate, IEEE Trans. Plasma Sci. 35 (2007) 1669–1676. https://doi.org/10.1109/TPS.2007.910743.

[37] Y. Li, G.-h. Xu, C.-j. Liu, B. Eliasson, B.-z. Xue, Energy Fuels 15 (2001) 299–302. http://dx.doi.org/10.1021/ef0002445.

[38] S. Ahmed, A. Aitani, F. Rahman, A. Al-Dawood, F. Al-Muhaish, Appl. Catal. A: Gen 359 (2009) 1–24. https://doi.org/10.1016/j.apcata.2009.02.038.

[39] C. De Bie, J. Van Dijk, A. Bogaerts, J. Phys. Chem. C. 120 (2016) 25210–25224. https://doi.org/10.1021/acs.jpcc.6b07639.

[40] D. Ren, G. Cheng, J. Li, J. Li, W. Dai, X. Sun, D. Cheng, Catal. Lett. 147 (2017) 2920–2928. https://doi.org/10.1007/s10562-017-2211-5.

[41] A. Chongterdtoonskul, J.W. Schwank, S. Chavadej, J. Mol. Catal. 372 (2013) 175–182. http://dx.doi.org/10.1016/j.molcata.2013.02.016.

THITIPORN SUTTIKUL[1,2]
SIRIMAS MANTHUNG[1]
SASIKARN NUCHDANG[3]
DUSSADEE RATTANAPHRA[3]
THONGCHAI PHOTSATHIAN[4]

[1]Division of Chemical Process Engineering Technology, Faculty of Engineering and Technology, King Mongkut's University of Technology North Bangkok, Rayong, Thailand

[2]The Plasma and Automatic Electric Technology Research Group, King Mongkut's University of Technology North Bangkok, Rayong, Thailand

[3]Research and Development Division, Thailand Institute of Nuclear Technology, Pathum Thani, Thailand

[4]Division of Instrumentation and Automation Engineering Technology, Faculty of Engineering and Technology, King Mongkut's University of Technology North Bangkok, Rayong, Thailand

NAUČNI RAD

JEDNOSTEPENA KONVERZIJA ETANA U ETILEN-OKSID U DIELEKTRIČNOM BARIJERNOM PRAZNJENJU PARALELNIH PLOČA

U ovom radu je proučavana konverzija etana (C_2H_6) u etilen oksid (EO) u jednom koraku u sistemu dielektričnog barijernog pražnjenja (DBP) sa dve paralelne mat staklene ploče na temperaturi okoline i atmosferskom pritisku. EO se direktno proizvodi iz etana u jednom koraku bez potrebe za odvajanjem i recikliranjem etilena. Ispitivani su efekti primenjenog napona, ulazne frekvencije i molskog odnosa O_2/C_2H_6 napojne smeše na performanse sinteze EO. Rezultati su pokazali da su veći primenjeni napon i niža ulazna frekvencija generisali više energetskih elektrona, što je rezultiralo većom strujom. Više elektrona se sudarilo sa molekulima gasa reaktanta da bi pokrenuli plazma reakcije, povećavajući konverzije C_2H_6 i O_2. Povećani molski odnos O_2/C_2H_6 dovode poboljšao je konverziju C_2H_6 i O_2. Utvrđeno je da su optimalni uslovi primenjeni napon od 7 kV, ulazna frekvencija od 550 Hz i molski odnos O_2/C_2H_6 od 1:1, koji je pokazao najveću selektivnost EO (42,6%), prinos EO (19,4%), i najmanja potrošnja energije po proizvedenom EO ($6,7 \times 10^{-18}$ Ws/molekul).

Ključne reči: dielektrično barijerno pražnjenje, epoksidacija, oksidativna dehidrogenacija etilen oksida, jednostepena reakcija.

CI&CEQ
Chemical Industry & Chemical Engineering Quarterly

Available online at
Association of the Chemical Engineers of Serbia *AChE*
www.ache.org.rs/CICEQ

Chem. Ind. Chem. Eng. Q. 30 (3) 243−256 (2024) CI&CEQ

RADMILA MILENKOVSKA[1]
NIKOLA GESKOVSKI[1]
PETRE MAKRESKI[2]
ANITA GROZDANOV[3]
EMIL POPOVSKI[2]
GJORGJI PETRUSHEVSKI[2,4]
MAJA SIMONOSKA CRCAREVSKA[1]
KRISTINA MLADENOVSKA[1]

[1]Faculty of Pharmacy, Ss. Cyril and Methodius University in Skopje, Skopje, Republic of N Macedonia

[2]Institute of Chemistry, Faculty of Natural Sciences and Mathematics, Ss. Cyril and Methodius University in Skopje, Skopje, Republic of N Macedonia

[3]Faculty of Technology and Metallurgy, Ss. Cyril and Methodius University in Skopje, Skopje, Republic of N Macedonia

[4]Alkaloid AD Skopje, Skopje, Republic of N Macedonia

SCIENTIFIC PAPER

UDC 66.097.3:546.26:54.03

FUNCTIONALIZED CARBON NANOSTRUCTURES AS TEMOZOLOMIDE CARRIERS: PHYSICOCHEMICAL AND BIOPHARMACEUTICAL CHARACTERIZATION

Article Highlights

- Oxidized and noncovalent PEGylated MWCNTs and MWCNTs-G are used as Temozolomide (TMZ) carriers
- Physicochemical characterization confirmed the PEGylation and drug loading in the nanocarriers
- Relatively high encapsulation efficacy and TMZ loading in the carbon nanostructures
- Particle size distribution and zeta potential values suitable for brain tumor delivery
- Sustained TMZ release was observed *in vitro,* indicating controlled drug release in brain tumors

Abstract

In this study, temozolomide (TMZ), a drug used in the treatment of anaplastic astrocytoma and glioblastoma multiforme, was incorporated in multiwalled carbon nanotubes (MWCNTs) and hybrid carbon nanotubes with graphene (MWCNTs-G) functionalized by polyethylene glycol (PEG). The aim was to evaluate the potential of these nanocarriers for targeted delivery and sustained release of TMZ in brain tumor cells. Oxidized MWCNTs and MWCNTs-G were noncovalently functionalized with PEGs of different molecular weights and subsequently loaded with TMZ following standard procedures. Thorough physicochemical and biopharmaceutical characterization of the TMZ-loaded carbon nanocarriers pointed to high encapsulation efficacy (up to 67%) and drug loading (up to 18% out of 25% theoretical value) and homogeneous particle size distribution, with z-average (160 to 300 nm) and zeta potential (-31 to -21 mV) of the particles adequate for crossing the blood-brain-tumor-barrier (BBTB) and entering into the tumor cells. Successful functionalization and TMZ loading were confirmed by SEM and TEM images, UV-Vis absorption, infrared and Raman spectroscopy, and TGA analyses. Sustained release of TMZ from the carbon nanocarriers was observed in vitro. The presented findings form a fundamental platform for further investigation of these formulations against different types of glioma cells and in adequate animal models.

Keywords: multiwalled carbon nanotube, graphene, polyethylene glycol, Temozolomide, physicochemical properties, sustained release.

The limited bioavailability and intrinsic toxicity of many drug substances drive the pharmaceutical industry towards the design and development of novel drug carriers, with a capacity to improve the physicochemical properties of the drugs and overcome the physiological, biochemical, and chemical barriers in their delivery at the site of action. Among them are carbon nanostructures such as graphene, a single layer of carbon below and above the plane, packed tightly into a hexagonal, honeycomb structure, and carbon nanotubes (CNTs) in the form of elongated enfolded graphene sheets such as single-wall (SWCNTs) and multiple layers of graphene sheets,

---

Correspondence: K. Mladenovska, Faculty of Pharmacy, Ss. Cyril and Methodius University in Skopje, Blv. Mother Theresa No. 45, 1000 Skopje, Republic of N Macedonia.
E-mail: krml@ff.ukim.edu.mk
Paper received: 5 May, 2023
Paper revised: 25 September, 2023
Paper accepted: 23 November, 2023

https://doi.org/10.2298/CICEQ230505027M

namely multiple-wall carbon nanotubes (MWCNTs) [1]. These carbon materials' excellent mechanical, physical, and chemical properties have made them promising blocks for synthesizing graphene-carbon nanotube hybrid structures (MWCNTs-G). The distinct structural properties of these carbon nanostructures, in particular, nanoscale structure and high aspect ratio, are an appropriate addition to their stability, high adsorption capacity, and suitability for functional modification, making them useful carriers for site-specific and controlled drug delivery. The internal cavities of the nanotubes provided high loading capacity for several therapeutic agents, including anticancer drugs [2,3], proteins [4], gene delivery and gene therapy [5–7], and a wide range of bioactive molecules were also covalently or noncovalently immobilized on the external surface of CNTs for specific targeting [8–10]. Furthermore, the tubular shape of CNTs enables them to better penetrate cell membranes through both receptor-mediated or adsorptive-mediated energy-dependent pathways (transcytosis) and passive energy-independent mechanisms (needle-like crossing) without causing cell changes and death, which is a major advantage compared to other nanocarriers [11].

Due to the oxidation of these carbon nanostructures, carboxylic groups become attached in the presence of concentrated acids, contributing to higher hydrophilicity and biocompatibility [12]. Oxidized nanostructures can be further coated to make them more stable and dispersible in various biological solutions, including serum. When coated with (poly)ethylene glycol (PEG), the dispersion gets extraordinary due to the irreversible adsorption of PEG molecules to the sidewalls of carbon structures through π-stacking, van der Waals, and hydrophobic interactions. In addition, PEG functionalization allows surprisingly high degrees of π-stacking of aromatic molecules, including drugs and combinations of molecules. PEGylated carbon nanostructures display relatively lower cytotoxicity and longer blood circulation half-life, which increases the chance of reaching the cancerous or tumorous tissues/cells and also impedes *in vivo* opsonization and reduces uptake by the reticuloendothelial system (RES). In addition, PEG is resilient under oxidizing and reducing conditions and is sufficiently stable against decomposition induced by acids and bases [13].

Having all these in regard, in the presented study (PEGylated), MWCNTs and MWCNT-G have been prepared as carriers of Temozolomide (TMZ), and their suitability for targeted and controlled delivery at the site of action has been evaluated by physicochemical and biopharmaceutical characterization. TMZ is an imidazotetrazine second-generation alkylating agent with a schedule-dependent anti-tumor activity against highly resistant malignancies, including high-grade malignant gliomas such as glioblastoma multiforme (GBM). GBM is among the most aggressive types of brain tumors, with rapid proliferation, diffuse brain invasion, as well as tumor-induced brain edema and neurodegeneration as pathological hallmarks. TMZ, as a prodrug, crosses the blood-brain barrier (BBB) and is converted *via* hydrolysis under physiological conditions in the active cytotoxic form of 5-(3-methyl-triazen-1-yl) imidazole-4-carboxamide (MTIC) that subsequently methylates DNA in the O^6 position of guanine residues. Considering that MTIC does not cross BBB and exhibits low cell availability, it is paramount to prolong the half-life of TMZ under physiological conditions and promote a greater accumulation at the GBM site prior to degradation in the bloodstream. In this way, the drug would be more effective and safer because lower doses could be administered to maintain the therapeutic level [14].

Several research groups investigated this approach in improving the TMZ therapeutic index by loading it in polylactide-based nanoparticles [15–17]. To our knowledge, this is the first paper in which MWCNTs and MWCNT-G hybrid are used as carriers of TMZ. In addition, carbon nanocarriers were noncovalently functionalized by PEGs of different molecular weights to prepare more soluble/dispersible drug delivery systems, with more active sites for TMZ loading, able to protect TMZ from degradation in the peripheral tissues, prolong its blood circulation half-life and provide greater accumulation in the region of GBM. One also expects that the resemblance of CNTs to specific neuronal structures (e.g., ion channels, signaling proteins, and elements of the neuronal cytoskeleton), as well as electrically conductive capacity and strong mechanical properties, may have an additional benefit to the established aim, with regard to enhancing neuronal interaction at the molecular level, improving the management of the physiological activity of neurons and processing of neuronal information [18].

MATERIALS AND METHODS

Materials

As carriers of TMZ, MWCNTs-COOH (purity > 95 wt.%, number of walls > 2, length 10-30 µm, outer diameter 30-50 nm, -COOH content 0.7 wt%, zeta potential -38*mV*, average size 136±20nm) were purchased from Sisco Research Laboratories Pvt, Ltd, India, while the MWCNTs-G hybrid (purity > 99 wt.%, length < 10 µm, inner diameter < 30 nm, outer diameter 30-100 nm, wall thickness 1-2 nm, zeta potential -29 mV, 810± 42 nm average size) from Incubation

Alliance, Inc., Japan. The MWCNTs-COOH and MWCNTs-G (previously activated to MWCNTs-G-COOH) were noncovalently functionalized by polyethylene glycol (PEGOH(C_2H_4O)n H) of different molecular weights (Mw): average Mw 1400–1600 g/mol, Mn/Mw ~ 1.1 (PEG1500), average Mw 3500–4500 g/mol, Mn/Mw ~ 1.1 (PEG4000) and average Mw 5000–7000 g/mol, Mn/Mw ~ 1.1 (PEG6000), all purchased from Merck Schuchardt OHG, Germany. For the functionalization procedure of the carbon nanostructures, 98% H_2SO_4 and 65% HNO_3 were used, both purchased from Carlo Erba Reagents S.A.S., Italy. TMZ was supplied by Sigma-Aldrich (Saint Louis, USA) and Polysorbate® 80 (Sigma-Aldrich, Poole, UK). All chemicals were of analytical grade.

Methods

Functionalization of carbon nanostructures

In the first step, the MWCNTs-G hybrid was oxidized by a modified procedure described by Zhang *et al.* [4], Zhao *et al.* [12], and Huang *et al.* [19] in which 1 g of MWCNTs-G was added to 400 mL of a mixture of 98% H_2SO_4 and 65% HNO_3 (v/v=3:1) initially equipping with ultrasound for 8 h, with subsequent vigorous stirring at 80 °C for another 8 h. The resulting product was separated by centrifugation (3000 rpm, Eppendorf, MiniSpin, Germany), and the sediment was thoroughly and repeatedly washed with deionized water until it reached neutral pH. Afterward, the oxidized MWCNTs-G (MWCNTs-G-COOH) were dried in an air dryer at 50 °C (ST-01/02, Instrumentaria Zagreb, Croatia).

For noncovalent PEGylation, cut and activated MWCNTs-G-COOH and commercially purchased MWCNTs-COOH, each per 20 mg, were dispersed in ultrapure water (200 mL) and pre-sonicated in an ultrasonic bath for 60 min (Ultrasons-H, J. P. Selecta s.a., Spain). Aqueous solutions of PEG1500, PEG4000, and PEG6000 (3 mg/mL, 20 mL) were added drop-wise into the suspensions accordingly while keeping sonication for another 10 min and then magnetically stirring for 24 h at room temperature (250 rpm, VARIO MAG Multipoint, USA). The samples were collected by centrifugation at 12 000 rpm for 15 min (Eppendorf, MiniSpin, Germany), washed five times with deionized water, and dried overnight under vacuum [20].

Temozolomide loading in PEGylated carbon nanostructures

To 10 mL acidified aqueous solution of TMZ (1 mg/mL, pH 2), 30 mg PEGylated carbon nanostructures were added. The dispersion was sonicated for two hours (Ultrawave Limited, Cardiff, UK) and then magnetically stirred for three days (250 rpm) at room temperature (VARIO MAG Multipoint, USA). Afterward, the drug-loaded carbon nanostructures (MCWNTs-PEG-TMZ and MWCNTs-G-PEG-TMZ) were isolated by centrifugation (12000 rpm, 15 min; Eppendorf, MiniSpin, Germany), washed with double-distilled water and left in air dryer (ST-01/02, Instrumentaria Zagreb, Croatia) at 37 °C during 72 h. For comparison, TMZ was also loaded in non-PEGylated carbon nanostructures, MWCNTs-TMZ and MWCNTs-G-TMZ, using the same procedure.

Biopharmaceutical characterization of Temozolomide loaded PEGylated carbon nanostructures

Drug loading efficacy and content

In all formulations, the efficacy of TMZ loading was determined as described in Eq. (1). The concentration of TMZ in the supernatant (nonencapsulated TMZ) was determined by UV-Vis absorption spectroscopy at λ_{max} 328 nm (UV/VIS Perkin Elmer Lambda 16, Arizona, USA).

$$\text{Drug loading efficacy}(\%) = \frac{total\ \ TMZ(mg) - nonencapsulated\ \ TMZ(mg)}{total\ \ TMZ(mg)} \cdot 100\% \qquad (1)$$

The content of TMZ in the carbon nanostructures was determined using Eq. (2).

$$TMZ\ \ content(\%) = \frac{encapsulated\ \ TMZ(mg)}{\text{mass of loaded } MWCNT\ \ formulation(mg)} \cdot 100\% \qquad (2)$$

All data were averaged from five measurements at least.

Size distribution and surface charge

The hydrodynamic diameter (z-average), polydispersity index (PDI), and zeta potential of blank and TMZ-loaded carbon nanostructures were determined by dynamic light scattering (NanoZS-100, Malvern Instruments Ltd., Worcestershire, UK) in the wet dispersions. The wet dispersions were prepared by dispersing the formulations (5–10 mg) in phosphate buffer saline (PBS) 0.0001M, by Ultra-turrax (T25 basic, IKA Werke, Cardiff, UK) for 1 min (13500 rpm). A small aliquot of the resulting suspension was transferred to the measurement cell. At least six measurements were done for each sample.

Morphology

The morphology of blank and TMZ-loaded carbon nanostructures was visualized by scanning electron microscopy (SEM, FEI Quanta 200, acceleration voltage 30 kV with EDS Oxford Inca Energy 350, equipped with a secondary electron detector, UK) and Transmission Electron Microscope (TEM–FEI Tecnai G2 Spirit TWIN equipped with LaB6, UK).

In vitro dissolution test

The release of TMZ from TMZ loaded (non)-PEGylated carbon nanostructures was followed *in vitro*, using the dialysis bag diffusion technique (dialysis membrane Mw cut-off 12000, Sigma-Aldrich, USA). Hermetically sealed formulations (~ 30 mg) were suspended in 50 mL PBS pH 7.4. The experimental temperature was kept at 37 ± 0.5 °C, with continuous magnetic stirring at 100 rpm. At selected time intervals up to 216 h, the drug sample was removed from the receptor compartment with the replacement of the same medium. The concentration of released TMZ was quantified by measuring the concentration of formed active hydrolytic product MTIC at pH 7.4 and 37 °C using UV-Vis absorption spectroscopy (λ_{max} 255 nm, UV/VIS Perkin Elmer Lambda 16, Arizona, USA) [15]. All data were averaged from three measurements.

Physicochemical characterization of Temozolomide loaded PEGylated carbon nanostructures

For physicochemical characterization of TMZ loaded (non)-PEGylated nanostructures with respect to interactions and stability during the preparation procedure, the formulations were characterized using infrared (IR), ultraviolet-visible (UV-Vis), and Raman spectroscopy and thermogravimetric analysis (TGA) as well.

Infrared spectroscopy

Infrared measurements were performed on blank and TMZ-loaded (non)-PEGylated carbon nanocarriers (2 mg of homogenized samples) using KBr pellets (200 mg dry potassium bromide per pellet). The characteristic absorption bands were recorded in a 4000–400 cm^{-1} wavenumbers range (Varian-660 FT-IR, Agilent Technologies, USA).

Ultraviolet-visible spectroscopy

UV-Vis absorption spectra of all samples were collected in a quartz cell with a 1.0 cm path length using a UV/Vis Perkin Elmer Lambda 16 (Arizona, USA) spectrophotometer.

Raman spectroscopy

Raman spectra were collected on a LabRam 300 Infinity micro-Raman multichannel spectrometer (Horiba JobinYvon, Japan) using the He:Ne laser at 632.81 nm. An 1800 lines/mm grating monochromator received the backscattered radiation (180° configuration). Raman intensities were collected with a thermo-electrically cooled CCD. An Olympus LMPlanFL ×50 objective (N.A = 0.5) with a long working distance (10.6 mm) was used for magnification. A LaserCheckTM Handheld Power Meter (Coherent Scientific, Australia) was used to measure the laser power on the samples, which was 1.82 mW. The spectral collection time was set to 5 seconds, and the spectrum averaged from 5 scans. For calibration purposes, the Rayleigh line at 0 cm^{-1} and the band of a Si standard centered at 520.5 cm^{-1} were used.

Thermogravimetric analysis

The TGA experiment on the same samples (7-10 mg per sample) was performed with a model Pyris 1 TGA (PerkinElmer, Shelton, CT, USA), under nitrogen atmosphere, at a heating rate of 10 °C/min in a temperature range of 30–800 °C.

RESULTS AND DISCUSSION

Biopharmaceutical characterization of Temozolomide loaded PEGylated carbon nanostructures

Loading efficacy, drug content, surface charge, and particle size distribution

The drug loading efficacy and content in all series (Table 1) ranged from 54% to 67% and 14% to 18% (out of 25% theoretical value), respectively, being highest in the MWCNTs-TMZ. Higher values for TMZ loading efficacy and content were obtained for non-PEGylated MWCTs-TMZ and MWCNTs-G-TMZ formulations relative to the adequate PEGylated formulations ($p < 0.05$). The MWCNTs-(PEG-)TMZ formulations demonstrated better TMZ loading capability relative to the hybrid MWCNTs-G-(PEG-)TMZ formulations ($p < 0.05$), while non-significant differences were observed among the PEGylated formulations, both MWCNTs-PEG-TMZ and MWCNTs-G-PEG-TMZ ($p > 0.05$). These data suggest dominantly physical entrapment of TMZ into the tubes, although wrapping around the tubes cannot be excluded. Taking into consideration the medium in which TMZ loading was performed, there could be a possibility for electrostatic interactions and hydrogen bonding from the proton of the carboxyl group in the MWCNTs-COOH/MWCNTs-G-COOH and hydroxyl group in the MWCNTs-PEG/MWCNTs-G-PEG with nitrogen atoms at positions 1, 2 and 7 and oxygen atoms at position 4 and from the amide group in the structure of TMZ (3-methyl-4-oxoimidazo[5,1-d][1,2,3,5]tetrazine-8-carboxamide). In addition, a competition between PEG and TMZ, regarding the entrapment into and the wrapping around the carbon nanostructures, cannot be excluded, despite the observed non-significant influence of a PEG molecular weight on TMZ loading. The slightly higher values for the drug loading observed in MWCNTs formulations, compared to hybrid MWCNTs-G, can be explained by the lower content of MWCNTs in MWCNTs-G hybrid in which TMZ is dominantly entrapped, also evident by the SEM images (Fig. 1d, e, f).

Table 1. Loading efficacy and content, particle size distribution, and zeta potential of blank and TMZ-loaded activated and PEGylated carbon nanostructures.

Series	Parameters			
	Loading efficacy (± SD, n=6) %	Content (± SD, n=6) % (theor. 25%)	d_{50}/PDI (nm)	Zeta potential (±SD, n=6) *mV*
MWCNTs (-COOH)	/	/	136/0.460	-38.38 ± 0.85
MWCNTs-PEG1500	/	/	185/0.443	-20.73 ± 1.33
MWCNTs-PEG4000	/	/	188/0.422	-21.51 ± 0.75
MWCNTs-PEG6000	/	/	192/0.437	-22.32 ± 1.31
MWCNTs-TMZ	66.96 ± 0.60	17.94 ± 0.60	163/0.385	-27.45 ± 1.37
MWCNTs-PEG1500-TMZ	56.79 ± 5.36	16.63 ± 0.62	201/0.466	-21.25 ± 0.21
MWCNTs-PEG4000-TMZ	56.44 ± 4.71	16.49 ± 0.41	236/0.429	-22.05 ± 0.64
MWCNTs-PEG6000-TMZ	55.41 ± 2.97	15.96 ± 1.29	248/0.301	-24.70 ± 1.33
MWCNTs-G (-COOH)	/	/	222/0.406	-46.05 ± 1.15
MWCNTs-G-PEG1500	/	/	248/0.481	-24.87 ± 0.58
MWCNTs-G-PEG4000	/	/	260/0.321	-24.09 ± 1.56
MWCNTs-G-PEG6000	/	/	276/0.392	-23.24 ± 0.42
MWCNTs-G-TMZ	58.20 ± 1.60	16.11 ± 0.45	255/0.479	-31.23 ± 2.02
MWCNTs-G-PEG1500-TMZ	58.64 ± 4.83	14.99 ± 1.29	264/0.485	-25.25 ± 0.91
MWCNTs-G-PEG4000-TMZ	56.98 ± 3.07	14.58 ± 0.43	278/0.385	-25.90 ± 0.83
MWCNTs-G-PEG6000-TMZ	54.97 ± 6.13	14.40 ± 1.25	303/0.372	-25.95 ± 0.55

The zeta potential in physiologically relevant pH was determined (Table 1) to examine the surface properties of the carbon nanocarriers. The commercially activated MWCNTs-COOH had a zeta potential of around -38 mV, while the negative zeta potential of approx. -26 mV for MWCNTs-G increased to approx. -46 mV due to COO^- groups on the surface of the functionalized MWCNTs-G-COOH carbon nanocarriers. The PEG functionalization of the carbon nanocarriers led to decreased zeta potential, most likely due to the capping of the surface-oriented -COOH groups. When TMZ was loaded in the non-PEGylated carbon nanocarriers, the zeta potential also decreased, probably due to the electrostatic interactions between the carbon carriers and TMZ and the location of TMZ into/on the carriers. A similar trend was not observed for the PEG functionalized carbon nanocarriers (Table 1), as the neutral PEG chains had already covered the carboxyl groups. Moreover, a non-significant difference in zeta potential between all PEGylated series was observed, thus implying the PEG dominance on the surface properties of the functionalized nanocarriers. Furthermore, loaded PEGylated carbon nanocarriers showed significantly lower negative zeta potential value compared to TMZ-loaded non-PEGylated carriers (Table 1), which confirms the effective PEG capping of the carboxylic end groups from the carbon nanocarriers.

These results correspond with the literature data on TMZ loaded in transferrin-appended PEGylated PLGA nanoparticles [21]. It is well-known that PEG's protective (stealth) action in the PEGylated nanoparticles is mainly due to the formation of a dense, hydrophilic cloud of flexible chains on the surface of the particles that reduces the hydrophobic interaction with the RES. Therefore, tethered and anchored PEG chains on the TMZ-loaded carbon nanostructures could prevent the opsonization of the particles by the RES macrophages, leading to a prolonged circulation time of the particles in the blood and preferential accumulation in the brain tumor cells.

Various literature data exist on the influence of the particle's surface charge on their internalization into the tumor cells. The surfaces of cancer cells are negatively charged due to the translocation of negatively charged constituents from the inner envelope of the cell membrane. However, in the intracellular space, a low pH prevails (around 5.7–7.4), depending on the tumor's histology, volume, and location [22]. Electrostatic interactions mediate the uptake of nanoparticles into the central nervous system (CNS) between positively charged ligands and negatively charged membranes of the BBB cells. Having this in regard, positively charged particles have an advantage in drug delivery across the BBB. They bind to anionic sites on the luminal surface of brain capillaries (derived from sialic acid residues of glycoproteins) and undergo absorptive-mediated endocytosis [23]. However, the presence of positively charged groups on their surface may increase non-specific uptake and reduce the efficiency of targeted delivery into the CNS due to binding to negatively charged plasma proteins. The advantage of particles with neutral and negative zeta potential is the lower adsorption of proteins on their surface in the circulation, as well as the lower ability to accumulate in the liver and spleen compared to positively charged nanoparticles [24]. Accordingly, during the distribution in the central circulation, the particles should have a negative or neutral zeta potential, while at the point of passage through the BBB, particles with a positive charge have an advantage. The different pH values in the blood circulation and healthy cells compared to tumor cells give the possibility to change the surface charge of the particles at the site of internalization, which was shown in a study with carbon nanotubes loaded with zwitterionic doxorubicin [25]. Hence, for effective delivery of nanoparticles into the tumor cells, a neutral or weakly negative charge upon i.v. application and a change in positive charge upon arrival at the tumor site are desired. Most nanoparticle formulations in the literature for brain delivery have moderately negative (between -1 mV and -15 mV) or high (between 15 mV and 45 mV) negative potential. It is also mentioned that formulations with moderate (up to 15 mV) or high positive zeta potential (above 15 mV) can pass through the BBB and, in some instances, have been proven to be effective delivery systems in the brain. Based on these literature data, the surface charge of the prepared carbon nanoformulations with TMZ suggests the potential for their delivery into the brain, that is, for treating brain tumors [26].

The z-average size of the activated MWCNTs-COOH and MWCNTs-G-COOH increased from around 136 nm and 222 nm to 163 nm and 255 nm, respectively, when TMZ was loaded (Table 1). After the PEG coating, the initial particle size also increased, being the highest in the formulations coated with PEG6000 (around 192 nm and 276 nm, respectively). When TMZ was loaded, an additional non-significant increase was evident, with the z-average between 201 nm (MWCNs-PEG1500-TMZ) and 303 nm (MWCNTs-G-PEG6000-TMZ). In all PEGylated series with TMZ, a relatively unimodal particle size distribution was observed, with PDI values not exceeding 0.485.

The size of the particles significantly affects their *in vivo* behavior and distribution. Larger size nanoparticles have a greater tendency after i.v. application to be trapped by the lungs, while the smaller ones to be eliminated through the kidneys. Also, particles larger than 200 nm tend to activate the lymphatic system and be more quickly removed from the circulation [27]. The particle size also affects the permeability across the BBTB. Compared to blood-tumor barriers, BBTB is characterized by smaller pores, indicating that larger delivery systems will have difficulty entering the brain tumor. For most of the particles intended for brain (tumor) delivery, a median size of 200 nm is commonly reported [28], a statistical value indicating a range from 50 to 400 nm. The size distribution of the TMZ-loaded formulations in the current study did not exceed these limits, pointing to their potential for crossing the BBTB. However, although most studies note greater anti-tumor efficacy of shorter CNTs [29], there are also literature data indicating that the cellular accumulation of CNTs is independent of length/size (studies with length distribution of SWCNTs and MWCNTs between 195 nm and 630 nm) [30]. Our data are very similar to the data obtained in the study of Ren *et al.* [31] in which dual-functionalized MWCNTs subsequently loaded with doxorubicin, with size between 147 and 202 nm (and zeta potential between -8 mV and -29 mV) were able to cross the BB(T)B and accumulate into the brain tumor cells *in vitro* in BCEC and C6 cells and *in vivo* in intracranial C6 glioma bearing Balb/c mice.

Morphology

The surface morphology of the TMZ loaded and unloaded PEGylated MWCNTs and MWCNTs-G hybrid was studied using SEM and TEM imaging (Fig. 1).

The SEM image of MWCNTs-COOH (Fig. 1a) shows a dense structure comprised of randomly aggregated highly tangled tubes. In the SEM and TEM images of MWCNTs-TMZ (Figs. 1b and 1h, respectively), the entrapment of TMZ into the tubes and its presence on the MWCNTs surface can be seen. The functionalization of the MWCNTs with PEG in the MWCNTs-PEG-TMZ was also confirmed by the non-uniform surface, which can be seen from the SEM and TEM images (Figs. 1c and 1i, respectively).

No clear distinction in the morphology between TMZ-loaded and non-loaded MWCNTs-PEG was observed with the imaging techniques. In the images of the MWCNTs-G hybrid (Fig. 1d–f), one can see that the MWCNTs are incorporated into the graphene layers, while the surface morphology exhibits a mixed structure with MWCNTs dispersed between different graphene sheets due to the interactions between the hydrophobic region of graphene and the side walls of MWCNTs. In Fig. 1h and 1i, bulging from the loaded TMZ and surface roughness can be seen due to the functionalization with PEG.

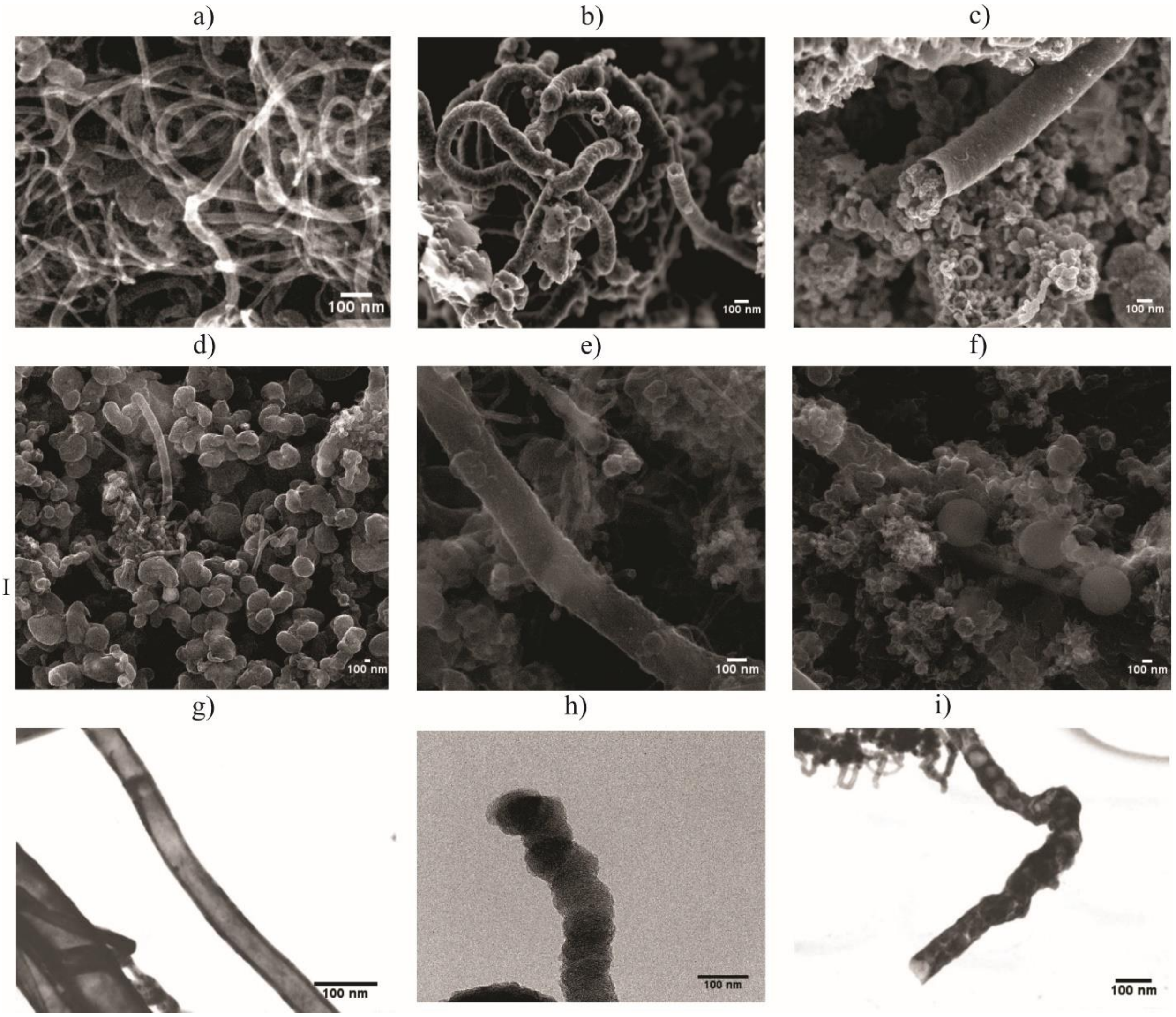

Figure 1. SEM images of (a) MWCNTs-COOH; (b) MWCNTs-TMZ; (c) MWCNTs-PEG-TMZ (x 50.000 mag.); (d) MWCNTs-G-COOH; (e) MWCNTs-G-TMZ; (f) MWCNTs-G-PEG-TMZ; the scale bar presents 100 nm and TEM images showing (g) MWCNTs-COOH; (h) MWCNTs-TMZ; (i) MWCNTs-PEG6000-TMZ.

In vitro drug release

Metabolic remodeling with increased glucose uptake compared to normal brain cells is a characteristic feature of glioblastoma. To sustain tumor cell proliferation and tumor growth, tumor cells increase their glycolytic activity, and additionally, most of the metabolized glucose is converted into lactate. Together with glutaminolysis, these two mechanisms are the major suppliers of lactic and carbonic acid concentrations in tumor cells. However, despite the high acid concentration in brain tumor cells, their intracellular pH is neutral (pH ~7.4) [32], which was the rationale for performing the *in vitro* dissolution studies in a medium with pH 7.4.

Regarding the TMZ release profile, all formulations (except MWCNTs-G-TMZ) showed a biphasic release pattern, characterized by an initial “burst” release in the first 2 hours, where between 20% (MWCNTs-PEG1500-TMZ) and 41% (MWCNTs-G-PEG6000-TMZ) of TMZ was released, which is most likely related to the fraction of the drug located on or close to the surface of the nanocarriers. The sustained release phase lasted for the next eight days, during which almost the entire TMZ content was released (between 84% and 99% from MWCNTs-TMZ and MWCNTs-G-PEG6000-TMZ, respectively) (Fig. 2). Slower drug release from the PEGylated MWCNTs compared to non-PEGylated formulations during eight days was evident (Fig. 2a), probably due to the increased diffusion barrier formed from the PEG chains and concurrent behavior of TMZ and PEG on the carbon nanotubes surface, having in regard the hydrophilic nature of TMZ. Similar results were presented in the paper of Jain *et al.* [21], where slower TMZ release from PEGylated PLGA nanoparticles compared to non-PEGylated ones was observed. Furthermore, faster TMZ release from all hybrid structures was noted compared to TMZ-loaded MWCNTs (Fig. 2b), probably due to the different ratios of the drug loaded inside the tubes and onto the surface of these different carbon nanostructures. The different PEGs did not cause different drug release patterns in MWCNTs and hybrid structures. From the dissolution curve of TMZ-loaded MWCNTs-G, it can be assumed that the graphene sheets probably block the drug's entrance into the tubes and subsequently restrict its location mainly on their surface, resulting in 99% of the drug being released within 10 hours.

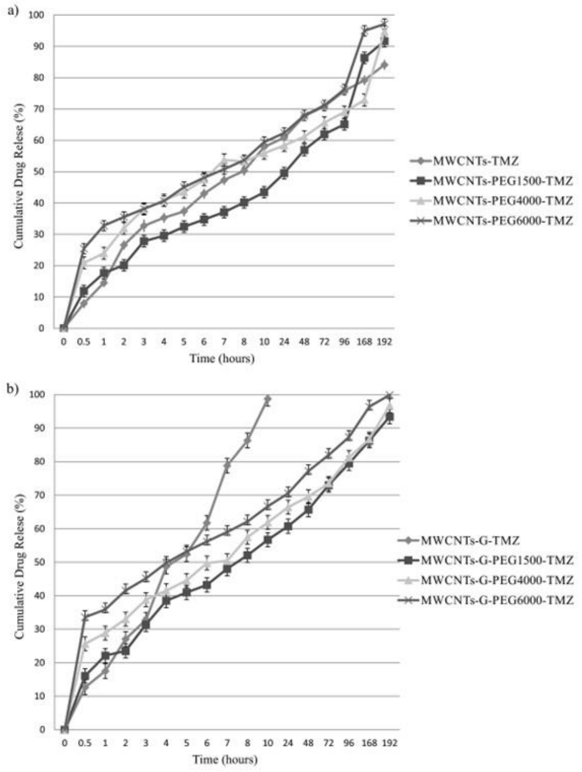

Figure 2. Cumulative TMZ release profile from (a) non-PEGylated and PEGylated MWCNTs and (b) non-PEGylated and PEGylated MWCNTs-G in medium with pH 7.4.

TMZ has a short half-life of 1.8 hours and requires repeated administration to maintain its efficacy. Hence, the controlled and sustained release of TMZ is a desired property for the developed nanoformulations because a prolonged drug release profile requires less frequent drug administration and reduces the toxic effects of TMZ [33]. Namely, it is well known that in terms of short- and long-term efficacy, the sustained-release chemotherapy within the tumor bed could significantly improve the therapeutic effect of patients with malignant recurrent glioma and prolong their survival [34]. Therefore, continuous chemotherapy with the slow-release of TMZ in tumor bed interstitium may promote postoperative radiotherapy sensitization, manifest a synergistic anti-tumor effect, kill tumor cells to a great extent, achieve a high clinical remission rate and improve the long-term survival of patients. In addition, preliminary *in vitro* and *in vivo* studies suggest that activated carbon nanostructures can be used as adjuvant therapy along with the standard treatment in malignant gliomas, concerning their capability to be endocytosed by tumor cells and induce lysosomal dysfunction and mitochondrial damage in the tumor cells [35].

Physicochemical characterization of Temozolomide loaded PEGylated carbon nanostructures

UV-Vis absorption spectroscopy

TMZ loading can be monitored using UV-Vis absorption spectroscopy because TMZ dissolved in water (0.1 mg/mL) displays two characteristic absorption peaks at 255 nm and 328 nm, corresponding to the active hydrolytic metabolite 5-(3-methyl triazen-1-yl) imidazole-4-carboxamide (MTIC) of TMZ and the prodrug TMZ, respectively. As shown in Fig. 3a and Fig. 3b, these two peaks did not appear in the free PEG, unloaded MWCNTs-(G)-COOH and MWCNTs-(G)-PEG. In the UV-Vis spectra of TMZ-loaded nanocarriers, MWCNTs-TMZ, MWCNTs-G-TMZ, MWCNTs-PEG-TMZ, MWCNTs-G-PEG-TMZ peaks at 328 nm and 255 nm clearly showed the successful loading of TMZ in the carbon nanocarriers.

Infrared spectroscopy

Infrared spectroscopy was performed to analyze the presence of different functional groups in the carbon nanocarriers and their interactions during PEG capping and TMZ loading (Fig. 4).

The oxidized carbon nanostructures MWCNTs-COOH and MWCNT-G-COOH (Fig. 4a and Fig. 4b, respectively) showed a characteristic band at 1695 cm^{-1} that can be ascribed to C=O stretching vibration of the carboxyl group. The observed shift of the C=O stretching band position to lower wavenumbers upon PEG modification (1665 cm^{-1}) is often attributed to the increased polarity and hydrogen bonding of the C=O functional group in the presence of PEG, leading to a more acidic C=O moiety. The shift can also result from a change in the local environment of the C=O functional group, such as changes in the molecular geometry and increased solvation. The shift should not be confused by the band at 1740 cm^{-1} that arises from the PEG, indicating the presence of the PEG moieties in the MWCNTs-PEG sample. In the PEGylated MWCNTs as well as in the non-PEGylated one, another band in the 3500–3400 cm^{-1} region can be observed, characteristic for H bonded O-H stretching vibrations from the PEG and the carboxylic OH group in the MWCNTs. In addition, three other bands emerged between 2950 cm^{-1} and 2850 cm^{-1}, typical for the C-H stretchings in both PEG and MWCNTs, being

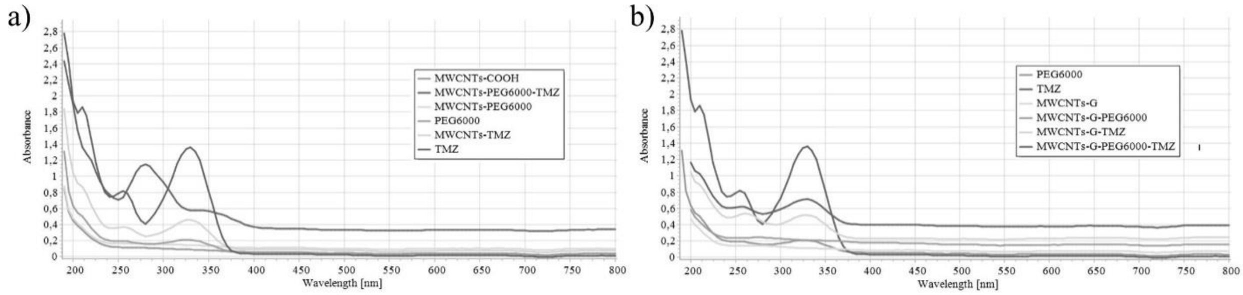

Figure 3. UV-Vis spectra of (a) TMZ, PEG, non-PEGylated and PEGylated blank, and TMZ loaded MWCNTs and (b) TMZ, PEG, non-PEGylated and PEGylated blank and TMZ loaded MWCNTs-G.

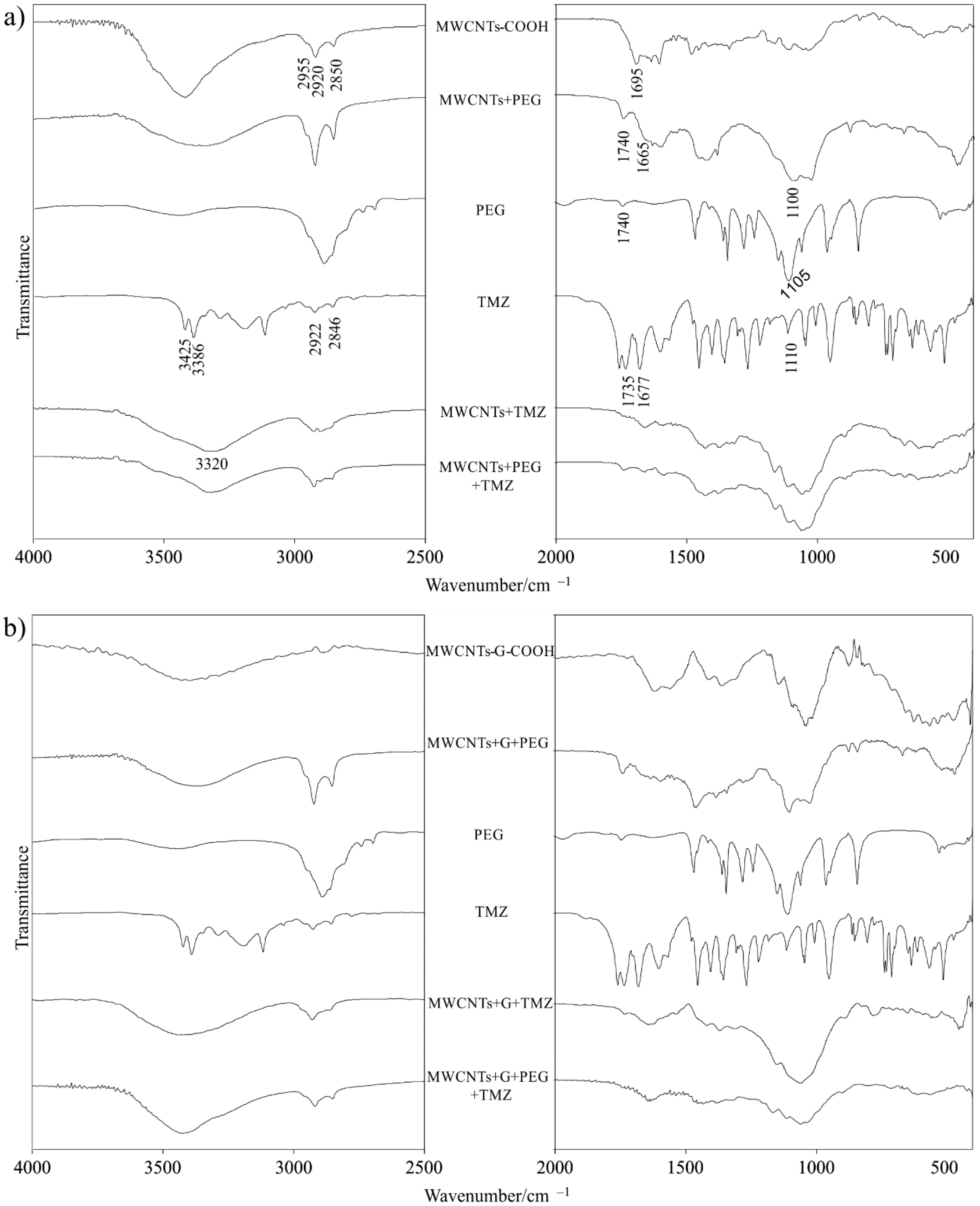

Figure 4. IR spectra of (a) TMZ, PEG, non-PEGylated and PEGylated blank, and TMZ loaded MWCNTs and (b) TMZ, PEG, non-PEGylated and PEGylated blank, and TMZ loaded MWCNTs-G.

more intense in the MWCNTs-PEG formulations. Moreover, a characteristic band at around 1100 cm^{-1} evolved in the spectra of MWCNTs-PEG, attributed to the C-O stretching vibration of the ether group in PEG. The band characteristic for PEG appeared both in the spectra of PEGylated formulations and pure PEG, again demonstrating the conjugation of PEG with MWCNTs.

To further examine the drug/carrier interactions, the IR spectra of blank and TMZ-loaded nanocarriers were analyzed (Fig. 4a, last three spectra). The IR spectrum of TMZ showed two broad bands at 3425 cm^{-1} and 3386 cm^{-1} attributed to the stretching vibration modes of N-H in NH_2, while the two bands at around 2922 cm^{-1} and 2846 cm^{-1} are related to the C-H stretch in position 6 and methyl group bonded to N in position 3. A band at around 1735 cm^{-1} in pure TMZ originates from the stretching C=O carbonyl vibration; the maximum at 1677 cm^{-1} corresponds to amide I mode, whereas the band at 1110 cm^{-1} is attributed to the C-N stretching vibration. TMZ loading in MWCNTs and MWCNTs-PEG weakened the hydrogen bonding, reducing the intensity and red-shifting the bands from 3420 cm^{-1} to 3320 cm^{-1}. Also, the other two C-H stretching bands positioned in the 2950-2850 cm^{-1} in spectra of the loaded particles appeared with obscured intensity. A similar behavior was observed for the strong band at around 1700 cm^{-1} in MWCNTs-COOH, which became weaker in the MWCNTs-TMZ spectrum (Fig. 4a), probably because the TMZ loading hindered to some extent the stretching carbonyl vibration by the interaction that affected the corresponding oxygen atoms. Furthermore, the peak at around 1100 cm^{-1}, characteristic of the C-N stretching band, was more intensive in the MWCNTs-TMZ compared to the MWCNTs-PEG-TMZ spectrum, which the difference in the TMZ loading can explain. The overall spectral impression is that the samples loaded by TMZ (MWCNTs-TMZ and MWCNTs-PEG-TMZ) do not markedly show characteristic TMZ bands either due to its low quantity or its likely position in the tunnels of the CNT, opposite to the larger PEG molecules that cannot easily enter and nest inside the tunneling regions.

In the spectrum of oxidized MWCNTs-G-COOH (Fig. 4b), the intensities of the bands mentioned above were not as strong compared to the spectrum of MWCNTs-COOH, which might suggest that the formulation with added graphene is less prone to oxidation and structural changes. However, in the spectrum of PEGylated MWCNTs-G, the characteristic bands at 3500–3400 cm^{-1}, 2950–2850 cm^{-1}, and 1100 cm^{-1} were also present, which indicates successful functionalization. TMZ loadings on the samples (MWCNTs-G-TMZ and MWCNTs-G-PEG-TMZ) led to a strong band at 3420 cm^{-1}, serving as a tracer for the presence of NH_2 group from TMZ. The intensity and shape of the infrared bands in the 2900–2800 cm^{-1} region were also changed, probably due to the interactions of these carbon nanocarriers with TMZ.

Overall, there was no strong similarity between the IR spectra of pure TMZ and that of the TMZ-loaded carbon nanostructures, suggesting the existence of electrostatic, hydrogen bonds, or/and Van der Waals forces between the TMZ molecules and the (PEGylated) carbon nanostructures. In addition, the functional groups in MWCNTs-(G)-COOH and MWCNTs-(G)-PEG could also overlap some of the TMZ bands in the IR spectrum, which were otherwise visible for the pure compound.

Raman spectroscopy

The functionalization of the carbon nanostructures can be further confirmed by Raman spectroscopy, which can provide molecular insights about the PEGylation and TMZ loading and the purity of the analyzed nanosystems. Two significant features evolve in the Raman spectrum of carbon nanostructures. The first spectral information is extracted from the D band, also known as the "disorder band," typically located around 1350 cm^{-1}, related to the degree of the disordered (sp^3-hybridized) carbon atoms in the carbon nanostructures (MWCNTs or MWCNTs-G). The second is given by the position and intensity of the G band or tangential mode (1500–1600 cm^{-1}) consisting of two sub-bands, G^+ and G^-, related to axial and circumferential in-plane vibrations in semiconducting nanotubes. It is associated with the in-plane stretching of sp^2-hybridized carbon atoms in a hexagonal lattice. The broadening of the bands and the intensities of D and G bands can shed light on the extent of functionalization by determining the intensity ratio of both bands, I_D/I_G [36–38].

Fig. 5a and 5b nest the Raman spectra of pristine MWCNTs and MWCNTs-G and the functionalized MWCNTs-PEG and MWCNTs-G-PEG, respectively. It is evident that the intensity ratio I_D/I_G after the attachment of PEG onto the surface did not significantly alter the I_D/I_G ratio and agrees with other PEGylated systems [13,39]. However, the MWCNTs spectra upon TMZ loading showed broadening of the D band, which can be explained by introduction of functional groups on MWCNTs and MWCNTs-PEG surfaces (Fig. 5a). Furthermore, the loading resulted in the increase of its intensity in comparison to the G band, leading to $I_D/I_G > 1$ for MWCNTs-TMZ and MWCNTs-PEG-TMZ spectra, contrary to the pristine and PEGylated samples were $I_D/I_G < 1$. The trend of dominance of D over G band upon TMZ loading ($I_D/I_G > 1$) was also confirmed for the

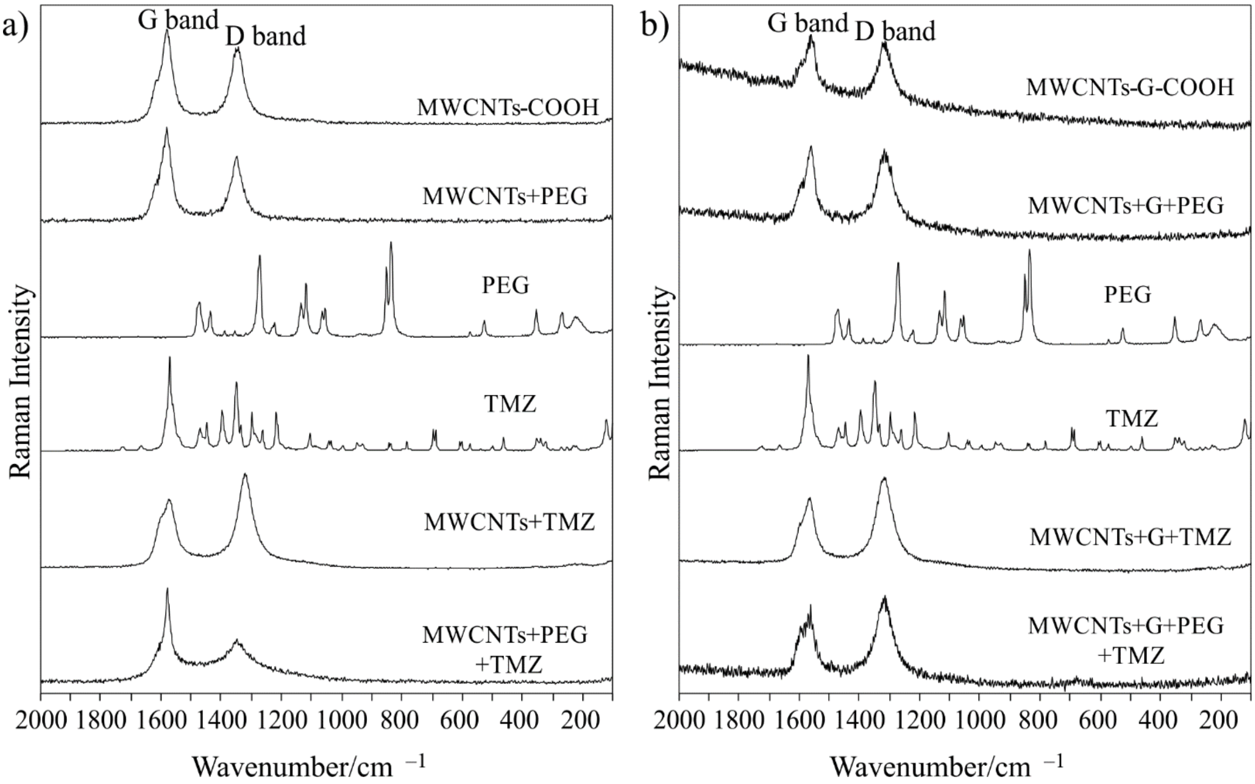

Figure 5. Raman spectra of (a) TMZ, PEG, non-PEGylated, and PEGylated blank and TMZ loaded MWCNTs and (b) TMZ, PEG, non-PEGylated and PEGylated blank, and TMZ loaded MWCNTs-G.

MWCNTs-G samples (Fig. 5b); the production of a higher number of defects in the functionalized material may explain this.

Thermogravimetric analysis

Thermogravimetric analysis was also used to explore and confirm the functionalization of MWCNTs-COOH and MWCNTs-G-COOH with PEG and the loading of TMZ. The results of TGA for both carrier groups are presented in Fig. 6a and 6b, respectively. The initial weight loss observed until 100 °C (in all formulations) was due to the water loss, as also pointed out by Zhao *et al.* [12]. In the weight loss profile of TMZ, there was a baseline temperature of 210 °C, shown also in the paper of Gürten *et al.* [40]. As shown in Fig. 6a, the weight of MWCNTs-COOH decreased with increasing temperature, but the weight loss was different compared to the weight loss of MWCNTs-PEG and PEG. Pure PEG weight decreased sharply with increasing temperature, showing almost 100% weight loss at ca. 400 °C. In the diagram of MWCNTs-PEG, 29% weight loss was noted at 800 °C, 10% more than that of MWCNTs-COOH. This weight loss was due to the decomposition of PEG chains. In the diagram of MWCNTs-TMZ, 22% loss at 800 °C was observed, which was only 3% more compared to the weight loss of pure MWCNTs-COOH, indicating strong interaction/entrapment of TMZ in MWCNTs-COOH. The weight loss of MWCNTs-PEG-TMZ at 800 °C was 19%, ca.10% less than that of MWCNTs-PEG, indicating that the drug/carrier interaction is much stronger in TMZ-loaded PEGylated systems.

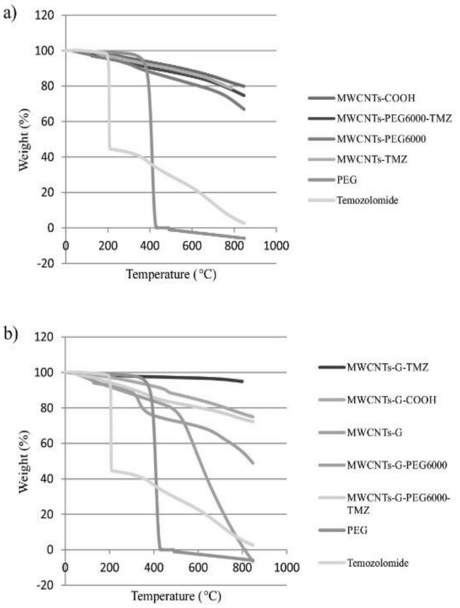

Figure 6. TGA plots of (a) TMZ, PEG, non-PEGylated and PEGylated blank, and TMZ loaded MWCNTs and (b) TMZ, PEG, non-PEGylated and PEGylated blank, and TMZ loaded MWCNTs-G.

In the TGA curve of MWCNTs-G (Fig. 6b), only one sharp weight loss peak before 500 °C was observed, indicating that the hybrid had a small amount of amorphous carbon and that the graphene and MWCNTs in the hybrid exhibit similar thermal stability. The same was observed by Zhao *et al.*, who fabricated and analyzed G/SWCNT hybrids [36]. The MWCNTs-G-COOH showed the highest thermal stability, with only 14% weight loss, which brought us to the fact that COOH groups crafted on the surface led to an increase in thermal stability. With modification and introduction of PEG molecules on the surface, a new thermo-diagram with two inclinations was formed. The first peak at approximately 115 °C resulted from the degradation of PEG, while the peak at 390 °C from the defects created during oxidation accordingly. When loaded with TMZ, the elevation of the decomposition temperature compared to the blank carriers indicates that strong interactions were formed between the drug and carriers (MWCNTs-G-COOH and MWCNTs-G-PEG).

CONCLUSION

In conclusion, the carbon nanostructures, MWCNTs, and their hybrid with graphene MWCNTs-G have been successfully functionalized with PEG and loaded with TMZ, an alkylating drug used to treat certain types of brain tumors. Simple procedures were used for functionalization and drug loading, providing relatively high TMZ loading and particle size and surface properties of the carbon nanocarriers suitable for crossing the BBTB and uptake into the tumor cells. As a desired property of the developed carbon nanocarriers, a sustained release of TMZ was achieved, suggesting the potential for less frequent TMZ administration and a better therapeutic index. Further studies are planned to evaluate the possible radiosensitization effect of TMZ-loaded carbon nanocarriers for glioma cells in vitro and in adequate animal models.

ACKNOWLEDGMENT

The authors express gratitude to the International Atomic Energy Agency (IAEA) for supporting this study, performed within the project for technical cooperation titled "Application of ionizing irradiation in nanotechnology (MAK1003)".

REFERENCES

[1] Y. Zhou, K. Vinothini, F. Dou, Y. Jing, A. A. Chuturgoon, T. Arumugam, M. Rajan, Arabian J. Chem. 15 (2022) 103649. https://doi.org/10.1016/j.arabjc.2021.103649.

[2] L. Wu, C. Man, H. Wang, X. Lu, Q. Ma, Y. Cai, W. Ma, Pharm. Res. 30 (2013) 412–423. https://doi.org/10.1007/S11095-012-0883-5

[3] R. Singh, N.K. Mehra, V. Jain, N.K. Jain, J. Drug Targeting 21 (2013) 581–592. https://doi.org/10.3109/1061186X.2013.778264.

[4] B. Zhang, Y. Xing, Z. Li, H. Zhou, Q. Mu, B. Yan, Nano Lett. 9 (2009) 2280–2284. https://doi.org/10.1021/nl900437n.

[5] D. Pantarotto, R. Singh, D. McCarthy, M. Erhardt, J.P. Briand, M. Prato, K. Kostarelos, A. Bianco, Angew. Chem. 43 (2004) 5242–5246. https://doi.org/10.1002/anie.200460437.

[6] A. Masotti, M.R. Miller, A. Celluzzi, L. Rose, F. Micciulla, P.W.F. Hadoke, S. Belluci, A. Caporali, Nanomed. Nanotehnol. Biol. Med. 12 (2016) 1511–1522. https://doi.org/10.1016/j.nano.2016.02.017.

[7] H. Sun, J. Ren, X. Qu, Acc. Chem. Res. 49 (2016) 461–470. https://doi.org/10.1021/acs.accounts.5b00515.

[8] N. Jawahar, A. De, S. Jubee, E.S. Reddy, Drug Dev. Res. 81 (2019) 305–314. https://doi.org/10.1002/ddr.21620.

[9] Y. Wu, J.A. Phillips, H. Liu, R. Yang, W. Tan, ACS Nano 2 (2008) 2023–2028. https://doi.org/10.1021/NN800325A.

[10] P. Wolski, K. Nieszporek, T. Panczyk, Phys. Chem. Chem. Phys. 19 (2017) 9300–9312. https://doi.org/10.1039/C7CP00702G.

[11] B.S. Wong, S.L. Yoong, A. Jagusiak, T. Panczyk, H.K. Ho, W.H. Ang, G. Pastorin, Adv. Drug Delivery Rev. 65 (2013) 1964–2015. https://doi.org/10.1016/j.addr.2013.08.005.

[12] X. Zhao, K. Tian, T. Zhou, X. Jia, J. Li, P. Liu, Colloids Surf. B 168 (2018) 43–49. https://doi.org/10.1016/j.colsurfb.2018.02.041.

[13] D. Ravelli, D. Merli, E. Quartarone, A. Profumo, P. Mustarelli, M. Fagnoni, RSC Adv. 3 (2013) 13569–13582. https://doi.org/10.1039/C3RA40852C.

[14] A. Di Martino, P. Kucharczyk, Z. Capakova, P. Humpolicek, V. Sedlarik, J. Nanopart. Res. 19 (2017) 1–16. https://doi.org/10.1007/s11051-017-3756-3.

[15] J.S. Ananta, R. Paulmurugan, T.F. Massoud, Neurol. Res. 38 (2016) 51–59. https://doi.org/10.1080/01616412.2015.1133025.

[16] A.A. John, A.P. Subramanian, M.V. Vellayappan, A. Balaji, H. Mohandas, S. Jaganathan, Int. J. Nanomed. 10 (2015) 4267–4277. https://doi.org/10.2147/IJN.S83777.

[17] C.Y. Lee, I.H. Ooi, Pharmaceuticals 9 (2016) 54. https://doi.org/10.3390/PH9030054.

[18] Q. Guo, X. Shen, Y. Li, S. Xu, Curr. Med. Sci. 37 (2017) 635–641. https://doi.org/10.1007/s11596-017-1783-z.

[19] H. Huang, Q. Yuan, J.S. Shah, R.D.K. Misra, Adv. Drug Delivery Rev. 63 (2011) 1332–1339. https://doi.org/10.1016/j.addr.2011.04.001.

[20] L. Niu, L. Meng, Q. Lu, Macromol. Biosci. 13 (2013) 735–744. https://doi.org/10.1002/mabi.201200475.

[21] A. Jain, G. Chasoo, S.K. Singh, A.K. Saxena, S.K. Jain, J. Microencapsulation 28 (2011) 21–28. https://doi.org/10.3109/02652048.2010.522257.

[22] X. Wei, X. Chen, M. Ying, W. Lu, Acta Pharm. Sin. B 4 (2014) 193–201.

https://doi.org/10.1016/j.apsb.2014.03.001.

[23] S. Honary, F. Zahir, Trop. J. Pharm. Res. 12 (2013) 255–264. https://doi.org/10.4314/tjpr.v12i2.19.

[24] Y. Yamamoto, Y. Nagasaki, Y. Kato, Y. Sugiyama, K. Kataoka, J. Controlled Release 77 (2001) 27–38. https://doi.org/10.1016/s0168-3659(01)00451-5.

[25] Y.Y. Yuan, C. Mao, X. Du, J. Du, F. Wang, J. Wang, Adv. Mater. 24 (2012) 5476–5480. https://doi.org/10.1002/adma.201202296.

[26] C. Saraiva, C. Praça, R. Ferreira, T. Santos, L. Ferreira, L. Bernardino, J. Controlled Release 235 (2016) 34–47. https://doi.org/10.1016/j.jconrel.2016.05.044.

[27] A. Prokop, J.M. Davidson, J. Pharma. Sci. 97 (2018) 3518–3590. https://doi.org/10.1002/jps.21270.

[28] H. Gao, Acta Pharm. Sin. B 6 (2016) 268–286. https://doi.org/10.1016/j.apsb.2016.05.013.

[29] N. Sciortino, S. Fedeli, P. Paoli, A. Brandi, P. Chiarugi, M. Severi, S. Cicchi, Int. J. Pharm. 521 (2017) 69–72. https://doi.org/10.1016/j.ijpharm.2017.02.023.

[30] X. Cui, B. Wan, Y. Yang, X. Ren, L. Guo, Sci. Rep. 7 (2017) 1–13. https://doi.org/10.1038/s41598-017-01746-9.

[31] J. Ren, S. Shen, D. Wang, Z. Xi, L. Guo, Z. Pang, Y. Qian, X. Sun, X. Jiang, Biomaterials 33 (2012) 3324–3333. https://doi.org/10.1016/j.biomaterials.2012.01.025.

[32] V. Miranda-Goncalves, R.M. Reis, F. Baltazar, Curr. Cancer Drug Targets 16 (2016) 388–399. https://doi.org/10.2174/1568009616666151222150543.

[33] A. Orza, O. Soriţău, C. Tomuleasa, L. Olenic, A. Florea, O. Pana, I. Bratu, E. Pall, S. Florian, D. Casciano, A. Biris, T. Yoshiyuki, Int. J. Nanomed. 8 (2013) 689–702. https://doi.org/10.2147/IJN.S37481

[34] L. Wang, Z. Wang, Z. Liang, G. Li, S. Duan, Y. Xi, Am. J. Transl. Res. 14 (2022) 5669–5676. https://www.ncbi.nlm.nih.gov/pmc/articles/PMC9452319/pdf/ajtr0014-5669.pdf.

[35] S. Romano-Feinholz, A. Salazar-Ramiro, E.M. Sandoval, R. Magaña-Maldonado, N.H. Pedro, E.R. López, G.A. Aguilar, A.S. Garcia, J. Sotelo, P.V. Cruz, B. Pineda, Int. J. Nanomedicine 12 (2017) 6005–6026. https://doi.org/10.2147/IJN.S139004.

[36] M.Q. Zhao, X.F. Liu, Q. Zhang, G.L. Tian, J.Q. Huang, W. Zhu, F. Wei, ACS Nano 6 (2012) 10759–10769. http://doi.org/10.1021/nn304037d.

[37] N. Hadidi, F. Kobarfard, N. Nafissi-Varcheh, R. Aboofazeli, Int. J. Nanomed. 6 (2011) 737–746. https://doi.org/10.2147/ijn.s17626.

[38] B.V. Farahani, G.R. Behbahani, N. Javadi, J. Braz. Chem. Soc. 27 (2016) 694–705. https://doi.org/10.5935/0103-5053.20150318.

[39] J. Chen, H. Liu, C. Zhao, G. Qin, G. Xi, T. Li, X. Wang, T. Chen, Biomaterials 35 (2014) 4986–4995. https://doi.org/10.1016/j.biomaterials.2014.02.032.

[40] B. Gürten, E. Yenigül, A.D. Sezer, S. Malta, Braz. J. Pharm. Sci. 54 (2018) e17513. http://dx.doi.org/10.1590/s2175-97902018000217513.

RADMILA MILENKOVSKA[1]
NIKOLA GESKOVSKI[1]
PETRE MAKRESKI[2]
ANITA GROZDANOV[3]
EMIL POPOVSKI[2]
GJORGJI PETRUSHEVSKI[2,4]
MAJA SIMONOSKA CRCAREVSKA[1]
KRISTINA MLADENOVSKA[1]

[1]Faculty of Pharmacy, Ss. Cyril and Methodius University in Skopje, Skopje, Republic of N Macedonia

[2]Institute of Chemistry, Faculty of Natural Sciences and Mathematics, Ss. Cyril and Methodius University in Skopje, Skopje, Republic of N Macedonia

[3]Faculty of Technology and Metallurgy, Ss. Cyril and Methodius University in Skopje, Skopje, Republic of N Macedonia

[4]Alkaloid AD Skopje, Skopje, Republic of N Macedonia

NAUČNI RAD

FUNKCIONALIZOVANE NANOSTRUKTURE UGLJENIKA KAO NOSAČI TEMOZOLOMIDA; FIZIČKOHEMIJSKA I BIOFARMACEUTSKA KARAKTERIZACIJA

U ovom radu, temozolomid (TMZ), lek koji se koristi u lečenju anaplastičnog astrocitoma i multiformnog glioblastoma, ugrađen je u višeslojne ugljenične nanocevi (VSUNC) i hibridne ugljenične nanocevi sa grafenom (VSUNC-G) funkcionalizovanim polietilen-glikolom (PEG). Cilj je bio da se proceni potencijal ovih nanonosača za ciljanu isporuku i produženo oslobađanje TMZ u ćelijama tumora mozga. Oksidovani VSUNC i VSUNC-G su nekovalentno funkcionalizovani sa PEG-ima različite molekulske mase i zatim je nanet TMZ prema standardnim procedurama. Temeljna fizičko-hemijska i biofarmaceutska karakterizacija nanonosača ugljenika sa nanetim TMZ ukazala je na visoku efikasnost inkapsulacije (do 67%) i punjenje lekom (do 18% od 25% teorijske vrednosti) i homogenu distribuciju veličine čestica, sa z-prosekom (160 do 300 nm) i zeta potencijala (-31mV do -21 mV) čestica adekvatnih za prelazak krvno-moždane-tumorske barijere i ulazak u tumorske ćelije. Uspešna funkcionalizacija i TMZ nanošenje potvrđeni su SEM i TEM slikama, UV-Vis apsorpcijom, infracrvenom i Raman spektroskopijom i TGA analizama. Produženo oslobađanje TMZ iz ugljeničnih nanonosača je zapaženo in vitro. Prikazani nalazi čine osnovnu platformu za dalje istraživanje ovih formulacija protiv različitih tipova ćelija glioma i na adekvatnim životinjskim modelima.

Ključne reči: višeslojne ugljenične nanocevi, grafen, polietilen-glikol, temozolomid, fizičko-hemijska svojstva, produženo oslobađanje.

CI&CEQ
Chemical Industry & Chemical Engineering Quarterly

Available online at
Association of the Chemical Engineers of Serbia *AChE*
www.ache.org.rs/CICEQ

Chem. Ind. Chem. Eng. Q. 30 (3) 257−264 (2024)
CI&CEQ

PERIASAMY MANIKANDAN SRINIVASAN
PRADEEP KUMAR CHINNUSAMY
RAGHUL THANGAMANI
SURIYA PALANIRAJ
PRANESH RAVICHANDRAN
SURYA KARUPPASAMY
YOKESHWARAN SANMUGAM

Department of Chemical Engineering, Kongu Engineering College, Erode, India

SCIENTIFIC PAPER

UDC 66.021.4:54

HEAT TRANSFER PERFORMANCE OF AN Al_2O_3-WATER-METHANOL NANOFLUID IN A PLATE HEAT EXCHANGER

Article Highlights

- Al_2O_3/Methanol/ Water mixed nanofluid were prepared using a high-pressure homogenizer
- The heat transfer performance of Al_2O_3 suspended base fluid was studied in a plate heat exchanger
- Individual and overall heat transfer coefficients were determined and analyzed by varying flow rate

Abstract

A plate heat exchanger is one of the smallest and most efficient heat exchangers on the market. This experiment aims to assess the performance of methanol-water as a base fluid in a plate heat exchanger that affects the heat transfer performance. For this study, aluminum oxide (Al_2O_3) nanoparticle was used in various ratios (0.25, 0.5, and 0.75 vol. %) in a base fluid (10 vol.% methanol & 90 vol.% water) to prepare a nanofluid. At two different temperatures, such as 55 °C and 60 °C, with varying flow rates (2 to 8 L/min) and varying nanoparticle concentrations (0.25 to 0.75%), thermo physical characteristics and convective heat transfer studies were performed, and the results are presented. The overall inference was that there was a notable enhancement in the hot side, cold side, and overall heat transfer coefficient by the combination of Al_2O_3 nanoparticle and methanol-water-based fluid. It was noted that utilizing Al_2O_3/methanol-water nanofluid could significantly reduce the temperature gradient in the heat exchanger and improve its performance. Maximum hot fluid coefficient of 4300 W/m^2 °C, cold fluid coefficient of 4600 W/m^2 °C, and overall coefficient of 2200 W/m^2 °C were noted for 0.75 vol.% nanoparticle concentration and at a flow rate of 8 L/min.

Keywords: Al_2O_3, base fluid, heat transfer, methanol, nanofluid, plate heat exchanger.

Particles with a size of less than 100 nm are known as nanoparticles. Nanoparticles naturally occur in the environment but are artificially synthesized [1]. Nanoparticles are inorganic materials. The human eye cannot see nanoparticles. They can be classified into different types based on their shapes, properties, and sizes. Nanoparticles have unique physical and chemical properties because of their nanoscale size and high surface area. Their unique size, shape, and structure play a major role in reactivity, toughness, and other properties. Due to their special characteristics, these minuscule particles are well suited for high chemical reactivity, bio mobility, and energy absorption [2]. Nanomaterials are classified into 0D, 1D, 2D, and 3D based on their overall shape. Nanoclusters have a modest size distribution with at least one dimension between 1 and 10nm. Industrial manufacturing processes involve heat exchangers for heating and cooling [3] the fluids. The most common base fluids in heat transfer applications are glycols, methanol, engine oil, and water [4]. Thermal conductivity and heat transfer properties of these fluids must be improved to improve heat transfer performance [5,6].

Correspondence: P.M. Srinivasan, Department of Chemical Engineering, Kongu Engineering College, Erode-638 060, India.
E-mail: sriperiasamy@gmail.com

Paper received: 26 July, 2023
Paper revised: 8 December, 2023
Paper accepted: 13 December, 2023

https://doi.org/10.2298/CICEQ230726028M

There has been a recent advancement in energy reduction using nanofluids, as evidenced by a sizable number of technical community research articles. A new engineering fluid, this nanofluid is known for its special applications and capacity to reduce costs in heat transfer operations based on altering suitable base fluids [7]. A complete review of synthesis, stability, thermophysical properties, and heat transfer applications of nanofluid was performed by Mehta *et al.* and was useful for framing the experimental conditions of the present study [8,9].

Researchers have developed nanoparticle-sustained heat transfer fluids in different heat transfer equipment [10,11]. Various metal oxides were utilized by many researchers, such as CuO nanoparticles added to water [12], aluminum oxide/water [13–17], Al_2O_3 in water-ethylene glycol [18], TiO_2, ZnO in water-ethylene glycol [19], Fe_2O_3 in engine oil-water mixture [20], Al_2O_3 and CuO nanoparticle suspension in engine oil, vacuum pump fluid, distilled water, and ethylene glycol [21] and the results showed that this addition considerably increases the thermal conductivities of fluid mixtures and heat transfer coefficient.

A heat transfer study was made to determine Nusselt number, pressure drop, and energy efficiency factor by Ajeeb *et al.*, and the results indicated a heat transfer enhancement of 27% at 0.2 vol% for DW-based Al_2O_3 nanofluid and 19.1% at 0.2 vol% for 30% of EG based Al_2O_3 nanofluid [22]. The experimental results of Al_2O_3 nanoparticle addition show that the Nusselt number increased significantly with respect to different volume fractions [23]. Heat transfer results on experimental and numerical investigations performed by Singh *et al.* with DW-Al_2O_3, graphene nanoplatelet (GnP), and multi-walled carbon nanotubes (MWCNT) nanofluids showed that at 1 Vol.% nanoparticle concentration, around 10, 15 and 18 % maximum enhancement in an average heat transfer rate observed with Al_2O_3, GnP and MWCNT nanofluids, respectively[24]. Pang *et al.* [25] used methanol-based nanofluids with 0.5 vol% at 293.15 K and reported 14.29% and 10.74% thermal conductivity enhancement for SiO_2 and Al_2O_3 nanoparticles, respectively. Methanol was used as a base fluid, and silver nanoparticles were added to the water in a thermo siphon heat exchanger [26]. Using Al_2O_3/water nanofluid, the heat transfer study was made numerically by Kumar *et al.* in a flat plate heat exchanger and bubble fin plate heat exchanger. Investigation on the effect of mass flow rate and volume fraction on heat transfer coefficient (HTC), Nusselt number, and pressure drop was performed, and it was reported that HTC increased with an increase in mass flow rate and volume concentration of nanofluid [27]. The result of the heat transfer effect showed energy savings of around 32% for cooling. Methanol has recently been used for various heat transfer applications [28] and different types of heat pipes vapor-dynamic thermosyphons, and conventional and micro heat pipes.

Many studies have examined these innovative fluids' unique characteristics and capacities since using nanofluids in various industries. Aluminum oxide (Al_2O_3) is a non-toxic, economically viable nanomaterial with good thermophysical and heat transport characteristics. For instance, Al_2O_3 and TiO_2 nanofluids were prepared to perform heat transfer analysis of prepared nanofluids flowing inside a compact plate heat exchanger. A study compared the experimental and numerical results (CFD analysis) and found a better correlation between the results of improved thermal performance [29]. A stable nanofluid of γ-Al_2O_3 was prepared by Mehta *et al.* to evaluate thermo physical properties (viscosity and thermal conductivity). The study was also performed with the addition of surfactant and found that there will be 20% and 8% enhancement in viscosity and thermal conductivity at 0.75% volume fraction. It also revealed that surfactant addition shows an average rise of 2% in viscosity and a drop of 3% in thermal conductivity for all volume fractions [30]. Using a two-step method and CTAB surfactant, a stable aqua-Al_2O_3 nanofluid was synthesized by Mehta *et al.*, and studies on thermo physical characteristics were made with prepared nanofluid. Experimental results show an enhancement of 76.2% in dynamic viscosity and 8.5% in thermal conductivity at 1% volume fraction [31].

There is potential to examine the heat transfer capabilities of this material in real-time heat exchangers. However, most studies are primarily interested in thermal conductivity investigations. While there are many benefits to using nanofluids, there are also some drawbacks, including fouling, surface erosion, and instability. While preparing a nanofluid, methanol offers a way to reduce fouling and prevent nanoparticle aggregation. Compact plate heat exchangers were chosen in our investigation since the literature also shows that compact plate heat exchangers are effective and perform better with nanofluids [32–34]. The heat transfer performance of a nanofluid mixture of Al_2O_3-water (W)-methanol (M) has not been investigated in a plate heat exchanger in the literature. Hence, heat transfer characteristics of Al_2O_3 nanoparticle addition in a base fluid (methanol + water) was performed by varying the nanoparticle concentration (0.25% to 0.75%), hot fluid inlet temperature (55 °C to 60 °C) and flow rate (2 L/min to 8 L/min) for a base fluid volume fractions of (10:90) and the results are presented.

MATERIALS AND METHODS

Preparation and properties of nanoparticle

Agglomerates of ultrafine particles, nanoparticles, or nanoclusters are called nanopowders. Nanoparticles comprise three layers: the surface, shell, and core. Nanoparticles are converted into nanofluids using two-step methods. In this study, the Al_2O_3 nanoparticle size of 50 nm was suspended in a water-methanol mixture using a two-step (sol-gel) technique. Base fluids with volume fractions (10% methanol + 90% water) were created using the amounts calculated by Eq. (1).

$$\varphi=\frac{(m/\rho)_{Al_2O_3}}{(m/\rho)_{Al_2O_3}+(m/\rho)_{W:M}} \tag{1}$$

A high-pressure homogenizer was utilized to ensure the stability of the prepared nanofluid, which was used as a cold fluid in the plate heat exchanger. The preparation of nanofluid using a homogenizer is shown in Fig. 1

Figure 1. Preparation of Al_2O_3-water-methanol nanofluid.

Because of the high-pressure homogenizer, the prepared nanofluid was uniformly suspended throughout the base fluid. The thermal conductivity of heating or cooling fluids was an essential attribute to consider when designing energy-efficient systems. One of the primary qualities considered while developing and regulating the process was the fluid's heat conductance. The ease of availability, prices, heat conductance, and inclination of the particles to keep them in the base fluid with little agglomeration are all important considerations. Metal oxide nanoparticles have a higher tendency to agglomerate despite their superior thermal conductivity. Aluminum oxide (Al_2O_3) nanofluid was used for the present heat transfer investigation.

SEM images of aluminum oxide nanoparticle

SEM is widely used to identify the microstructure and chemistry of materials. It projects and scans the focused stream of electrons over the surface to produce an image. The electrons in the beam interact with the sample and produce various signals to obtain details about the surface's composition. Fig. 2 shows the SEM Images of Al_2O_3 nanoparticles.

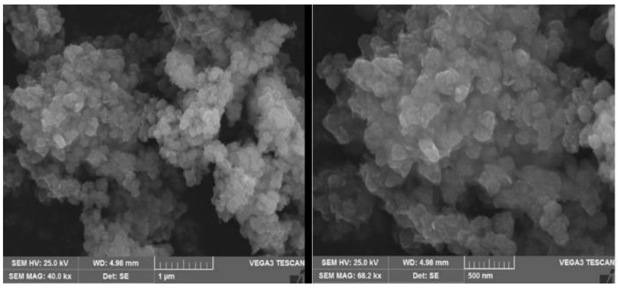

Figure 2. SEM image of Al_2O_3 nanoparticle.

Experimental setup and estimation of thermophysical properties

The experiments were carried out on a plate-type heat exchanger described in the previous work [35,36]; the experimental setup is shown in Fig. 3. Methanol-based nanofluids using Al_2O_3 nanoparticles were prepared for various volume concentrations, such as 0.25%, 0.5%, and 0.75%. The density, dynamic viscosity, heating value, and heat conductance were then computed [37,38] premised on experimental results.

Figure 3. Photographic view of the experimental setup.

Determination of Nusselt number, convective and overall heat transfer coefficient of Al_2O_3/water-methanol nanofluid

Eq. (2) was used to determine the Nusselt number of nanofluid [39] (Kim model), and Eq. (3) was used to find the heat transfer coefficient of hot and cold fluid. Eq. (4) was used to find the overall heat transfer coefficient.

$$Nu = 0.295(N\mathrm{Re})^{0.64}(N\mathrm{Pr})^{0.32}\left(\left(\frac{\Pi}{2}-\beta\right)\right) \qquad (2)$$

$$h = \frac{NuD_H}{K} \qquad (3)$$

$$U = \frac{Qavg}{A\nabla Tlmtd} \qquad (4)$$

RESULTS AND DISCUSSION

Effect of flow rate on hot fluid heat transfer coefficient (h_h) at 55 °C

Before conducting detailed experiments with selected nanofluids, the study was performed with deionized water to ensure reliability. Figure 4 represents the influence of flow rate on hot fluid heat transfer coefficient (h_h) at a hot fluid inlet temperature of 55 °C for different nanofluid concentrations and water.

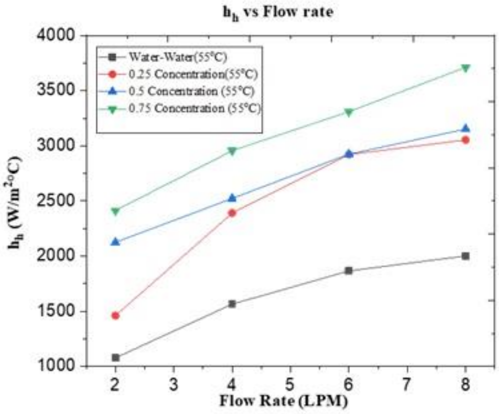

Figure 4. Effect of flow rate on hot fluid heat transfer coefficient (h_h) at 55 °C.

According to Fig. 3, ranges of heat transfer coefficient on the hot side (h_h) vary from 1700 W/m^2°C for water-water, and this value is increased to 3300 W/m^2°C at a flow rate of 6 L/min for a nanofluid with a nanoparticle concentration of 0.75 vol.%. When the flow rate increased to 8 L/min, the heat transfer coefficient range also increased to 1850 W/m^2°C for water-water and 3800 W/m^2°C for 0.75 vol.%. It shows that flow rate has a significant effect on heat transfer enhancement.

Effect of flow rate on cold fluid heat transfer coefficient (h_c) at 55 °C

The flow rate variations on the cold side heat transfer coefficient at 60 °C are presented in Fig. 5. A similar trend of heat transfer enhancement was also observed on the cold side fluid, as shown in Fig. 4. It was noted that, at a low flow rate (2 L/min) and low nanoparticle concentration (0.25 vol.%), the heat transfer coefficient was almost the same for water as a base fluid; however by increasing the flow rate gradually, the rate of heat transfer starts increasing gradually. For instance, at a flow rate of 4 L/min, the heat transfer coefficient increased to 2400 W/m^2°C (for 0.75 vol.%) from 1250 W/m^2°C (for water).

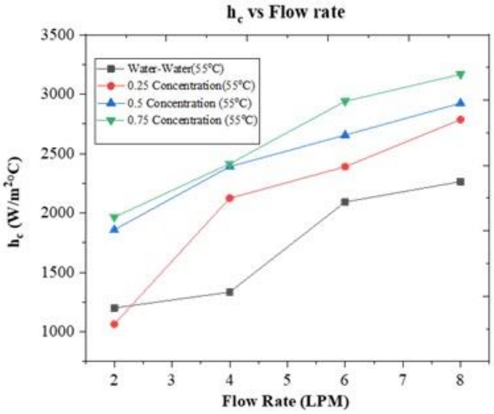

Figure 5. Effect of flow rate on cold fluid heat transfer coefficient (h_h) at 55 °C.

Results showed that the convective heat transfer coefficient and Nusselt number for Al_2O_3/methanol-water nanofluid were comparatively higher than those for the base fluid. This effect was due to the heat transport by thermally conductive nanoparticles, which was enhanced through the interfacial layers of fluids. Finally, the maximum enhancement was observed at 8 L/min with a heat transfer coefficient value of 3300 W/m^2°C (for 0.75 vol.%); however, the rate of enhancement was decreased by the flow rate. Hence, the flow rate needs to be optimized to utilize nanoparticles efficiently.

Effect of flow rate on overall heat transfer coefficient (U) at 55 °C

Although the heat transfer coefficient was calculated individually, it is very useful to calculate the overall heat transfer coefficient for extracting the benefits from nanoparticles. Hence, the result concerning an overall heat transfer coefficient at 55 °C is presented in Fig. 6.

Fig. 5 shows that, at the flow rate of 4, 6, and 8 L/min, the range of U was 850, 990, and 1100 W/m^2°C (for 0.25 vol. % nanoparticle) and 1350, 1440, and 1720 W/m^2°C (for 0.75 vol. %). Hence, it may be concluded that the individual and overall heat transfer coefficients were enhanced notably because of the nano-sized solid particles.

Effect of flow rate on hot fluid heat transfer coefficient (h_h) at 60°C

Since temperature plays a major role in heat

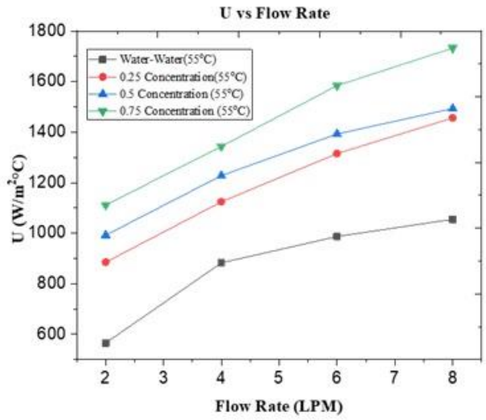

Figure 6. Effect of flow rate on overall heat transfer coefficient (h_h) at 55 °C.

transfer, the study was repeated by increasing the hot fluid temperature by 60 °C, and the effect of flow rate on the hot fluid heat transfer coefficient can be seen in Fig. 7.

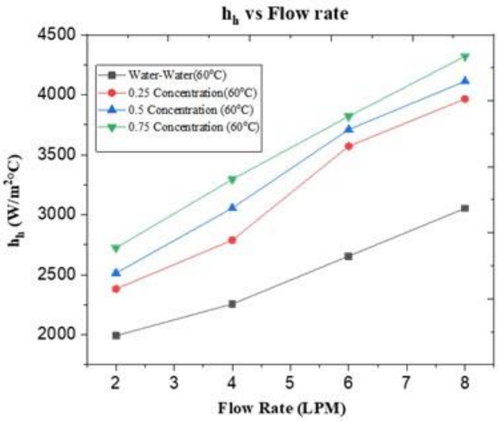

Figure 7. Effect of flow rate on hot fluid heat transfer coefficient (h_h) at 60 °C.

The experimental results in Fig. 6 point that for the concentration of 0.25 vol.% through 0.75 vol.%, the heat transfer coefficient on the hot side was 1950 W/m^{2}°C (for water), 2310 W/m^{2}°C (for 0.25 vol.%), and 2790 W/m^{2}°C (for 0.75 vol.%) at a flow rate of 2 L/min and 2700 W/m^{2}°C (for water), 3600 W/m^{2}°C (for 0.25 vol.%), and 4300 W/m^{2}°C (for 0.75 vol.%) at a flow rate of 8 L/min. This result again supports the ability of nanoparticle suspension to help in heat transfer enhancement.

Effect of flow rate on cold fluid heat transfer coefficient (h_c) at 60 °C

The effect of flow rate on the cold-side heat transfer coefficient at 60 °C is presented in Fig. 8. The effect on the cold-side heat transfer coefficient shows an increase from 2600 (for water) to 4600 W/m^{2}°C (for 0.75 vol.% nanoparticle concentration). When comparing the coefficient at 55 °C, the enhancement was significantly high. It shows a similar increasing pattern on the heat transfer rate, and the increment was linear with respect to nanoparticle concentration and temperature.

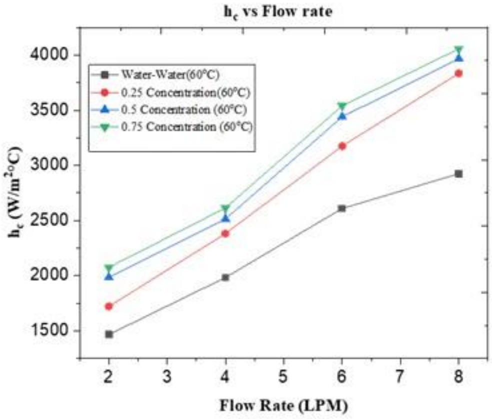

Figure 8. Effect of flow rate on cold fluid heat transfer coefficient (h_h) at 60 °C.

Effect of flow rate on overall heat transfer coefficient (U) at 60 °C

The effect of the flow rate variations on the overall heat transfer coefficient at 60 °C is presented in Fig. 9.

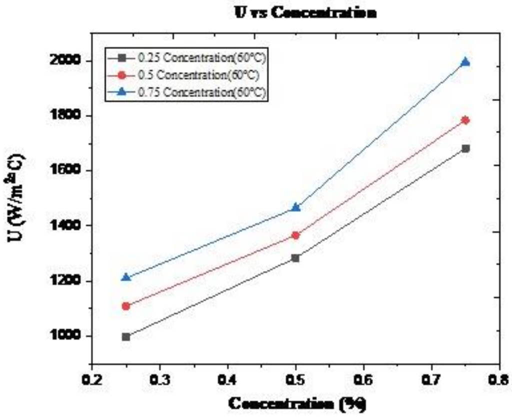

Figure 9. Effect of flow rate on overall heat transfer coefficient (h_h) at 60 °C.

Fig. 9 shows that the increase in temperature favors heat transfer; however, the temperature cannot increase more than the boiling point of methanol. Hence, a study was performed up to 60 °C. The result shows a uniform enhancement in the overall heat transfer rate with respect to all the concentrations (0.25, 0.5, and 0.75 vol. %) and all the flow rates. The ranges were 1380 to 2200 W/m^{2}°C (for 0.25 vol. % and 0.75 vol. % nanoparticle concentrations, respectively) at a flow rate of 8 L/min.

It shows that flow rate significantly affects heat transfer enhancement due to the relative increase in thermal conductivity because of the highly conducive solid nanoparticle to the prepared base fluids. Other significant factors for this heat transfer enhancement are Brownian motion, interfacial layer between base and nanofluid, thermo physical properties other than thermal conductivity (Viscosity, density, and specific heat capacity), and fluid flow rate [40]. The results are consistent with the reported results that the thermal conductivity, viscosity, and density of the Al_2O_3 nanofluids increase with nanoparticles in the base fluid [41–43].

CONCLUSION

The following conclusions were derived from the present study. The overall inference was a significant improvement in heat transfer with the addition of nanoparticles because the high conductive solid nanoparticle augments the heat transfer rate of base fluids. Utilizing the Al_2O_3/methanol-water nanofluid could significantly reduce the temperature gradients in the heat exchanger and improve the performance of heat exchangers. As temperature and nanoparticle concentration increase, the heat transfer coefficient also increases at various flow rates; the maximum hot fluid coefficient of 4300 W/m^2°C, cold fluid coefficient of 4600 W/m^2°C, and overall coefficient of 2200 W/m^2°C were noted for 0.75 vol.% nanoparticle concentration and at a flow rate of 8 L/min. The minimum fluid flow rate is sufficient to get the maximum enhancement for heat transfer rate since 8 L/min provides considerable improvement in heat transfer. Because of the addition of methanol, some drawbacks, including fouling, surface erosion, and instability, were rectified. Hence, future studies will be explored with alcohol-based base fluids to extract further benefits from the nanofluids.

ACKNOWLEDGMENT

The authors are grateful to the management of the Kongu Engineering College and the Department of Chemical Engineering for the facility provided.

NOMENCLATURE

Al_2O_3	Aluminum Oxide
TiO_2	Titanium dioxide
ZnO	Zinc Oxide
Fe_2O_3	Iron Oxide
CuO	Copper Oxide
SiO_2	Silicon dioxide
CNT	Carbon Nano Tubes
D	Dimension
D_H	Hydraulic diameter, m
ΔT_{LMTD}	Logarithmic Mean Temperature Difference
M	Methanol
W	Water
m	Mass, kg
U	Overall Heat transfer coefficient, W/m^2 °C
N_{Nu}	Nusselt number, dimensionless
N_{Pr}	Prandtl Number, dimensionless
N_{Re}	Reynolds number, dimensionless
Q	Heat Flux, W
Cp	Specific heat capacity, J/(kg °C)
PHE	Plate Heat Exchanger
Pr	Prandtl number, dimensionless
H	Heat transfer coefficient, W/m^2 °C
H_h	Hot Fluid Heat transfer coefficient, W/m^2 °C
Hc	Cold Fluid Heat transfer coefficient, W/m^2 °C
vol. %	Volume %
Greek symbols	
β	corrugation angle, °
ρ	density, kg/m^3
μ	dynamic viscosity, Pa s
ø	nanoparticle volume fraction, dimensionless
k	thermal conductivity, W/(m K)

REFERENCES

[1] S.U.S. Choi, S. Lee, S. Li, J.A. Eastman, J. Heat Transfer 121 (1999) 280–289. https://doi.org/10.1115/1.2825978.

[2] M. Sabiha, R. Saidur, S. Mekhilef, O. Mahian, Renewable Sustainable Energy Rev. 51 (2015) 1038–1054. https://doi.org/10.1016/j.rser.2010.11.035.

[3] T. Mare, S. Halelfadl, S. Duret, P. Estelle, Exp. Therm. Fluid Sci. 35 (2011) 1535–1543. https://doi.org/10.1016/j.expthermflusci.2011.07.004.

[4] D. Huang, Z. Wu, B. Sunden, Int. J. Heat Mass Transfer 89 (2015) 620–626. https://doi.org/10.1016/j.ijheatmasstransfer.2015.05.082.

[5] S.P. Manikandan, N. Dharmakkan, M.D. Sri Vishnu, H. Prasath, R. Gokul, Hem. Ind. 75 (2021) 341–352. https://doi.org/10.2298/HEMIND210520031S.

[6] S.P. Manikandan, R. Baskar, Period. Polytech., Chem. Eng. 62 (2018) 317–322. https://doi.org/10.3311/PPch.11676.

[7] M.M. Sarafraz, A.D. Baghi, M.R. Safaei, A.S. Leon, R. Ghomashchi, M. Goodarzi, C.X. Lin, Energies 12 (2019) 1–13. https://doi.org/10.3390/en12224327.

[8] B. Mehta, D. Subhedar, H. Panchal, Z. Said, J. Mol. Liq. 56 (2022) 120034, p.120034. https://doi.org/10.1016/j.molliq.2022.120034.

[9] B. Mehta, D. Subhedar, Mater. Today: Proc. 56 (2022) 2031–2037. https://doi.org/10.1016/j.matpr.2021.11.374.

[10] Y.H. Kwon, D. Kim, L. Chengguo, J.K. Lee, J. Nanosci. Nanotechnol. 11 (2011) 5769–5774. https://doi.org/10.1166/jnn.2011.4399.

[11] S. Zeinali Heris, H. Taofik, H. Nassan, S. H. Noie, H. Sardarabadi, M. Sardarabadi, Int. J. Heat Fluid Flow 44 (2013) 375–382. https://doi.org/10.1016/j.ijheatfluidflow.2013.07.006.

[12] B. Sahin, E. Manay, E. F. Akyurek, J. Nanomater. 2015 (2015) 1–10. https://doi.org/10.1155/2015/790839.

[13] I. Rashidi, O. Mahian, G. Lorenzini, C. Biserni, S.

Wongwises, Int. J. Heat Mass Transfer 74 (2014) 391–402. https://doi.org/10.1016/j.ijheatmasstransfer.2014.03.030.

[14] D. Wen, Y. Ding, Int. J. Heat Mass Transfer 47 (2004) 5181–5188. https://doi.org/10.1016/j.ijheatmasstransfer.2004.07.012.

[15] L.S. Sundar, M.K. Singh, A. Sousa, Int. Commun. Heat Mass Transfer 44 (2013) 7–14. https://doi.org/10.1016/j.icheatmasstransfer.2013.02.014.

[16] S.D. Pandey, V.K. Nema, Exp. Therm. Fluid Sci. 38 (2012) 248–256. https://doi.org/10.1016/j.expthermflusci.2011.12.013.

[17] P.V. Durga Prasad, S. Gupta, M. Sreeramulu, L.S. Sundar, M.K. Singh, A.C.M. Sousa, Exp. Therm. Fluid Sci. 62 (2015) 141–150. https://doi.org/10.1016/j.expthermflusci.2014.12.006.

[18] S.P. Manikandan, N. Dharmakkan, S. Nagamani, Chem. Ind. Chem. Eng. Q. 28 (2022) 95–101. https://doi.org/10.2298/CICEQ210125021M.

[19] S.E.B. Maiga, C.T. Nguyen, N. Galanis, G. Roy, Superlattices Microstruct. 35 (2004) 543–557. https://doi.org/10.1016/j.spmi.2003.09.012.

[20] S.P. Manikandan, R. Baskar, Chem. Ind. Chem. Eng. Q. 24 (2018) 309–318. https://doi.org/10.2298/CICEQ170720003M.

[21] S.P. Manikandan, N. Dharmakkan, M.D. Sri Vishnu, H. Prasath, R. Gokul, G. Thiyagarajan, G. Sivasubramani, B. Moulidharan, Chem. Ind. Chem. Eng. Q. 29 (2023) 225–233. https://doi.org/10.2298/CICEQ220430029S.

[22] W. Ajeeb, R.R.T. da Silva, S.S. Murshed, S.S., Appl. Therm. Eng. 218 (2023) 119321. https://doi.org/10.1016/j.applthermaleng.2022.119321.

[23] X. Wang, X. Xu, J. Thermophys. Heat Transfer 13 (1999) 474–480. https://doi.org/10.2514/2.6486.

[24] S. Singh, S.K. Ghosh, Int. J. Numer. Methods Heat Fluid Flow 32 (2022) 2750–2777. https://doi.org/10.1108/HFF-08-2021-0580.

[25] M.M. Sarafraz, Chem. Biochem. Eng Q. 30 (2017) 489–500. https://doi.org/10.15255/CABEQ.2015.2203.

[26] C. Pang, J.Y. Jung, Y.T. Kang, Int. J. Heat Mass Transfer 56 (2013) 94–100. https://doi.org/10.1016/j.ijheatmasstransfer.2012.09.031.

[27] S. Kumar, S.K. Singh, D. Sharma, Heat Transfer Eng. 44 (2023) 1703–1718. https://doi.org/10.1080/01457632.2022.2148342.

[28] E. Firouzfar, M. Soltanieh, S.H. Noie, S.H. Saidi, Appl. Therm. Eng. 31 (2011) 1543–1545. https://doi.org/10.1016/j.applthermaleng.2011.01.029.

[29] W. Ajeeb, S.S. Murshed, S.S., Nanomaterials 12 (2022) 3634. https://doi.org/10.3390/nano12203634.

[30] B. Mehta, D. Subhedar, Mater. Today: Proc. 62 (2022) 418–425. https://doi.org/10.1016/j.matpr.2022.01.448.

[31] B. Mehta, D. Subhedar, H. Panchal, K.K. Sadasivuni, Int. J. Thermofluids 20 (2023) 100410. https://doi.org/10.1016/j.ijft.2023.100410.

[32] X. Yang, Y. Yan, D. Mullen, Appl. Therm. Eng. 33–34 (2012) 1–14. https://doi.org/10.1016/j.applthermaleng.2011.09.006.

[33] M.M. Sarafraz, A.D. Baghi, M.R. Safaei, A.S. Leon, R. Ghomashchi, M. Goodarzi, C.X. Lin, Energies 12 (2019) 1–13. https://doi.org/10.3390/en12224327.

[34] N. Dharmakkan, P.M. Srinivasan, S. Muthusamy, A. Jomde, S. Shamkuwar, C. Sonawane, H. Panchal, Case Studies in Thermal Engineering 44 (2023) 102805. https://doi.org/10.1016/j.csite.2023.102805.

[35] S.P. Manikandan, R. Baskar, Chem. Ind. Chem. Eng. Q. 27 (2021) 15–20. https://doi.org/10.2298/CICEQ191220020P.

[36] S.P. Manikandan, R. Baskar, Chem. Ind. Chem. Eng. Q. 27 (2021) 177–187. https://doi.org/10.2298/CICEQ200504036P.

[37] N. Putra, P. Thiesen, W. Roetzel, J. Heat Transfer 125 (2003) 567–574. https://doi.org/10.1115/1.1571080.

[38] B. Barbés, R. Páramo, E. Blanco, M.J. Pastoriza-Gallego, M. M. Piñeiro, J.L. Legido, J. Therm. Anal. Calorim.111 (2013) 1615–1625. https://doi.org/10.1007/s10973-012-2534-9.

[39] L.S. Sundar, M.K. Singh, A. Sousa, Int. Commun. Heat Mass Transfer 49 (2013) 17–24. https://doi.org/10.1016/j.icheatmasstransfer.2013.08.026.

[40] B. Bakthavatchalam, K. Habib, R. Saidur, B. Baran, K. Irshad, J. Mol. Liq. 305 (2020), 112787. https://doi.org/10.1016/j.molliq.2020.112787.

[41] S.M.S. Murshed, P. Estell´e, Renew. Sustain. Energy Rev. 76 (2017) 1134–1152. https://doi.org/10.1016/j.rser.2017.03.113.

[42] S.M.S. Murshed, Heat Transf. Eng. 33 (8) (2012) 722–731. https://doi.org/10.1080/01457632.2011.635986.

[43] R. Martínez-Cuenca, R. Mondragón, L. Hernández, C. Segarra, J.C. Jarque, T. Hibiki, J.E. Juliá, Appl. Therm. Eng. 98 (2016) 841–849. https://doi.org/10.1016/j.applthermaleng.2015.11.050.

PERIASAMY MANIKANDAN SRINIVASAN
PRADEEP KUMAR CHINNUSAMY
RAGHUL THANGAMANI
SURIYA PALANIRAJ
PRANESH RAVICHANDRAN
SURYA KARUPPASAMY
YOKESHWARAN SANMUGAM

Department of Chemical Engineering, Kongu Engineering College, Erode, India

NAUČNI RAD

UTICAJ NANOFLUIDA Al_2O_3-VODA-METANOL PRENOS TOPLOTE U PLOČASTOM IZMENJIVAČU TOPLOTE

Pločasti izmenjivač toplote je jedan od najmanjih i najefikasnijih izmenjivača toplote na tržištu. Ova studija ima za cilj da proceni uticaj metanol-vode kao osnovnog fluida na prenos toplote u pločastom izmenjivaču toplote. Za ovu studiju, nanočestice aluminijum oksida (Al_2O_3) su korišćene u različitim odnosima (0,25, 0,5 i 0,75 vol. %) u baznoj tečnosti (10 vol.% metanola i 90 vol.% vode) za pripremu nanofluida. Na dve različite temperature (55 °C i 60 °C), sa različitim brzinama protoka (2 do 8 L/min) i različitim koncentracijama nanočestica (0,25% do 0,75%), istražene su termofizičke karakteristike i konvektivni prenos toplote. Opšti zaključak je da je kombinacijom nanočestica Al_2O_3 i tečnosti na bazi metanola i vode došlo do značajnog poboljšanja na toploj i hladnoj strani i u ukupnom koeficijentu prenosa toplote. Primećeno je da korišćenje nanofluida Al_2O_3/metanol-voda može značajno smanjiti temperaturni gradijent u izmenjivaču toplote i poboljšati njegove performanse. Maksimalne vrednosti koeficijenta sa strane toplog fluida od 4300 V/m^2°C, koeficijenta sa strane hladnog fluida od 4600 V/m^2°C i ukupnog koeficijenta od 2200 V/m^2°C određene su za koncentraciju nanočestica od 0,75 vol.% pri brzini protoka od 8 L/min.

Ključne reči: Al_2O_3, bazni fluid, prenos toplote, metanol, nanofluid, pločasti izmenjivač toplote.

Chemical Industry & Chemical Engineering Quarterly

Available online at
Association of the Chemical Engineers of Serbia *AChE*
www.ache.org.rs/CICEQ

Chem. Ind. Chem. Eng. Q. 30 (3) 265−273 (2024) CI&CEQ

IMENE GHEZAL[1,2]
ALI MOUSSA[1,2]
IMED BEN MARZOUG[1,3]
AHMIDA EL-ACHARI[4,5]
CHRISTINE CAMPAGNE[4,5]
FAOUZI SAKLI[1,3]

[1]Textile Engineering Laboratory, University of Monastir, Ksar-Hellal, Tunisia

[2]National Engineering School of Monastir, University of Monastir, Monastir, Tunisia

[3]Higher Institute of Technological Studies of Ksar-Hellal, Ksar-Hellal, Tunisia

[4]Université Lille Nord de France, Lille, France

[5]ENSAIT, GEMTEX, 2 Allée Louise et Victor Champier, Roubaix, France

SCIENTIFIC PAPER

UDC 677

DEVELOPMENT OF A MULTI-LAYERED, WATERPROOF, BREATHABLE FABRIC FOR FULL-WEATHER APPAREL

Article Highlights

- A multi-layered, waterproof, breathable fabric was designed by assembling five layers
- The five layers were a coated knit, a non-woven fabric, a membrane, a veil, and an open-work knit
- The waterproof and breathable properties of the designed laminate were evaluated
- Mechanical performances of the obtained system were investigated

Abstract

In this research, a laminate was produced by assembling five textile layers. These layers were a coated double-sided knitted structure, a non-woven fabric, a hydrophilic membrane that was thermally assembled to a surface veil, and an open-work knitted fabric. The laminated textile's breathability, windproofness, and waterproofness were evaluated. The multi-layered fabric was windproof, and its water vapor permeability was 347.297 $g\cdot m^{-2}\cdot s^{-1}$ *(CV= 8.902%). Its resistance to water penetration was equal to 117.68 Schmerber (CV = 7.81%). The assembled fabric's mechanical properties were also evaluated. Young's modulus values were equal to 2 MPa (CV= 8.613%) and 1.6 MPa (CV= 8.349%) for both fabric directions. Its flexural rigidity was 5056.659 mg·cm and its surface total deformation was lower than 450 µm when measured under 20, 40, 60, and 80 mN loads. Based on the results obtained, it was concluded that the developed multi-layered fabric could be used to produce raincoats and jackets to protect the wearer from light rain and drizzle.*

Keywords: multi-layered fabric, waterproof fabric, windproof laminate, breathable textile, tensile resistance, flexural rigidity.

Over the last few years, waterproof, breathable fabrics (WBFs) have been gaining interest [1–3]. They were considered an alternative to waterproof fabrics known for causing discomfort to the wearer because of moisture condensation in their inner sides [4]. Since then, the breathability concept has appeared. It was defined as the ability of a garment to evacuate insensible and sensible perspirations and to assure thermophysiological comfort to the wearer. This capacity was always considered a basic need [5–8]. WBFs that are mostly obtained with coating and laminating processes assure not only the protection of the wearer from wind and rain and their moisture evacuation from the skin to the outer side of the fabric [1,8–11]. They were first used for medical gowns, military and fireman uniforms, and space suits for producing traditional apparel [3,10].

Unfortunately, WBF manufacturing processes are quite complex, and the garments produced are expensive [16]. In our previous study [17], an attempt was made to produce a waterproof, breathable fabric

---

Correspondence: I. Ghezal, Textile Engineering Laboratory, University of Monastir, 5070 Ksar-Hellal, Tunisia.
E-mail: elghezalimene@hotmail.com
Paper received: 7 April, 2023
Paper revised: 12 November, 2023
Paper accepted: 18 December, 2023

https://doi.org/10.2298/CICEQ230407029G

by coating a double-sided knitted structure with a mixture of fluorocarbon and acrylic resins. The coating process was optimized to obtain the best performance in terms of waterproofness and breathability. Based on the results obtained, we reported that the coated knitted structure was hydrophobic and breathable; however, its windproofness and resistance to water penetration needed to be ameliorated [17]. Since fabric's breathability and surface hydrophobicity are senseless without windproofness and water resistance, in this study, four other layers were added to the already coated fabric to enhance its performance. The aim of this research was the development of a multi-layer fabric by using a flexible manufacturing process and unsophisticated equipment. The obtained laminate comprises a knitted lining, two non-woven fabrics, a hydrophilic membrane, and a coated double-sided knitted structure. The waterproof, breathable properties and the mechanical performances of the designed textile laminate were finally evaluated and discussed.

MATERIALS AND METHODS

Materials and used chemicals

The laminate outer layer was a double-sided knitted structure coated with an acrylic paste (CHTT GLOSSY FINIH) and a fluorocarbon resin (Fluorotex FO/57W). Both products were kindly supplied from CHIMITEX-Tunisia. The coated laminate outer layer was reproduced based on our previous study [17] and using the screen coating method.

To produce the hydrophilic membrane, an aliphatic polyester polyurethane copolymer dispersion (Appretan® N 5122 liq.) and an acrylic ester copolymer dispersion (Appretan® N 92101 liq.) were used. Archroma, Spain, kindly provided used products for the membrane synthesis. A Werner Mathis laboratory coating machine AG (Oberhasi, Switzerland) with a knife on a roller was used to obtain the hydrophilic non-porous membrane. The obtained membrane thickness was equal to 293 µm ± 3.94%.

The remaining laminate layers, i.e., the polyester non-woven fabrics and the knitted lining, were purchased from the Tunisian textile market.

Laminate development

A five-layer laminate was developed (Fig. 1). The inner layer of the multi-layered fabric (in direct contact with the wearer's skin) is an open-work knitted polyester structure. The second layer is a carded polyester veil thermally assembled with a polymeric membrane (third layer). The hydrophilic membrane was produced with 16 g of polyester polyurethane and 40 g of acrylic ester copolymers. It was dried at 115 °C and reticulated at 165 °C. Drying and reticulation times were equal to 3 minutes each. The fourth laminate layer is a non-woven fabric produced with the carding method. The laminate outer layer is a coated cotton-polyester double-sided knitted fabric in contact with the surrounding environment. The coating applied to the polyester face was prepared with 2.71% fluorocarbon resin and 412 g (m^{-2}) acrylic paste. Coating treatment conditions were already described and optimized by Ghezal *et al.* [17]. The five layers were finally assembled with an overlock stitch on the edges.

Figure 1. A real image of the produced multi-layered fabric and the hydrophilic membrane.

Air permeability and windproofness measurement

The clothing's air permeability influences the wearer's thermophysiological comfort [18]. For this reason, it is important to evaluate this factor when designing waterproof, breathable fabrics. The different textile layers and the laminated fabric air permeabilities were measured with an FX3300 measuring device (TEXTEST Instrument, Zürich, Switzerland). Tests were done according to the ISO 9237 standard [19]. Samples were cut in a circular form with an area equal to 20 cm^2 each and subjected to an airflow with 100 Pa pressure. Each test was repeated three times.

Water vapor permeability measurement

A breathable fabric is a textile that ensures wearing comfort by evacuating insensible and sensible perspirations from the microclimate between the skin and the clothing layer to the surrounding atmosphere [8,20,21]. The water vapor permeability was measured using a gravimetric method. For this purpose, a water vapor permeability tester (type M 261, SDL Atlas, Rock Hill, USA) was used. Water vapor permeabilities for the different layers were determined as specified in the BS 7209 standard [22].

Resistance to water penetration measurement

The resistance to water penetration was measured using the hydrostatic pressure method as specified in the ISO 811: 2018 standard [23]. Measurements were carried out with a TEXTEST

Automatic Hydrostatic Head Tester device type FX 3000 HYDROTESTER III from Textest Instrument, Zürich, Switzerland. Obtained values are the results of three replicates.

Tensile strength measurement

The ultimate tensile strength was evaluated with an LLOYD LS5 machine (AMETEK, Pennsylvania, USA) as specified in the ISO 13934-1 standard [24]. Samples were cut in a rectangular form with length and width equal to 150 and 50 mm, respectively. The applied preload and cross-head speed were equal to 5 kN and 10 mm.min^{-1}, respectively. Measurements were done in both sample directions, and the presented results were the average of five tests each.

Fabric stiffness evaluation

The fabric's bending behavior was tested to evaluate the laminate stiffness with a Cantilever tester (SDL Atlas, Rock Hill, South Carolina, USA) as specified by the ASTM D1388 standard [25]. Sampling was performed according to the laminate warp direction.

Outer surface deformation analysis

To investigate the micro-mechanical deformation of the laminate outer surface, a universal surface tester (UST) was used. A fabric square with a 30 mm edge was placed under the sample stage. A rounded-shaped steel ball tip with a diameter equal to 5 mm was moved along the tested surface. The scanned distance was fixed at 20 mm. The same sample path was scanned three times. Under 20, 40, 60, and 80 mN loads, tests were done. Total, permanent, and elastic deformations were recorded and plotted for each applied load with software connected to the UST device.

RESULTS AND DISCUSSION

Study of the physical properties of the multi-layered fabric

To produce the waterproof, breathable fabric, a five-layer laminate was designed by assembling a coated cotton-polyester double-sided knitted structure, two non-wovens, a hydrophilic membrane, and an open-work knitted fabric. The developed laminate and its different layers and positions are presented in Figure 2.

Due to its surface hydrophobicity, the coated double-sided knitted fabric was used as an outer layer for the developed laminate. The polyester outer face of the knitted structure was coated with a fluorocarbon resin and an acrylic paste. The use of the coated fabric as an outer layer of the laminate would guarantee the protection of the wearer against rain and wind. In previous studies, water repellency and breathability of the outer layer were evaluated [17,26]. The coated double-sided knitted fabric was found to be breathable, and its coated polyester outer surface was hydrophobic; however, its water resistance and windproofness must be ameliorated [17,26].

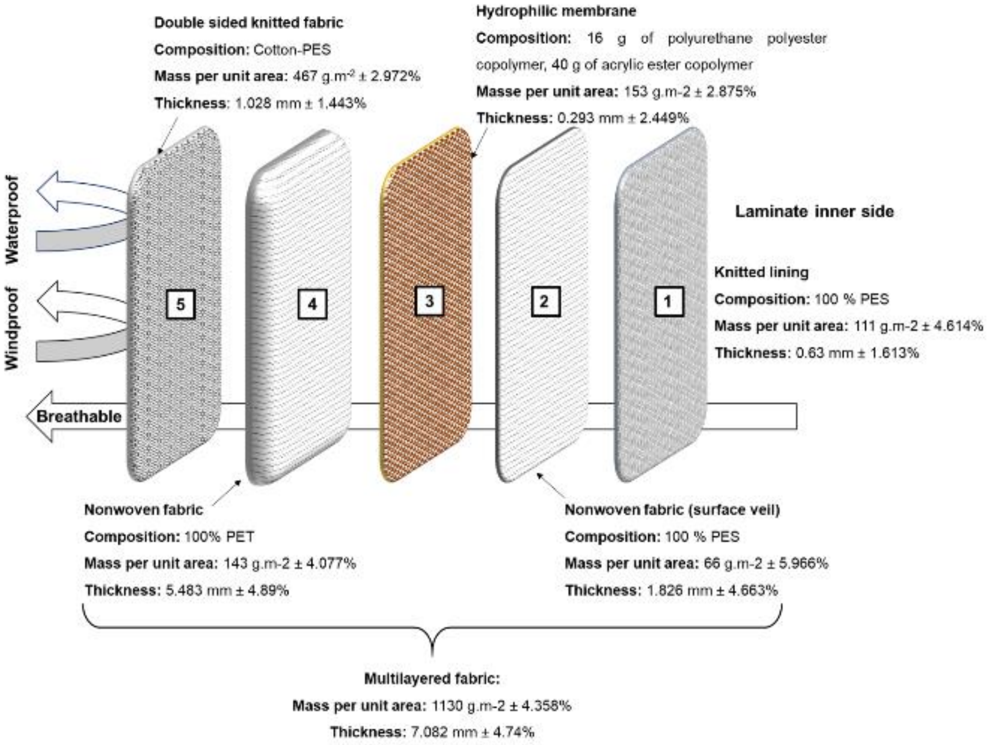

Figure 2. Different laminate layers and characteristics.

The lamination of additional layers was investigated to enhance the performances of the coated fabric in terms of water resistance and windproofness. First, a polyester non-woven fabric was assembled with the coated knitted structure to enhance its resistance to water penetration and windproofness without restricting its breathability. An open-work knitted structure was added as a lining layer to give the assembly a cloth-like feel. It was found that the non-woven structure did not really enhance the assembly resistance to water and wind. For this reason, the idea of adding a non-porous membrane emerged. The hydrophilic membrane would not restrict the other layers' breathability. On the other hand, it would impart resistance to wind and water penetration to the already assembled three layers.

In a previous study [27], a super-absorbent material was joined to the back of a hydrophobic lining. The hydrophobic material was placed in direct contact with the skin to facilitate moisture transport to the super-absorbent material and to ensure the wearer's skin was dry [27].

The fragile, non-porous hydrophilic membrane was thermally assembled to a hydrophobic polyester veil to preserve it and prevent its direct contact with the wearer's skin. The hydrophobic veil would also ensure rapid moisture transport from the skin to the non-porous hydrophilic membrane to prevent sweat accumulation near the wearer's skin. The non-woven hydrophobic veil was inserted at the other side of the hydrophilic membrane to facilitate moisture evacuation and avoid microclimate saturation.

The fabric's physical properties affect a garment's manufacturing process and comfort properties. Thereby, masses per unit area and thicknesses were measured for the different layers and the developed laminate, respectively, according to ISO 3801 [28] and ISO 5084 [29] standards. Obtained results are shown in Table 1. Each value is the average of three measurements.

Table 1. Characteristics of the different used layers and the produced laminate.

Layers	Structure and composition	Mass per unit area (g.m^{-2})	Thickness (mm)
Layer 1 (Laminate inner layer)	Polyester open-work knitted structure.	110.767 ± 4.614%	0.630 ± 1.613%
Layer 2	Polyester surface veil.	66.218 ± 5.966%	1.826 ± 4.663%
Layer 3	Non-porous membrane mainly composed of acrylic ester and polyester polyurethane copolymers.	152.96 ± 2.875%	0.293 ± 2.449%
Layer 4	Polyester non-woven fabric.	143.124 ± 4.077%	5.483 ± 4.890%
Layer 5 (laminate outer layer)	Double-sided knitted structure with a cotton inner face and a polyester outer face.	466.96 ± 2.972%	1.028 ± 1.443%
Laminate	_	1130.329 ± 4.358%	7.028 ± 4.74%

Evaluating the laminate breathability and waterproofness

The air permeability was measured to evaluate the breathability of the different layers used and the produced laminate. Obtained results are shown in Table 2. The air permeability of the knitted polyester lining was equal to 2779 L.m^{-2}.s^{-1} ± 2.771%. The highest air permeabilities were obtained for the non-woven structures. Values were equal to 3188 L.m^{-2}.s^{-1} ± 2.832% and 3603 L.m^{-2}.s^{-1} ± 3.474% for the non-woven fabric and the surface veil, respectively. The hydrophilic membrane is a pore-free medium, so its air permeability was equal to 0 L.m^{-2}.s^{-1}. Based on the previous study of Ghezal *et al.* [17], it was found that the double-sided knitted structure pores were clogged with the applied coating, which explains the low air permeability value of the laminate outer face. The final laminated fabric was also windproof since the hydrophilic membrane was used to produce the five-layer system.

The hydrophilic membrane's water vapor permeability was 504.148 g.m^{-2}.day^{-1} ± 1.283%. Hence, the hydrophilic membrane is impermeable to air but can still evacuate water vapor through its section into the surrounding environment. Based on the obtained results, it is obvious that the outer layer has a higher vapor permeability than the dense membrane. Indeed, the passage of water vapor through a porous medium is easier and faster than through a non-porous one. So, it can be deduced that the water vapor permeability is related to the chemical nature and structure of the tested layer. On the other hand, the hydrophilic membrane indeed restricted the air passage through the five-layer system. However, it was found that the laminated fabric is still breathable. In a previous study, Ghezal *et al.* [17] determined the water vapor permeability index of the coated cotton- polyester double-sided knitted structure. It was equal to 83.852% ± 0.589% [17]. Based on both results, it is obvious that the absence of pores in the tested structures does not restrict water vapor evacuation.

Body thermophysiological comfort is related to the garment's porosity and air permeability [30,31]. Nevertheless, moisture can be evacuated, and breathability can be achieved even with non-porous structures via physico-chemical mechanisms [8,12]. Indeed, for a porous structure, the water vapor evacuation can occur through pores according to Poiseuille, transitional, or Knudsen flows. For non-porous media, water vapor molecule evacuation is assured by the adsorption-diffusion-desorption (solution-diffusion) mechanism [32,33]. The water vapor permeability of the developed multi-layered system was determined to be 347.9 g.m^{-2}.day^{-1} (CV= 8.902%). Based on the obtained result, the multi-layered system was judged breathable.

In the literature, many test methods were used to evaluate fabrics' breathability [34,35]. Mukhopadhyay and Midha [36] reported water vapor transport (WVT) values for some laminates. The WVT for two-layer and three-layer polytetrafluoroethylene laminates were equal to 205 and 174 g.h^{-1}m^{-2}, respectively [36]. A lower value of 119 g.h^{-1}.m^{-2} was reported for a hydrophilic polyurethane laminate [36]. In a previous study [34], the WVT value for Pertextion fabric was measured with the upright cup method and according to the ASTM E 96 B standard. The obtained value was 446.4 g.m^{-2}.day^{-1} [34]. Gugliuzza and Drioli [35] also reported the water vapor transmission rates (WVTR) measured according to the ASTM E96B for Dermizax® (a laminate with a non-porous membrane) and Helly-Tech Extreme® (a laminate with a microporous membrane) to be 700 and 785.2 g.m^{-2}.day^{-1}, respectively [34,35]. Although breathability is a fundamental characteristic when producing a waterproof, breathable fabric, comparing the water vapor permeabilities, water vapor transmission rates, or water vapor resistance values is arduous due to the variety of procedures and standards used to evaluate a fabric's breathability [34,36].

The resistance to water penetration was also investigated with the hydrostatic pressure method. The obtained results are presented in Table 2. The non-porous membrane resistance to water penetration is the lowest one. This value is insufficient for producing a waterproof fabric. The resistance to water penetration of the coated double-sided knitted structure was previously determined [17]. Even though the outer layer of the laminate fabric was coated, its resistance to water penetration is still very low due to the presence of pores in the coated structure and the deformation of the coated knitted fabric under the applied hydrostatic pressure [17]. After assembling the five layers, the resistance to water penetration of the multi-layer system increased and reached 117.68 Schmerber ± 7.81% due to the decrease in the fabric-free volume and the higher resulting thickness obtained after layers assembling.

In general, fabric type, structure, and properties influence its air permeability, water vapor permeability, and resistance to water penetration [37,38]. Knitted structures' high porosity and deformability rate originate from their high air and water vapor permeability, low windproofness, and insufficient water penetration resistance [11]. Based on the obtained results, it can be deduced that the developed multi-layer system is windproof and breathable. However, its resistance to water penetration needs to be ameliorated. To conclude, the developed multi-layer system can produce raincoats and jackets to protect the wearer from drizzle and light rain.

Table 2. Waterproof, breathable characteristics of the coated double-sided fabric, the non-porous membrane, and the multi-layer fabric.

Characteristics	Air permeability (ISO 9237, 1995)	WVP/ WVPI (BS 7209, 1990)	RWP (ISO 811, 2018)
Coated double-sided fabric [17]	147.75 L.m^{-2}.s^{-1} ± 1.156%	80.490% ± 0.589%	78.453 Schmerber ± 1.8%
Non-porous membrane	0 L.m^{-2}.s^{-1}	504.148 g.m^{-2}.day^{-1} ± 1.283%	88.260 Schmerber ± 1.6%
Multi-layered fabric	0 L.m^{-2}.s^{-1}	347,927 g.m^{-2}.day^{-1} ± 8.902%	117.680 Schmerber ± 7.8%

WVP is the water vapor permeability (g.m^{-2}.day^{-1}), WVPI is the water vapor permeability index (%), and RWP (Schmerber) is the resistance to water penetration.

Study of the tensile strength

Tensile strength was evaluated for the different used layers and the resulting laminate. The obtained results are recapitulated in Table 3. The strain was also measured according to warp and weft directions for the knitted lining. It was equal to 0.484 ± 5.843% and 1.332 ± 1.069%, respectively. The loop geometry explained the important deformation mode when the load was applied according to the weft direction.

For the two used non-wovens, the strain according to both tested directions was almost the same. For the non-woven fabric (layer 3), the strain was equal to 0.515 ± 3.088% and 0.720 ± 6.277%, respectively, according to the production direction and transverse one. For the non-woven surface veil, deformation values according to the production direction and the transverse one were equal to 0.479 ± 4.085% and 0.433 ± 4.111%, respectively.

When testing the tensile strength of the hydrophilic membrane, the strain was 3.194 ± 2.940% and 1.951 ± 0.327%, respectively, according to the production and transverse directions. Even though the deformation rate for the hydrophilic membrane was the highest according to the production direction, the highest deformation of the multi-layered system was obtained when tests were done according to direction (2).

To evaluate the tensile strength of the laminate, strain, stress, work at maximum load, and Young's modulus were determined from the stress-strain curves (Fig. 3) and recapitulated in Table 3.

Tests were done according to both laminate directions. The first direction, which was noted as direction (1), is defined by the warp directions of the coated fabric and the knitted lining and the production directions of the two used non-wovens and the hydrophilic membrane. The direction (2) is the transverse one.

The stress at maximum load and Young's modulus values were almost similar for both multi-layer fabric directions. The highest strain value was equal to 1.844 ± 0.289%. It was obtained when tests were done according to direction (2). This direction corresponds to the weft direction of both used knitted structures and the production direction of the other three layers.

Table 3. Tensile strength tests result for the laminate according to both directions.

Tensile mechanical properties	Direction (1)	Direction (2)
Strain (mm/mm)	0.581 ± 3.350%	1.844 ± 0.289%
Stress at maximum load (MPa)	1.438 ± 3.194%	1.864 ± 1.450%
Work at maximum load (J)	11.512 ± 4.440%	33.332 ± 5.575%
Young's modulus (MPa)	2 ± 8.613%	1,6 ± 8.349%

Based on the results obtained, it was found that the deformation aspect of the multi-layered fabric is very similar to the deformation mode of the double-sided knitted structure already investigated by Ghezal et al. [39]. Therefore, it can be deduced that the laminate mechanical behavior is governed by its knitted-coated outer layer.

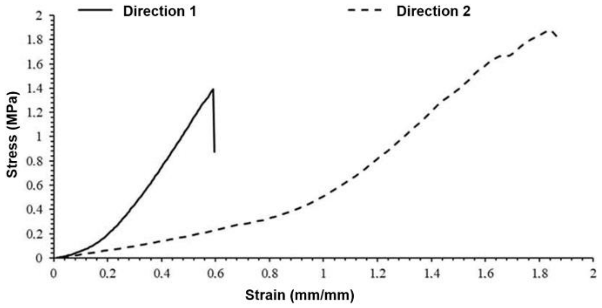

Figure 3. Stress (MPa) versus strain (mm/mm) for the multi-layer fabric in both directions.

Study of the flexural rigidity of the multi-layered fabric

The flexural rigidity of the multi-layer fabric was evaluated with a Cantilever Tester. The bending length was determined according to the laminate warp direction and was equal to 3.55 cm (CV= 1.99%). Using flexural rigidity and mass per unit area of the designed laminate, the flexural rigidity was determined to be 5057 mg.cm as specified by the ASTM D1388 standard. The high obtained flexural rigidity value results from the coating treatment applied to the laminate polyester outer face, the properties of the different layers, and the assembling technologies used for producing the multi-layered system.

Study of the surface profile and deformation of the multi-layered fabric

The polyester face of the laminate outer layer was tested under different loads before and after the coating treatment. Measurements were recorded under 20, 40, 60, and 80 mN loads. The results obtained were almost the same under the different loads used. Thus, only profiles and deformations under 20 mN loads were represented in Fig. 4.

The uncoated laminate outer layer surface profile is presented in Figure 4a. The polyester multifilament pattern was easily perceptible, and the total deformation reached 1200 µm. A smoother surface was obtained after the coating treatment (Fig. 4b). Also, elastic and permanent deformation values decreased significantly. Therefore, it can be deduced that the coating treatment ameliorated the deformation

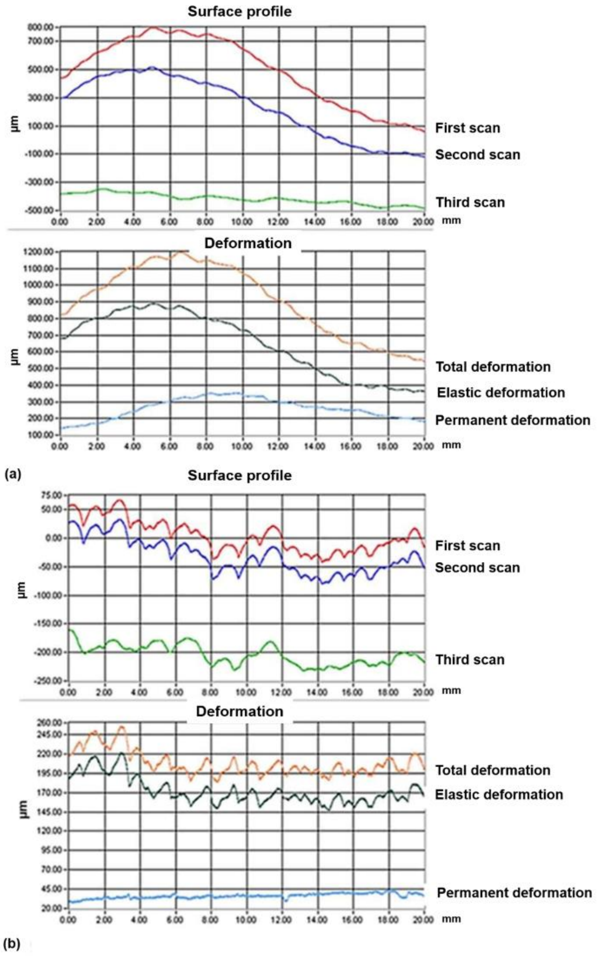

Figure 4. . Surface profiles and deformations of the polyester face of the laminate outer layer under 20 mN applied load. (a): Uncoated layer, (b): Coated layer.

resistance of the laminate outer layer.

To analyze the effect of the applied load on the laminate outer layer, the coated polyester surface was tested under 20, 60, and 80 mN loads. From Fig. 4b, it can be noticed that the highest elastic and total deformations obtained under a 20 mN load were equal to 220 and 260 µm, respectively. When the applied load was increased to 60 and 80 mN, the total deformation increased significantly and reached 400 µm (Figure 5). From Figs. 4b and Figure 5, it can be noticed that the elastic deformation is more important than the permanent one for low solicitations. Thus, the coated surface can return to its initial state after deformation.

CONCLUSION

The aim of this research was to employ simple methods for producing a waterproof, breathable laminate. For this purpose, the final product was assembled into a coated knitted structure, a non-woven fabric, a membrane, a surface veil, and an open-work knitted lining. The multi-layered fabric air permeability, water vapor permeability, and resistance to water penetration were equal to 0 L.m^{-2}. s^{-1}, 347.927 g.m^{-2}.day^{-1}, and 117.68 Schmerber, respectively. The developed fabric was judged windproof and breathable. However, its resistance to water penetration needed improvement. Considering that the mechanical properties affect the final product handle, manufacturing process, and durability, the tensile strength, flexural rigidity, and surface deformation were also investigated. The strain-stress curves of the tested laminate showed that it has the same tensile behavior as its coated knitted outer layer. The multi-layered fabric tensile strength could be ameliorated by using other assembling techniques. The laminate outer surface deformation was also evaluated. It was found that the laminate outer layer had almost an elastic behavior under low loads. To conclude, the developed multi-layered fabric can produce raincoats and jackets to protect the wearer from light rain and drizzle.

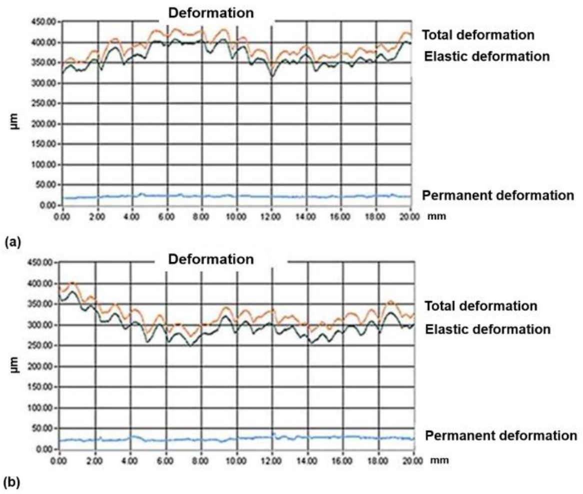

Figure 5. Surface deformations of the coated polyester face of the laminate outer layer under different applied loads. (a): Applied load: 60 mN, (b): Applied load: 80 mN.

REFERENCES

[1] I. Ozen, J. Eng. Fiber. Fabr. 7 (2012) 63-69. https://doi.org/10.1177/155892501200700402.

[2] J. Zhao, X. Wang, Y. Xu, P. He, Y. Si, L. Liu, J. Yu, B. Ding, ACS Appl. Mater. Interfaces 12 (2020) 15911-15918. https://doi.org/10.1021/acsami.0c00846.

[3] Y. Liu, X. Zhu, Y. Chen, C. Zhou, Z. Chen, M. Hao, X. Hu, B. Yan, Text. Res. J., 93 (2023) 2273-2289. https://doi.org/10.1177/00405175221144086.

[4] Y.J. Ren, J.E. Ruckman, Int. J. Cloth. Sci. Technol. 16 (2004) 335-347. https://doi.org/10.1108/09556220410527255.

[5] S. Kaplan, A. Okur, The meaning and importance of clothing comfort: A case study for Turkey, J. Sens. Stud., 23 (2008) 688-706. https://doi.org/10.1111/j.1745-459X.2008.00180.x.

[6] B. Das, A. Das, V.K. Kothari, R. Fanguiero, M. de Araújo, Autex Res. J. 7 (2007) 100-110. https://www.autexrj.com/cms/zalaczone_pliki/4-07-2.pdf.

[7] B. Das, A. Das, V.K. Kothari, R. Fangueiro, M. de Araújo, Autex Res. J. 7 (2007) 194-216. https://www.autexrj.com/cms/zalaczone_pliki/5-07-3.pdf.

[8] H.Z. Özek, in Waterproof and Water Repellent Textiles and Clothing, J. Williams Ed., Woodhead Publishing, Sawston (2018), p. 25. https://doi.org/10.1016/B978-0-08-101212-3.00002-2.

[9] A. Sadighzadeh, M. Valinejad, A. Gazmeh, B. Rezaiefard, Polym. Eng. Sci. 56 (2016) 143-149. https://doi.org/10.1002/pen.24200.

[10] T. Zhang, Z. Xu, J. Zhao, L. Huang, Macromol. Mater. Eng. 305 (2020) 2000370. https://doi.org/10.1002/mame.202000370.

[11] N. Oğlakcıoğlu, C. Akduman, B. Sarı, Polym. Eng. Sci. 61 (2021) 669-679. https://doi.org/10.1002/pen.25607.

[12] A. Mukhopadhyay, V.K. Midha, J. Ind. Text. 37 (2008) 225-262. https://doi.org/10.1177/1528083707082164.

[13] A. Mukhopadhyay, V.K. Vinay Kumar Midha, J. Ind. Text. 38 (2008) 17-41. https://doi.org/10.1177/1528083707082166.

[14] I. Jahan, Adv. Res. Text. Eng. 2 (2017). https://austinpublishinggroup.com/textile-engineering/fulltext/arte-v2-id1018.php.

[15] D. Sun, in High-Performance Apparel, J. McLoughlin, T. Sabir Eds., Woodhead Publishing, Sawston (2017), p. 307. https://doi.org/10.1016/B978-0-08-100904-8.00015-8.

[16] Market Research Report (UC 6368), https://www.marketsandmarkets.com/Market-Reports/waterproof-breathable-textiles-market-243428009.html [accessed 5 November 2023].

[17] I. Ghezal, A. Moussa, I. Ben Marzoug, A. El-Achari, C. Campagne, F. Sakli, Coatings, 12 (2022) 1572. https://doi.org/10.3390/coatings12101572.

[18] E. Öner, A. Okur, J. Text. Inst. 106 (2015) 1403-1414. https://doi.org/10.1080/00405000.2014.995931.

[19] International Organization for Standardization, ISO 9237: Determination of the Permeability of Fabrics to Air (1995). https://www.iso.org/standard/16869.html.

[20] S. Wenger, R. Csapo, M. Hasler, B. Caven, T. Wright, T. Bechtold, W. Nachbauer, Text. Res. J. 89 (2019) 528-540. https://doi.org/10.1177/0040517517750648.

[21] T.H. Chen, W.P. Chen, M.J.J. Wang, J. Occup. Environ. Hyg. 11 (2014) 366-376. https://doi.org/10.1080/15459624.2013.875181.

[22] The British Standards Institution, BS 7209, (1990). https://knowledge.bsigroup.com/products/specification-for-water-vapour-permeable-apparel-fabrics/standard.

[23] International Organization for Standardization, ISO 811 (2018). https://www.iso.org/standard/65149.html.

[24] International Organization for Standardization, ISO 13934-1, (2013). https://www.iso.org/standard/60676.html.

[25] American Society for Testing Materials, ASTM D1388-18 (2002). https://www.astm.org/d1388-18.html.

[26] I. Ghezal, A. Moussa, I. Ben Marzoug, A. El-Achari, C. Campagne, F. Sakli, Fibers Polym. 21 (2020) 910-920. https://doi.org/10.1007/s12221-020-8936-6.

[27] S. Houshyar, R. Padhye, O. Troynikov, R. Nayak, S. Ranjan, J. Text. Inst., 106 (2015) 1394-1402. https://doi.org/10.1080/00405000.2014.995930.

[28] International Organization for Standardization, ISO 3801 (1977). https://www.iso.org/standard/9335.html.

[29] International Organization for Standardization, ISO 5084 (1996). https://www.iso.org/standard/23348.html.

[30] R. Mishra, J. Militky, M. Venkataraman, in Nanotechnology in Textiles: Theory and Application, R. Mishra, J. Militky Eds., Woodhead Publishing, Sawston (2019), p. 311. https://doi.org/10.1016/B978-0-08-102609-0.00007-9.

[31] P. Li, Q. Zhang, T.T. Chadyagondo, G. Li, H. Gu, N. Li, Fibers Polym. 21 (2020) 1444-1452. https://doi.org/10.1007/s12221-020-9860-5.

[32] A.R. Tehrani-Bagha, Adv. Colloid Interface Sci. 268 (2019) 114-135. https://doi.org/10.1016/j.cis.2019.03.006.

[33] W. Zhou, X. Yu, Y. Li, W. Jiao, Y. Si, J. Yu, B. Ding, ACS Appl. Mater. Interfaces, 13 (2021) 2081-2090. https://doi.org/10.1021/acsami.0c20172.

[34] E.A. McCullough, M. Kwon, H. Shim, Meas. Sci. Technol., 14 (2003) 1402-1408. https://doi.org/10.1088/0957-0233/14/8/328.

[35] A. Gugliuzza, E. Drioli, J. Memb. Sci., 446 (2013) 350-375. https://doi.org/10.1016/j.memsci.2013.07.014.

[36] A. Mukhopadhyay, V.K. Midha, Waterproof breathable fabrics, in Handbook of Technical Textiles: Volume 2: Technical Textile Applications, A. Richard Horroks, Subhash C. Anand Eds., Woodhead Publishing, Sawston (2016),p. 27. https://doi.org/10.1016/B978-1-78242-465-9.00002-1.

[37] Y. Yang, L. Chen, T. Naveed, P. Zhang, A. Farooq, Text. Res. J. 89 (2019) 1983-1996. https://doi.org/10.1177/0040517518783349.

[38] A.H. Taieb, S. Msahli, F. Sakli, J. Text. Eng. Fash. Technol. 5 (2019) 111-117. https://doi.org/10.15406/jteft.2019.05.00191.

[39] I. Ghezal, A. Moussa, I. Ben Marzoug, A. El-Achari, C. Campagne, F. Sakli, Cloth. Text. Res. J. 37 (2019) 235-248. https://doi.org/10.1177/0887302X19850637.

IMENE GHEZAL[1,2]
ALI MOUSSA[1,2]
IMED BEN MARZOUG[1,3]
AHMIDA EL-ACHARI[4,5]
CHRISTINE CAMPAGNE[4,5]
FAOUZI SAKLI[1,3]

[1]Textile Engineering Laboratory, University of Monastir, Ksar-Hellal, Tunisia
[2]National Engineering School of Monastir, University of Monastir, Monastir, Tunisia
[3]Higher Institute of Technological Studies of Ksar-Hellal, Ksar-Hellal, Tunisia
[4]Université Lille Nord de France, Lille, France
[5]ENSAIT, GEMTEX, 2 Allée Louise et Victor Champier, Roubaix, France

NAUČNI RAD

RAZVOJ VISESLOJNE, VODOOTPORNE, PROZRAČNE TKANINE ZA ODEĆU ZA SVE VREMENSKE USLOVE

U ovom istraživanju laminat je proizveden sklapanjem pet tekstilnih slojeva. Ovi slojevi su bili obložena dvostrano pletena struktura, netkana tkanina, hidrofilna membrana, koja je termički spojena na površinski veo, i pletena tkanina otvorenog tipa. Procenjivane su prozračnost, vetrootpornost i vodootpornost laminiranog tekstila. Višeslojna tkanina je bila otporna na vetar, a propustljivost vodene pare iznosila je 347,3 g m^{-2} s^{-1} (CV= 8,9%). Njena otpornost na prodiranje vode iznosila je 117,7 Schmerber (CV = 7,8%). Takođe, procenjena su mehanička svojstva sastavljene tkanine. Vrednosti Jangovog modula bile su 2 MPa (CV= 8,6%) i 1,6 MPa (CV= 8,3%) za oba smera tkanine. Njena krutost na savijanje iznosila je 5056,7 mg cm, a ukupna deformacija površine bila je niža od 450 µm kada je merena pod opterećenjem od 20, 40, 60 i 80 mN. Na osnovu dobijenih rezultata, zaključeno je da se razvijena višeslojna tkanina može koristiti za proizvodnju kabanica i jakni za zaštitu korisnika od slabe kiše.

Ključne reči: višeslojna tkanina, vodootporna tkanina, laminat otporan na vetar, prozračni tekstil, otpornost na zatezanje, krutost na savijanje.